DANMARKS OG GRØNLANDS GEOLOGISKE UNDERSØGELSE RAPPORT 2001/75

Three-Phase Immiscible WAG Injection: Transport Mechanisms and Multiscale Reservoir Models

Technical Report for EFP-99 project
ENS J.nr. 1313/99-0011

A. Winter, J.K. Larsen (DTU),
N. Bech and D. Olsen

Edited by A. Winter

GEOLOGICAL SURVEY OF DENMARK AND GREENLAND
MINISTRY OF ENVIRONMENT AND ENERGY

GEUS

DANMARKS OG GRØNLANDS GEOLOGISKE UNDERSØGELSE RAPPORT 2001/75

Three-Phase Immiscible WAG Injection: Transport Mechanisms and Multiscale Reservoir Models

Technical Report for EFP-99 project
ENS J.nr. 1313/99-0011

A. Winter, J.K. Larsen (DTU),
N. Bech and D. Olsen

Edited by A. Winter

GEOLOGICAL SURVEY OF DENMARK AND GREENLAND
MINISTRY OF ENVIRONMENT AND ENERGY

GEUS

PREFACE

This report is concerned with three-phase transport in porous media at two distinct levels:

- microscopic or pore network scale;
- macroscopic scale.

The microscopic scale in reservoir modeling has undergone a paradigm shift initiated in the late 1980's: the introduction of *randomness* at the pore network scale to explain key mechanisms of multiphase transport underlying relative permeabilities and capillary pressure functions.

Randomness is a dominating feature at the microscale. However, the final goal of most reservoir engineering tasks is at the macroscale. This is the reason why so many current research efforts dealing with complex porous media are concerned with *upscaling*. One of the goals of upscaling is to replace microscopic randomness by more reliable *deterministic* variables and parameters. This is achieved by transforming multiscale systems into *single-scale* systems. An alternative approach to upscaling is that of *multiscale modeling*. Multiscale modeling does not involve any transformations of multiscale systems to systems with a single scale. On the contrary, different models are employed at different physical scales to build a comprehensive description of systems that could not be modeled otherwise. More specifically, multiscale modeling is particularly suitable in the case of systems controlled by mechanisms requiring a very accurate and computationally expensive description at one scale and a coarser description at another scale.

The role of multiscale modeling in this project has been to provide the parameters pertaining to the multiphase flow (relative permeabilities and capillary pressure functions) with the same status as that created by geostatistical methods for their counterparts pertaining to the single phase flow (porosities and absolute permeabilities). In the latter case, a large number of measurements is conducted by oil companies and routinely assigned to grid blocks. A successful completion of this task would stop the unfortunate practice of using a *single* relative permeability function in computer simulations of complex hydrocarbon reservoirs.

One of the central themes of this project has been the design of a two-scale reservoir simulator consisting of a network model sequentially linked with a macroscopic reservoir model. This hybrid reservoir simulator was subsequently used to develop an iterative procedure for the determination of three-phase relative permeabilities for gas injection and WAG injection recovery processes, respectively. In the former case, the method performed satisfactorily leading to a set of relative permeabilities for the two-scale system. In the case of the WAG injection, however, emerging oil ganglia destroyed the coupling between the constituent models of the two-scale simulator. Consequently, the iterative procedure collapsed. The problem could be avoided by applying a more sophisticated network model. The design of such a network model and its application in a multiscale reservoir simulator encompassing length scales spanning the microscopic to the macroscopic is a challenging topic for a new research project.

Anatol Winter

GEUS, August 4, 2001

List of More Important Symbols

Roman letters
a = Archie's constant
A = Area [m^2]
A = Hamaker constant [J]
B = Formation volume factor
B = Width of inlet chamber [m]
b = Klinkenberg correction factor
C = Kozeny's constant,
C = Concentration [m^{-3}],
C = Constant in hysteresis model
C = Compressibility [bar^{-1}]
Ca = Capillary number
d = Characteristic length [m]
D = Weighting factor for scanning curves
D = Depth [m]
E_{pump} = Work delivered by pump [J]
e = Elementary charge [C]
f = Fractional flow function
f = Mobility ratio
$f(\varepsilon)$ = function used for calculation of entry pressure as a function of height to width ratio.
F = Formation factor
f_1, f_2 = Parameters in analytical expression for dimensionless resistance factor
g = Conductance [$m^3/s*Pa$]
g = Gravitational constant [m/s^2]
G = Conductance matrix [$m^3/s*Pa$]
h = Thickness [m]
h = Height [m]
h_w = Pseudo water film thickness [m]
I = Identity matrix
$J(S_w)$ = Leverett-J function
K = Boltzman's constant [J/K]
K = Absolute permeability [mD]
k = Single-phase Permeability [m^2]
k_{ocw} = Relative permeability to oil at connate water saturation
k_0 = Shape factor
l = Length [m]
L = Length [m]
L_e = effective length [m]
M = Viscosity ratio
$M_{accumulate}$= Accumulated mass inside control volume [kg]
M_{in}= Mass entering control volume [kg]
M_{out}= Mass leaving control volume [kg]
M_{sink}= Mass leaving the control volume as a sink [kg]
$M(t)$= Magnetization at time t
m = Cementation factor

m_{in} = Mass flux rate into control volume [kg/s∗m^2]
m_{out} = Mass flux rate out of control volume [kg/s∗m^2]
n = Saturation exponent
n = Number of a node or grid cell
n_{corner} = Number of corners in an angular pore cross-section
n = total number of fluid phases
N = Total number of nodes in a network
N_b = Bond number
P = Pressure [Pa]
P_a = Attractive component in disjoining pressure isotherm [Pa]
P_r = Repulsive term in disjoining pressure isotherm [Pa]
p_c = Capillary pressure [Pa]
P_c = Capillary pressure [Pa]
$P_{r,c}$ = Reduced capillary pressure [Pa]
P_{cd} = Bounding drainage capillary pressure curve [Pa]
P_{ci} = Bounding imbibition capillary pressure curve [Pa]
$P_{critical}$ = Critical capillary pressure for pore level mechanism [Pa]
P^* = Critical pressure for breakdown of a thin film [Pa]
$\boldsymbol{P}$ = Pressure vector [Pa]
Q = Flow rate [m^3/s]
q = Flow rate between two nodes [m^3/s]
q = Strength of sink [Kg/m^3·s]
$\boldsymbol{Q}$ = Flow vector [m^3/s]
Re = Reynolds number
r = Radius [m]
r_d = Roundness of corner
R = Ratio of interfacial curvatures
R = Radius of grain [m]
R_c = Critical ratio of interfacial curvatures
R_o = Resistivity of 100% saturated formation [ohm·m]
R_w = Resistivity of formation brine [ohm·m]
R_t = Resistivity of formation [ohm·m]
S_{gc} = Critical gas saturation, fraction
S_{org}= Oil saturation at residual gas saturation
S_{orw}= Oil saturation at residual water saturation
S_{wc}= Connate water saturation
S_{wirr} = Irreducible water saturation
S_{wi} = Initial water saturation
S_{why} = Saturation reversal point
S_{or} = Residual oil saturation
S^*_{or} = Residual oil saturation for scanning curves
S = Saturation
S = Spreading coefficient [N/m]
S_p = Specific surface with respect to porosity [m^{-1}]
S_g = Specific surface with respect to grain volume [m^{-1}]
S_{tot} = Specific surface with respect to total volume [m^{-1}]
T = Temperature [K]
T_2= Spin-spin relaxation constant [ms]
t = Time [s]

t_e = NMR echo time [ms]
u = Velocity [m/s]
v = Velocity [m/s]
v_e = Effective velocity [m/s]
v_{darcy} = Darcy velocity [m/s]
V = Volume [m^3]
w = Bandwidth of preconditioning matrix
x = Coordinate
x = Eigenvector [m/sec]
x = width of rectangle
Δx = Axial increment [m]
y = Coordinate
y = Height of rectangle
Δy = Axial increment [m]
z = Coordinate
z = Thickness [m]
Δz = Axial increment [m]

Greek Letters

α = Half angle
β = Dimensionless resistance factor,
β = Inertia parameter
δ = Partial derivative symbol
ε = Scanning Parameter
ε = Ratio between height and width of rectangle
ε_0 = Permitivity of vacuum [C^2/J·m]
ε_r = Relative permitivity
ϕ = Porosity
λ = Phase mobility or eigenvalue
μ = Viscosity [cp]
η = Characteristic speed [m/s]
Γ = Curvature [m^{-1}]
φ = Angle
λ_d = Debye screening length [m]
μ = Viscosity [Pa·s]
ψ_0 = Surface Potential [V]
ψ_1 = Dimensionless resistance factor parameter
ψ_2 = Dimensionless resistance factor parameter
ψ_3 = Dimensionless resistance factor parameter
ψ_4 = Dimensionless resistance factor parameter
π = 3.141593
$\Pi(z)$ = Disjoining pressure isotherm [Pa]
θ = Contact angle [Rad]
ρ = Density [kg/m^3]
σ = Interfacial Tension (IFT) [mN/m]
τ = Dimensionless water conductance factor

Φ = Potential for a pore-level displacement mechanism [Pa]
Ω = Discriminant

Indices

b = bulk
c = chamber
$drain$ = drainage
g = gas
h = hydrocarbon
imb = Imbibition
lw = least wetting
ma = matrix
max = maximum
min = minimum
nw = nonwetting
net = network
o = oil
ow = oil-water
og = oil-gas
oo = oil-oil
$rock$ = rock
$scan$ = scanning
t = throat
T = total
tot = total
u = umbilic point
w = water, wetting
wo = water-oil
wg = water-gas
ww = water-water
x = coordinate direction x
y = coordinate direction y
z = coordinate direction z

Abbreviations

CSI = Chemical Shift Imaging
FWHM = Full Width Half Maximum
FWL = Free Water Level
GOC = Gas Oil Contact
OIP = Oil In Place
OWC = Oil Water Contact
MDSS = Measured Depth Sub Sea
NMR = Nuclear Magnetic Resonance

1. Introduction

1.1 Overview of the project

Development of improved and enhanced oil recovery methods involves numerical simulations of multiphase fluid transport. Reservoir simulations require a reliable geological model of the reservoir. Geological models contain a faithful representation of spatial heterogeneity consistent with available measurements of reservoir properties, such as porosity and permeability. In most cases, reservoir engineers have sufficient information to define reliable distributions of these properties. On the other hand, multiphase properties, such as relative permeabilities, are usually given less attention. For improved oil recovery projects, such as e.g., water-alternating-gas (WAG) injection processes, accurate measurements of relative permeability functions, which control recovery rate, are crucial. Unfortunately, experimental procedures for determination of relative permeabilities are expensive, time consuming, and often unreliable. In many cases, a *single* set of relative permeabilities is assigned to a given rock type, or even to whole regions of an oil field. Consequently, development decisions, concerning e.g., possible improved oil recovery projects, are often erroneous leading to huge financial losses and abandonment of planned activities.

In principle, both absolute and relative permeabilities can be computed numerically as space and time averages of the appropriate pore-scale quantities. These methods are feasible under conditions not far from equilibrium. Unfortunately, many transport mechanisms, e.g., that governing three-phase transport in WAG-injection processes, often occur very far from equilibrium. This is due to strong gradients of pressure and composition. This is why reservoir rock properties, such as relative permeabilities, become history dependent emerging as highly nonlinear functions of phase saturations.

This project deals with multiscale modeling of three-phase water-alternating-gas (WAG) injection processes. The adopted research strategy consists of three steps. In the first step, the displacement physics is examined using artificial pore networks (micromodels) as model media. A catalog of pore-scale transport mechanisms governing three-phase transport mechanisms is created and implemented in a network simulator. In the second step, the network simulator is coupled in series with a 1-D, grid-based reservoir simulator. The two models are then combined to determine relative permeabilities and capillary pressure functions for a prespecified sequence of saturation changes. Finally, the third step is to assign the relative permeabilities and capillary pressure functions determined by the multiscale reservoir simulator to a geological model implemented in the grid-based reservoir simulator.

1.2 Relative permeabilities and capillary pressures functions for three-phase transport

Presence of three phases may have important implications for hydrocarbon recovery efficiency. For example, it is well known that gas injection increases oil recovery efficiency because it enables oil to flow at lower saturations than with water alone.

Macroscopic models of three-phase transport involve two basic ingredients: capillary pressures and relative permeabilities.

Capillary pressures are defined by the following relationship:

$$P_{cij} = P_i - P_j, \tag{1.2.1}$$

where the subscripts describe the three phases, gas, oil, and water and P_i is the pressure of the phase i.

Relative permeabilities can be determined from the Darcy law generalized to multiphase flow,

$$v_i = \frac{kk_{ri}}{\mu_i \nabla (P_i - \rho_i g z)} \tag{1.2.2}$$

where v_i is the Darcy velocity of phase i, μ_i is the viscosity, ρ is the density, g is the gravitational acceleration, k is the absolute permeability, and z is the vertical coordinate.

Three-phase relative permeability functions are usually depicted using an equilateral saturation triangle. The saturation of a single phase is represented by a vertex of the saturation triangle while the opposite base line represents a saturation of 0% of that phase corresponding to a two-phase situation (cf. Figure 1.1). In this limit, the transport problem is reduced to that of the classical Buckley-Leverett theory (cf. Buckley-Leverett, 1941).

It is often convenient to draw the so-called iso-perms in the saturation triangle defined as the lines where the magnitude of the relative permeability functions are the same. The iso-perm lines parallel to a base line indicate that the relative permeability of a phase is a function of its own saturation only. On the other hand, curved iso-perm lines indicate that the relative permeability also depends on saturations of the other phases.

Irreducible and residual saturations of fluid phases are represented as regions in the three-phase saturation triangle with either two phases or a single phase mobile. The boundaries separating these regions are dependent on the saturation history and, consequently, difficult to establish experimentally. Considerable inter- and extrapolation may be needed to describe the residual regions within the entire saturation triangle. Moreover, the boundaries between the regions are not necessarily straight lines. Finally, it should be noted that all three phases are mobile only within a limited region of the saturation triangle (cf. Figure 1.1).

Experimental measurements of three-phase relative permeabilities are quite time consuming due to the large number of experiments required to obtain data points from the entire saturation triangle. Consequently, a limited number of experimental measurements has been reported in the literature. Saraf et al. (1982) gives an overview of the published experimental studies of three-phase relative permeability functions. These measurements indicate that the relative permeability to the water and gas phases in a water-wet system is a function of its own saturation only. On the other hand, the relative permeability function to the oil phase is dependent on two saturations. Moreover, the relative permeability function to oil is saturation history dependent. Chatzis et al. (1988 a), Kalaydjian et al. (1993), Zhou, Blunt (1997), and Blunt et al. (1995) presented results showing that when the oil phase spreads between the gas and the water phases, the residual oil saturation is significantly reduced. In addition, the relative permeability to the oil phase generally increases.

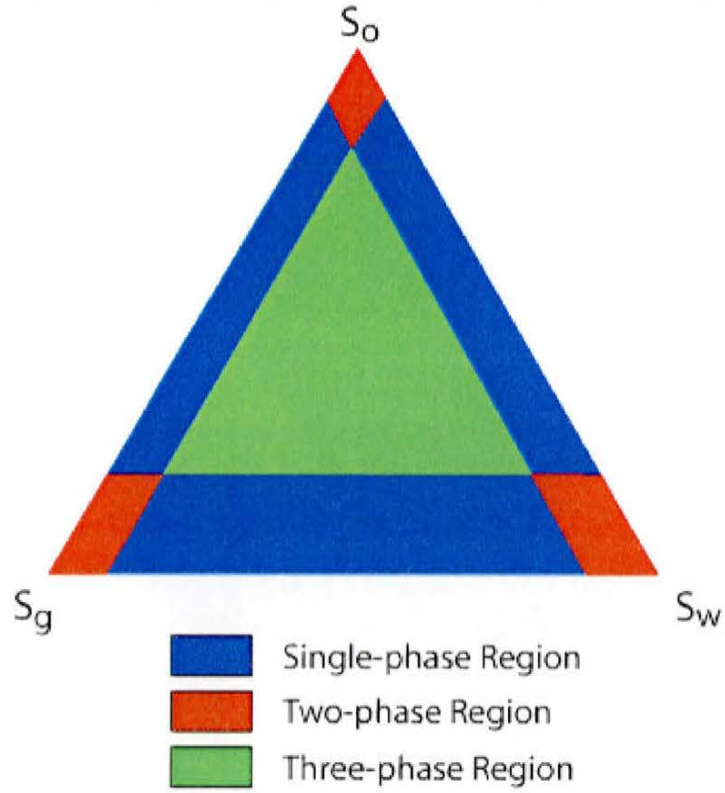

Figure 1.1 An idealized three-phase saturation triangle. The green color indicates the area where all three phases are mobile. The blue areas are saturation regions where two phases are mobile. The red areas are saturation regions where only a single phase is mobile.

The choice of a mathematical model of the three-phase relative permeability functions is crucial to the existence of solutions of a three-phase flow problem. For the Corey-type models of relative permeabilities (cf. eqs. (5.1), (5.2), (5.3) and Section 6.3.3) it has been shown that at an isolated point in the three-phase saturation triangle, the eigenvalues of the Jacobian matrix of f in the (2x2) system of partial differential equations describing mass (volume) conservation,

$$s_t + f_x = 0 \qquad (1.2.3)$$

are real but coincident. In eq. (1.2.3) s is a vector of conserved quantities (e.g. mass), f is the vector of flux terms, x is the space dimension, and t is time. This point is referred to as the umbilic point.

One of the models for relative permeability that have been studied by many authors is the Corey-type model. It is based on the assumption that the relative permeability of each phase is a unique function of its own saturation, and that the first and second derivatives of the relative permeabilities are positive at all points of the saturation triangle where the phases are mobile. In Stone-type models the relative permeabilities to the wetting and nonwetting phases are assumed be unique functions of their own saturations. One the other hand, the relative permeability to the intermediate phase is assumed to be dependent on two saturations.

In a seminal paper dealing with the three-phase flow problem with gravity effects Trangenstein (1989) has shown that the only models that always result in hyperbolic equations are those in which relative permeabilities are unique functions of their own phase saturation. He also demonstrated that for the Stone-type relative permeability functions the so-called elliptic regions might arise within the saturation triangle (cf. Chapters 5 and 6).

Direct measurements of three-phase relative permeabilities for all possible saturation paths in the saturation triangle are not yet established as a part of standard industrial practice. In fact, Stone (Stone, 1970, 1973) assumes that the relative permeability functions can be extracted from two sets of two-phase relative permeabilities. However, some of the predictions obtained from his models were found to be inconsistent with experimental measurements (cf. Nordvedt, 1996). This is why one of the aims of this project has been to find out why the existing models of three-phase flow lead to relative permeability functions that in many cases are incompatible with available experimental data. Our initial strategy was to test one of the important assumptions of macroscopic models of multiphase flow in porous media, namely the assumption that the three fluid phases coexisting in the pore space *do not interact* with each other. Another questionable assumption underlying multiphase transport in porous media is that relative permeabilities to a phase depend only on the saturation of that phase. In fact, the influence of all other properties, such as e.g., saturation history, viscosity ratio (cf. Morrow and Collins, 1965, Killough, 1976, Chatzis et al., 1988 and Avraam and Payatakes, 1995) has been entirely neglected. This is probably the main reason why reliability of empirical model of three-flow is much less satisfactory at low oil saturations in comparison with high oil saturations.

In addition to relative permeabilities, another key parameter governing three-phase transport in porous media are capillary pressure functions associated with the interfaces occurring in the pore space: oil-water, oil-gas and gas-water interface. Three-phase capillary pressure measurements are, like three-phase relative permeability functions, difficult to conduct and are rarely measured in the laboratory. This is due to the vast number of measurement points required, difficulties in simultaneous handling of the three phases and interpretation of the results. However, knowledge of three-phase capillary pressure functions is indispensable in most reservoir simulators. Usually, only oil-water and oil-gas capillary pressure functions are measured and the third capillary pressure is deduced from a relation between the three capillary pressures given by

$$P_{cgw} = P_{cow} + P_{cog} \tag{1.2.4}$$

where P_{cgw} is the gas-water capillary pressure, P_{cow} the oil-water capillary pressure, and P_{cog} the oil-gas capillary pressure. This relation assumes that the three phases coexisting in the subsurface are continuous with oil spreading as a thin layer between water and gas.

The capillary pressure usually is regarded as a static property, which describes a static equilibrium between gravitational forces and capillary forces. However, viscous forces arising during fluid flow in the reservoir can balance capillary forces. In the latter case, the capillary pressure actually describes a dynamic equilibrium. In that case the pressure jump across the oil-water interface can not be determined from the Laplace equation alone. In most reservoir simulations, no distinction is made between static and dynamic equilibrium. Experimentally, it has been shown that the capillary pressures functions associated with the two equilibria are not the same (cf. Kalaydjian, 1992a).

The organization of this report is as follows.

Appendix A contains a description of structural properties of the mathematical network model underlying the quasistatic network simulator developed in the course of this project. It extends brief information on this same topic given in Chapter 4.

Appendix B describes a pilot study dealing with a method involving Nuclear Magnetic Resonance (NMR) techniques for determination of phase saturations in the case of three-phase flow through

chalk reservoir rock samples. This study uses the model fluid system consisting of water, n-decane, and benzyl alcohol. The same mixture was used by Grader et al. (1988) in their investigations of three-phase relative permeabilities measured by conventional methods. The initial results indicate that the selected model system is a suitable candidate for determination phase saturations via NMR techniques. Additional investigations of saturation trajectories determined by applying multiscale modeling and a comparison with their counterparts originating from NMR studies are needed.

Appendix C contains three papers written during this project. The first paper entitled *Three-Phase Immiscible WAG Injection: Micromodel Experiments and Network Models was* presented during the SPE/DOE Symposium on Improved Oil Recovery held in Tulsa in April 2000. The second paper entitled *Thin Films, Oil Layers, and Three-Phase Flow in Porous Media* was presented at the 14-th Symposium on Thermophysical Properties held in Boulder, Colorado, in June 2000. It has been submitted to International Journal of Thermophysics. Finally, the third paper entitled *Multiscale Modeling of Relative Permeabilities* has been accepted for presentation at the 22-nd Workshop and Symposium organized by the International Energy Agency (IEA) which will be held in Vienna, Austria (September 9-12, 2001).

Finally, Appendix D contains some additional details concerning the iterative procedure described in Chapter 6 aimed at the determination of three phase relative permeability functions.

1.3 Adopted research strategy

The research strategy adopted in this project consists of the following steps (cf. Figure 1.2):

- A collection of micromodels is manufactured by applying the reactive ion etching (RIE) technique used in the semiconductor industry (cf. Chapter 2).
- The pore-level displacement mechanisms and configuration of the three phases coexisting in a pore space are studied for a given transport process using a collection of micromodels as artificial porous media. A catalog of the observed transport mechanisms is created (cf. Chapter 3).

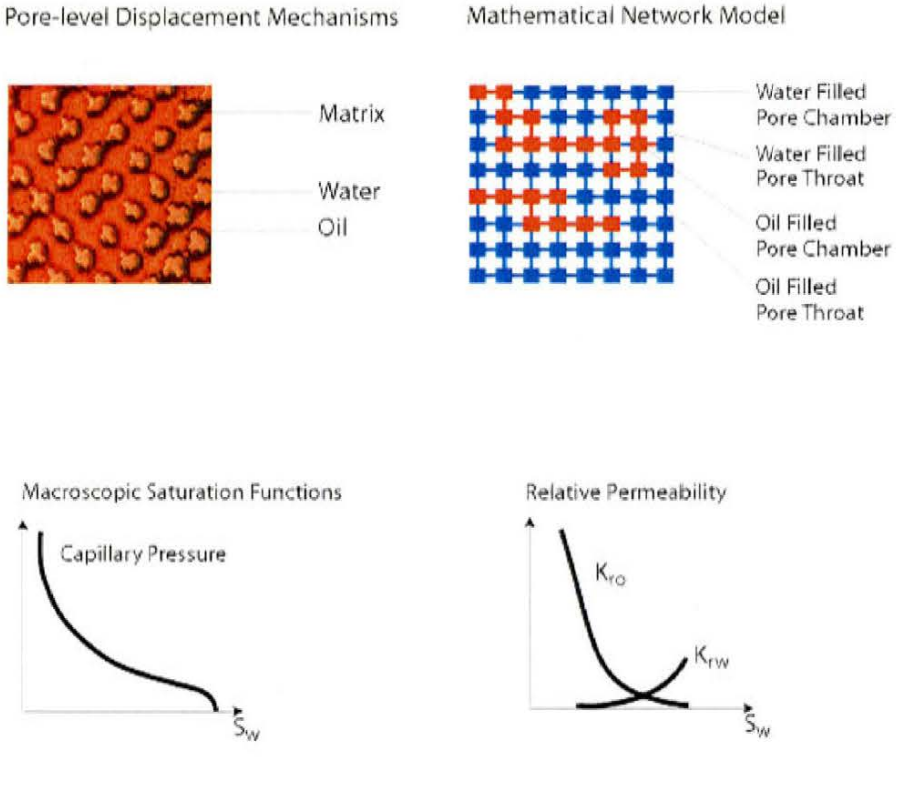

Figure 1.2 The overall strategy: network simulators are used to derive petrophysical properties like saturation paths, capillary pressures, and relative permeabilities that also apply to the macroscopic level.

- The pore-scale three-phase transport mechanisms obtained from the micromodel experiments are implemented in a quasistatic network simulator (cf. Chapter 4). The network simulator contains a mathematical network model describing porous media as a lattice of pore chambers connected by constrictions called pore throats. Their effective size, length, and cross-sectional geometry describe the pores appearing in the network model. The three-phase quasistatic network simulator describes the transport in the pore space as a series of pore-scale events controlled by the magnitude of the capillary pressure. The motion of the fluid phases is assumed to be slow. More specifically, the selection of a particular pore-scale mechanism from the catalog containing all such mechanisms is controlled by the so-called critical capillary pressure, P_c^*, associated with a particular type of displacement. P_c^* can be calculated from the configuration of the fluid phases at the pore level and the local pore geometry.

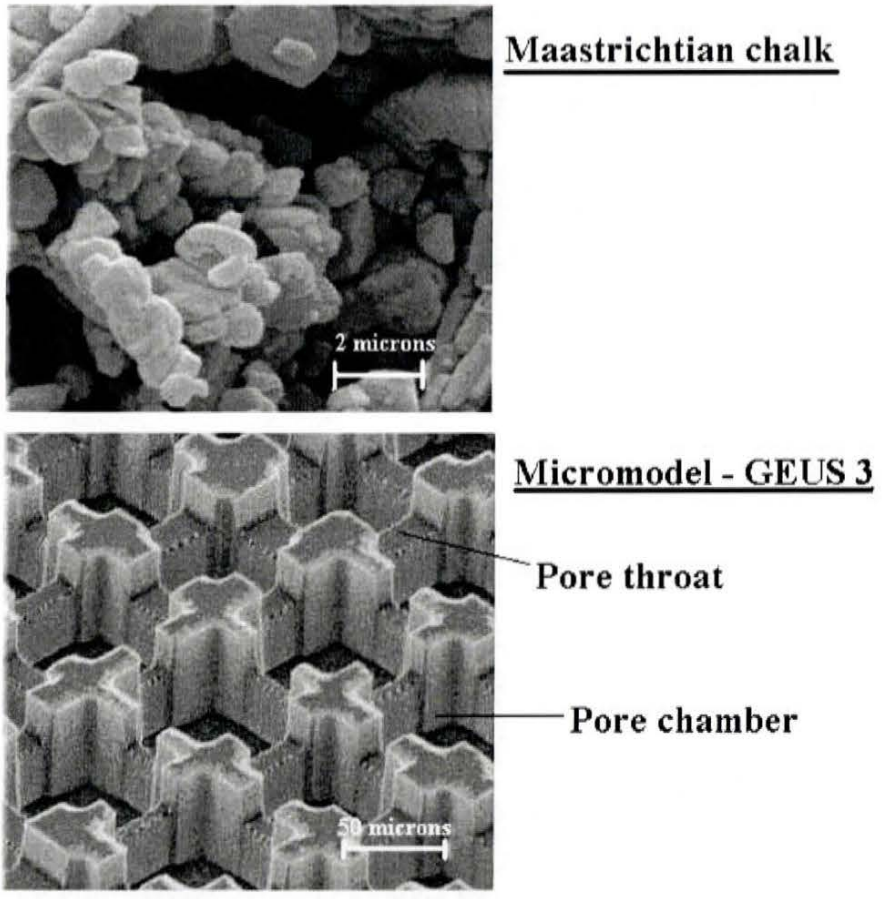

Figure 1.3. Two SEM pictures: (1) pore space of Maastrichtian chalk from the North Sea. (2) Pore space of an artificial porous network, (micromodel) etched in a silicon wafer.

- The three-phase quasistatic network simulator and macroscopic reservoir simulator are used in a iterative procedure to determine a scale-invariant, three-phase relative permeability functions for a prespecified recovery strategy, e.g. the Water-Alternating-Gas (WAG) injection process. The obtained relative permeability functions are *selfconsistent*, i.e. they are representative of both the displacement processes related to the pore-scale level where the capillary forces control the transport properties and to the macroscopic level where the viscous forces dominate the flow (cf. Chapter 6).

- Based on the pore-level configuration of the fluid phases, the conductance of a pore or throat is determined. The conductance between connecting pores is determined using the harmonic mean. By letting the network simulator follow a specific saturation path, the relative permeability functions for a specific saturation path is determined. Assuming that the saturation path obtained from the network simulator also represents the macroscopic displacement process the relative permeability functions can be assumed to create a link between the macroscopic level and the network level (cf. Chapter 6).

1.4 Acknowledgements

The micromodels used in experimental studies of three-phase transport during this project have been manufactured in cooperation with *Mikroelektronik Centret (MIC)* at the Technical University of Denmark (DTU).

2. Design and manufacturing of micromodels

2.1 Micromodels as artificial porous media

This chapter describes design and manufacturing process of physical network models, also referred to as *micromodels*, aimed at studies of three-phase transport mechanisms in chalk reservoirs. The applied design strategy is the same as that used in the production of printed circuits: the reactive ion etching (RIE) applied to silicon wafers. The micromodels were manufactured at the *Mikroelektronik Centret (MIC)* affiliated with the Technical University of Denmark (DTU). The applied design method has been developed in a previous EFP-project (cf. Winter et al., 1998).

The idea of using micromodels as model porous media has been implemented by many researchers. Early investigators used containers filled with glass beads as artificial porous media (cf. Ng et al. 1978, Egbogah and Dawe, 1980). Another approach was to etch a pore network into a glass plate (cf. Mattax and Kyte, 1961, McKellar and Wardlaw, 1982, Chen and Wilkinson, 1985, Chatzis et al., 1988 a, Soll et al., 1991, Øren and Pinczewski, 1994, Avraam and Payatakes, 1995, Coskuner, 1997 and Bernadiner, 1998). Still another widely applied manufacturing strategy was to etch two mirror images of a designed pore network into two separate glass plates. The two plates were subsequently fused together forming a transparent porous medium where pore-level events can be readily observed. The networks etched in glass plates were equipped with varying coordination numbers, pore size distribution functions and chamber-to-chamber distances. Moreover, a layer of silane covering the glass surface modified their wettability properties (cf. Laroche et al., 1998)).

The etching process applied in the design of glass micromodels results in eye-shaped cross-sections of the pores because the etching depth is greater in the center of the pores as compared to their outer parts. The smallest dimension of the pores in glass micromodels is typically in the range of 40-50 microns. The permeability of the glass micromodels is typically several Darcies and thus much larger than in most authentic reservoir rocks.

The accuracy of the desired pore geometry of capillary tubings was greatly improved by using a silicon wafer as matrix material etched by applying the reactive ion etching (RIE) technique (cf. Owete and Brigham, 1987 and Keller et al., 1997). In particular, pore widths as small as 3 microns and nearly perfectly square cross-sections of capillary tunings were obtained by Keller et al. (1997). The disadvantage of using silicon wafers is that they are not transparent. Consequently, a transparent glass plate must cover the etched network and a reflected light microscope must be used for observations of pore-scale transport mechanisms. The surface properties of the porewalls are nonuniform because the surface of the porewalls etched in silicon in general has surface properties different from those of the encapsulating glass plate.

When constructing three-dimensional pore networks in micromodels, special consideration must be given to the details of the design procedure in order to optimize the conditions for visual studies of pore-scale transport mechanisms. For example, bead packs in combination with fluids with identical refractive indices have successfully been used in three-dimensional displacement experiments (Frette et al., 1992). Tzimas et al. (1997) constructed a non-planar micromodel with two layers of pore chambers and throats by fusing three glass plates together. Two networks were etched on either side of the center glass plate. The two etched networks were then connected by drilled holes in the

center glass plate. Two mirror images of the networks situated in the center glass plate were etched in the bounding glass plates, which were subsequently fused on either side of the center glass plate.

2.2 Design and Manufacturing of GEUS Micromodels

The fabrication of GEUS 1, GEUS 2 and GEUS 3 involved four stages:

- Lithographic process
- Etching process
- Surface treatment processes
- Encapsulation of the pore network

2.2.1 Lithographic Process

The activities involved in the lithographic and etching processes are shown in Figure 2.1.
The goal of the lithographic process is to transfer an exact replica of the designed network pattern from a photomask to the surface of the silicon wafer creating a temporary mask for the etching process. A polymeric material sensitive to UV-radiation is used as photoresist. The resist is developed in a negative process where the surface of the resist is exposed to light remains on the wafer while photo resist not exposed to light is removed by a chemical treatment. In most cases, the photoresist is a poor mask for the etching process. Therefore, the wafer has to be covered by a thin layer of aluminium (3000Å) using the Physical Vapour Deposition method (PVD). The PVD method involves three basic steps:

- Evaporation
- Transport
- Condensation

The first step of the PVD method is evaporation of aluminium by heat in vacuum. The *Al* atoms in the vapour have considerable kinetic energy and therefore move away from the heat source. Since the ambient pressure and corresponding gas concentration are low, the *Al* atoms suffer only few collisions, if any, and travel along straight lines. The wafer, where they condense out as the solid aluminum forming a thin and homogeneous layer on the silicon wafer, intercepts some of these atoms.

The wafer's pore network is covered by resist and aluminum. The remaining areas of the wafer are covered by aluminum only. The wafer is then exposed to organic solvents leaving only the aluminum deposited directly on the wafer while aluminum with underlying resist is lifted off.

2.2.2 Reactive Ion Etching (RIE) Technique

The RIE technique is used to etch the pore network into the silicon wafer. RIE is a dry etching technique based on the use of ionised gases. There are two different processes involved in RIE: One of the ionised gases has radicals reacting chemically with the wafer material (reactive etching). Another of the ionised gases provides atoms that are accelerated by electric field acting towards the surface of the wafer. The ionised atoms dislodge the silicon atoms by momentum transfer (nonreactive etching - called sputtering). Thus, RIE is a combination of chemical and physical processes. The right combination of these two processes yields an anisotropic etching. The rate of etching in the vertical direction is much higher as compared to the horizontal direction. Consequently, capillary tubings with nearly perfectly vertical porewalls are created (Figure 2.2). The selection and quantity of gases in addition to a number of other process parameters influences the etching rates and the degree of anisotropy. For more details on the reactive etching process, the reader is referred to Thompson et al. (1994) and Anner (1990).

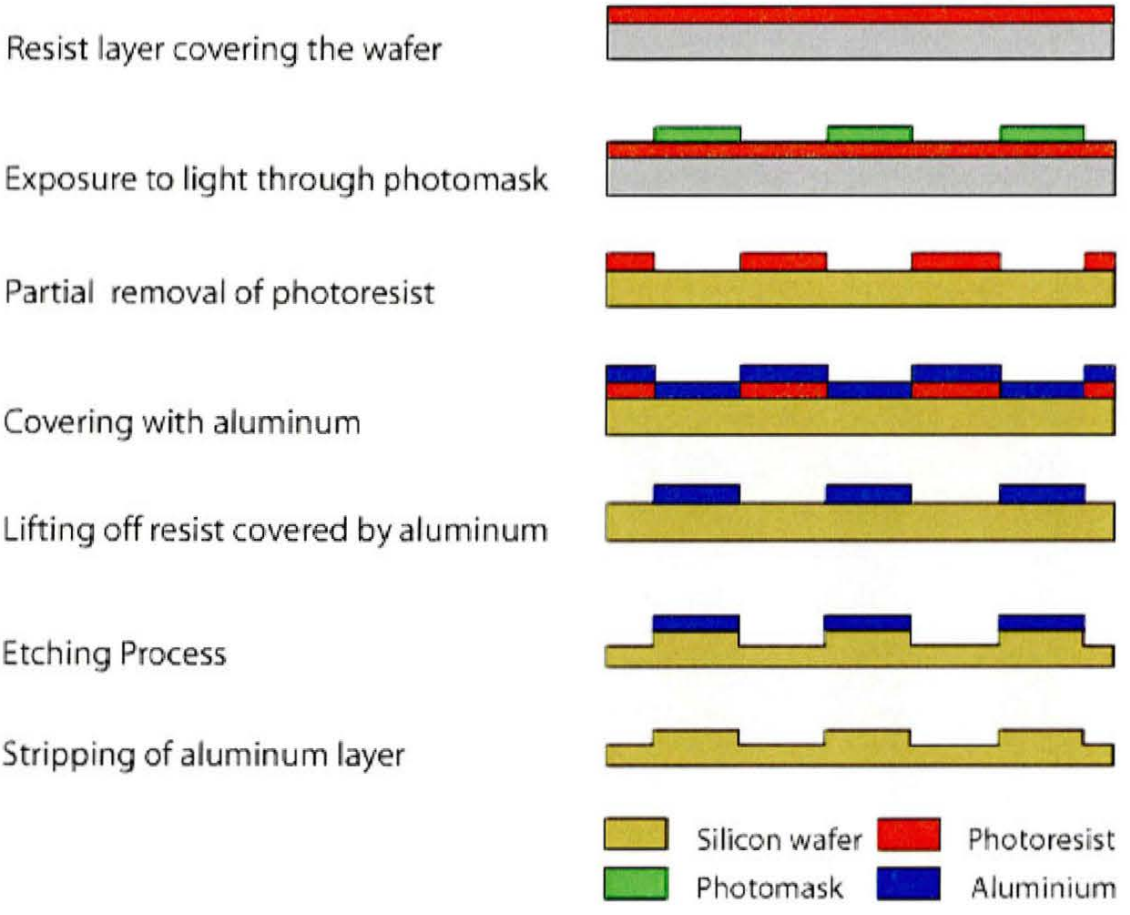

Figure 2.1 Schematic representation of the steps of the lithographic and etching processes in manufacturing of micromodels made of silicon. A Pyrex glass plate subsequently encapsulates the etched network.

The combination of the lithographic technique and the RIE process allows the pore network to be designed with pore throats as small as 4 microns i.e., almost the same size as pore sizes appearing in natural hydrocarbon reservoirs. However, this is still one order of magnitude larger than the pores of

most North Sea chalk reservoirs. The minimum pore width in GEUS micromodels is 8 microns. The reason for using 8 microns, as the minimum pore width is that the quality of the images obtained by the reflected light microscope is better for the width to depth ratio not too small.

2.2.3 Surface Treatment

Two surface treatment processes are applied prior to encapsulation of the network by a glass plate in order to reduce the roughness of the etched porewalls of the network. First, the porewalls are exposed to a wet oxidation process forming a layer of silicon oxide 0.5 microns thick. This layer is then removed with fluoride acid. The second surface treatment process is a dry oxidation process forming a layer of silicon oxide with thickness equal to 0.1 μm. The two oxidation processes level out small irregularities resulting in a smoother surface. Consequently, roughness of the silicon surface approaches that of the encapsulating glass plate.

2.2.4 Encapsulation of Micromodels

The final step of the manufacturing process is the encapsulation of the etched network by a 500 μm thick Pyrex glass plate. The thickness of the plate is a critical parameter because it limits the focusing depth of the microscope caused by collision of the lens of the microscope with the underlying glass plate. The thickness of the applied Pyrex plate is smaller as compared to the previous generation of micromodels (cf. Winter et al., 1998). This allows greater magnification of observed pore-scale transport events. Prior to chemically bonding of the wafer and the Pyrex glass plate, the inlet holes are drilled in the glass plate for injection and production of fluids from the inlet and outlet chambers.

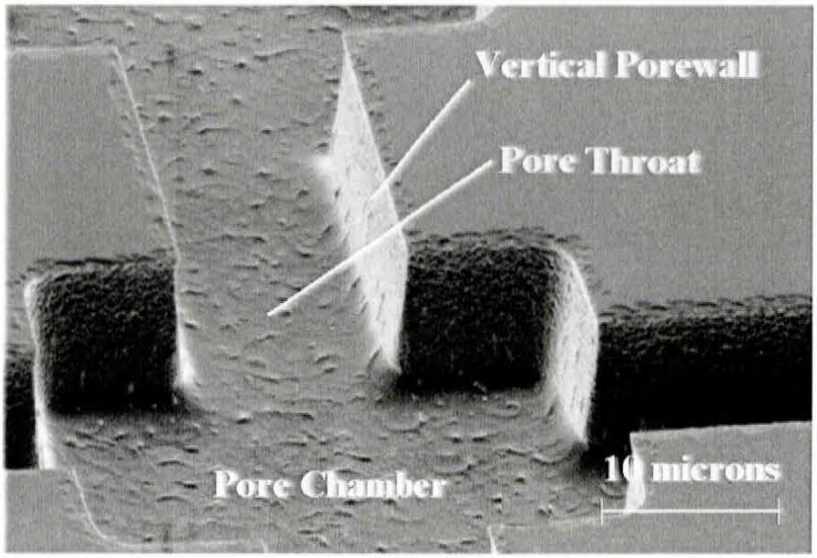

Figure 2.2 SEM photograph of a pore throat and a pore chamber taken at the *Mikroelektronik Centret (MIC)*. The widths of the throat and the chamber are 10 and 30 microns, respectively. The channel depth is 10 microns. The anisotropic ion etching results in strictly rectangular cross-sections of the pores. The subsequent oxidation of the silicon ensures highly smooth porewalls. The Pyrex glass is bonded to the top of the etched network.

2.2.5 Design of Pore Space in GEUS' Micromodels

Three different pore networks were designed for GEUS 1, GEUS 2 and GEUS 3 micromodels. A small Fortran program was written to create a file in the CIF format used by manufacturers of the photomasks containing blueprints for the designed pore networks. In particular, the pores were defined as rectangles with widths, lengths, and positions on the wafer.

The pore space of a micromodel was designed with 45000 pore chambers and approximately twice the number of throats. The pore network was subsequently replicated three times on a single silicon wafer. The pore chambers were positioned on a regular lattice which had been rotated 45° (cf. Figure 2.3). The rotation of the pore network gives a higher tortuosity as the shortest distance through the network is increased by a factor $\sqrt{2}$. The distance between the centers of two pore chambers, the node distance, is 52 microns. The short node distance compared to the size of the largest chamber of 40 microns was chosen in order to capture the largest section possible with the maximum magnification.

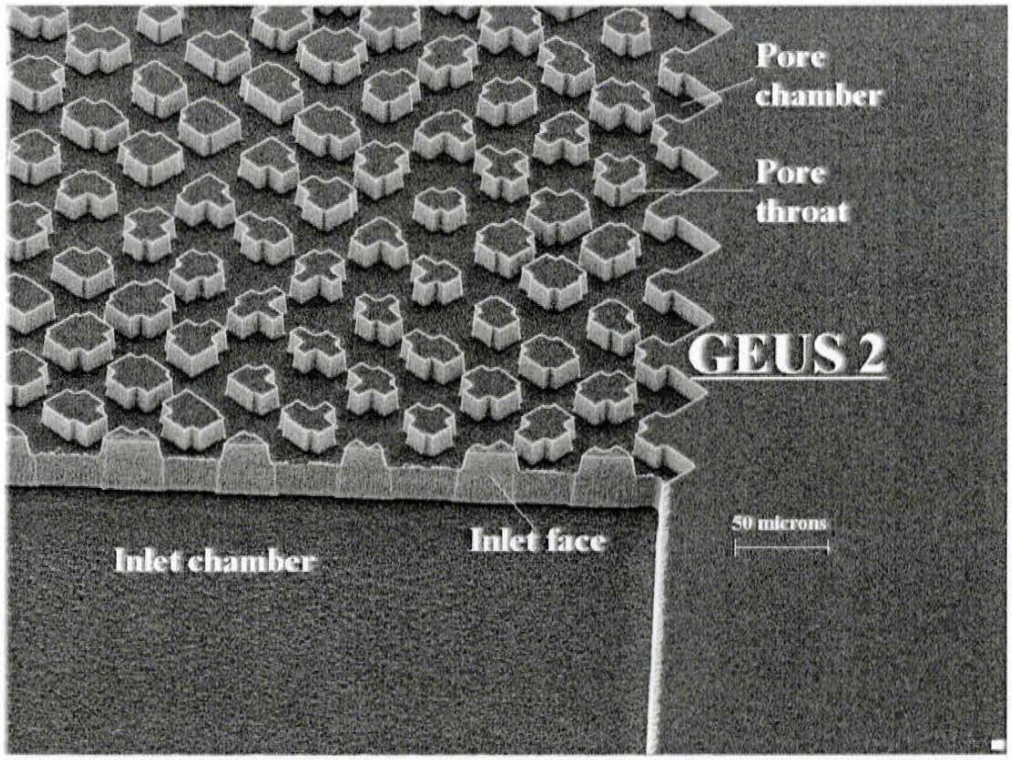

Figure 2.3 SEM picture of GEUS 2 taken at the *Mikroelektronik Centret (MIC)*, DTU. The etching depth of the inlet chamber is 40 microns while the etching depth of the network is 15 microns. The chambers are positioned on a regular lattice, which is rotated 45°. The chamber-to-chamber distance is 52 microns.

The main difference among the pore networks implemented in GEUS 1, GEUS 2, and GEUS 3 micromodels is in the distribution functions of their pore sizes (cf. Table 2.1). More specifically, the GEUS micromodels contain nine different pore classes. GEUS 1 is designed with five pore classes for the pore throats and five pore classes for the pore chambers. The width of a pore is assigned randomly. Two different sets of seeds are used for the random number generators of the chambers and the throats. The frequency distribution of GEUS 1 is a discretized lognormal distribution. GEUS 2 is designed with nine pore classes of pore throats and chambers and the pore size distribution is uniform.

Model	**GEUS 1**				**GEUS 2**			**GEUS 3**		
Node distance	52 μm				52 μm			52 μm		
Throat depth	15 μm				15 μm			10 μm		
Chamber depth	15 μm				15 μm			40 μm		
I/O depth	40 μm				40 μm			40 μm		
Pore class	Throat width (μm)	Chamber width (μm)	Frequency Throat /chamber		Throat width (μm)	Chamb. width (μm)	Frequency Throat/ chamber	Throat width (μm)	Chamb. width (μm)	Frequency Throat/ chamber
1	8	-	16	-	8	24	11	8	24	11
2	-	-	-	-	10	26	11	10	26	11
3	12	-	21	-	12	28	11	12	28	11
4	-	30	-	16	14	30	11	14	30	11
5	16	32	26	21	16	32	11	16	32	11
6	-	34	-	26	18	34	11	18	34	11
7	20	36	21	21	20	36	11	20	36	11
8	-	38	-	16	22	38	11	22	38	11
9	24	-	16	-	24	40	11	24	40	11

Table 2.1. Main design parameters of GEUS 1, GEUS 2, and GEUS 3 micromodels.

The pore networks of GEUS 3 micromodel (cf. Figure 2.4) contain some important features. The distribution of pore sizes in GEUS 3 is similar to that of GEUS 2. These features are due to the fact that during the design process, instead one etching mask used for the entire network, two etching masks are used. More precisely, the pore chambers are created with one etching depth and pore throats with another etching depth. In GEUS 1 and GEUS 2 micromodels, the matrix of the micromodels' pore space appears as a system of isolated pillars while in GEUS 3 the shape of the matrix is more complicated and irregular. Initially, all pores were etched to the same depth. Later, however, the pore chambers were additionally etched to a greater depth.

There are two significant advantages associated with the double etching depth. The first advantage is that in all previous micromodels etching depths are of the order of the smallest pore. This means that capillary pressures within the pore network are to a large extent controlled by the etching depth and not the assigned pore size. The second advantage is that the wedges of the porewall are connected through the etched network. In all previous constructions of micromodels, uniform etching depth throughout the network or eye-shaped pores caused the wedges to be isolated restricting the flow of the wetting phase controlled by thin wetting films. This was unfortunate, since presence of continuous wetting films is believed to represent a crucial transport property of natural porous rocks.

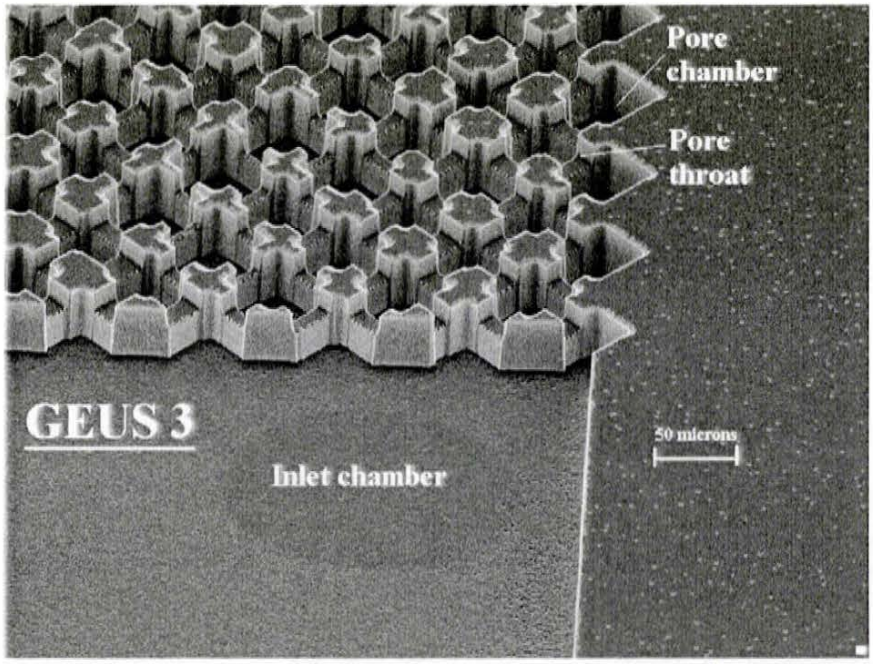

Figure 2.4 SEM picture of GEUS 3 taken at the *Mikroelektronik Centret (MIC)* at DTU. Two etching depths were used for the network. The corners of the pores form a network of wedges, which spans the entire etched network.

2.2.6 Design of Inlet and Outlet Chambers

The properties of the inlet and outlet chambers can influence the flow of the etched network (Figure 2.5). In GEUS' micromodels the inlet and outlet chambers were designed as deep as possible in order to reduce the resistance to flow.

The depth of the inlet and outlet chambers was primarily limited by the time required for the etching process to reach a certain depth. Normally, the etching depth of a print plate is a few microns. 40 micron was chosen as a compromise for maximizing the depth of the inlet and outlet chambers without using excessive etching times. A depth of 40 microns leads to an approximate capillary pressure of 3.500 Pa for a perfectly wetting air-water system with interfacial tension of 72 mN/m compared to a capillary pressure of 19.200 Pa for a pore throat with depth and width of 15 microns.

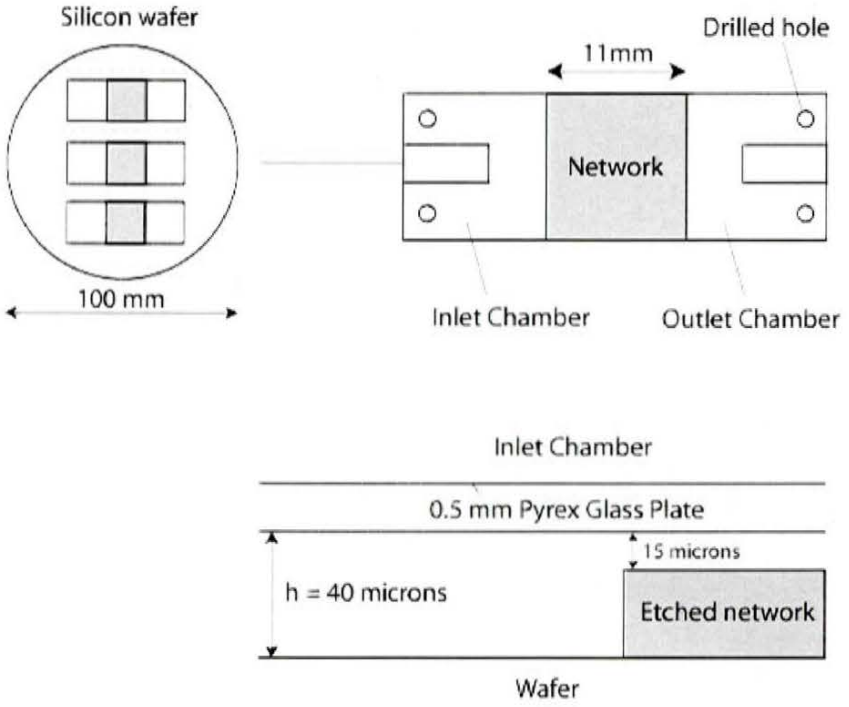

Figure 2.5. Top left: Sketch of three etched pore networks on a silicon wafer. Top right: The design of inlet and outlet chambers is shown with drilled holes in the Pyrex glass plate for injection of fluids. Bottom: Profile of the inlet chamber with the etched pore network.

The depth of the inlet and outlet chamber also determines the hydraulic conductance of the inlet and the outlet chambers. The hydraulic conductance is important because the pressure during flow experiments is measured outside the inlet chamber. If the viscous pressure drop in the inlet chamber is comparable to the pressure drop of the network, it is necessary to compensate the measured pressure for the viscous pressure drop in the inlet chamber in order to obtain the pressure of the fluid prior to entering the network. Likewise, the pressure in the outlet chamber, where the fluid leaves the network, is not the atmospheric pressure due to a viscous pressure drop in the outlet chamber. The pressure drop in the inlet can be estimated by assuming that the flow in the inlet and outlet chambers is a Couette flow. The pressure drop is then given by

$$\frac{dp}{dx} = \frac{12 \cdot Q \cdot \mu}{B \cdot h^3} \tag{2.1}$$

where B is the width of the network and h is the distance between the two parallel plates, μ is the viscosity of the fluid, Q is the injection rate of the fluid, and dp/dx the pressure drop.

For a distance $h = 40$ microns, B=1100 microns, viscosity $\mu = 1$ cP, injection rate, $Q = 1.0$ ml/h, and the viscous pressure drop is $5 \cdot 10^3$ Pa/m. The permeability of the network is 1000 mD. This yields the pressure drop of $2 \cdot 10^6$ Pa/m. Thus, the pressure drop is three orders of magnitude larger in the network as compared to its counterpart in the inlet and outlet chambers. It should be noted that the depth of the inlet and outlet chambers enters the expression of the pressure drop in the third power.

Consequently, a smaller depth would have greatly increased the viscous pressure drop of the inlet and outlet chambers.

The inlet and outlet chambers were designed with two entrances. The two entrances make it possible to inject two fluids simultaneously at a constant rate and make steady state measurements possible. The entrance holes were placed sufficiently far away from the network in order to avoid the micromodel holder to obstruct the free movement of the lens of the microscope. The outlet chamber was designed with a wall in the middle of the inlet and outlet chambers for support of the glass covering the micromodel.

2.2.7 Petrophysical Properties of GEUS' Micromodels

Some of the petrophysical properties of the GEUS micromodels can be calculated directly from pore geometry and structural properties of the designed network. Some of the other macroscopic properties were measured in the laboratory using micromodels as porous media by applying the usual measuring strategies. Table 2.2 shows some of the determined petrophysical properties of the GEUS micromodels. Typical values for chalk rocks are also shown for comparison. For calculation of the single-phase permeability and the porosity, the depth of the network is assumed to be the same as the depth of the inlet chamber.

	GEUS 1	GEUS 2	GEUS 3	Maastrichtian chalk
Porosity	0.23	0.24	0.45	0.15-0.40
Permeability	900 mD	900 mD	1000 mD	1-10 mD
Specific Surface - S_{tot}	$5.4 \cdot 10^{4}$ m^{-1}	$5.4 \cdot 10^{4}$ m^{-1}	$9.2 \cdot 10^{4}$ m^{-1}	$2.5 \cdot 10^{6}$ m^{-1}

Table 2.2 Selected petrophysical properties of the pore networks in GEUS micromodels. Typical values for Maastrichtian chalk are also shown for comparison.

3. Experimental micromodel studies

This chapter describes pore-scale mechanisms observed during experimental studies of multiphase transport in three different micromodels: GEUS 1, GEUS 2, and GEUS 3. All micromodels were manufactured in cooperation with the *Mikroelektronik Centret (MIC)* at the Technical University of Denmark (DTU). The goal of the experiments has been twofold: (1) to provide a basic understanding of the pore-scale, three-phase transport events governing gas injection and Water-Alternating-Gas (WAG) injection processes; (2) to create a catalog of elementary transport events for use in the network simulators described in Chapter 4.

It should be noted that the catalog of transport mechanisms created during this project is by no means unique. Additional mechanisms are likely to exist in real life hydrocarbon reservoirs. Also, it should be kept in mind that micromodels are not natural porous media. Consequently, some of the observed transport mechanisms are closely linked with the adopted micromodel design strategy and/or manufacturing processes of micromodels. Recent micromodel studies described in the literature have shown that pore-level transport mechanisms observed in nonplanar micromodels are similar to their counterparts observed in two-dimensional micromodels (cf. Avraam et al., 1994 and Tzimas et al., 1997). Thus, the limitation of the adopted experimental program to two-dimensional micromodels should not have any serious impact on the nature of observed transport mechanisms.

The displacement mechanisms observed during micromodel studies have been implemented in the quasistatic network simulator described in Chapter 4. The difference in pressure between the non-wetting and wetting phases must be larger than the critical capillary pressure associated with a given displacement mechanism in order to activate that mechanism. (cf. Section 3.4 and Section 4.4). More precisely, the mechanism with the lowest critical capillary pressure is assumed to be the most probable candidate to be activated.

In the next section, the influence of wettability and pore geometry on the configuration of the coexisting phases at the microscale is described.

3.1 Configuration of Immiscible Phases in Single Pore

The description of configurations containing two and three immiscible phases is a starting point for understanding multiphase transport mechanisms.

More specifically, in the case of two fluid phases coexisting in a single pore, the wetting phase is adsorbed on the surface of the porewall. Also, it is present in wedges, nooks and crannies of capillaries while the nonwetting phase occupies the center of pores. Configuration of reservoir fluids basically controls the transport properties at the pore level. For the pores with angular cross-sections the areas occupied by the coexisting phases can be calculated from curvatures of fluid-fluid interfaces and from macroscopic contact angles.

In the case where three phases coexist in a single pore, the phase placed between the remaining two phases can spread between the most wetting phase and the least-wetting phase. Alternatively, it creates a lens. The choice between the configurations is governed by the relative magnitude of the interfacial tensions associated with interfaces separating the coexisting phases. In a confined space

the oil phase can exist as a layer which is much thicker than thin wetting films residing on a flat (unconfined) surface. The transport properties of oil layers are entirely different from those of thin wetting films, which often do not have the same properties as the bulk phase.

In this chapter, only the case of uniformly water-wet pores is considered. Other wettability types may lead to quite complex phase configurations and entirely different transport properties. In particular, fractionally-wet systems may result in phase configurations much different from those observed in uniformly wet systems. In addition, local wettability changes in a pore caused by the injection of different fluid phases may lead to a change of transport properties during a displacement process (cf. Hui and Blunt, 2000a and 2000b and van Dijke et al., 2000 a-c).

Although pores in natural porous media do not have regular cross-sections, the influence of phase configurations on the transport properties can be studied by investigating simple pore geometries such as triangular, circular or rectangular cross-sections. The cross-sectional geometry of the capillary tubings implemented in GEUS 1, GEUS 2 and GEUS 3 micromodels is rectangular. The configuration of the coexisting phases in more complex angular cross-sectional pore cross-sections can be determined in the same manner as presented in this chapter (cf. Wong et al., 1992, Mason and Morrow, 1991 and 1994 and Tsakiroglou and Payatakes).

3.1.1 Two Immiscible Phases in Square-sectional Capillary Tubes

In a capillary tube with angular cross-section the configuration of two immiscible phases is determined by the capillary pressure P_{cow}, the macroscopic contact angle θ_{ow} and the half angle of the corner α. The subscript ow refers to an oil-water system where water is assumed to be the wetting phase. The interface separating the wetting and the nonwetting phase intersects the porewall creating a macroscopic contact angle. The macroscopic contact angle depends, like in the case of the unconfined situation, on whether the advancing phase is the wetting or nonwetting phase and on the roughness of the surface.

For illustrative purposes an infinitely long tube made of some mineral with a square cross-section of constant area is shown in Figure 3.1. It has been assumed that the head meniscus advances through the pore and the phase pressures are constant through the entire length of the capillary tube.

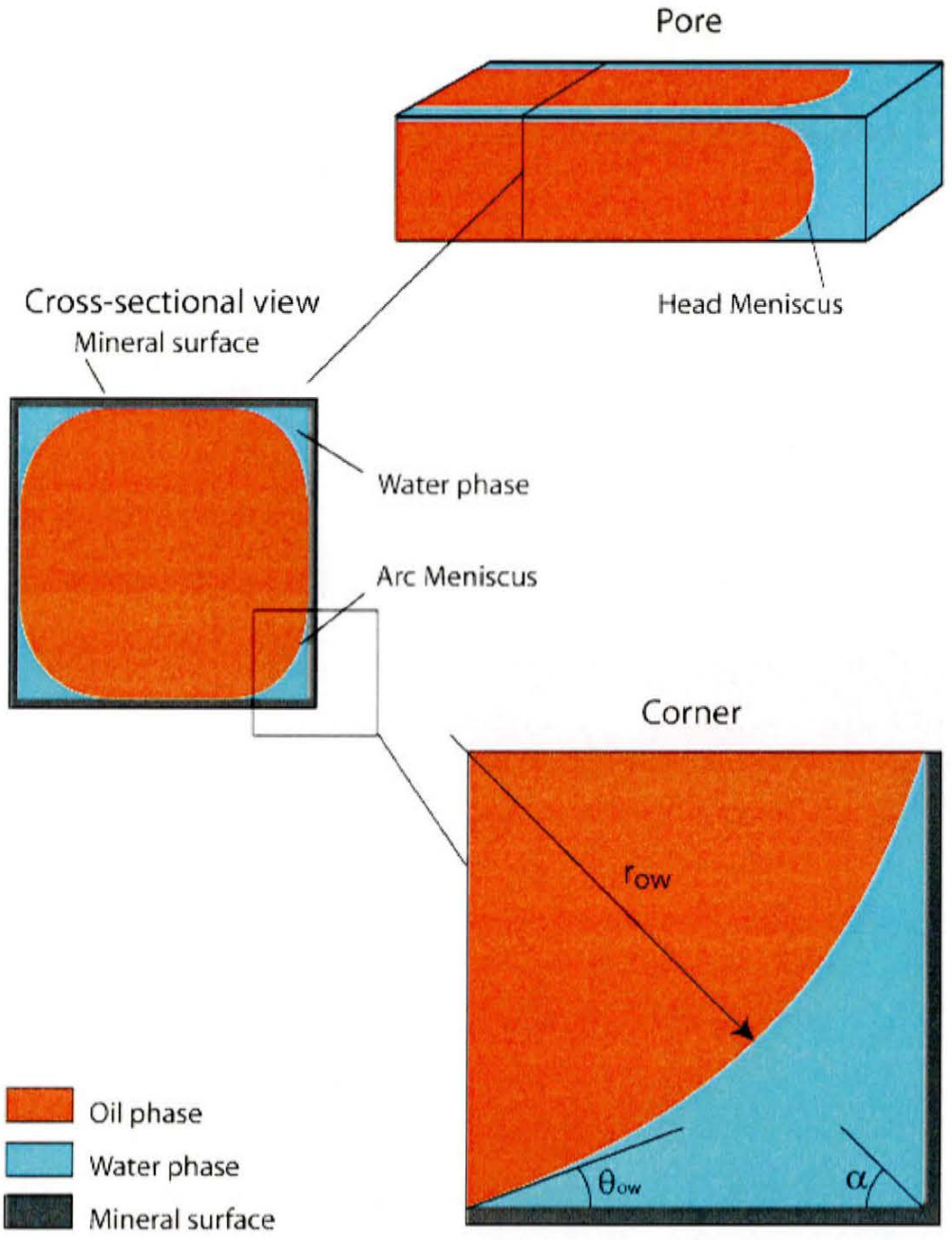

Figure 3.1 Configuration of two phases in a square-sectional capillary tube. The interface separating wetting and non-wetting phase intercepts the porewall creating the macroscopic contact angle θ_{ow}. The cross sectional geometry of an angular pore is defined by the half angle α. In the case of a square cross-section $\alpha = 45°$. The radius of curvature of the oil-water interface is r_{ow}. In areas where the oil-water interface is parallel to the porewall, the film thickness z is controlled by the disjoining pressure isotherm of the augmented Young-Laplace equation.

The curvature of the oil-water interface varies along the circumference of the interface. The interface follows the porewall away from the sides of the pore while it is curved in the corners forming an arc meniscus. For an interface in the mechanical equilibrium the intermolecular forces balance the capillary pressure. The balance is described by the augmented Young-Laplace equation. In the corners of the tube, where the distance between the oil-water interface and the porewall is large, the disjoining pressure is negligible. Consequently, the augmented Young-Laplace equation is reduced to the classical Young-Laplace equation. Moreover, the curvature of the interface in the

direction perpendicular to the plane of the cross-sectional area the pore is zero when the phase pressures are assumed constant throughout the tube. Consequently, there is only one principal radius of curvature of the oil-water interface, which can be calculated by the Young-Laplace equation. It is given by the following expression,

$$r_{ow} = \frac{\sigma_{ow}}{P_{cow}}, \tag{3.1}$$

where r_{ow} is shown in Figure 3.1. It should be noted that for a given capillary pressure the meniscus changes position for different magnitudes of the macroscopic contact angle. In particular, in a pore with square cross-section and assuming positive capillary pressure, the meniscus moves to the corner for contact angles larger than 45°.

3.1.2 Cross-sectional Area of Reservoir Fluids

The cross-sectional area of the wetting phase in the corners is usually much larger than the cross-sectional area of the thin wetting films along the porewalls. Thus, the cross-sectional area of the wetting phase present in a corner of a pore determines many of the transport properties associated with the wetting phase. The area of the water phase A_w located in the corners can be given as a general expression for a pore with a polygonal cross-section as

$$A_w = n_{corner} \cdot r_{ow}\left[\left(\cot(\alpha)\cdot\cos^2(\alpha+\theta_{ow})\right)-\left(\frac{\pi}{2}-(\alpha+\theta_{ow})\right)+\cos(\alpha+\theta_{ow})\cdot\sin(\alpha+\theta_{ow})\right] \tag{3.2}$$

where n_{corner} is the number of corners in the cross-section of the capillary tube.

The cross-sectional area of the oil phase A_o is given by subtracting the area of the water phase from the area the total cross-sectional area of the pore A_{pore}

$$A_o = A_{pore} - A_w . \tag{3.3}$$

It should be noted that the half-angle of the pore, the macroscopic contact angle and the curvature of the oil-water interface determine the area of the coexisting fluid phases, which again is proportional to the capillary pressure.

In the case of a circular tube water is present as a wetting film along the porewall only. Moreover, in the case of a square cross-section there is a critical contact angle $\theta_{ow} = 45°$. For contact angles larger than 45° water is only present as a wetting film for positive capillary pressures because the arc meniscus is forced towards the corner of the pore. Thus, the nonwetting phase will occupy the entire pore space except for the thin wetting film.

3.1.3 Three Immiscible Phases in Single Pore

When unlimited amounts of oil, water, and gas are present in an unconfined space, oil can either spread as a thin film on the surface of the water, or create lenses. Whether spreading occurs depends on the magnitude of the equilibrium spreading coefficient S defined as

$$S = \sigma_{gw} - \sigma_{ow} - \sigma_{og}, \tag{3.4}$$

where σ_{gw} is the interfacial tension between gas and water phases, σ_{ow} is the interfacial tension between the oil and water phases, and σ_{og} is the interfacial tension between the gas and the oil phases. If the *equilibrium* spreading coefficient is zero, oil spreads as a thin film on the water surface. Alternatively, if the *equilibrium* spreading coefficient is negative, oil is present as lenses (Figure 3.2). It should be noted that the initial spreading coefficient can change as the system approaches the thermodynamical equilibrium. One possible scenario is that the oil phase initially spreads and then forms lenses as the interfacial tensions are modified. The initial spreading coefficient is usually larger than the equilibrium spreading coefficient because the interfacial tension between the gas and the water phase is affected by the presence of the oil phase (cf. Adamson, 1990).

In the case of three phases present in the pore space, the water-solid interface has the lowest interfacial energy. Consequently, water wets the porewall. The gas phase is typically the least wetting phase and therefore occupies the center of the pores. The oil phase is present either as a thin film between the water phase and the gas phase or as an intermediate layer separating the gas and water phase (cf. Figure 3.2). The configuration of the water and the gas phases is similar to the two-phase case where the wetting water phase is located closest to the porewall while the gas phase occupies the center of the pore. Thus, the curvature of the oil-water interface and the cross-sectional area of the wetting water phase can be calculated by eq. (3.1) and eq. (3.2) for a given oil-water capillary pressure.

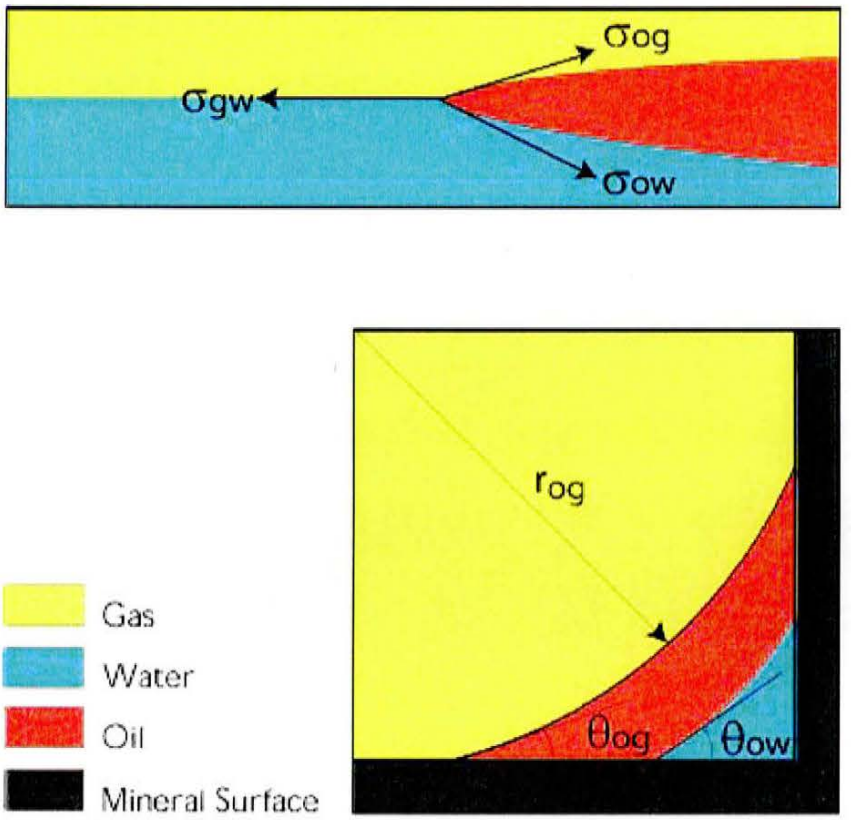

Figure 3.2 Configuration of three phases in an unconfined space and in a square-sectional capillary tube. The oil-water interface intersects the porewall at one contact angle, θ_{ow} while the oil-gas interface intersects the porewall at another contact angle θ_{og}. The curvature of the interfaces is given by eq. (3.1) and eq. (3.5) for prespecified oil-water- and oil-gas capillary pressure functions.

The presence of an intermediate oil layer separating gas and water in a pore space, is important for the continuity of the oil phase and therefore also for the transport properties related to the oil phase (cf. Blunt et al., 1994 and 1995). The presence of an oil layer is controlled by the equilibrium spreading coefficient of the oil-water-gas system, the contact angles between oil and gas, oil and water, and the half angle of the pore. In the case of an unstable oil layer only gas and water will be present in the pore and the configuration is similar to the two-phase case.

3.1.4 Curvature of Oil-Gas Interface

The curvature of the oil-water interface for a large distance between the oil-water interface and the porewall is given by eq. (3.1). The curvature of the oil-gas interface under similar conditions is given by the Young-Laplace equation

$$r_{og} = \frac{\sigma_{og}}{P_{cog}}, \tag{3.5}$$

where P_{cog} is the oil gas capillary pressure and r_{og} is the principal radius of curvature.

The area of the intermediate oil phase can be calculated by considering the cross-sectional areas of the wetting water phase and the cross-sectional area of the intermediate and wetting oil and water phase. The area of the oil phase is the difference between the two cross-sectional areas. For a polygonal cross-section the area of the oil phase can therefore be calculated as

$$\begin{aligned} A_o = {} & n_{corner} \cdot r_{og}\left[\left(\cot(\alpha)\cdot\cos^2(\alpha+\theta_{og})\right)-\left(\frac{\pi}{2}-(\alpha+\theta_{og})\right)+\cos(\alpha+\theta_{og})\cdot\sin(\alpha+\theta_{og})\right]- \\ & n_{corner} \cdot r_{ow}\left[\left(\cot(\alpha)\cdot\cos^2(\alpha+\theta_{ow})\right)-\left(\frac{\pi}{2}-(\alpha+\theta_{ow})\right)+\cos(\alpha+\theta_{ow})\cdot\sin(\alpha+\theta_{ow})\right] \end{aligned} \tag{3.6}$$

The area of the gas phase, A_{gas}, can then be calculated as the total cross-sectional area of the pore minus the cross-sectional area of the oil and the water phase i.e.,

$$A_g = A_{pore} - A_o - A_w. \tag{3.7}$$

It should be noted that the saturation of the three phases in a single pore can be defined by specifying the cross-sectional area of the phases because the cross-sectional areas of the phases do not change along the tube.

3.2 Visualization of Fluid Configurations in Micromodels

Micromodel experiments described in the previous section have shown that two or more fluid phases may coexist in a single pore. However, the configuration of a fluid phase is not always accessible for visual studies because one fluid phase may block for observations of another fluid phase. Thus, the configuration of the fluid phases is often revealed by means of indirect observations. This is the reason why it is often necessary to deduce configurations of the coexisting fluid phases from pore-scale displacement mechanisms. Moreover, small dimensions of the etched pore spaces in the GEUS-family micromodels exclude using the naked eye for observations of the pore-scale displacement mechanisms. The pore-scale studies are performed using a reflected light microscope with a video camera mounted on top of a microscope. The signal from the video camera is forwarded to a monitor, which is hooked up to video-recorder. The pore-level displacement mechanisms are recorded and inspected later for analysis of the pore-scale events. A schematic drawing of the experimental set-up is shown in Figure 3.3. The injection of fluids is either performed with a constant pressure using a constant head of the injected fluid or by using a constant injection rate delivered by a pump.

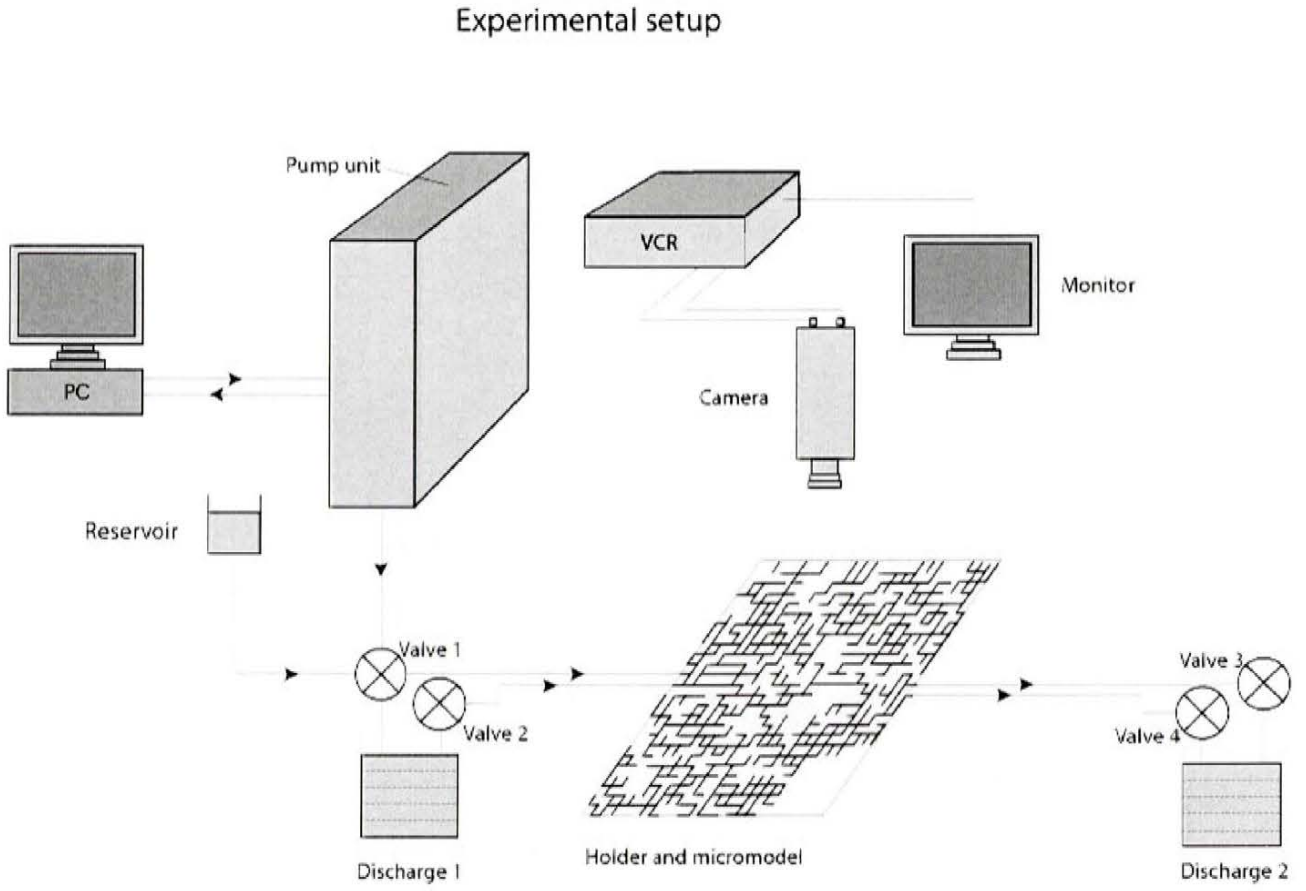

Figure 3.3. Experimental setup. The computer controls the pump delivering a constant injection rate and collects pressure data from the pressure transducer mounted on the pump unit. Alternatively, the fluid reservoir can be elevated and a constant head acts as the driving force for injection. The camera, VCR, and monitor are used for observations of transport mechanisms in the micromodels. The reflected light microscope is not shown.

In order to distinguish the phases in the micromodels the oil phase was colored by Ölrot (Merck art.11669) which is a commercially available dye. The oil was saturated with dye in order to establish a distinguishable system of the coexisting fluid phases. Water appears transparent in the micromodels while gas appears blue. The blue color of gas is due to the refractive indices of Pyrex glass and air. Along the porewall a black line is seen on all the photographs, which is a shading effect caused by the use of a reflected light microscope. The color of the images is affected by the focusing of the microscope and the light intensity. Consequently, photographs are not readily comparable in terms of color and light intensity.

3.3 Pore-Level Displacement Mechanisms of WAG-injection

Pore-level displacement mechanisms were observed during a double WAG cycle of an air-water-dodecane system followed by injection of dodecane. The initial interfacial tensions of the fluids were 70 mN/m, 23 mN/m and 40 mN/m for the air-water, the dodecane-water and the dodecane-air system, respectively. Thus, the initial spreading coefficient was 7 mN/m.

The study of the three-phase pore-level displacement mechanisms was conducted using the micromodel GEUS 2. The micromodel was initially cleaned with chromic sulfuric acid to ensure strongly water-wet conditions for the WAG injection sequence. It was subsequently saturated with

distilled water and filled with dodecane colored with Ölrot at a constant pressure. The micromodel was then flooded with water and air was injected at a constant pressure to complete the first WAG cycle. Another WAG cycle was conducted prior to injection of dodecane into the micromodel. The reason for injecting dodecane was to observe the pore-level displacement mechanisms associated with increased oil saturation in a three-phase system. Increased oil saturations on the pore level may occur during WAG injection as a consequence of a travelling oil bank at the macroscopic scale.

3.3.1 Two-phase Pore-Level Displacement Mechanisms

During the two-phase WAG injection involving dodecane and water, the pore-scale mechanisms reported in Section 3.2 were observed. Moreover, additional two-phase displacement mechanisms also occurred for dodecane-water interfaces. More precisely, air-invading dodecane created Haines' jumps. The invading air then displaced dodecane via a continuous dodecane cluster, which was connected to the outlet chamber. It should be noted, however, that dodecane only remained connected to the outlet chamber as long as the outlet chamber was filled with dodecane. If water was present in the outlet chamber dodecane was produced in droplets similarly to the dodecane-water system.

The injection of dodecane into the micromodel sometimes led to retraction of dodecane-air interfaces. However, the motion was most often associated with displacement of the water phase because water was always connected to the outlet phase while the air phase was quickly disconnected and thus the air had to be produced as air droplets. However, the principles of the two-phase dodecane-air mechanisms were entirely analog to the two-phase dodecane-water mechanisms.

Two-phase air-water displacement mechanisms were not observed because dodecane spread between the air phase and the water phase. However, in some cases the so-called direct drainage or imbibition mechanisms were observed where air displaced water only separated by a layer of dodecane. Alternatively, water displaced air separated by a layer of dodecane. It should be noted that the direct drainage mechanism and the direct imbibition mechanism along with the two-phase dodecane-water and dodecane-air mechanisms were the most frequently observed displacement mechanisms. In addition, a number of displacement mechanisms where all three phases were involved have been investigated.

3.3.2 Double Displacement Mechanisms during Air Injection

The injection of air into the micromodel was an overall drainage process where dodecane and water saturation of the micromodel was continuously lowered because of injection of air. The invasion of dodecane by air was often associated with a second displacement event. The scenario was that air displaced dodecane by a Haines' jump similarly to the two-phase case. Dodecane subsequently displaced the water phase at a different location by one or more Haines' jumps (cf. Figure 3.4). The net result of the displacement mechanism was that air displaced water. However, the side effect was

that stranded dodecane ganglia were mobilized and reconnected to the outlet chamber because dodecane spread on the air phase.

The double displacement mechanism can be divided into a primary air-dodecane mechanism and a secondary dodecane-water displacement mechanism. Both the primary and the secondary displacement mechanisms are drainage displacement processes. The combination of the two mechanisms is thus often referred to as double drainage displacement (Keller et al., 1997, Chatzis et al., 1988 a, Kantzas et al., 1988 a, 1988b, Soll, et al., 1993 and Øren et al., 1992).

It should be noted that the invasion of dodecane not always caused a secondary displacement. Dodecane was sometimes redistributed around the gas phase and no secondary event occurred. Especially, for larger ganglia, dodecane adjusted its dodecane-water interface and thus avoided the secondary displacement. Moreover, in the case where the gas phase displaced a large pore chamber, it sometimes caused two secondary displacement mechanisms. Thus, the volume balance of the phases controlled whether one, two or no secondary event occurred.

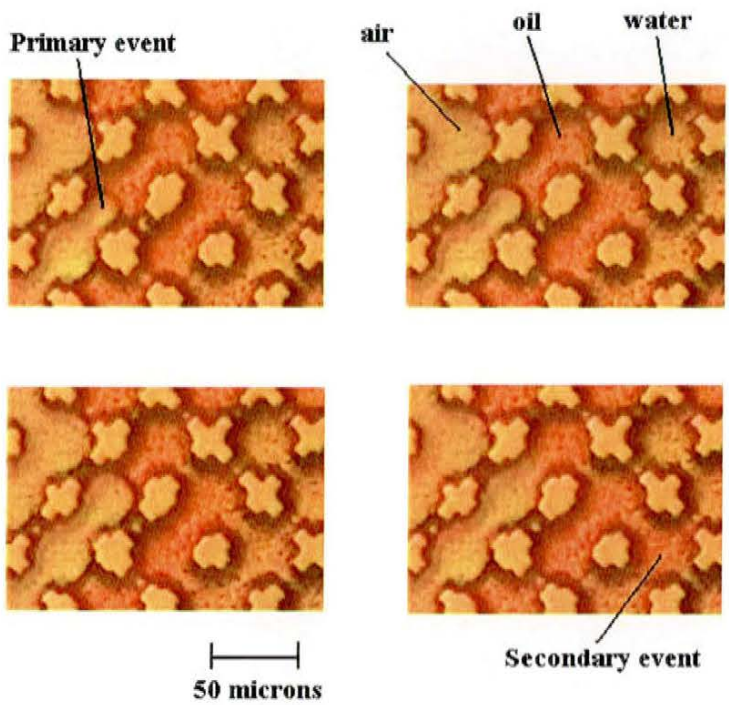

Figure 3.4 Double drainage mechanism in GEUS 2. Air displaced dodecane in a primary event, which was followed, by a secondary event where dodecane displaced water. The two displacement mechanisms occur immediately after each other.

3.3.3 Double Displacement Mechanism during Water Injection

During the first WAG injection cycle no air was present in the network. Thus, three-phase overall imbibition only occurred during the second WAG injection cycle. Similarly to the injection of air injection of water led to two-phase imbibition processes where water displaced dodecane by I_1- and I_2-mechanisms. The so-called double imbibition mechanisms were observed during the water injection (see Figure 3.5). The water phase displaced dodecane, which subsequently displaced the gas phase. The primary event where water displaced dodecane was an imbibition displacement and occurred either as an I_1- or an I_2-mechanism. The secondary event also occurred as a dodecane-gas I_1- or I_2-displacement mechanism.

The double imbibition mechanisms occurred only when the primary water-dodecane displacement was 'close' to the secondary dodecane-air displacement and the air phase was continuous to the outlet. By 'close' we mean 1-2 pores away. If the distance was longer than a couple of pores dodecane was produced directly at the outlet chamber without a secondary displacement. This showed that continuity of dodecane to the outlet chamber might inhibit other displacement mechanisms from occurring. In other words the double imbibition mechanism was a local phenomenon which depended on the local phase pressure conditions.

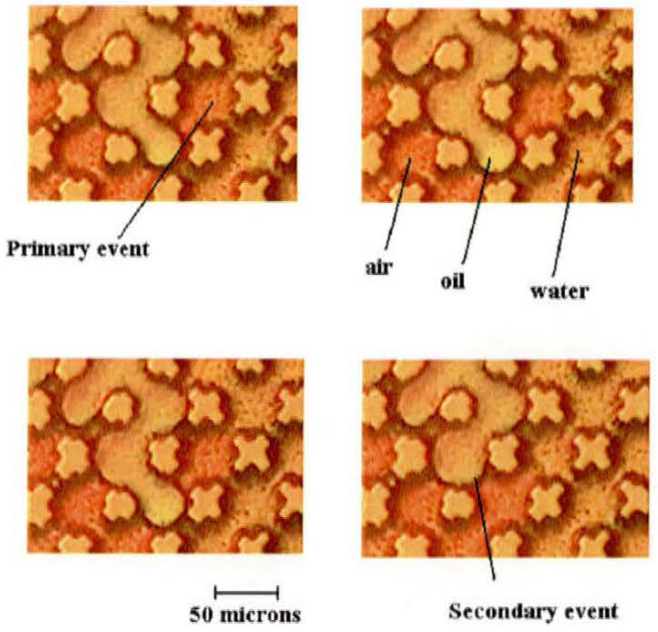

Figure 3.5 Double imbibition mechanism in GEUS 2. Water displaced dodecane, which subsequently displaced air. The two events typically occur in the proximity of each other.

3.3.4 Dodecane-dragging-air during Dodecane Injection

After the completion of the two WAG cycles dodecane was injected into the micromodel. The displacement mechanisms were primarily dominated by Haines' jumps where dodecane displaced water and by I_1-and I_2-mechanisms of dodecane displacing air. However, the spreading dodecane was sometimes capable of 'dragging' the air phase into the next pore chamber as a consequence of dodecane performing a Haines' jump (cf. Figure 3.6). The mechanism occurred by dodecane performing a Haines' jump and because of insufficient conductance of dodecane. Dodecane pressure was locally lowered causing dodecane to drag the air phase into the pore chamber. Sometimes the dodecane-air interface was not stable and the air retracted backwards out of the pore chamber it had just filled. Dodecane was supplied to the pore chamber via the wetting layers.

The occurrence of the dodecane-dragging-air mechanism depends, like the double imbibition displacement, on the local pressure conditions. Dodecane-dragging-air only occurred over a length of a single pore. Consequently, dodecane-dragging-air displacement mechanisms appear to be sensitive to the conductance of dodecane layer or film separating the air from the water phase. It should be noted that the dodecane-dragging-air displacement mechanism contributed far less to the overall displacement of air than the I_1- and I_2-mechanisms of dodecane displacing air. However, the dodecane-dragging-air displacement mechanism created by the injection of dodecane was the only mechanism that could mobilize the stranded air ganglia.

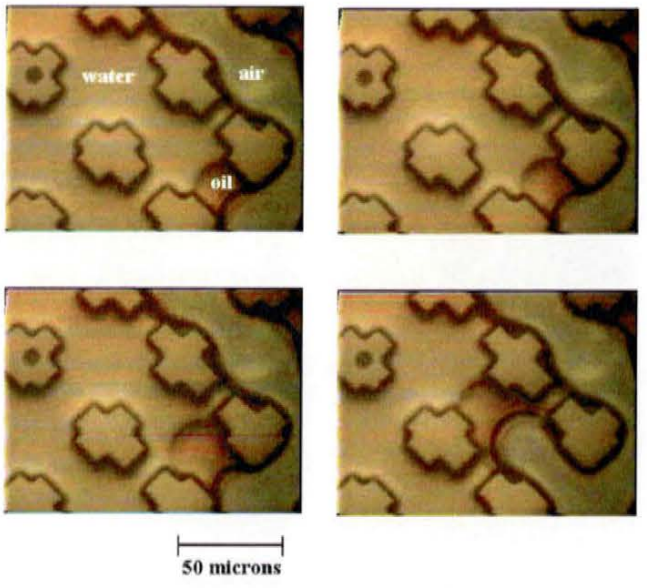

Figure 3.6 Dodecane-dragging-gas displacement. Dodecane advances into a pore chamber and the local pressure of dodecane decreases, which causes an invasion of the pore chamber by air. The air sometimes retracts from the pore chamber when oil enters the pore chamber through the oil layers.

3.4 Critical Pressures for Displacement Mechanisms

The micromodel study has shown that the pore-level displacement mechanisms are initiated as sudden movements of pore space fluids caused by instabilities of static interface configurations.

More precisely, when the difference in phase pressure exceeds a critical value, which cannot be supported by the curvature of a static interface separating the coexisting fluid phases, a sudden movement of an interface occurs. Thus, each elementary pore-level displacement mechanism is associated with a critical pressure $P_{critical}$ that must be exceeded in order for the displacement mechanism to occur.

The critical pressure for displacement mechanisms defines the probability of occurrence of pore-level displacement in the quasistatic network simulator described in Chapter 4. More precisely, for a given change in capillary pressure, the sequence of admissible pore-level mechanisms is ordered according to the same principle as that underlying the invasion percolation process: the size of a pore is equivalent to its critical pressure. However, in order to avoid confusion it is useful to distinguish between a local capillary pressure associated with the pore level and a global capillary pressure associated with the network level. The local capillary pressure is defined as the difference in pressure between two phases located on either side of a particular interface. On the other hand, the global capillary pressure is defined as the difference between two phases in the case where both phases are connected to the inlet or outlet and there is no pressure gradient within the two phases. Thus, global capillary pressure is usually the condition imposed on the system while the local capillary pressure typically is associated with movement of an interface.

When pore-level displacement mechanisms take place the distribution of the phases in the pore space changes and several new pore-level displacement mechanisms may become possible. As a consequence of more than one possible pore-level displacement mechanism it is necessary to order the displacement mechanisms according to their displacement potential. The displacement potential Φ can be regarded as the 'driving force' of a displacement mechanism.

For a two-phase single displacement mechanism the displacement potential is defined as

$$\Phi^{single}_{mechanism} = P_1 - P_2 - P_{critical}, \tag{3.8}$$

where P_1 is the pressure of the displacing phase and P_2 is the pressure of the displaced phase. It should be noted that this definition of potential requires assignment of negative critical pressures to imbibition mechanisms. On the other hand, drainage mechanisms are assigned a positive critical pressure. Thus, for a given set of phase pressures, the mechanisms can be ordered according to their displacement potential.

Double displacement mechanisms are essentially a combination of two single displacement mechanisms where phase 1 in a primary displacement displaces phase 2 which in turn displaces phase 3 (cf. Øren et al., 1994). Two critical pressures can thus be defined, one for each elementary displacement mechanism. The potential of the double displacement mechanisms can be defined as

$$\Phi^{double}_{mechanism} = P_1 - P_3 - P^1_{critical} - P^2_{critical}, \tag{3.9}$$

where P_1 is the phase pressure of the displacing phase, P_3 the phase pressure of the displaced phase, $P^1_{critical}$ the critical pressure for the primary elementary displacement mechanisms and $P^2_{critical}$ the critical pressure for the secondary elementary displacement mechanisms. The phase pressures of the displacing phase and the displaced phase are global phase pressures for the network. Consequently, the displacing and the displaced phase must be connected to the inlet or the outlet of the network.

Øren et al. (1994) added film flow resistance to eq. (3.9), i.e. they modeled the pressure drop inside the oil phase and examined the effect of resistance to flow in the oil phase on the global displacement efficiency. Resistance to flow in the oil phase causes secondary event to occur closer to the primary event because the difference in phase pressure between phase 1 and phase 2 must exceed the resistance to flow in addition to the critical capillary pressure of the primary and secondary events.

3.4.1 Haines' Jump

In order for the oil phase to perform a Haines' jump, the oil-water head meniscus must enter the pore throat connecting two pore chambers. Thus, the capillary pressure must exceed the entry pressure of the pore throat. The entry pressure depends on the interfacial tension, contact angle, and the size of the pore. It can be calculated for various simple cross-sectional geometries (cf. Mason and Morrow, 1991 and Lenormand et al., 1983). The entry pressure also controls the piston-like motion of the meniscus inside a square tube. The critical pressure for the Haines' jump is referred to as the critical pressure for piston-like displacement. Legait (1983) calculated the entry pressure for tubings of square cross-section. For an oil-water system it is given by

$$P_{critical}^{piston,drainage} = \frac{\sigma_{ow}}{r_{pore}} \left(\frac{\theta_{ow} + \cos^2(\theta_{ow}) - \frac{\pi}{4} - \sin(\theta_{ow})\cos(\theta_{ow})}{\cos(\theta_{ow}) - \sqrt{\frac{\pi}{4} - \theta_{ow} + \sin(\theta_{ow})\cos(\theta_{ow})}} \right). \tag{3.10}$$

For a tube of rectangular cross-section in GEUS 1, GEUS 2, and GEUS 3 micromodels, the critical capillary pressure for an oil-water interface can be calculated as

$$P_{critical}^{piston,drainage} = f(\varepsilon) \cdot 2\sigma_{ow} \left(\frac{1}{x} + \frac{1}{y} \right), \tag{3.11}$$

where x and y are the height and width of the rectangular cross-section and $\varepsilon = y/x$ is the ratio of height to width. $f(\varepsilon)$ is a complex function of the height to width ratio but generally varies between 0.94 and 1.0. Thus, a rough estimate of the critical pressure for a square-sectional tubing can be obtained by assuming $f(\varepsilon) = 1$. It should be noted that the critical pressure for a pore chamber could be defined as well.

3.4.2 Piston-like Imbibition

The mechanisms controlling the piston-like motion of a meniscus inside a pore throat are similar to those underlying the drainage displacement. For the oil-water capillary pressure equal to the entry pressure of a pore, the meniscus is in mechanical equilibrium and its motion is reversible provided that the advancing and receding contact angles are identical. Thus, the capillary pressures smaller than the entry pressure result in the retraction of the meniscus from the pore throat provided that a

head meniscus exists in the throat. Thus, the critical capillary pressure of the imbibition process of a pore with square cross-section is given by the following expression,

$$P_{critical}^{piston,imbibition} = -\frac{\sigma_{ow}}{r_{pore}}\left(\frac{\theta_{ow} + \cos^2(\theta_{ow}) - \frac{\pi}{4} - \sin(\theta_{ow})\cos(\theta_{ow})}{\cos(\theta_{ow}) - \sqrt{\frac{\pi}{4} - \theta_{ow} + \sin(\theta_{ow})\cos(\theta_{ow})}}\right), \tag{3.12}$$

It should be noted that the piston-like imbibition displacement from a pore throat often follows the retraction of a meniscus from an adjacent pore chamber. The piston-like retraction occurs as a consequence of break-up of an oil filament after an I_2-mechanism or following an I_1-mechanism. The piston-like imbibition displacement in a pore throat is an unstable process because the potential for the piston-like displacement usually is much larger than the potential associated with the preceding retraction from a pore chamber.

3.4.3 I_n-Mechanisms

The critical capillary pressure for I_n-mechanisms depends on the contact angle, the interfacial tension, the number of pore throats filled with nonwetting phase, the geometry of the filled pore throats and the relative position of the filled pore throats (cf. Lenormand et al., 1983 and Tsakiroglou and Payatakes, 1998). Tsakiroglou and Payatakes (1998) presented a detailed analysis for calculation of the critical capillary pressure for various I_n-mechanism based on the eye-shaped geometry of the pores of their glass micromodels. They included the size and depth of the pore chamber and the adjacent pore throats. Also, they differentiated between the position of filled pore throats. In general exact calculation of the critical pressures I_n-mechanisms higher than $n = 1$ can be rather complex.

The phase configurations of the I_1- and I_2-mechanism of GEUS 1, GEUS 2and GEUS 3 (Figures 3.6 and 3.7) may be analyzed in a similar manner as done by Tsakiroglou and Payatakes (1998). However, the rupture of the oil filament of an I_2-mechanism may occur at four different points on the matrix pillar. The point where the oil filament ruptures depends on quite a few parameters including the size of two pore chambers and three pore throats. The variation in critical pressure is small and for practical reasons the critical pressure of the I_n-mechanisms may be summarized in a more simple expression given by Fenwick and Blunt (1998)

$$P_{critical}^{I_n} = -\frac{\sigma_{ow} \cdot C_n}{r_{chamber}}, \tag{3.13}$$

where C_n is a constant dependent on the number of neighbors n filled with nonwetting phase and the contact angle, and $r_{chamber}$ is the size of the pore chamber. The number of neighbors can be as large as the coordination number, but in general C_n decreases with increasing number of filled pore throats. Thus, the critical capillary pressure of an I_1-mechanism is generally favored over I_2-mechanisms, which is in agreement with the observations in GEUS 1, GEUS 2, and GEUS 3 micromodels.

3.4.4 Snap-off and Choke-off

The mechanism underlying production of dodecane at the outlet face has previously been described by Roof (1970) who observed nonwetting phase leaving a constriction. Roof (1970) named this mechanism "snap-off". The instability of the snapped-off oil occurs because the curvature of the oil-water interface is much larger than the interface curvature at the front of the meniscus (cf. Figure 3.7). For static conditions the oil phase pressure inside the constriction and at the tip of the head meniscus must be the same. However, if the curvature of the of the oil-water interface is different at the points *a*, *b* and *c* in Figure 3.7, the water pressure at the three locations is different. This leads to a pressure gradient in the water phase. The curvature of the oil-water interface is larger inside the throat. Consequently water flows towards the constriction and snaps the oil phase off.

Roof (1970) defined a criterion for the instability to occur for a simple tore shaped pore constriction. He has shown that the meniscus had to travel at least 7 times the radius of the tore in order for the instability to occur. This is in agreement with the observations performed in GEUS 1, GEUS 2 and GEUS 3. Consequently, it appears that the volume of the droplet governs the snap-off mechanism.

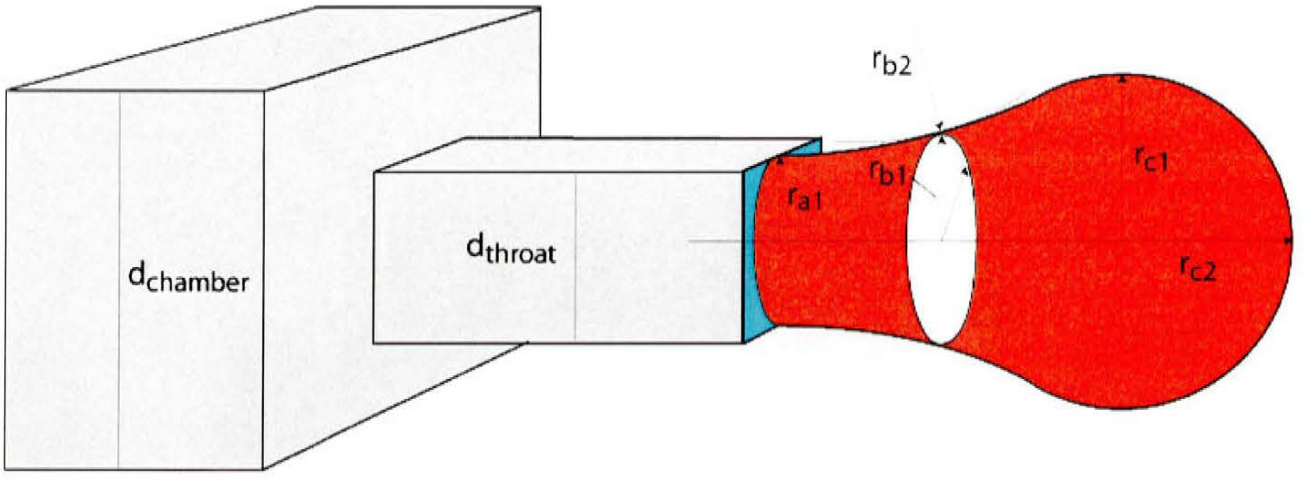

Figure 3.7 Snap-off by Roof (1970). Water enters the constriction and chokes the oil filament off. The curvature of the interface can be evaluated at various points along the length of the oil filament by the Young-Laplace equation. For static conditions the curvature of the oil-water interface must be the same everywhere.

3.4.5 Snap-off in Pore Throat

The snap-off event inside the network of GEUS 1, GEUS 2, and GEUS 3 micromodels was effectively suppressed by I_1- and I_2-mechanisms due to the short lengths of the pore throats. However, several authors (cf. Lenormand et al., 1982) have observed snap-off inside a pore throat. The critical pressure is quite easy to derive for a square cross-section and thus easy to implement in a quasistatic network model described in Chapter 4.

Consider now the fluid configuration shown in Figure 3.1. Assume that the capillary pressure has decreased causing a smaller curvature of the fluid interface. The nonwetting fluid collapses at a critical capillary pressure where the two arc menisci intercept the porewall at the same point. The critical pressure for snap-off can be derived for a square cross-sectional pore by simple geometric consideration, assuming small curvature in the longitudinal direction of the pore throat, as

$$P_{critical}^{snap-off} = \frac{\cos(\theta_{ow}) - \sin(\theta_{ow})}{r_{pore}} \tag{3.14}$$

Lenormand et al. (1983) stressed that piston-like displacement is always favored over snap-off in a pore throat and that snap-off only takes place when piston-like motion is not possible for topological reasons i.e. no head meniscus is present in the pore throat. The snap-off mechanism is sensitive to the supply of wetting phase to perform the snap-off. Thus, in reality snap-off is often controlled by the access to the wetting phase and, consequently, the potential for the mechanism might be significantly lower than its counterpart corresponding to globally imposed phase pressures. Consequently, the snap-off mechanism may be inhibited in systems where transport of the wetting phase is controlled by film flow.

3.4.6 Double Displacement Mechanisms

In order to determine the critical pressures associated with double displacement mechanisms one has to consider six elementary double displacement events, see Figure 3.8 (cf. Blunt and Fenwick, 1995). These elementary displacement events may be either drainage or imbibition process. Also, the combination of the elementary processes may lead to an overall drainage or imbibition process. However, only double drainage, double imbibition and oil-dragging gas was observed in GEUS 2 micromodel during the WAG injection. The oil-dragging-gas mechanism can be classified as imbibition drainage with overall drainage (DID) in the scheme of Keller et al. (cf. Figure 3.8).

Double drainage and double imbibition are indeed the most common double displacement mechanisms (Keller et al., 1997). Keller et al. (1997) observed oil displacing water displacing gas which was referred to as drainage imbibition with overall imbibition (IDI) and gas displacing water displacing oil which was referred to as drainage imbibition with overall drainage (DDI). The latter mechanisms were only observed prior to oil contacting the gas phase. One of the reasons why not all theoretical displacement mechanisms have been observed is that some pore-level double displacement mechanisms are local phenomena. Consequently, they are only possible when one of the phases is restricted in its movement causing a build up of a local pressure gradient. The quasistatic flow condition is therefore a global condition that is not always fulfilled on the local pore level.

Gas	➡	Oil	➡	Water	Double Drainage (DD)
Water	➡	Oil	➡	Gas	Double Imbibition (II)
Oil	➡	Water	➡	Gas	Drainage - Imbibition with overall Imbibition (IDI)
Oil	➡	Gas	➡	Water	Imbibition - Drainage with overall Drainage (DID)
Gas	➡	Water	➡	Oil	Drainage - Imbibition with overall Drainage (DDI)
Water	➡	Gas	➡	Oil	Imbibition - Drainage with overall Imbibition (IID)

Figure 3.8 List of admissible double displacement mechanisms. The arrow indicates that phase 1 to the left displaces phase 2 which again displaces phase 3 to the right. The last two letters in the parenthesis indicate the nature of the elementary displacement mechanisms where *D* stands for drainage and *I* for imbibition. The first letter indicates the combined nature of the two elementary processes.

There are two separate critical pressures that control the possibility for a double drainage displacement mechanism.

The critical pressure for the primary event of gas invading oil is given by

$$P^1_{critical} = P_{entry,og}\,, \tag{3.15}$$

where $P_{entry,\,og}$ is the critical pressure for gas entering an oil filled pore throat.

The critical pressure for the second event is for oil invading a water filled pore which is given by

$$P^2_{critical} = P_{entry,ow}\,, \tag{3.16}$$

where $P_{entry,\,ow}$ is the critical pressure for oil entering the water filled pore throat. In this case the critical entry pressures can be calculated by eq. (3.13). It should be noted that oil needs not to be continuous to the outlet chamber and the oil pressure does not necessarily have to be known for calculation of the potential of the displacement mechanism because the potential is related to the pressure drop of the gas and water phase.

It should be stressed that the oil phase involved in the two elementary displacement mechanisms must be continuous between the locations of the primary and the secondary event. Moreover, when a large oil cluster is invaded by gas the oil may have several options of pores from which water can be displaced. However, the location where the water phase is displaced is the one with the largest displacement potential. The potential of the double displacement mechanism is readily calculated by eq. (3.12) once the critical pressures are known.

The critical pressures used to calculate the potential of the double imbibition mechanism are defined by the critical pressure of the first imbibition mechanism minus the critical pressure of the second imbibition mechanism. Like in the case of the double drainage displacement mechanism, the oil phase must be continuous between the locations of the primary and the secondary event. Double imbibition displacements may occur for combinations of different imbibition mechanisms. In other

words, the primary and the secondary imbibition mechanism could be a combination of a piston-like imbibition of a throat, an I_1- or an I_2-mechanism. Consequently, quite a few combinations for double imbibition may exist.

The criterion for the oil-dragging-gas displacement mechanism is different from the other three-phase displacement mechanisms presented. The criterion for the oil phase entering the pore throat is straightforward and can be calculated by eq. (3.12). However, the criterion for the gas entering the pore throat is that the local difference in pressure between the oil phase and the gas phase exceeds the entry pressure of the pore throat for an oil-gas piston-like drainage displacement. Thus, the oil-gas displacement criterion is a local condition. Consequently, the phase pressures are controlled by the conductance of oil in the region separating the oil-gas and the oil-water menisci.

4. Quasistatic network simulator

4.1 Introductory remarks

The network simulator developed in the course of this project controls the saturation in a two-step procedure: (1) modification of the global capillary pressure across the oil-water or the oil-gas interfaces; (2) performance of discrete pore-level displacement mechanisms. More precisely, for a given change in capillary pressure the network simulator follows a five-step algorithm: (a) the critical capillary pressure is selected; (b) all admissible transport mechanisms are looked; (c) the mechanism with the highest critical capillary pressure is chosen; (d) the selected transport mechanism is activated; (e) pore contents are updated leading to a change in fluid saturations.

Another function of the network simulator is to keep track of the continuity of the fluid phases in the porous network and to examine the stability of oil layers separating the aqueous and gas phases.

Fluid saturations in the pore space are determined by analyzing the distribution of the reservoir fluids within a specified section of the pore network. Each pore is assigned one of the basic fluid phase configurations containing either one, two, or three phases in the pore. Calculations of the saturation at the pore-level are based on the fluid configurations shown in Figures 3.1 and 3.2. It should be noted that fluid saturations depend on the invasion history and the capillary pressures associated with interfaces separating the coexisting fluid phases.

The relative permeabilities associated with a given saturation in the porous network are obtained by assigning conductances to each phase in all the connections. The conductance of a phase depends on the fluid phase configuration, the capillary pressure and the continuity of the phase in the porous network. The pressure field in the porous network is determined by adopting the analogy of the fluid conductance to a conductance of a network of electrical resistors. Finally, the relative permeability of a fluid phase is obtained by inserting the pressure drop and the flow rate to Darcy's law extended to the multiphase flow.

The network simulator is set up on a regular lattice in two or three spatial dimensions. The number of nodes in each direction is lx, ly, and lz. The total number of nodes is $N = lx \cdot ly \cdot lz$. The distance between the nodes, l_{node}, is set equal to a lattice constant. Each node is connected to four or six other nodes for the two- and three-dimensional network, respectively. The inlet face is represented by the first row of nodes in the x-direction and the outlet face by the last row of nodes. Flow takes place from the inlet face towards the outlet face. Periodic boundary conditions are imposed on the faces transversal to the flow direction in order to reduce the finite size effects.

The nodes represent pore chambers and the links between the nodes stand for pore throats. Pore sizes are described by the uniform distribution function with the limiting values given by $r_{t,max}$, $r_{c,max}$ and $r_{t,min}$, $r_{c,min}$ for the pore chambers and the pore throats, respectively.

The cross-sectional areas of the pores are assumed to be squares with half angles of the corners $\alpha = \pi/4$ and the roundness $r_d = 0$. The pore chambers are assumed cubic and the length of the pore chamber l_c is thus given by the size of the pore chamber while the pore throats are assumed to be tubes with length l_t calculated as the node distance minus the size of the connected pore chambers. For a more detailed description of the network model the reader is referred to Appendix A.

4.2 Basic Fluid Configurations and Stability of Oil Layers

The coexistence of three fluid phases in a single pore was described in section 3.1.3. The cross-sectional area of the oil layer was calculated using eq. (3.9) and the curvature of the oil-gas interface by eq. (3.7). As pointed out in the Chapter 3, the stability of the oil layer depends on equilibrium spreading coefficients (cf. eq. (3.4)), contact angles, and the cross-sectional geometry of the pore. By analyzing the admissible two- and three-phase fluid configurations described in Chapter 3, one can establish that there are 4 basic configurations of fluid phases in square-sectional pores (cf. Figure 4.1).

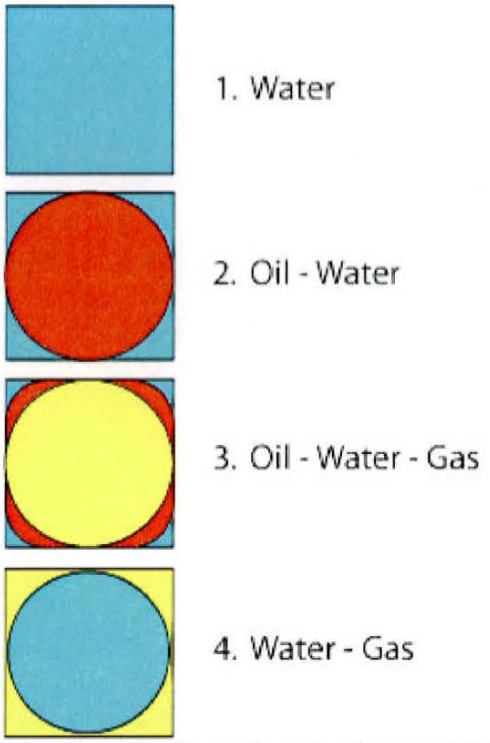

Figure 4.1 The four basic pore-scale phase configurations implemented in the quasistatic network simulator. Water can occupy an entire pore, oil, water, and gas can coexist in a pore, and all three phase can coexist in a pore provided that the oil layers are stable.

Stability of the fluid configurations depends on properties of the capillary pressure functions associated with the oil-water and oil-gas interfaces, tfluid properties and pore geometry. The stability criterion for the two-phase configurations (configurations 2 and 4) is that the capillary pressure between the coexisting phases cannot be lower than the critical pressures of the snap-off imbibition mechanisms. Similarly, the oil-gas capillary pressure must be larger than the critical pressure for snap-off of the gas phase in the configuration 3 pores.

In an unconfined space oil in the presence of gas and water either forms lenses or spreads at the water-gas interface. More precisely, for the equilibrium spreading coefficient smaller than zero, oil forms lenses while it spreads as a thin wetting film for the equilibrium spreading coefficient equal zero. Experimental results have shown that residual oil saturations less than 10% for systems with (nonequilibrium) positive initial spreading coefficient can be obtained (cf. Fenwick and Blunt, 1996 a, Øren and Pinczewski, 1994 and Vizika and Lombard, 1996). The high recovery efficiency was attributed to the dynamic effect due to spreading of oil at the water-gas interface ensuring hydraulic

continuity of the oil phase in the pore space. The importance of hydraulic continuity of the oil phase for low saturations of the oil phase has been stressed by several authors (Kantzas et al., 1988 a and b, Chatzis et al., 1988 a, Øren et al, 1992, Kalydjian et al., 1993, Zhou and Blunt, 1997, Blunt et al., 1995 and Fenwick and Blunt, 1998). Moreover, the presence of oil layers has important consequences for the gas phase. More precisely, the gas phase cannot destroy continuity of oil by breaking up a connected oil cluster into a number of smaller, individual clusters.

Several experiments described in the literature have shown that low residual oil saturations can also be obtained for fluid systems with negative initial spreading coefficients. Moreover, the gravity drainage experiments described in the literature indicate that the rate of oil production is much higher than can be justified by film flow where the typical dimension is in the order of nanometers (Blunt et al., 1995). The above conclusions are consistent with the calculations performed by Dong et al. (1995) who argued that oil may exist as stable layers in the corners of angular pores even though the equilibrium spreading coefficient is less than zero. The thickness of the oil layers is of the order of microns and can thus account for the higher drainage rates observed during gravity drainage experiments.

Blunt and Fenwick (1995) developed a simple criterion for stability of an oil layer used in their quasistatic network simulator. This stability criterion operates with the distance from the corner of a pore to the intersection of the oil-water interface with the porewall, L_{ow} and the distance to the oil-gas intersection with the porewall, L_{og} (cf. Figure 4.2). Calculations of L_{ow} and L_{og} are based on geometric considerations. In particular, L_{ow} and L_{og} depend on contact angles θ_{og} and θ_{ow}, the half angle of the wedge α, and the curvature of the fluid interfaces r_{ow} and r_{og}.

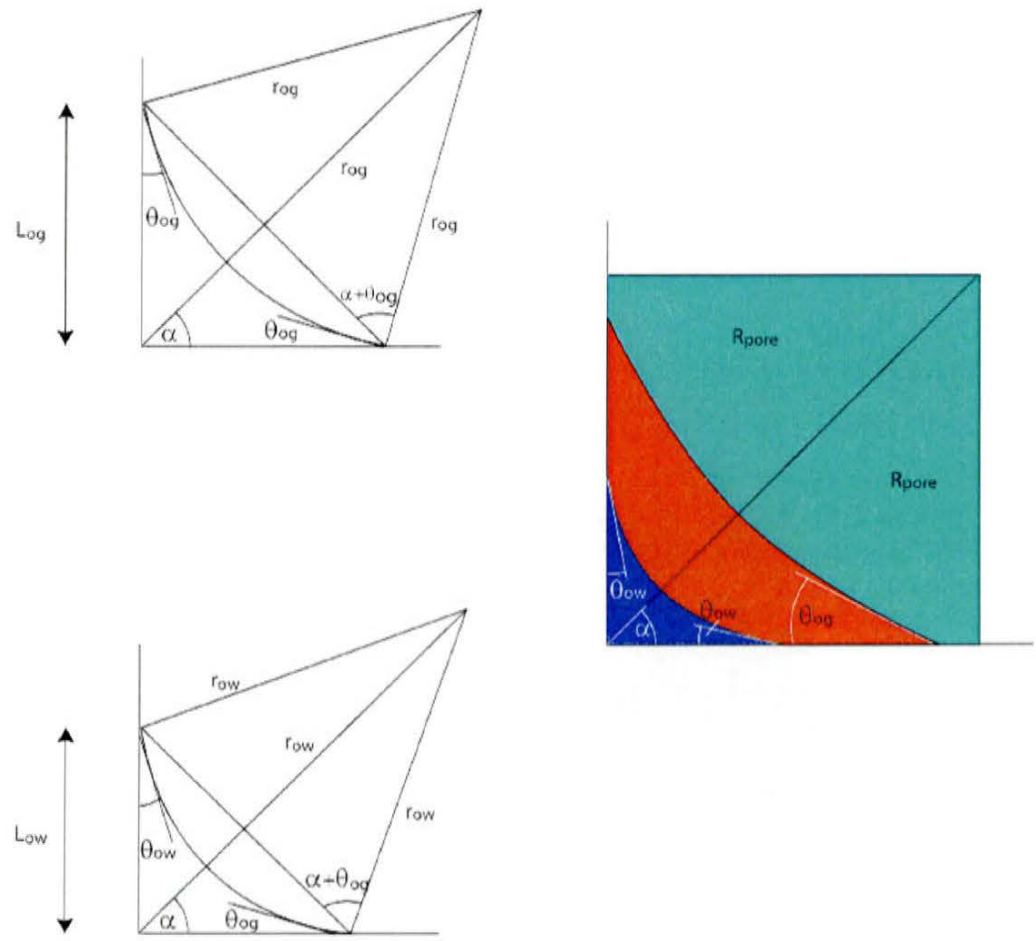

Figure 4.2 Calculation of the critical ratio of interfacial curvatures based on the distance between the corner and the oil-water interface and oil-gas interface intersection with the porewall.

The point where $L_{og} = L_{ow}$ is characterized by the critical ratio of the interface curvatures R_c given by

$$R_c = \frac{\cos(\theta_{og} + \alpha)}{\cos(\theta_{ow} + \alpha)} . \tag{4.1}$$

The ratio of the interfacial curvatures R of the oil-water interface and the oil-gas interface is defined as

$$R = \frac{r_{ow}}{r_{og}} = \frac{P_{cog} \cdot \sigma_{ow}}{P_{cow} \cdot \sigma_{og}} . \tag{4.2}$$

Thus, for the ratio of interface curvatures smaller than R_c the oil layers are stable while for larger ratios of interface curvatures the oil layers are unstable.

In the network model where all pores have the half angle of $\alpha = 45°$, the critical ratio of interface curvatures is the same over the entire network and can be calculated at the beginning of the simulation. Moreover, the ratio of interface curvatures during simulation is given solely by the

global capillary pressures because the interfacial tensions of the phases are constant during the simulations.

4.3 Continuity of Fluid Phases

Continuity of a fluid phase in a pore has an impact on the following two fluid properties; (1) connectivity of the phase to the inlet or outlet; (2) the location of discontinuous clusters. A phase may be connected to the inlet or the outlet, which ensures that the phase responds to changes in global capillary pressure i.e. the saturation, may gradually change in response to the external pressure changes. Also, the phase may participate in pore-level displacement mechanisms (cf. Figure 4.3). Fluid phases connected to both the inlet and the outlet contribute to conductance of the phase through the network. An isolated phase does not contribute to transport of the phase and is considered as being immobile except for the case of the oil phase participating in double displacement mechanisms.

The water phase is assumed to be always continuous in the pore space because the water phase wets the surface of the pores. Consequently, only the continuity of the oil and gas phase needs to be checked. The continuity of the phases is checked after each pore-level displacement event. More precisely, following a pore-level displacement the contents of the pores are updated and each pore is assigned one of the 4 possible phase configurations. It should be noted that updating the continuity status of a phase residing in the pore network follows every pore-level displacement mechanism. In fact, any single pore-level displacement event resulting in a break-up or coalescence of oil clusters may change transport properties of the oil phase.

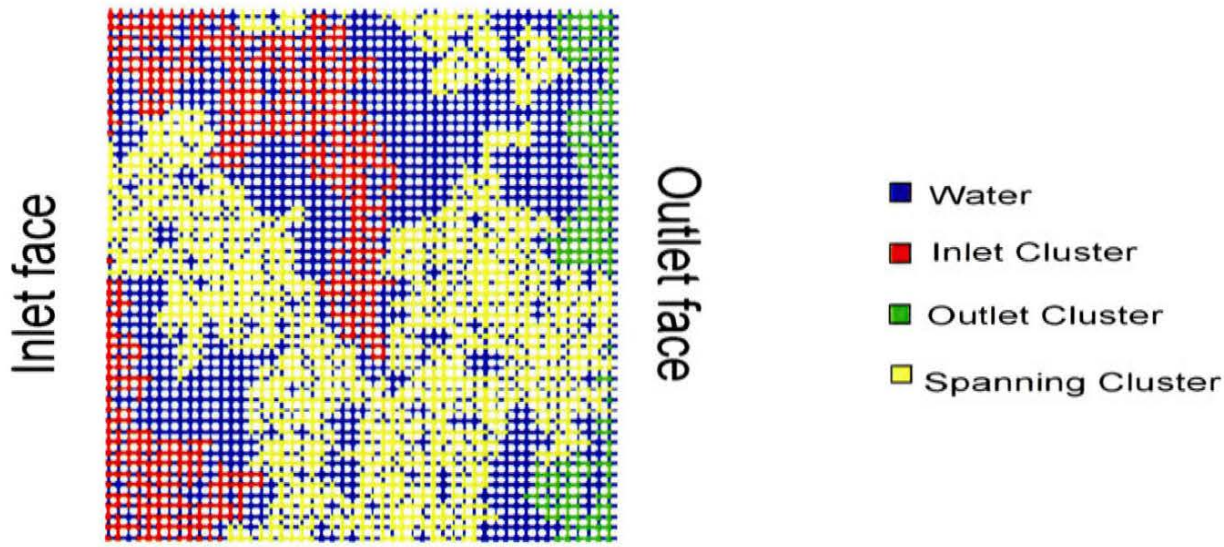

Figure 4.3. Continuity properties of the oil phase in a 50 × 50 network. The water phase (blue) is always connected to the inlet and the outlet face of the network. However, oil may be connected either to the inlet face (red cluster), the outlet face (green cluster) or connect the inlet and outlet by a spanning cluster (yellow cluster). Moreover, oil may be isolated in ganglia (not shown). It should be noted that only the spanning cluster contributes to the transport of reservoir fluids. The clusters containing gas can be characterized in the same way.

In computer algorithms implementing network models, integer labels are assigned to all pores containing oil. Each pore containing oil is then checked to find out whether it is in direct contact with another pore containing oil. If this is the case, both pores are assigned the smaller label value

of the two labels. The network is traversed until no more pores are assigned smaller label values. The result is a labeling of all the oil clusters in the network by an integer. The gas phase is labeled in a similar manner. The algorithm for labeling the clusters is rather slow because several sweeps of the network is necessary before all pores belonging to the same cluster have been assigned a single label value. The algorithm may be significantly reduced by starting out with the old label values and just assign new label values to the pores where a pore-level displacement has caused a change in content of a pore.

As soon as all the clusters have been labeled, the connection of the phases to the inlet or the outlet is checked by simply checking whether a pore has a cluster label which can be found on either the inlet, outlet or both faces of the network.

4.4 Critical Pressures of Pore-scale Displacement Mechanisms

The mechanisms observed in the micromodel experiments described in Chapter 3 were implemented in the network simulator except for the oil-dragging gas mechanism. Moreover, the snap-of mechanism was implemented because unstable fluid phase configurations may otherwise develop in the network. The parameters needed for the determination of critical pressures of the single event displacement mechanisms are the interfacial tensions between oil, water and gas σ_{ow}, σ_{og} and σ_{gw} and the contact angles θ_{ow}, θ_{og} and θ_{gw} which are given as input parameters. Single displacement mechanisms are allowed for both oil-water, gas-oil and gas-water interfaces.

The double drainage (DD) and double imbibition (II) have been defined as admissible double displacement mechanisms. Moreover, direct drainage and imbibition are allowed. The oil-dragging-gas mechanism has not been implemented because the calculation of the critical pressure for that mechanism to occur requires knowledge of the local pressure conditions, which was not determined in this project.

The choice of pore-level displacement mechanism includes two stages: (a) establishment of the criteria for a pore-level mechanism to occur have been met; (2) calculation and comparison of the pore-level displacement potentials (critical capillary pressures). Calculation of critical pressures of the single displacement mechanisms involving oil-water, oil-gas and gas-water can be performed and stored prior to commencing the tracking the macroscopic saturation trajectory. Moreover, each displacement mechanism may be ordered according to its critical pressure.

The two-phase displacement mechanisms in pore throats include the piston-like drainage and imbibition with critical pressures determined from eq. (3.10) and eq. (3.12), respectively. Also, the snap-off mechanism with the critical capillary pressure calculated from eq. (3.14) is implemented. For the pore chambers the two-phase displacement mechanisms include I_1- and I_2-mechanisms using the critical pressure given by Fenwick and Blunt (1998) given by eq. (3.13) with $C_1 = 2.0$ and $C_2 = 1.25$. Allowing the piston-like drainage of pore chambers and calculating the critical pressure from eq. (3.10) incorporates Haines' jumps. The sizes of the pore chambers are significantly larger than the pore throats. Consequently, piston-like drainage of a pore throat is naturally followed by piston-like drainage of a pore chamber in agreement with micromodel observations of the Haines' jump event.

The critical pressures of the double displacement mechanisms are calculated by summing the critical pressures of single displacement mechanisms. In particular, the critical pressures for double

imbibition mechanisms are calculated as superpositions of the snap-off, I_1-mechanism, I_2–mechanism, and piston-like imbibition displacement mechanisms. This leads to quite a few possible combinations for double imbibition displacements. Te critical pressures for double drainage mechanisms are calculated by summation of their counterparts for two piston-like displacements.

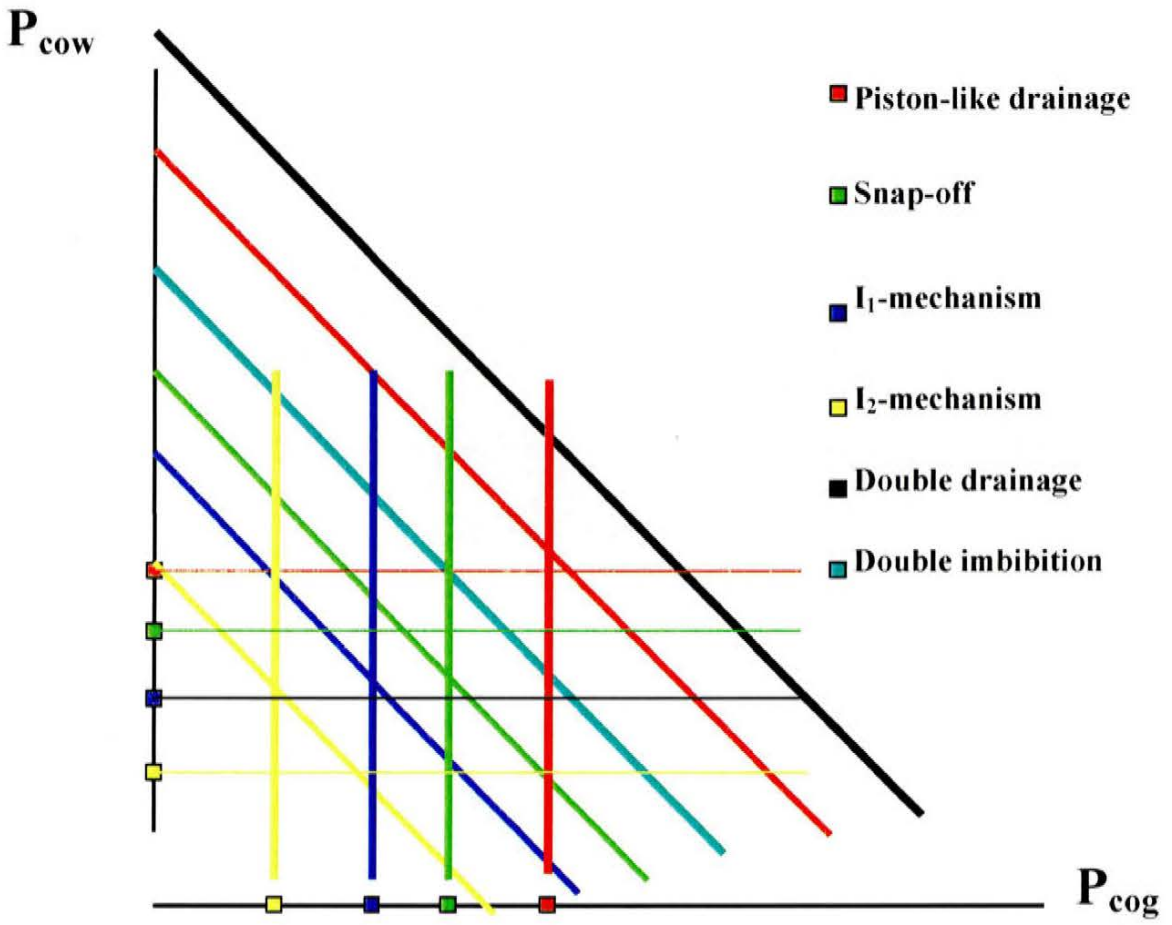

Figure 4.4 Critical pressures of pore-level displacement mechanisms depicted in the capillary pressure space for a pore throat and a pore chamber. It should be noted that critical pressures assigned to imbibition mechanisms are negative with their absolute values depicted in the figure. The oil-water displacement mechanisms are shown as horizontal dashed lines, oil-gas mechanisms as vertical solid lines, and gas-water mechanisms are depicted as dotted lines with the slope equal to –1.

The fluid saturations of the micromodel's pore network are controlled by the change in global capillary pressure associated with the three phases. The change of the capillary pressure is described by summing two quantities: the change in oil-water capillary pressure P_{cow} and the change in oil-gas capillary pressure P_{cog}. More precisely, the total capillary pressure between water and gas, P_{cwg}, is calculated as the sum of the oil-water and oil-gas capillary pressures.

$$P_{cwg} = P_{cow} + P_{cog} \tag{4.3}$$

where P_{cow}, P_{cog} , and P_{cwg} are the global capillary pressures. The absolute values of the critical pressures of single displacement mechanisms can be depicted in the capillary pressure space as horizontal and vertical lines for the oil-water and oil-gas displacement mechanisms, respectively (cf. Figure 4.4). The water-gas displacement mechanisms can be depicted as lines with slope –1

corresponding to a certain global water-gas capillary pressure. The absolute value of the critical pressures for double imbibition mechanisms are also lines that require a certain water-gas capillary pressure to be activated. Similarly, the double drainage mechanisms require a certain water-gas capillary pressure in order for the displacement mechanisms to occur and the critical pressures are thus also lines with gradient –1 in the capillary pressure space.

Thus, when the capillary pressure is changed in the network simulator, either for the oil-water interface or the oil-gas interface, a number of criteria regarding the critical pressures may be met and new displacement mechanism become possible. The choice of mechanism then depends on which displacement mechanism has the largest critical capillary pressure.

In order for two-phase drainage and imbibition displacement mechanism to occur the displacing phase must be connected to the inlet and the displaced phase to the outlet of the network. Discontinuous phases can not be mobilized by two-phase displacement mechanisms. For double displacement mechanisms the displacing phase of the primary event and the displaced phase of the secondary event must be connected to the inlet or the outlet of the network. Moreover, the phase being displaced in the first event must be connected to the phase displacing the third phase in the second event. In other words, one can not displace an oil ganglion and obtain a second displacement process involving a different ganglion.

It should be noted that double displacement mechanisms may lead to volume inconsistencies in the network model (cf. Mani and Mohanty, 1998). This is due to the fact that volume changes of the phases involved in the elementary events constituting double displacement mechanisms are in general different. More precisely, consider a double drainage mechanisms where gas displaces oil from a pore chamber. The displaced oil subsequently displaces water from another pore chamber. In general, the sizes of the pore chambers are different and thus they have different volumes. Consequently, the computational effort required to keep track of different volumes of the disconnected phases can be quite extensive.

4.5 Algorithm for Choosing Pore-level Displacement Mechanisms

The algorithm for the selection of pore-level displacement mechanisms is based on a prespecified set of capillary pressure functions, P_{cow}, P_{cog}, and P_{cgw}. The pore-level displacement mechanisms are successively checked one by one to verify whether the pore mechanism is feasible or not. For the I_1- and I_2-mechanism this includes checking that the right number of adjacent pores are filed with the phase considered. For each pore the relevant continuity properties of the phases are checked and the potential (critical capillary pressure) of the displacement mechanism is calculated and compared against the maximum potential of the previously checked displacement mechanisms. If the new potential is larger than those assigned to those previously checked, it is selected as the next displacement mechanism. The contents of the pores, which the selected displacement mechanism affects, are updated and the continuity of the phases is examined. The sweeping of the network in the search for the displacement mechanisms is quite laborious. Consequently, it limits the size of the pore space in network simulators.

4.6 Fluid Saturations in Pore Space

Phase saturations in the pore space are calculated for a specified section of the network limited by two rows of nodes in the x-direction. The section is usually placed in the center of the network. Alternatively, it can be placed in the part of the network close to the outlet to avoid inlet effects. The volume of each phase is calculated for each pore as the cross sectional area of the phase multiplied by the length of the pore. The volumes of each phase are summed over all the pores in the specified section of the network and divided by the total pore volume of the section,

$$S_i = \frac{\sum_{j=1}^{n_{total}} A_{i,j} \cdot l_{pore,j}}{\sum_{j=1}^{n_{total}} V_j} \qquad i = \text{w, o, g} \qquad (4.4)$$

where n_{total} is the total number of pores in the prespecified section of the network and $A_{i,j}$ is the cross sectional area of phase i in pore j. The volume of discontinuous ganglia is calculated in the same manner. The only exception was that the capillary pressure corresponding to the moment where the ganglion became disconnected from the inlet or outlet face is used instead of the global capillary pressure. Thus, the saturation changes due to changes in global capillary pressure only affect the saturation of the continuous part of a fluid phase.

4.7 Tracking Macroscopic Saturation Path

Tracking the saturation path originating from the macroscopic simulator $S_{macro} = (S_{g,macro}, S_{w,macro})$ is conducted by controlling the movement in the global capillary pressure space (cf. Figure 4.5) by imposing a capillary pressure on the network. At the microscopic level, movement in the capillary pressure space requires that the network simulator follow the saturation trajectory originating from the macroscopic simulator. Consequently, a difference in saturation of the network model S_{net} and a desired saturation point of the macroscopic saturation trajectory S_{macro} larger than a specified tolerance must be associated with a change in either oil-gas or oil-water capillary pressure in order to control the saturation of the network simulator.

The task of finding a change in capillary pressure corresponding to the correct change in saturation path is not trivial: in general, there exist no function relating points of the saturation triangle to points in the capillary space. In other words, a saturation point can be obtained by more than one path in the capillary space and a point in capillary space may correspond to different saturations depending on the followed saturation path followed (cf. Fenwick and Blunt, 1996).

Considering the configuration of the phases in a single pore, it appears that the water saturation decreases for increasing oil-water capillary pressure because the oil-water interface is pushed towards the corner of the pore. Likewise, gas saturation increases for increasing oil-gas capillary pressure because the oil-gas interfaces of the continuous parts of a phase are pushed outward. These observations are in agreement with the plot of the displacement mechanism in the capillary pressure space (cf. Figure 4.4). Increased oil-water capillary pressures lead to the displacement mechanisms where oil displaces water and increased oil-gas capillary pressure leads to the displacement mechanisms with gas displacing either oil through single displacement mechanisms or water through single or double displacement mechanisms. The oil saturation depends on both the oil-water

and the oil-gas capillary pressures. However, it is indirectly given by the saturation of the water and the gas phase. Experience derived from using the developed tracking algorithm indicates that adjusting the capillary pressure of the oil-water interface accelerates the tracking of the macroscopic saturation trajectory by the network simulator.

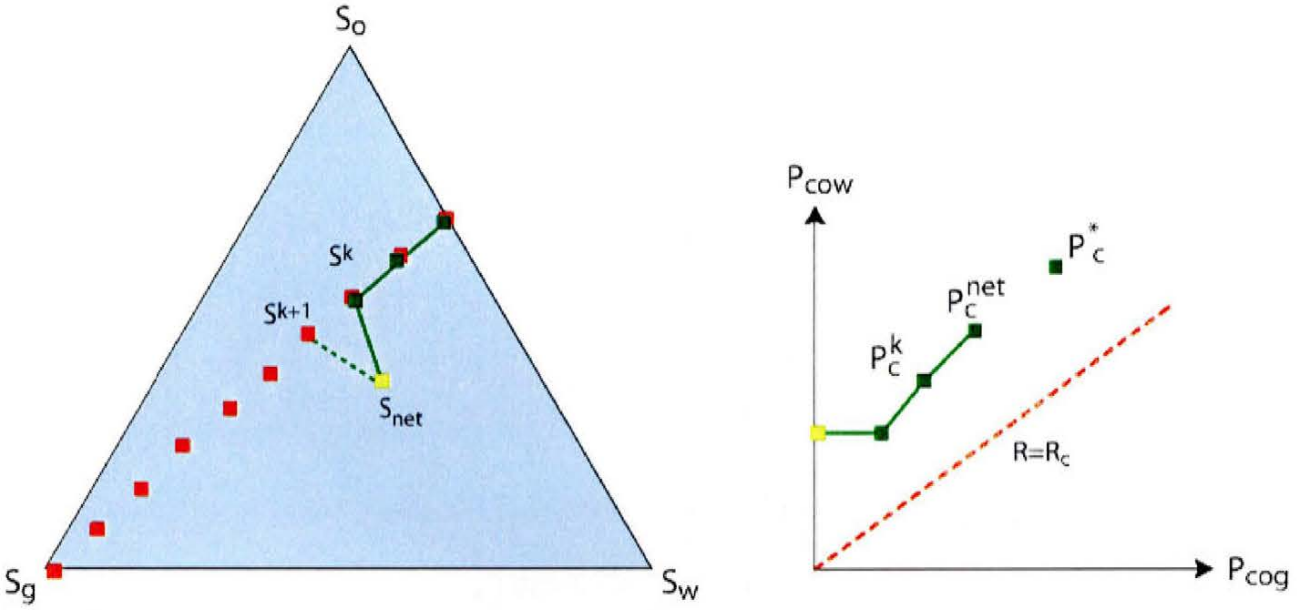

Figure 4.5. Tracking the saturation path. The goal of tracking is to control the saturation change in the network model by moving from the current saturation of the network S_{net} to the next point on the macroscopic saturation trajectory S^{k+1}. Tracking is performed by modifying the global capillary pressure from P_c^{net} to P_c^*.

Tracking of the macroscopic saturation trajectory by a network model ends either when all points of that trajectory have been 'visited' in a correct sequence, or when the residual saturation of oil or gas has been reached. The residual saturations of oil or gas are obtained when either gas or oil can no longer be displaced from the pore network in spite of the fact that this is required in order to continue tracking of the macroscopic saturation trajectory.

The ' tracking rules' can be summarized in the following algorithm.

IF $S_{w,net} > S_{w,macro} \Rightarrow$ Increase P_{cow} - GOTO 5

ELSE IF $S_{w,net} < S_{w,macro} \Rightarrow$ Decrease P_{cow} - GOTO 5

ELSE IF $S_{g,net} > S_{g,macro} \Rightarrow$ Decrease P_{cog} - GOTO 5

ELSE IF $S_{g,net} < S_{g,macro} \Rightarrow$ Increase P_{cog} - GOTO 5

Perform displacement mechanism with largest potential

Calculate S_{net}

IF $|S_{net}-S_{macro}|_2 >$ Tolerance GOTO 1 ELSE continue to next macroscopic saturation point.

The tolerance of the saturation deviation was typically set to 0.5 saturation units where the deviation was calculated as the two norm of the vector S_{net}-S_{macro}.

4.8 Determination of Relative Permeabilities

The relative permeability functions are determined for a limited section of the pore network. More precisely, the total flow of each phase through the network is determined by solving the pressure field of each phase for a given pressure drop across the conducting cluster. The conductance of a phase in a connection between two node points depends on the content of the pore, the capillary pressure between the phases, and the continuity of the phase. Conservation of volume is then invoked at each node point under the assumption that the phases is incompressible. Once the conductances of the phases have been established for all the connections, the pressure field can be found by solving the equation system

$$\mathbf{G} \cdot \mathbf{P} = \mathbf{Q}, \tag{4.5}$$

where **G** is the conductance matrix, **P** the pressure of the node points, and **Q** is the flow rate vector representing the boundary conditions. The equations are linear and unlike the dynamic simulator the conductance matrix does not depend of the pressure solution because the capillary pressure is assumed fixed. As soon as the pressure field has been solved, the flow rate and the pressure drop can be inserted into Darcy's law for multiphase flow and solved for the relative permeability of the phase. The absolute permeability of the network is determined at the beginning of the simulation by assuming that all pores are filled with water.

The conductance matrix depends on the content of the pores and the continuity of the flowing phase. It is thus only necessary to solve the pressure field for the spanning cluster, which reduces the size of the conductance matrix. In principle, it is only necessary to determine the pressure field for the backbone of the cluster, because the 'dangling' bonds do not contribute to flow of the fluid phase through the network. In particular, it should be noted that if no spanning cluster connecting the inlet to the outlet exists in the network for a given fluid phase, the conductance of that particular phase is zero. Consequently, the relative permeability is also zero.

Moreover, the linearity of the matrix equation (4.5) makes the relative permeability independent of the viscosity of the phase. Thus, the relative permeability only depends on the distribution of the coexisting phases within the network and the capillary pressure i.e. the path followed in the capillary pressure space.

4.9 Relative Permeability of Water Phase

The water phase is assumed to be connected throughout the network. Thus, all four basic fluid configurations (cf. Figure 4.1) must be considered when calculating the conductance of water between two nodes. In the configuration 1 where water is the only phase present in a pore the conductance is calculated as

$$g_w = \frac{8 \cdot r_{effective}^4}{\pi \cdot \mu_w \cdot l_{pore}} \tag{4.6}$$

where l_{pore} is the length of the pore and the effective radius $r_{effective}$ is given by eq.(A-6). For the configurations 2 and 3 the conductance of the water phase is given by

$$g_w = \frac{A_w \cdot r_{ow}^2}{\pi \cdot \mu_w \cdot l_{pore}} \tag{4.7}$$

where r_{ow} is the curvature of the oil-water interface given by, A_w the area of the water phase and β is the dimensionless resistance factor introduced in Section A.3.1. Calculation of the conductance of the water phase for configuration 4 is similar to eq. (4.7) with the exception that r_{ow} is replaced by the curvature of the gas-water interface r_{wg} given by the capillary pressure of the gas-water interface P_{cwg}.

It should be noted that for pores where disconnected oil or gas ganglia are present the curvature of the oil-water interface and the gas-water interface is in reality unknown because the capillary pressure of a ganglion is a local capillary pressure which is not related to the global capillary pressure. Therefore the curvature of the oil-water or a gas-water interface is calculated based on the local capillary pressure. The local capillary pressure is assumed to be given by the global capillary pressure at the moment the ganglion became isolated.

4.10 Conductances of Oil and Gas Phases

The pores belonging to the configuration 2 and the configuration 3 pores may conduct the oil phase. In the configuration 2 pores the conductance of the oil phase is given by eq. (4.7) where the effective radius is given by eq.(A-19). In the configuration 3 pores the conductance of the oil phase is calculated by

$$g_o = \frac{(A_o + A_w) \cdot r_{og}^2}{\beta \cdot \mu_o \cdot l_{pore}} - g_w \tag{4.8}$$

where $A_o + A_w$ is the sum of the area of the oil phase and the area of the water phase in the pore. Thus, the conductance is given by the total conductance of the oil and water phases as if there was no interface present minus the conductance of the water phase. Thus, it is inherently assumed that the presence of the oil-water interface does not affect the conductance of the oil.

The conductance of the gas phase is calculated by use of eq. (4.6) where the effective radius is calculated by eq. (A-19) using the area of the gas phase instead of the oil phase. In the configuration 3 the area of the gas phase is calculated based on the position of the oil-gas interface while for the the configuration 4, the area of the gas phase is calculated based on the position of the gas-water interface.

4.11 Conductance of Connection

The conductance of an entire connection is given as the sum of the resistance to flow of the pore throat and the two connecting pore chambers

$$g_{total,ij} = \frac{1}{\frac{1}{g_{chamber,i}} + \frac{1}{g_{throat,ij}} + \frac{1}{g_{chamber,j}}} \tag{4.9}$$

Thus, the conductance between two nodes is a function of the contents of the two pore chambers and the connecting throat. It should be noted that the conductance of the water phase in pores with gas or oil connected to the outlet or inlet is independent of the size of the pore. In other words, given the curvature of the oil-water interface and the gas-water interface, the conductance of the water phase is given by the half angle of the pores alone which is constant for a similar pore geometry. In other words, the relative permeability of the water phase is controlled by the geometry of the corners at low water saturations.

5. Macroscopic reservoir model and three-phase transport

A simple 1-D ECLIPSE model has been set-up for the study of WAG injection into an oil reservoir. It is assumed that the reservoir is horizontal and homogeneous with a uniform initial saturation distribution. The three phases are incompressible, the fluid and rock properties are constant and the saturation functions are simple Corey type power functions. We use the same values as do Marchesin and Plohr (1999) except for the capillary pressure, which is set to zero in order to facilitate theoretical analysis. Two injection wells, one for water injection and one for gas injection, are located in the first grid cell. One producer is located in the last grid cell. The simulator input data are:

5.1 Reservoir Dimensions and Grid

Reservoir dimensions: $L_x = L_y = L_z = 1.$ m

Grid cell numbers: $n_x = 1000,\ n_y = n_z = 1$

Grid cell lengths: $\Delta x = 0.001$ m, $\Delta y = \Delta z = 1.$ m

5.2 Rock Properties

Porosity: $\varphi = 0.2$

Absolute permeability: $K = 100.$ mD

Rock compressibility: $C_{rock} = 1.E\text{-}6$ 1/bar

5.3 PVT Properties

The oil is dead and the gas is dry.

Viscosity of oil: $\mu_o = 1.0$ cp

Viscosity of gas: $\mu_g = 0.3$ cp

Viscosity of water: $\mu_w = 0.5$ cp

Formation volume factors: $B_o = B_g = B_w = 1.$

5.4 Saturation Functions

All critical and irreducible saturations are zero.

Relative permeability of water: $k_w = S_w^2$ (5.1)
Relative permeability of oil: $k_o = S_o^2$ (5.2)
Relative permeability of gas: $k_g = S_g^2$ (5.3)
Capillary pressure: $p_{cow} = p_{cgo} = 0.$ bar

5.5 Initial Conditions

Pressure: $p(x,0) = 1.$ bar

Oil saturation: $S_o(x,0) = 0.76$

Water saturation: $S_w(x,0) = 0.16$ or 0.10

Gas saturation: $S_g(x,0) = 0.08$ or 0.14

5.6 Operating Conditions

Each WAG cycle comprises of 67% water followed by 33% gas. During each cycle 1/100 of the pore volume is injected. The total number of cycles is 40. The pore volume is 0.2 m^3.

5.7 Results

Figure 5.1 shows the calculated saturation distributions after injection of 0.4 pore volumes. In both cases the left state is the same corresponding to the injection condition 67% water followed by 33% gas while the right states are still undisturbed and equal to the initial conditions. In Figure 5.2 are shown the calculated saturation paths.

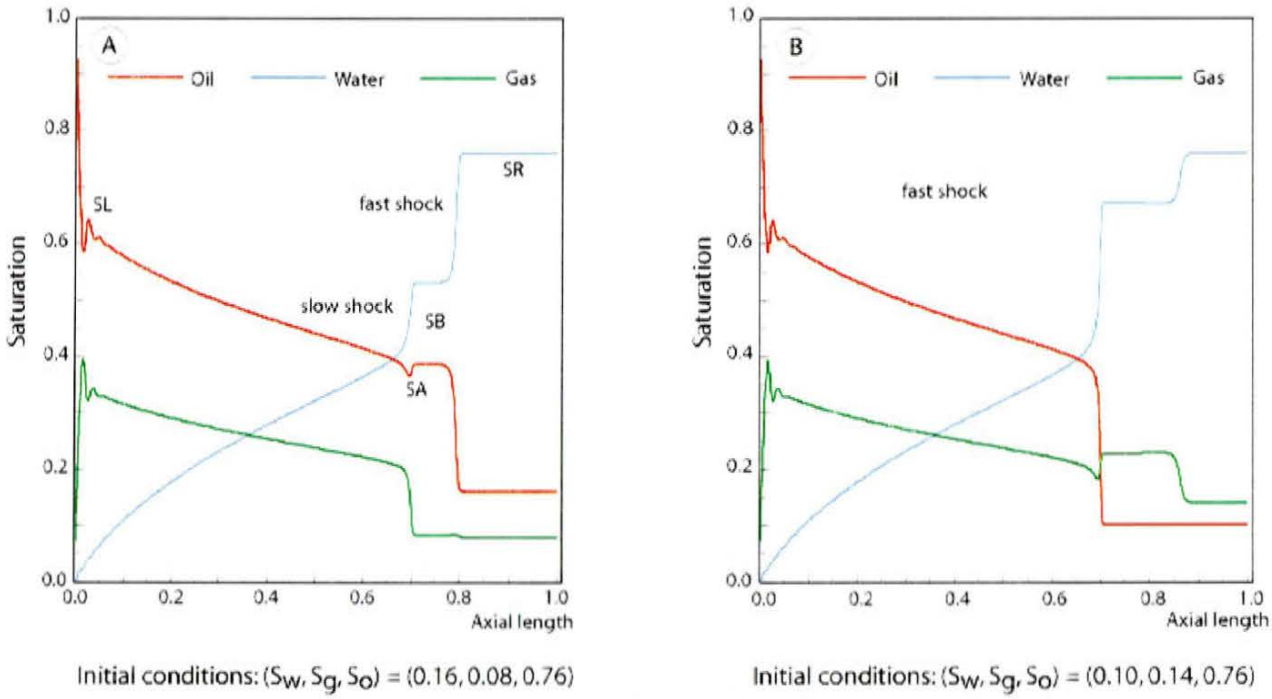

Figure 5.1 WAG_67_33 axial saturations after injection of 0.4PV

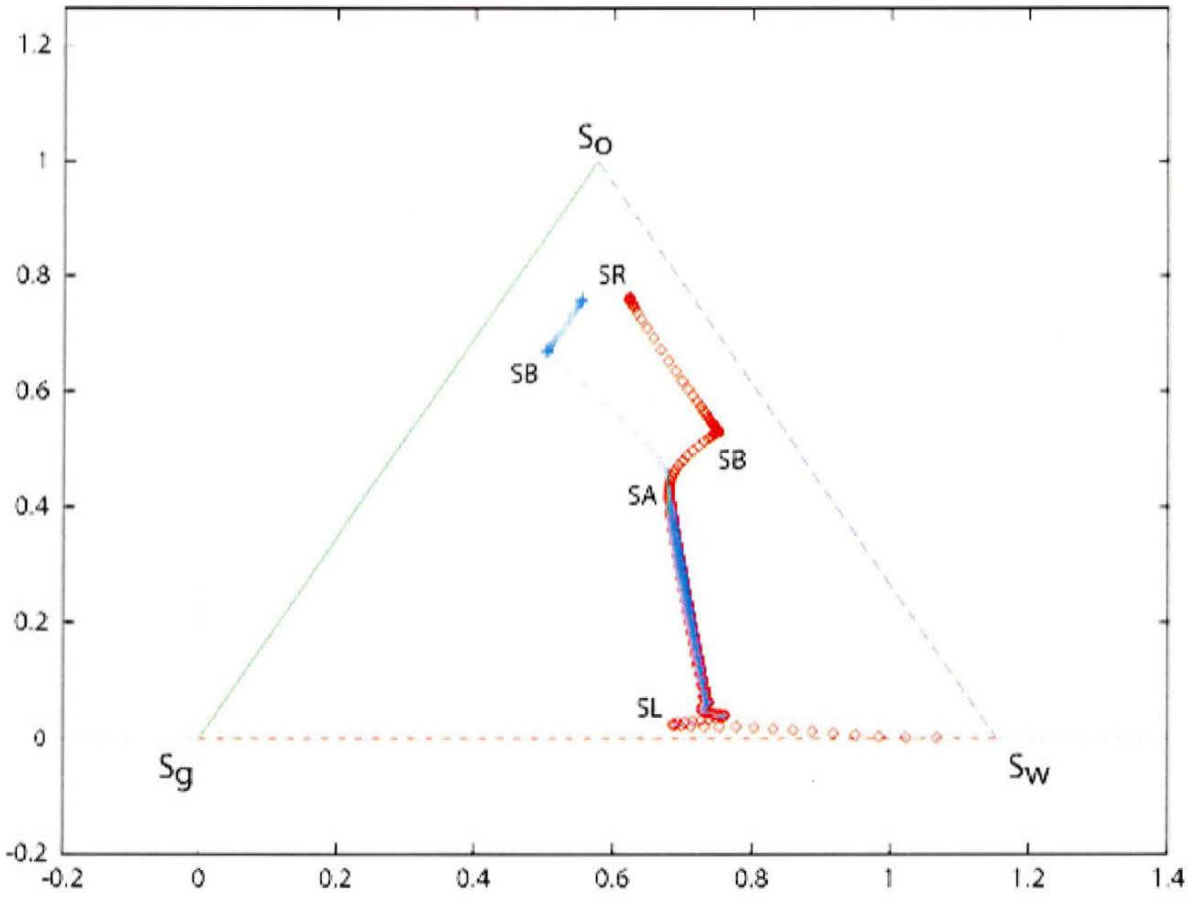

Figure 5.2 WAG_6733 saturation paths for two different initial conditions

Considering that the two cases are pretty close to each other the calculated solutions are remarkably different. In order to understand what happens reference is made to Figure 5.3 which shows possible rarefactions, i.e. continuous solutions of the hyperbolic conservation laws, corresponding to the fast and slow characteristic speed, respectively. The two sets of curves are defined as described below.

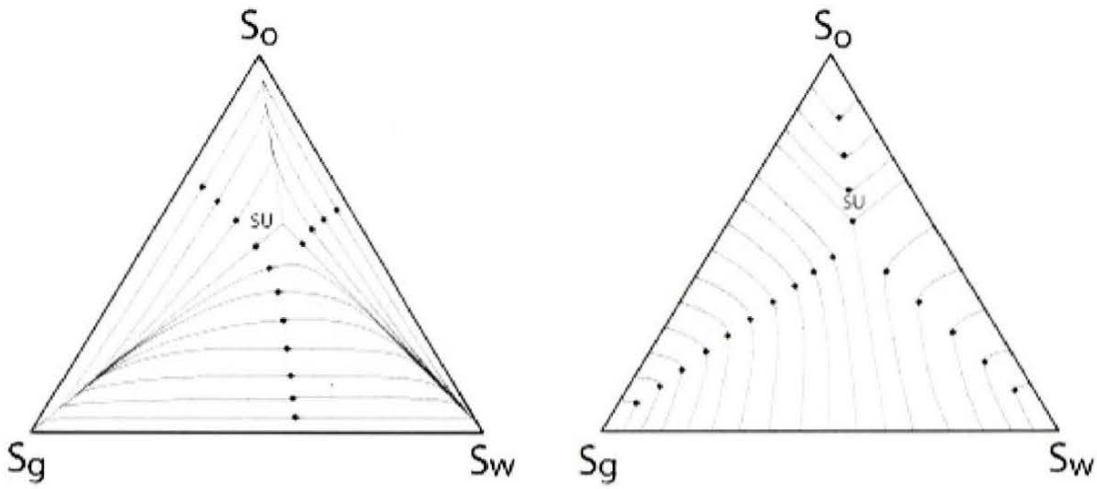

Figure 5.3. Rarefaction curves for the fast (left figure) and slow characteristic speeds.

The fast and slow characteristic speeds are equal to the eigenvalues of the matrix A, where

$$A = \begin{Bmatrix} \frac{\partial v_w}{\partial S_w} & \frac{\partial v_w}{\partial S_g} \\ \frac{\partial v_g}{\partial S_w} & \frac{\partial v_g}{\partial S_g} \end{Bmatrix} = \begin{Bmatrix} A_{11} & A_{12} \\ A_{21} & A_{22} \end{Bmatrix} \tag{5.4}$$

The eigenvalues are

$$\lambda_1, \lambda_2 = \frac{1}{2}\left\{A_{11} + A_{22} \pm \sqrt{(A_{11} - A_{22}) + 4A_{12}A_{21}}\right\} \tag{5.5}$$

The corresponding eigenvectors $(x_1, 1)^T$ and $(1, x_2)$ are given by

$$x_1 = -\frac{A_{12}}{(A_{11} - \lambda)} = -\frac{(A_{22} - \lambda)}{A_{21}} \tag{5.6}$$

$$x_2 = -\frac{(A_{11} - \lambda)}{A_{12}} = -\frac{A_{21}}{(A_{22} - \lambda)} \tag{5.7}$$

where $\lambda = \lambda_1, \lambda_2$
Now, the conservation laws in the quasilinear form can be written as follows

$$\frac{\partial \bar{S}}{\partial t} + A\frac{\partial S}{\partial x} = 0\,. \tag{5.8}$$

Substituting in eq. (5.7)

$$u = \frac{x}{t} \tag{5.9}$$

leads to the following equation which the rarefactions or continuous solutions must obey:

$$\{A - Iu\}\frac{d\bar{S}}{du} = 0 \tag{5.10}$$

where I is the identity matrix. This means that the two eigenvectors are

$$\bar{x}^T = const\left\{\frac{dS_w}{du}, \frac{dS_g}{du}\right\} \tag{5.11}$$

and hence

$$x_1 = \frac{dS_w}{dS_g} \tag{5.12}$$

$$x_2 = \frac{dS_g}{dSw} \tag{5.13}$$

eqs.(5.6), (5.7), (5.12) and (5.13) then show that

$$\frac{dS_w}{dS_g} = -\frac{A_{12}}{(A_{11} - \lambda)} = -\frac{(A_{22} - \lambda)}{A_{21}} \tag{5.14}$$

$$\frac{dS_g}{dS_w} = -\frac{(A_{11} - \lambda)}{A_{12}} = -\frac{A_{21}}{(A_{22} - \lambda)} \tag{5.15}$$

Now, each of the rarefaction curves in Figure 5.3 are calculated by integrating either eq. (5.14) or eq. (5.15) from 0.0 to 1.0 with the eigenvalue λ equal to λ_1 and λ_2, respectively.

The point in the saturation space where the two eigenvalues, eq. (5.5) are equal is called the umbilic point. It can be shown (Trangenstein (1988)) that when the relative permeabilities are all of the Corey type, as are eqs. (5.1) – (5.3) then the umbilic point is given by

$$S_{u,o} = \frac{\mu_o}{\mu_o + \mu_g + \mu_w} \tag{5.16}$$

$$S_{u,g} = \frac{\mu_g}{\mu_o + \mu_g + \mu_w} \tag{5.17}$$

$$S_{u,w} = \frac{\mu_w}{\mu_o + \mu_g + \mu_w} \tag{5.18}$$

Now we return to the two quite different solutions obtained corresponding to the two sets of initial conditions, Figures 5.1 and 5.2. In the first case with $(S_W, S_g) = (0.16, 0.08)$. This solution has the classical wave structure consisting of a slow wave group and a fast wave group (Marchesin and Plohr (1999)). The slow wave group comprises a slow rarefaction fan from the state S^L to the state S^A (see Figures. 5.2 and 5.3) and an adjoining slow shock wave from S^A to the constant state S^B. The fast wave group is a Buckley-Leverett shock wave, i.e. an oil bank from S^B to the state S^R.

In the second case with the initial state $(S_w, S_g) = (0.10, 0.14)$ the solution is different, containing three wave groups. The slow wave group contains only a rarefaction fan from S^L to S^A , see Figures 5.2 and 5.3. The fast wave group is a Buckley-Leverett shock from S^B to S^R. Between the slow and fast wave groups is a transitional shock wave with left state S^A and Right State S^B.

Now, Marchesin and Plohr (1999) observe that the amplitude of the transitional wave is larger than the amplitude of the fast shock wave and conclude that the transitional shock wave makes a substantial contribution to total oil recovery. This conclusion is however not substantiated by the results presented in the paper and neither by our results. The total oil recovery after injection of 0.4 pore volumes in the first case with $(S_w, S_g) = (0.16, 0.08)$ where no transitional wave occured is in fact 2% larger than in the second case (Figure 5.1).

Another thing is, that some of the parameters used in the present example are not very realistic in relation to Danish chalk reservoirs. The gas viscosity is much too large and the capillary pressure is neglected. Consequently, new calculations were run with the gas viscosity $\mu_g = 0.03$ cp and an oil-water capillary pressure measured on a North Sea chalk plug. The results can be summed up as follows:

- Due the high capillary pressure the front of the injected water is smeared out and the transitional waves disappear. The cumulative amount of oil produced at a given time is however, more or less unaffected.

- The reduced gas viscosity smears out the front of the injected gas, whereas the height of the waterfront is increased. The transitional wave still exists but it moves slower and the cumulative amount of oil produced at a given time is somewhat smaller. After injection of about 40% pore volume the total amounts of oil produced are 54% and 43%, respectively.

6. Multiscale modeling of relative permeability functions

6.1 Introduction

Hydrocarbon reservoir simulators describe transport processes at the scale of a grid block (~1000 m^3). However, relative permeabilities are measured in laboratory experiments using small plugs cut from reservoir core (~ 100 cm^3). Thus, the characteristic size of a typical plug represents a minute fraction of the total grid block volume. Consequently, a major task in performing realistic field simulations is that of relating laboratory core measurements to the grid-block scale. This is the upscaling problem reducing a *multiscale* system to a system with a *single* effective scale.

This chapter describes an alternative approach to modeling of relative permeabilities. In contrast to upscaling, none of the models pertaining to a single scale would suffice to reliably describe the entire system. More precisely, the modelling problem under consideration requires a very accurate and computationally expensive description at one scale and a coarser description at another scale. Consequently, the models pertaining to each scale are applied in combination to build a comprehensive description of the entire system exhibiting multiple scales.

More specifically, this chapter deals with the application of two-scale modeling to determination of three-phase relative permeabilities for gas injection and Water-Alternating-Gas injection processes, respectively. It is assumed that a large separation exists between the two scales, and, consequently, that they are weakly coupled. The models describing three-phase transport at the pore- and macroscopic scales are formulated. The relative permeabilities determined from a computation at a pore-scale are iteratively fed into a computation at a grid scale. At the fixed point of the iteration procedure the selfconsistent saturation trajectories and the associated relative permeability functions for three coexisting phases (oil, water, and gas) are determined. Finally, conditions under which the iterative procedure leads to the selfconsistent three-phase relative permeabilities are discussed. In particular, the class of relative permeability functions ensuring hyperbolicity of the model equations, properties of transitional waves as the solutions to these equations, and their impact on hydrocarbon recovery efficiency are described.

6.2 Selfconsistent Relative Permeability Functions

Consider a one-dimensional horizontal reservoir of the extent of 1000 m (cf. Figure 6.1).

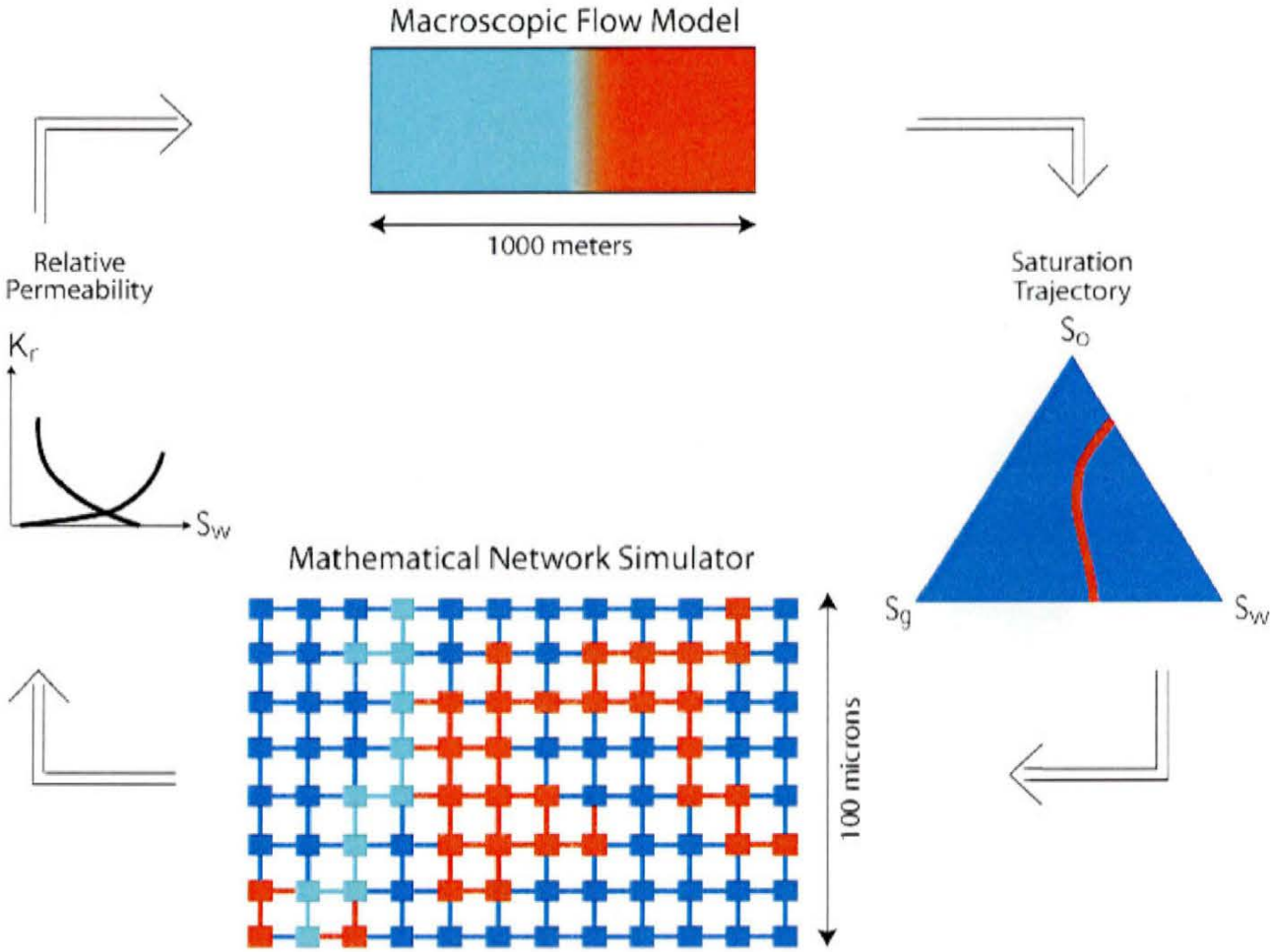

Figure 6.1 Schematic diagram of the selfconsistent procedure. An initial guess of relative permeability is fed to the macroscopic flow model, which generates a saturation trajectory. The saturation trajectory is followed by the network simulator, which gives a set of relative permeability functions. The iterative procedure continues until there is no more change in the saturation path.

Gas or water is injected in one end of the reservoir and oil is produced in the opposite end of the reservoir. At the macroscopic scale (the characteristic size is approximately 100 m) the viscous forces dominate and control the flow. The variation of water and gas saturations with position along the reservoir, dS, is small except for the region where the front of the displacement is advancing. However, on the microscopic scale of a few thousand pores, even on the front, the saturation changes are small and the saturation can be assumed constant. Thus, transport properties are mainly governed by the capillary forces.

The macroscopic scale is represented by a horizontal, one-dimensional macroscopic reservoir model set up on an ECLIPSE 100 simulator of three-phase fluid transport. The underlying reservoir model neglects the capillary and gravitational forces. More precisely, the transport problem is described by the classical Buckley-Leverett model extended to three-phase flow. The input to the macroscopic model consists of three relative permeability functions and the viscosities of the three phases. Moreover, the injection conditions are given by an injection sequence of water, oil and gas. The

output of the macroscopic model is a saturation trajectory in the saturation triangle connecting the initial and final phase saturations in the reservoir.

The microscopic scale is represented by a quasistatic network simulator. The sequence of the pore-scale displacement mechanisms in the network simulator is controlled by a series of changes in the capillary pressure associated with the curvature of the fluid phase interfaces. More precisely, the sequence of changes in the capillary pressure creates a path in $P_{cgo} - P_{cow}$ space (cf. Figure 6.5). The two-phase displacements are limited to P_{cow} and P_{cgo} axes.

The relative permeability functions for the three phases are calculated by the network simulator, which determines the pressure field corresponding to a prespecified path in the capillary pressure space, or in the saturation triangle.

More precisely, the applied procedure for obtaining selfconsistent three-phase relative permeability functions for three-phase flow in porous medium is as follows:

1. Given initial conditions, injection conditions, viscosities of the phases, the network simulator performs a displacement into three-phase region of the saturation triangle.

2. The displacement results in a set of three-phase relative permeabilities tabulated as functions of their own saturations for the selected path.

3. The tabulated values are input into a one-dimensional reservoir simulator based on Buckley-Leverett model for three-phase flow. The reservoir simulator performs displacement for the same initial and injection conditions. The resulting saturation path is obtained by plotting the saturations of all grid plots on a ternary triangle.

4. The saturations paths produced by the network simulator and those determined by the reservoir simulator are compared. If the two paths are different, the network simulator follows the path obtained from the reservoir simulator. If the paths coincide, the iteration stops.

The above iteration procedure was applied by Fenwick and Blunt (1997) for gas injection into a waterflooded reservoir. By linking the relative permeability functions determined by the network simulator to the macroscopic reservoir simulator and iteratively computing a saturation path, until the relative permeability functions converged to a fixed point, the selfconsistent saturation paths and the associated relative permeability functions were obtained. Thus, the relative permeability functions create a link between the pore-level scale and the macroscopic scale.

In another publication, Fenwick and Blunt (1998) emphasize the role of stable oil layers to ensure high conductivity of the oil phase at low oil saturation for high recovery efficiencies in gas injection processes.

Another recovery method, which received considerable attention, is the water-alternating-gas (WAG) injection process. Its popularity is due to the increased recovery efficiency as compared to the single-phase injection of either gas or water (Christensen et al., 1998). WAG injection on the field scale leads to saturation trajectories on the pore level much different than those typical for gas injection investigated by Fenwick and Blunt (1998). Consequently, trajectories in the capillary pressure space are also much different from those appearing during gas injection. The goal of our investigations of the iterative procedure for WAG processes has been to characterize the WAG

trajectories in the saturation space, to investigate the role of oil layers on the microscopic scale, and to evaluate their impact on recovery efficiency.

6.3 Macroscopic Three-phase Flow Model

Macroscopic three-phase flow model in two- or three spatial dimensions leads to complex flow scenarios which depend on a large number of parameters such as gravity, capillary forces, injection rate of water and gas and shape of the reservoir. Consequently, a number of simplifications of the macroscopic model were necessary in order to establish a practical macroscopic model for the iterative procedure. The adopted simplifications are as follows:

- Negligible capillary forces,
- Negligible gravitational forces,
- Incompressible phases,
- Gas is insoluble in oil,
- One-dimensional flow.

The mathematical model is thus reduced to specification of initial conditions for the phase saturations, relative permeability functions, viscosity and an injection sequence of the fluid phases. The solution to the one-dimensional three-phase Buckley-Leverett model is quite challenging and far from understood (cf. Trangenstein, 1988). Consequently, it deserves to be reviewed for better understanding of the behavior of the macroscopic model.

6.3.1 Three-Phase Flow: Buckley-Leverett Model

Under the assumptions stated above the pressure equations of the three-phase flow become equivalent to the three-phase one-dimensional Buckley-Leverett model. By introducing dimensionless time and space variables the conservation of the gas phase may be described by

$$\frac{\partial S_g}{\partial t} + \frac{\partial f_g}{\partial x} = 0, \tag{6.1}$$

where S_g is the gas saturation and f_g is the fractional flow curve of gas. Similarly the conservation of water is given by

$$\frac{\partial S_w}{\partial t} + \frac{\partial f_w}{\partial x} = 0, \tag{6.2}$$

where S_w and f_w are the saturation and fractional flow curves for water. The fractional flow functions are defined as

$$f_g = \frac{k_{rg}/\mu_g}{k_{rg}/\mu_g + k_{rw}/\mu_w + k_{ro}/\mu_o}, \tag{6.3}$$

and

$$f_w = \frac{k_{rw}/\mu_w}{k_{rg}/\mu_g + k_{rw}/\mu_w + k_{ro}/\mu_o}, \tag{6.4}$$

where k_{rw}, k_{rg} and k_{ro} are the relative permeability functions for water, gas and oil. μ_w, μ_g, and μ_o are the viscosities of water, gas and oil respectively. Only two fractional flow functions are needed to describe the flow due to the restriction that the sum of the phase saturations must equal unity

$$S_w + S_o + S_g = 1. \tag{6.5}$$

For analysis of a given injection sequence such as gas injection or WAG injection, the Buckley-Leverett model is referred to as the Riemann problem. The solution to the Riemann problem with a given injection sequence depends solely on $\eta = x/t$ and the initial saturations of the model. The initial conditions and the injection sequence are given as a right state, describing the initial phase saturations of the model, defined by

$$S(x > 0, t = 0) = S_r = \left(S_g^r, S_w^r\right), \tag{6.6}$$

and a left state, describing the injection sequence, defined by

$$S(x < 0, t = 0) = S_l = \left(S_g^l, S_w^l\right). \tag{6.7}$$

By invoking the self-similarity $\eta = x/t$, the Riemann problem is transformed into an eigenvalue problem given by

$$\begin{vmatrix} \frac{\partial f_w}{\partial S_w} - \eta & \frac{\partial f_w}{\partial S_g} \\ \frac{\partial f_g}{\partial S_w} & \frac{\partial fg}{\partial Sg} - \eta \end{vmatrix} = 0. \tag{6.8}$$

The resolution of eq. (6.8) leads to a quadratic equation. The solutions to eq. (6.1) and eq. (6.2) propagate as waves through the medium with propagation speeds equal to the eigenvalues determined by eq. (6.8). More precisely, the eigenvalues are given by

$$\eta = \frac{\frac{\partial f_w}{\partial S_w} + \frac{\partial f_g}{\partial S_g} \pm \sqrt{\Omega}}{2}, \tag{6.9}$$

where Ω is the discriminant given by

$$\Omega = \left(\frac{\partial f_w}{\partial S_w} - \frac{\partial f_g}{\partial S_g}\right)^2 + 4 \cdot \frac{\partial f_w}{\partial S_g} \cdot \frac{\partial f_g}{\partial S_w}. \tag{6.10}$$

The eigenvectors are given by

$$\xi = \begin{pmatrix} \frac{dS_w}{d\eta} \\ \frac{dS_g}{d\eta} \end{pmatrix}. \qquad (6.11)$$

The eq. (6.1) and eq. (6.2) are said to be hyperbolic if all eigenvalues (cf. eq. (6.9)) are real. The sign of the discriminant (eq. (6.10)) determines whether the eigenvalues are real or complex. Furthermore, if the two eigenvalues are different ($\Omega = 0$) for all permissible saturation values, the equations are said to be strictly hyperbolic. Finally, the equations are said to be genuinely nonlinear if

$$\frac{\partial \Omega}{\partial S}\xi = 0\,. \qquad (6.12)$$

A small Fortran program was written to evaluate the eigenvalues of different polynomial forms of the relative permeability functions similar to those proposed by Sahni et al. (1996). The eigenvalues of a Corey-type relative permeability function with identical viscosities of the three phases are shown in Figure 6.2. The smaller eigenvalue corresponding to the minus sign in eq. (6.9) is called the slow characteristic speed and the larger eigenvalue corresponding to the plus sign is called the fast characteristic speed.

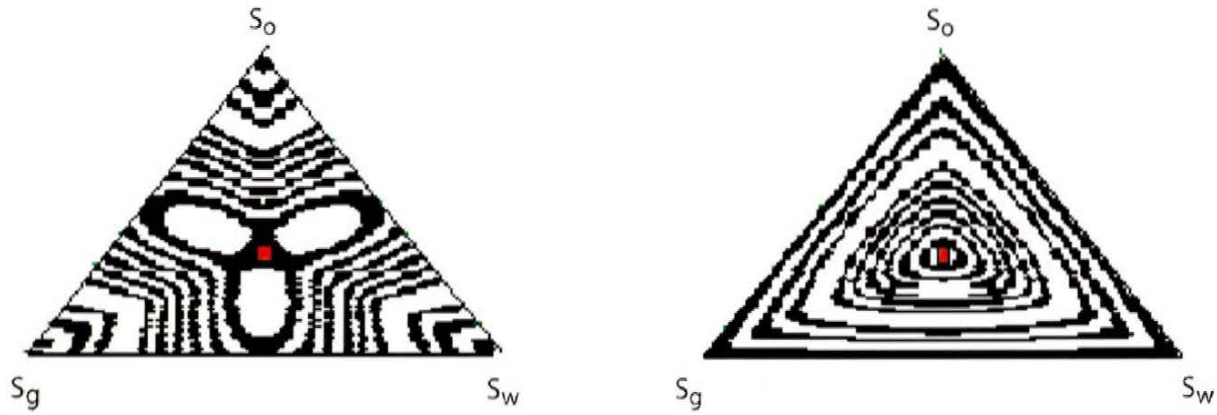

Figure 6.2 Eigenvalue plot of a Riemann problem using Corey-type relative permeability functions and equal viscosities of the phases. The left side shows the eigenvalues corresponding to the fast characteristic speed and the right side the eigenvalues corresponding to the slow characteristic speed. The red dot indicates the location of the umbilic point. The lines correspond to eigenvalues that are within 5 percent of the difference between the maximum and the minimum eigenvalues.

6.3.2 Solution of Three-phase Buckley-Leverett Model

Solutions to the two-phase Buckley-Leverett model are constructed from two kinds of basic solutions: shocks and rarefaction waves. Rarefaction waves are continuous solutions and shocks are discontinuous solutions to the underlying Riemann problem. The solutions can be constructed by

use of Oleinik chords or Lax's characteristics which are simple versions of the so-called entropy condition. These conditions basically state that the solution of eq. (6.1) and eq. (6.2) must be the limit of the flow problem including capillary pressure for capillary forces approaching zero (cf. Trangenstein, 1988).

For three-phase Buckley-Leverett flow the construction of the solution is more complex, but still involves rarefaction and shock waves. For strictly hyperbolic genuinely nonlinear equations the wave solutions may be constructed by determining a constant state which connects the elementary solutions (cf. Trangenstein, 1988).

Unfortunately, the Riemann problem underlying three-phase Buckley-Leverett model is in general neither strictly hyperbolic nor genuinely nonlinear. In fact, simple forms of the relative permeability functions and certain combinations of phase viscosities can yield the so-called elliptic regions in the saturation triangle where the eigenvalues are complex numbers corresponding to a negative discriminant ($\Omega < 0$). On the boundary of the elliptic regions the eigenvalues are identical corresponding to the discriminant being zero. For special types of relative permeability functions the curve where the discriminant is zero is located at a single point called the umbilic point. The umbilic point generally acts as the so-called organizing center for the solution of the Riemann problem (Guzman and Fayers, 1996 and Marchesin and Plohr, 1999).

The location of the umbilic points and existence and extent of elliptic regions depends on viscosity and relative permeability functions of the three phases. The variation of the eigenvalues can be analyzed by considering the terms of the discriminant (eq. (6.10)). The first term of eq. (6.10) contains the difference between the diagonal elements of the Jacobian matrix and is never negative. On the other hand, it is equal to zero only when the diagonal elements are identical. The second term can be either positive or negative depending on the viscosities of the phases and their respective relative permeability functions. For oil viscosities much larger than the viscosity of water and gas the term is positive for most the saturation space (Fayers, 1989). Consequently, an elliptic region is small if it exists.

6.3.3 Special Types of Relative Permeability Functions

Because of the complexity of the solution to the Riemann problem underlying the three-phase Buckley-Leverett model it is often necessary to use simple forms of the relative permeability functions in order to study the effects of various parameters. Especially, Corey-type relative permeability functions have been studied because they are easy to differentiate and generally capture many features of experimentally measured relative permeability functions. A special feature of the Corey-type relative permeability function is the absence of an elliptic region and the presence of a single umbilic point (Marchesin and Plohr, 1999). For fixed relative permeability functions the position of the umbilic point is determined by the viscosity ratios of the phases.
For the case where $k_{ro} = S_o^2$, $k_{rw} = S_w^2$ and $k_{rg} = S_g^2$, the position of the umbilic point can be calculated analytically by insertion of the differentiated fractional flow curves into eq. (6.8). The umbilic point given by

$$S_w = S_g \cdot \frac{\mu_w}{\mu_g}, \tag{6.13}$$

and

$$S_g = 1 - 2 \cdot S_w \cdot \frac{\mu_o}{\mu_w}. \qquad (6.14)$$

With increasing viscosity of a phase the umbilic point is attracted towards the vertex of the saturation triangle of representing that phase. Thus, for fixed relative permeability functions the umbilic point can be moved around the saturation triangle by change of viscosity ratios (cf. Figure 6.3).

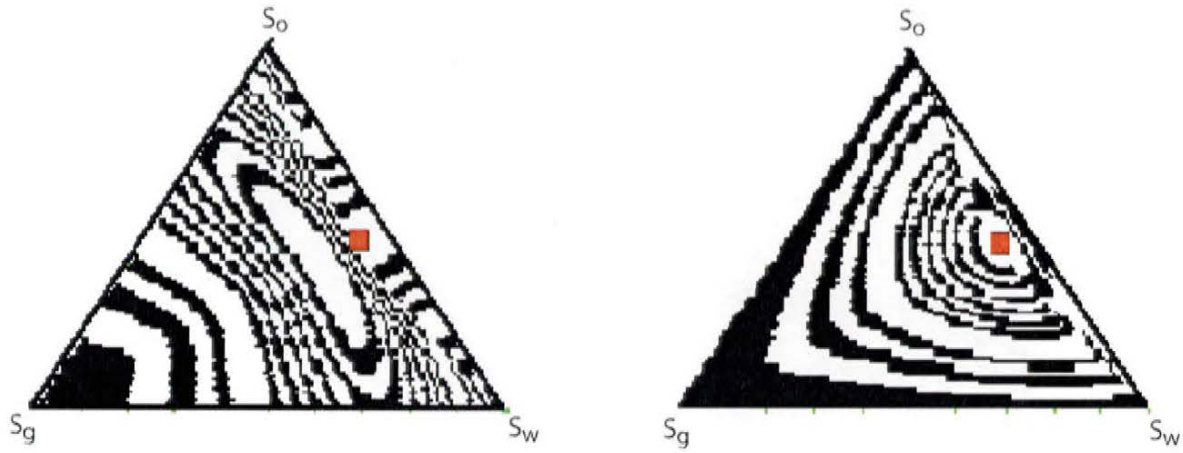

Figure 6.3 Eigenvalues with Corey-type relative permeability functions. The viscosity of oil and water is 1.0 while the viscosity of gas is 0.1. The umbilic point (red point) is 'pushed away' from the vertex of the saturation triangle representing the phase which viscosity is lowered as compared to the other two phases.

6.3.4. Numerical Solutions to Riemann Problem

The solutions of the Riemann problem may be found by use of a numerical simulator such as the ECLIPSE 100, which is a commercial reservoir simulator. Despite the possibility of encountering elliptic regions it should be noted that the presence of elliptic regions does not necessarily leads numerical problems. If the left and the right states of the solution to the Riemann problem are located away from the elliptic region (Figure 6.4), the system behaves as if it were strictly hyperbolic (cf. Bell et al., 1986). Numerical solutions indicate that in the case where the left or the right state are located on either side of the elliptic region, stable meaningful solutions may be obtained (cf. Bell et al., 1986 and Jackson and Blunt, 2000). This is also the case when either the left or the right state is located within the elliptic region.

However, even though capillary forces have been ignored in the formulation of the problem, the numerical discretization of the problem stabilizes the system because numerical diffusion has a similar effect on the governing equations as inclusion of capillary terms in the governing equation. In fact, introduction of capillary terms into problems where both the left and the right state of the Riemann problem are located inside the elliptic region can have such a stabilizing effect ensuring that smooth meaningful solutions can be obtained (cf. Jackson and Blunt, 2000).

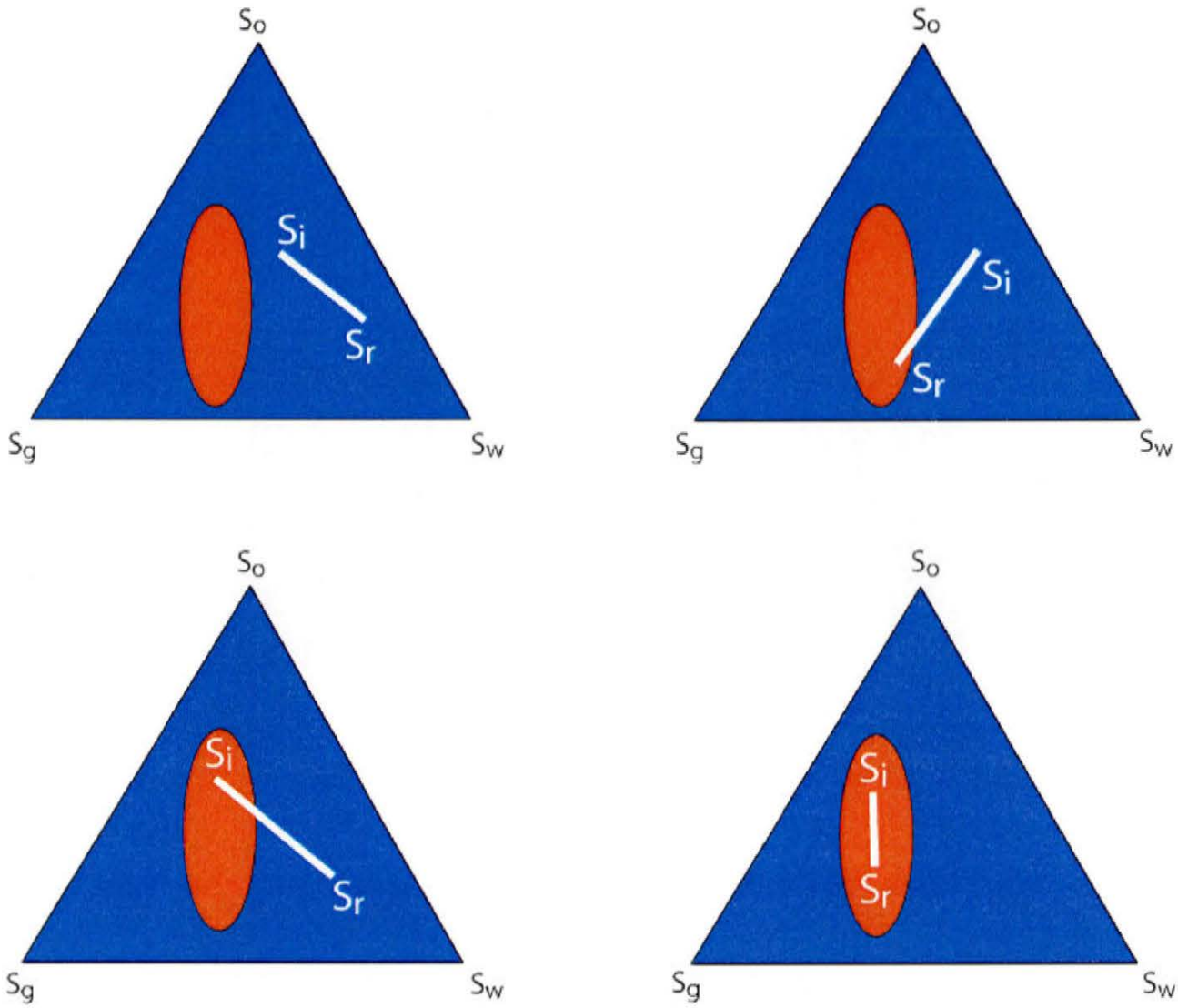

Figure 6.4 Sketch of elliptic regions (red) in the saturation triangle with different left and right states. Top left: Both left and right state are far away from the elliptic region. Top right: Right state is located inside the elliptic region while the left state is located outside. Bottom left: Left state is inside the elliptic region while the right state is located outside the elliptic region. Bottom right: Both the left and the right states are located inside the elliptic region.

6.3.5 WAG-injection and Transitional Waves

Water Alternating-Gas (WAG) injection is a secondary recovery method. WAG injection usually yields higher recovery efficiency than injection of only water or gas. The wave structure of the WAG recovery is special because of the presence of a so-called transitional wave which is a third wave group in addition to the rarefaction and shock wave (Marchesin and Plohr, 1999). The transitional wave can contribute significantly to the overall oil recovery. Consequently, understanding the role of the transitional wave is important for the efficient design of WAG processes. The transitional waves are sensitive to the form of the capillary pressure. Unfortunately, it is sometimes difficult to separate the effects of numerical dispersion and the capillary term.

Marchesin and Plohr (1999) have shown that a solution to the WAG injection problem is practically indistinguishable from its counterpart pertaining to the Riemann problem. The reason is that fast moving oscillating waves originating from the alternating injection sequence either decay with time and turn into a rarefaction wave, or sharpen into a shock wave.

6.4 Selfconsistent Relative Permeability Functions for Gas Injection

The iterative procedure was initially applied to a gas injection process. A saturation trajectory was generated by the macroscopic flow model by using Corey-type relative permeability functions, $k_{rw} = S_w^2$, $k_{ro} = S_o^2$ and $k_{rg} = S_g^2$, and viscosities $\mu_w = 1.0$, $\mu_o = 0.3$ and $\mu_g = 0.2$. Initial conditions were $S_w = 0.4$ and $S_o = 0.6$. The injection of gas corresponded to the left state given by $S_l = (1.0, 0)$. The network simulator was tested both on a 50×50 network with coordination number 4 and a 30 × 15 × 15 three-dimensional network. The key parameters of the iterative procedure are shown in Table 6.1. Contents of the pores are only shown for the 50 × 50 network while the relative permeability functions of the three coexisting phases are shown for the three-dimensional case. The initial guess of relative permeability functions resulted in a saturation trajectory shown in Figure 6.5.

6.4.1 Network- and Fluid- Parameters and Initial Conditions

The initial condition of the network prior to the start of the iteration procedure was obtained by an invasion percolation process filling of the reservoir with oil. The injection pressure was set to a fraction of the entry pressure of the smallest throat. The saturation of the water phase was $S_w = 0.3$ after injection of oil. The network was then allowed to imbibe water to reach the initial saturation point at $S_w = 0.4$. It should be noted that the first part of the saturation trajectory is a two-phase displacement process where no gas was present. Thus, the gas saturation did not increase until $S_w = 0.34$. The tracking algorithm successfully followed the saturation trajectory of the macroscopic flow model. The distance between the nodes was typically 0.5 saturation units and the network model needed between 20-40 pore-level displacement mechanisms to reach the each desired saturation point on the macroscopic saturation trajectory. It should be noted that some pore-level displacement mechanisms did not lead to a change in saturation because the pore was located outside the zone where saturation was calculated. In the case where no critical pressure lines were crossed by a change in capillary pressure, no pore-level displacement mechanisms occurred. However, the saturation still changed because interfaces changed curvature on the pore-level leading to a small change in saturation.

Viscosity water	**1.0**	**cP**
Viscosity oil	**0.3**	**cP**
Viscosity gas	**0.2**	**cP**
Interfacial tension oil-water	**45**	**mN/m**
Interfacial tension oil-gas	**25**	**mN/m**
Interfacial tension water-gas	**70**	**mN/m**
Spreading Coefficient	**0**	**mN/m**
Contact angle oil-water	**0**	**rad**
Contact angle oil-gas	**0**	**rad**
Contact angle gas-water	**0**	**rad**
$r_{t,min}$	**5**	**μm**
$r_{t,max}$	**10**	**μm**
$r_{c,min}$	**15**	**μm**
$r_{c,max}$	**20**	**μm**

Table 6.1 Network and Fluid parameters

6.4.2 First Iteration by Network Simulator

The network simulator successfully followed the macroscopic saturation trajectory during the first iteration within a deviation of the specified 0.5 saturation units (cf. Figure 6.5). The corresponding movement in the capillary pressure space is shown in Figure 6.6. In most cases, the injection of gas resulted in both increased oil-gas and oil-water capillary pressure. It should be noted that the oil layers remained stable along the entire saturation trajectory. Consequently, the oil phase remained well connected. The stable oil layers were a consequence of the direction of the saturation trajectory which generally 'demanded' less water causing increased oil-water capillary pressure and more gas causing increased oil-gas capillary pressure.

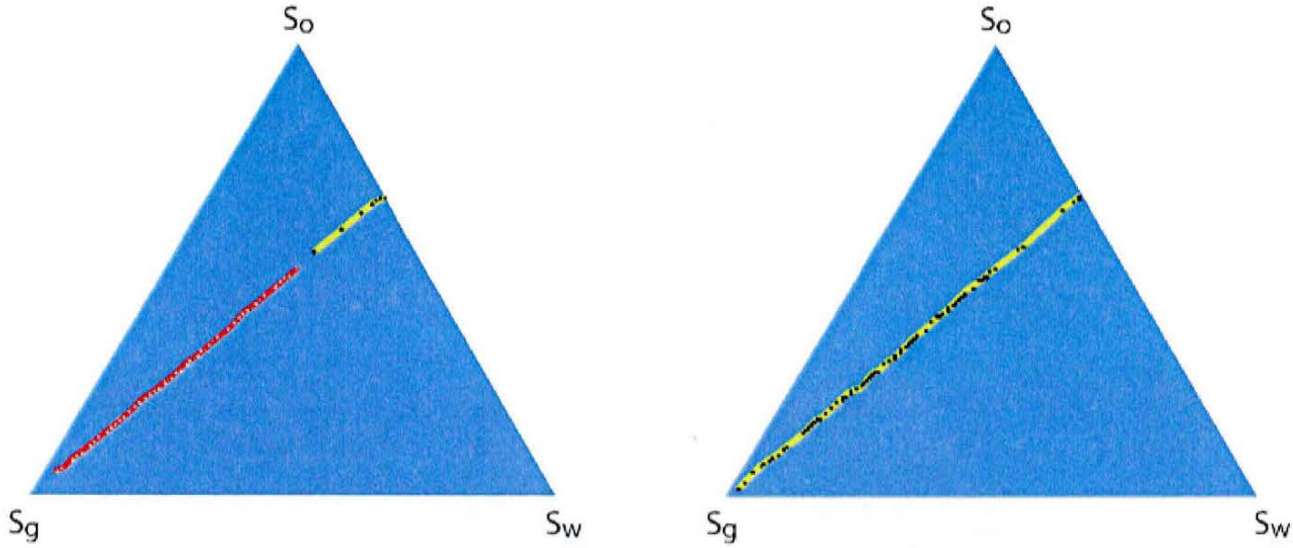

Figure 6.5 Tracking of the saturation trajectory by the network simulator. The saturation triangle to the left shows the saturation trajectory to be followed in red and the actual saturation trajectory followed by the network simulator in green. To the right the actual followed saturation trajectory at the final state of the simulation. An accuracy of 0.5 saturation units was used.

Thus, the displacement mechanisms were dominated by single oil-water Haines' jumps followed by Haines' jumps of gas into the continuous oil phase. The oil-gas Haines' jumps have significantly lower critical pressure than double drainage mechanisms because secondary events are absent when gas invades the continuous oil phase. Consequently, no double drainage mechanisms were activated during tracking of the macroscopic saturation trajectory.

Figure 6.6 also shows the calculated relative permeability functions of the three phases and the initial Corey type relative permeability functions on a logarithmic scale. The relative permeability functions span 4 orders of magnitude. The relative permeability function of the gas phase was zero for saturations below $S_g = 0.32$. At $S_g = 0.32$ the gas cluster first spanned the network and connected the inlet to the outlet. The relative permeability at this point was 10^{-2}. For gas saturations in the interval $0.32 < S_g < 0.43$ the relative permeability of the gas slightly increased because the conductance of the gas phase was controlled by the 'red' bonds in the backbone of the gas cluster. Consequently, the increased relative permeability was solely due to larger effective flow area of the gas phase inside the pores making up the backbone of the gas cluster. At a gas saturations above $S_g = 0.43$ the gas phase began to form a well-connected cluster.

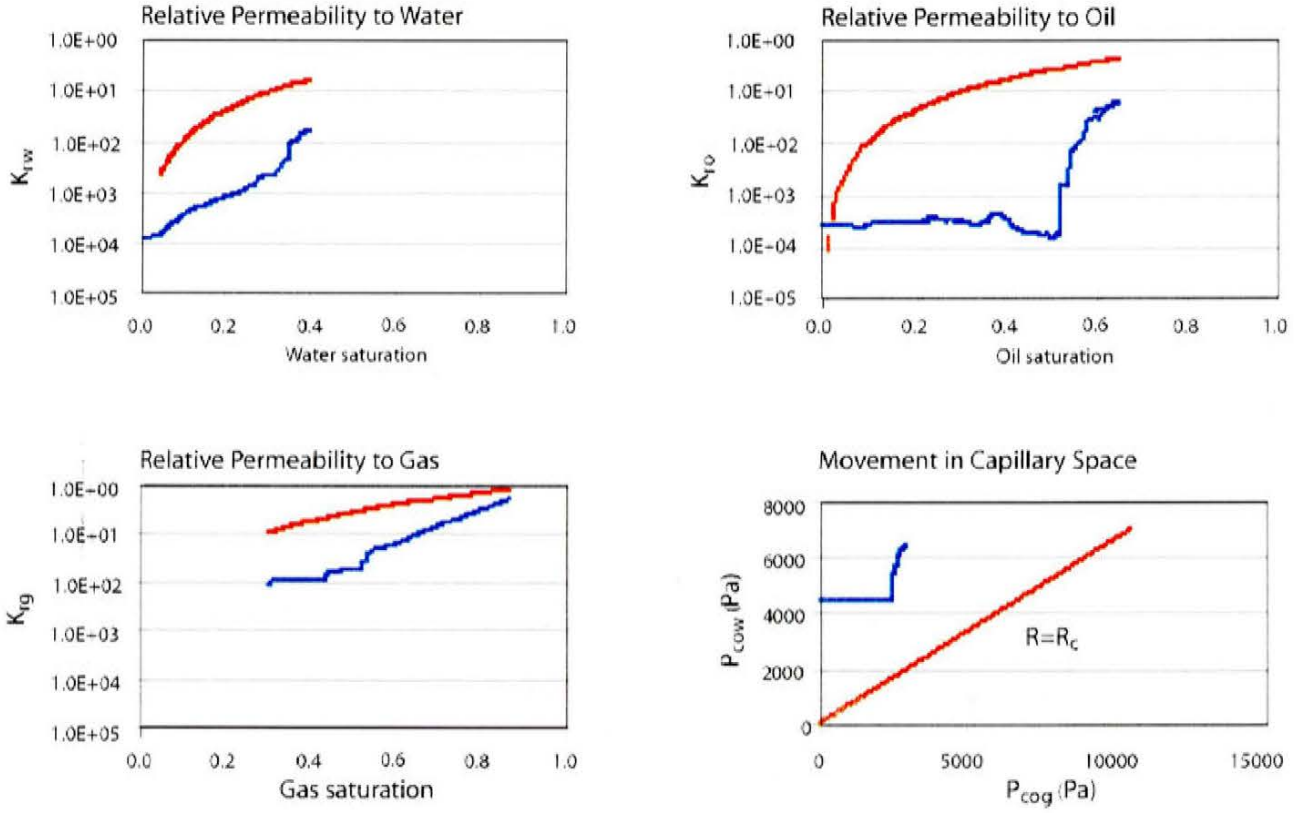

Figure 6.6. Relative permeability functions for oil, water and gas calculated by the network simulator are shown in blue. The initial Corey-type relative permeability functions are shown in red. The movement in capillary space is shown in the lower right hand corner where the red line indicates the line of stability.

The water phase was continuous through the entire saturation trajectory. At the initial two-phase conditions $S_w = 0.4$ the relative permeability was approximately10^{-2}. The relative permeability function decreased gradually to a value as low as 10^{-4}. A crossover in relative permeability behavior was observed around $S_w = 0.35$. This cross-over heralds a transition from the relative permeability of the water phase controlled by the configuration 1 pores entirely filled with water to the configuration 2, configuration 3 and configuration 4 pores with the conductance of the water phase controlled by the corner flow. The relative permeability of water below the crossover point approximately scaled with saturation to the second power in agreement with the observations of Fenwick and Blunt (1998).

The relative permeability of the oil phase was initially controlled by the the configuration 2 pores where oil flowed through the pore centers. It quickly decreased as gas displaced oil. In particular, the conductivity of the oil phase was reduced nearly two orders of magnitude with a corresponding change of the oil saturation from $S_o = 0.6$ to $S_o = 0.5$. Further reduction of the oil saturation led to an interesting phenomenon. The increased oil-water capillary pressure forced the oil to invade new pores and the oil phase therefore formed a better-connected cluster on the network level. Although the effective flow area of the oil phase within the individual pores was reduced, the overall conductance of the oil phase on the network level increased. Thus, below the oil saturation $S_o = 0.5$, the relative permeability to oil fluctuated between 10^{-4} and 10^{-3}. Consequently, the relative permeability of the oil phase below $S_o = 0.5$ was primarily controlled by how well that phase was connected in the porous network.

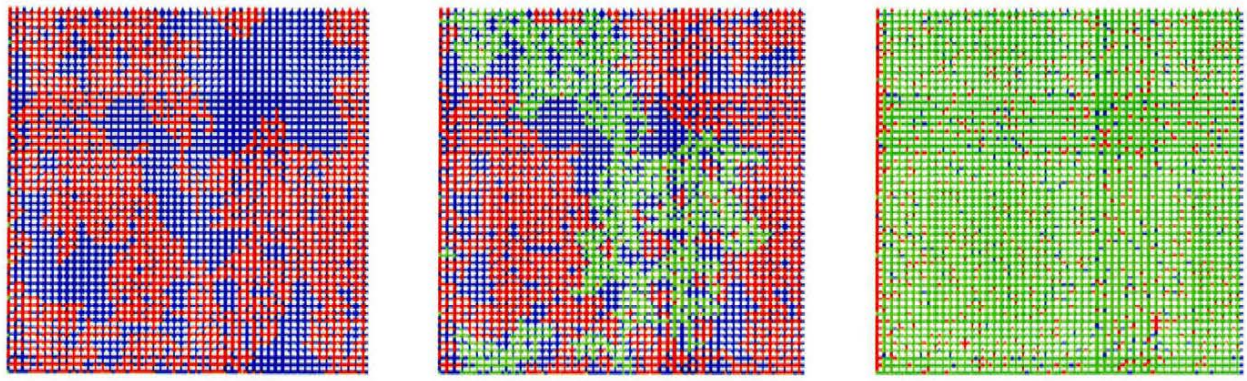

Figure 6.7. Initial, intermediate, and final stages of phase distributions in a 50 × 50 network during gas injection. Blue color indicates water-filled pores; red color represents oil-filled pores and water filled pores. The pores with three coexisting phases are represented by green color.

The initial, intermediate, and final phase distributions in the 50 × 50 network are shown in Figure 6.7. The three stages of the phase distributions in the network show how gas displaced oil that was forced to displace water. The initial distribution corresponds to the condition $S_w = 0.4$ and $S_o = 0.6$ with the oil phase spanning the pore space. Continuity of the oil phase is controlled by the configuration 2 with the oil phase flowing through pore centers (see Figure A2, Appendix A). At the intermediate stage, the gas phase has displaced the oil phase from some of the pore centers causing a significant reduction of the oil phase relative permeability. At the final stage, gas has effectively displaced the oil phase to the corners of the pores where it forms stable layers. Thus, at the final stage the gas phase occupies the pore centers creating a well connected cluster with a high relative permeability. Similarly, the effect of higher oil connectedness appearing at the final stage leading to higher oil relative permeabilities at lower oil saturations can be attributed to spreading of the oil phase on the water-gas interface at high gas saturations.

6.4.3 Selfconsistent Relative Permeability Functions for Gas Injection

The search for selfconsistent relative permeability functions was pursued by the iterative procedure. The selfconsistent relative permeability functions of the seventh iteration are shown in Figure 6.8 along with the relative permeability functions of iteration 6 and the various movements in capillary pressure space performed by the network simulator in the previous iterations. The complete iteration series is shown in Appendix D. The selfconsistent relative permeability functions of water and gas were found in the second iteration. The relative permeability functions of gas and water did not change much during the remaining iterations. Consequently, the water and gas relative permeability functions appeared to be functions of their own saturation only during the search for selfconsistent relative permeability functions although the movement in capillary pressure space was very different during the seven iterations.

The relative permeability function of oil posed some difficulties because the ECLIPSE 100 simulator requires that relative permeability functions for the oil phase are monotonically increasing as the oil saturation increases. This requirement was not always fulfilled by the relative permeability functions delivered by the network simulator. In particular for the higher oil saturations the network model yielded increasing relative permeability for decreasing oil saturation. The higher conductivity

was caused by the fact that oil displaced water which caused formation of highly conductive configuration 2 pores while the gas displaced the oil from pores which did not belong to the backbone of the oil cluster. Consequently, smaller oil saturation could cause an increase in oil conductance and thus non-increasing relative permeability functions of the oil phase.

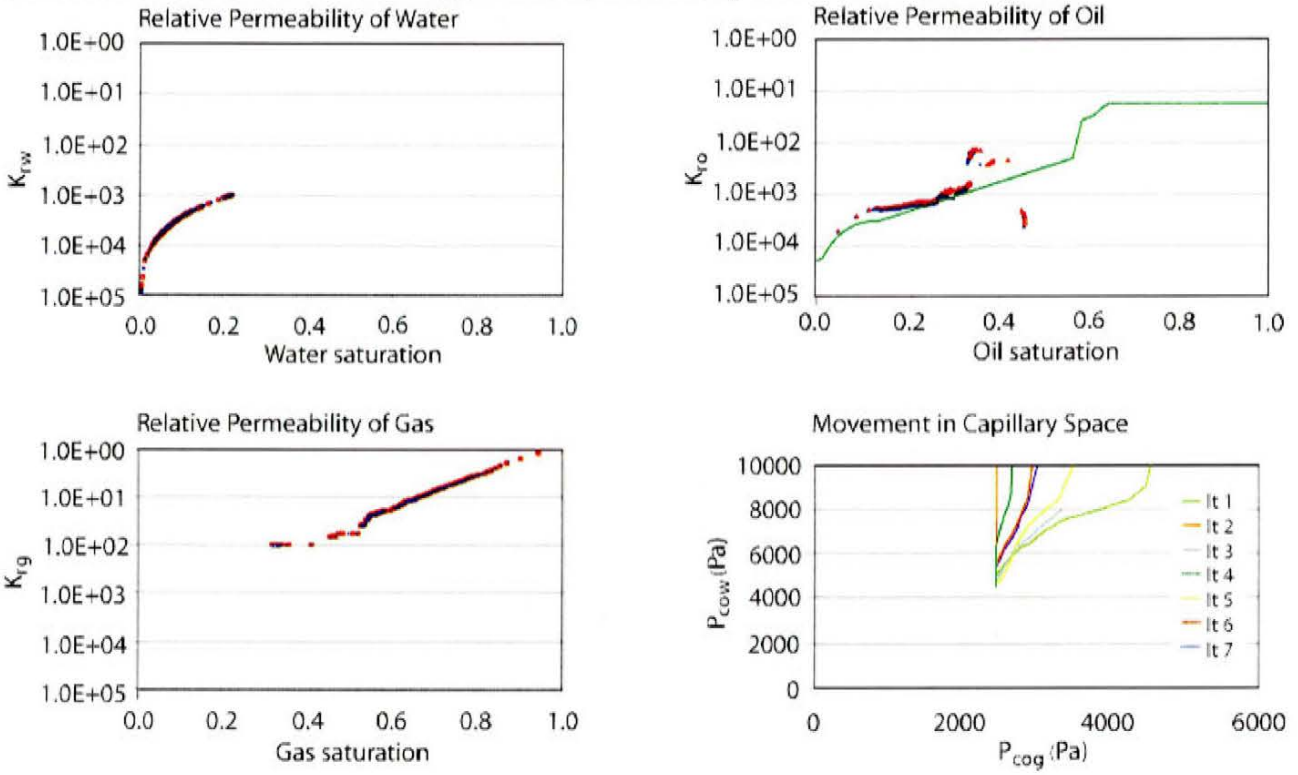

Figure 6.8 Selfconsistent relative permeability functions for gas injection with initial conditions S = (0.0, 0.4) using Corey-type relative permeability functions as initial guess for the saturation trajectory. The movement in the capillary pressure space is shown for all seven iterations.

Consequently, it was necessary to approximate the relative permeability function of the oil phase in the range $0.176 < S_o < 0.57$ by a straight line and search for the selfconsistent relative permeability function by changing the slope of the line. Thus, tracking of the relative permeability functions originating from the network model by the macroscopic model was associated with non-physical adjustments of the relative permeability function. Nevertheless, the iterative procedure converged in spite of the fact that as much as seven iterations were needed. The slow convergence was caused by oscillations of the relative permeability function of the oil phase around the selfconsistent relative permeability function. More precisely, every second relative permeability function had a significant part of its saturation trajectory located on the oil-gas base line in the region of very low water saturations (cf. Figure 6.9).

The movement in the capillary space can be interpreted by considering the saturation trajectories associated with the movements in capillary pressure space. The saturation trajectories oscillated around the selfconsistent saturation trajectory. This oscillation reflects the movements in the capillary pressure space either above or below the selfconsistent trajectory. More precisely, the saturation trajectories with their significant parts located on the oil-water base line correspond to movements in capillary space with the oil-water capillary pressure being too large as compared to that associated with the final selfconsistent trajectory.

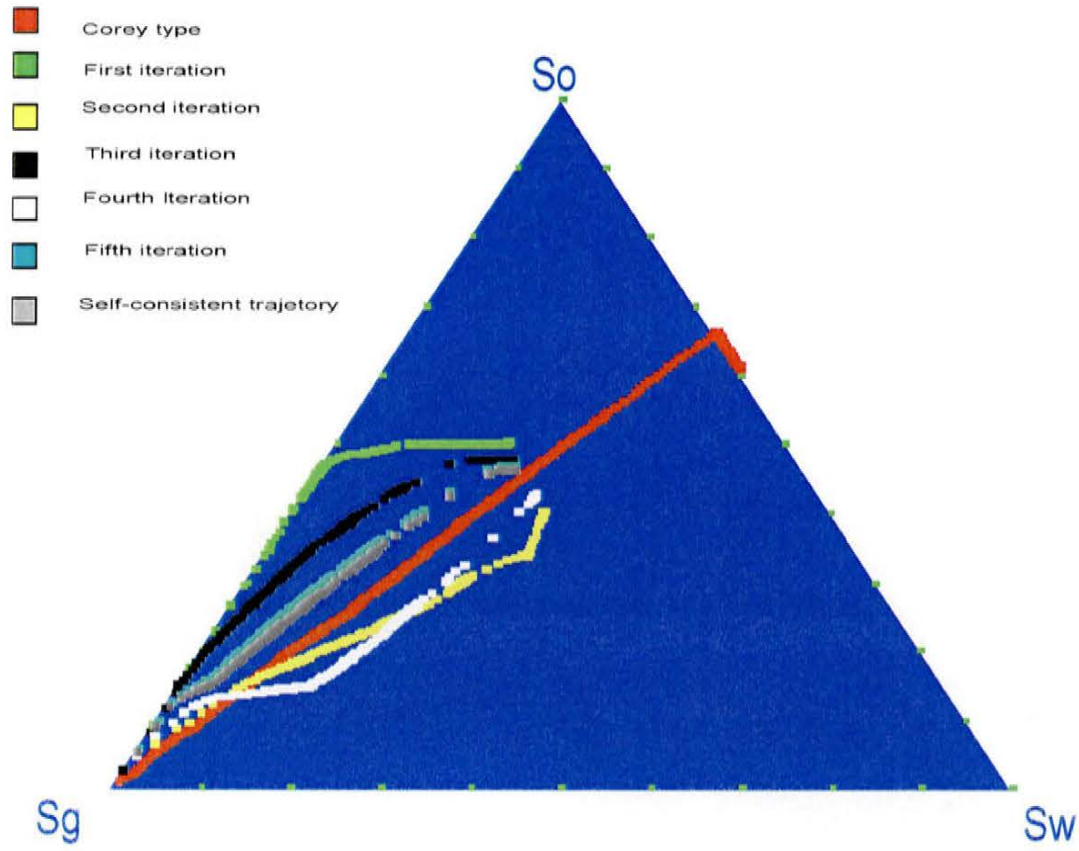

Figure 6.9 Saturation trajectories of the seven iterations followed by the network simulator. The initial saturation of all the trajectories is S_r = (0.0, 0.4), but is only shown for the saturation trajectory of the initial Corey-type relative permeability functions. The convergence of the iterative procedure is slow because the iterations oscillate around the selfconsistent saturation trajectory. It should be noted that some of the trajectories are located on the gas-oil base line corresponding to no water. Low water content corresponds to a high oil-water capillary pressure.

Comparisons of the different movements in capillary pressure space and the corresponding movements in the saturation triangle have shown that the capillary pressure response is structurally stable: it appears to be moderate for moderate changes in saturation trajectory. In other words, two saturation trajectories close to each other are followed by movements in capillary pressure space, which are also close to each other. However, that is not to say that the relative permeability functions do not change drastically. Moreover, the macroscopic simulator does not exhibit the property of structural stability in the case where a small change in relative permeability functions results in a drastic change of a saturation trajectory.

6.5 Selfconsistency of WAG Injection Sequences

The iterative procedure was applied to a WAG injection sequence. Three cases were tested corresponding to different injection ratios between water and gas. The initial state was chosen as $S_r = (S_g, S_w) = (0.08, 0.16)$. Injection ratios corresponding to the left state $S_l = (S_g, S_w) = (0.35, 0.65)$, $S_l = (S_g, S_w) = (0.40,0.60)$ and $S_l = (S_g, S_w) = (0.45, 0.55)$ were investigated using the Corey-type relative permeability functions. More specifically, $k_{rw} = S_w^2$, $k_{ro} = S_o^2$ and $k_{rg} = S_g^2$ were used as initial relative permeability functions. The applied viscosities were as follows: $\mu_w = 0.5$ $\mu_o = 1.0$ and $\mu_g = 0.3$. The initial saturation trajectories of the macroscopic model are shown in Figure 6.10. Interfacial tensions and contact angles were identical to those given in Table 6.1.

6.5.1 Movement in Capillary Pressure Space

The movement in the capillary pressure space for the WAG injection sequence with $S_I = (S_g, S_w) = (0.45, 0.55)$ is shown in Figure 6.10. The combination of increased water and gas saturations of the trajectories led to the use of the snap-off, I_1- ,and I_2- imbibition displacement mechanisms implementing the mechanism responsible for water displacing oil. The decreasing oil-water capillary pressure caused the imbibition displacement mechanisms. In addition, the increasing gas saturation resulted in increasing oil-gas capillary pressure. Consequently, the movement in the capillary space occurred in the region of the capillary pressure space where oil layers were unstable.

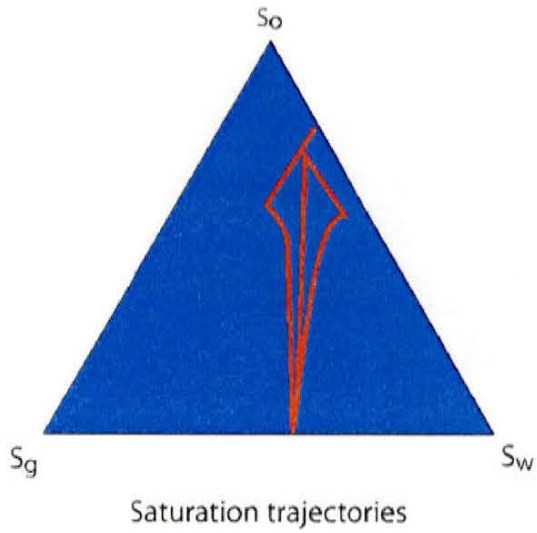

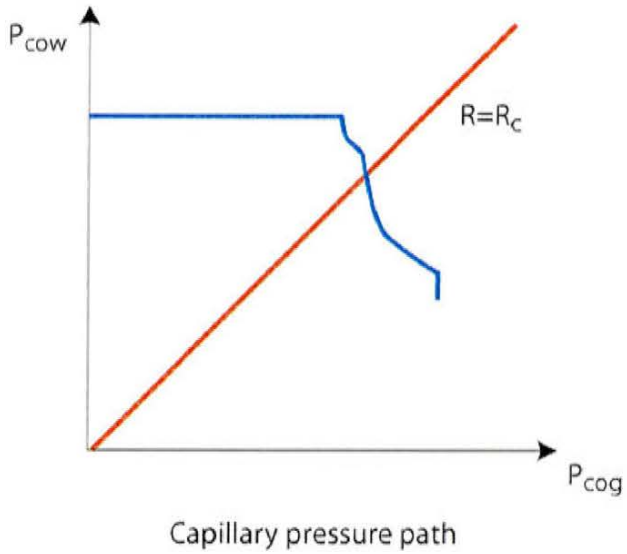

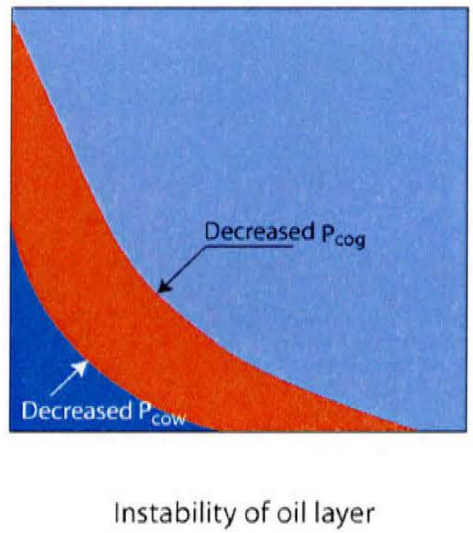

Figure 6.10. Trajectories in the saturation and capillary pressure spaces during WAG injection. The movement is generally towards the unstable oil layer. The saturation trajectories impose higher water saturation and higher gas saturation causing the oil-water and the oil-gas interfaces to move towards each other causing the collapse of the oil layer.

The movement in the capillary pressure space in the network simulator corresponds to movement of the oil-water interface towards the center of the pore. The oil-gas interfaces are pushed towards the corner of the pores (cf. Figure 6.10) which reduces both the effective flow area available to the oil phase on the pore-level and the connectivity of the oil phase in the pore space.

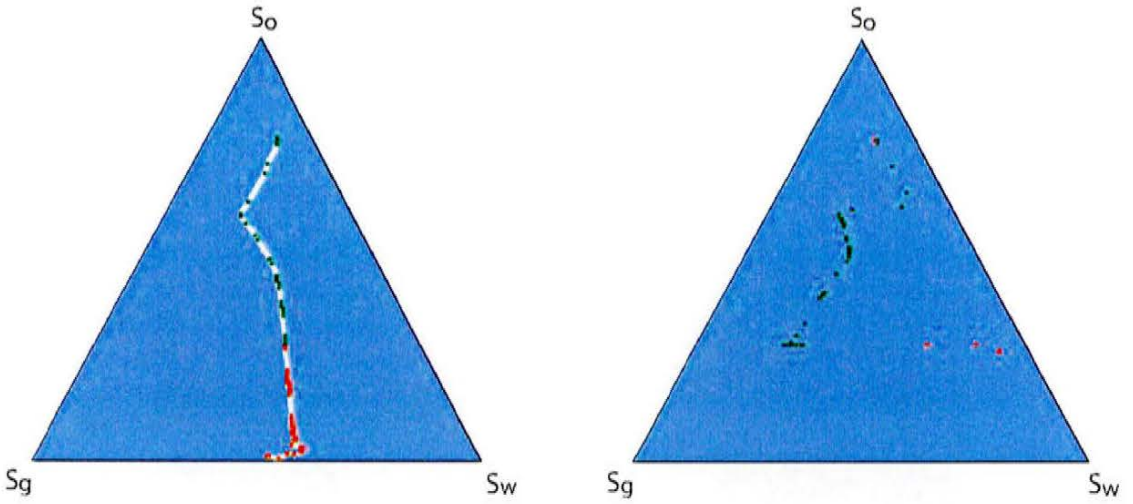

Figure 6.11. Saturation trajectories for the initial two iterations. The initial trajectory of the macroscopic simulator is shown to the left while the second iteration trajectory based on the relative permeability functions of the first trajectory is shown to the right.

6.5.2 Residual and Discontinuous Oil

The movement in capillary pressure space causes the network model to encounter the residual oil saturation much earlier than the saturation corresponding to the injection condition given by the left state S_l. Once the oil layers became unstable, the injection of gas caused break-up of the oil phase into discontinuous oil ganglia, which could be mobilized only by the double drainage mechanisms. This was in particular the case with $S_l = (S_g, S_w) = (0.35, 0.65)$ and $S_l = (S_g, S_w) = (0.4, 0.6)$. The lowest residual oil was encountered for the left state $S_l = (S_g, S_w) = (0.45, 0.55)$. This case was then investigated more thoroughly.

In the first iteration of the network model residual oil was encountered at $S_o = 0.3$. Consequently, the macroscopic saturation model cannot yield a saturation trajectory below the residual oil saturation, because the oil phase becomes immobile at this saturation.

The iterative procedure collapsed after the second iteration when the network model generated relative permeability functions, which caused the macroscopic model to return a saturation trajectory, located in the upper third of the saturation triangle. The oil phase had lost continuity at the oil saturation $S_{oc} = 0.59$ (cf. Figure 6.12). It should be noted that the relative permeability of a discontinuous phase by definition is equal to zero. However, in a network model an isolated oil filament can be connected to the inlet and the outlet face and is thus classified as a displaceable oil phase.

There were two causes of the high S_{oc} saturation. The first cause was that the gas phase invaded the oil phase by Haines' jumps while the oil layers were still stable and good connectivity of the oil phase existed. This invasion of oil by gas took place in the larger pores. Subsequently, when oil layers became unstable, the connectivity of the oil phase was effectively reduced in the most conductive pores. The second cause that leading to high discontinuous oil saturation was that the gas phase invaded the oil phase unable to establish stable oil layers. Consequently, it broke up into ganglia, which could not conduct oil. Nevertheless, the gas phase was capable of pushing the discontinuous oil phase thereby reducing the saturation of that phase.

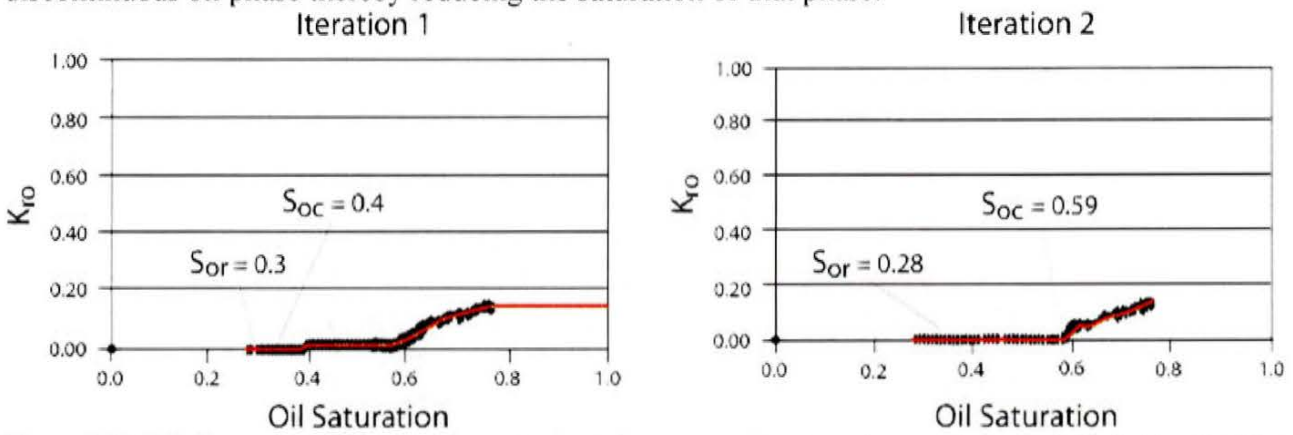

Figure 6.12 Relative permeability functions obtained for the two first iterations of the S_I = (0.55, 0.45). The blue markers indicate the relative permeability functions obtained by the network model while the red lines indicate the relative permeability function forwarded to the macroscopic flow model. S_{or} indicates the residual oil while S_{oc} marks discontinuous oil saturation where the conductance of the oil phase becomes zero.

6.6 Collapse of Iterative Procedure for WAG Injection Process

The collapse of the iterative procedure during WAG injection process raises two questions concerning the iterative procedure aimed at determination of selfconsistent relative permeability functions. The first question concerns calculations of conductance of the oil phase for saturations below the discontinuous oil saturation. The second question deals with the high residual oil saturations, which appears to be in disagreement with the field observations according to which WAG recovery yields increased recovery efficiency.

Mani and Mohanty (1998) have studied problems concerning the definition of relative permeabilities in the network model. In their work the saturation of a phase in the pore space can change inside the network even in the case where the relative permeability to a phase is zero. However, the macroscopic flow model can describe changes in phase saturation only in the case of a nonzero mobility of that phase. Consequently, the area in the saturation triangle where the phase is mobile is different for the two models. This creates an obstacle for the convergence process, because by changing saturation of the oil phase in the network model one cannot follow the saturation trajectory produced by the macroscopic model into the region of residual oil saturation.

Mani and Mohanty (1998) have developed a network model where the conductance of a phase consists of two contributions: steady-state conductance and unsteady-state conductance. They proposed the following formulation of Darcy's law extended to the multiphase flow

$$v_i = -\frac{k \cdot k_{ri}}{\mu_i} \nabla P_i + v_{unsteady-state} \tag{6.15}$$

The mechanisms governing steady-state transport are similar to that underlying determination of relative permeabilities in the quasi-static network model. Given the total flow into or out of the section of the network, the phase viscosity, the imposed pressure drop, and the absolute permeability, transport coefficients are calculated from the multiphase Darcy's law. The flow can take place through films, layers or in pores where the conductance of the phase can be described by the laminar flow. The key assumption in the definition of the steady-state conductance is that the flowing phase is continuous and the pressure drop can be determined from the generalized Darcy's law.

The unsteady-state conductance is represented by the response of the system to a change in capillary pressure. The response leads to a time dependency of the saturation change and the time for an event to happen must be introduced in the network model as a dynamic element. More precisely, a dynamic network simulator must replace the quasistatic network simulator in order to capture the relative permeability concept of the network model.

The change in capillary pressure due to change in one phase pressure therefore can cause changes in the saturation of another phase. Consequently, the inclusion of the unsteady-state conductance can be regarded as a coupling between the conductance of one phase and the pressure gradient within a different phase.

In conclusion, the use of the iterative procedure in the search for selfconsistent relative permeability functions can be affected by improper formulation of the mathematical models.

6.7 Recovery Efficiency of WAG Injection Processes

The high residual oil saturation of the WAG injection processes predicted by the network simulator is in disagreement with high recovery efficiencies reported in field studies (cf. Christensen, Stenby, and Skauge, 1998). The recovery factor is usually controlled by three basic recovery mechanisms: the vertical sweep, horizontal sweep and microscopic displacement efficiency. The negligence of these effects by the network- and macroscopic models may significantly influence efficiency of oil recovery.

In general, increased oil-water capillary pressure in the network model leads to thicker oil layers. Compared to gas injection, the WAG injection is characterized by a movement in the capillary pressure space towards the region where oil layers are unstable. Thus, it appears that the increased oil recovery efficiency may not be explained by the presence of oil layers on the pore-level. In addition, the network simulations have shown that computational results were sensitive to the initial placement of the gas phase in the network. More precisely, oil conductivity was lost faster when gas was assigned to the entire end-face of the network as compared to the assignment to a single pore or to a limited number of pores.

Gravitational segregation and compressibility of the gas phase were ignored in the macroscopic model in spite of their significance for the vertical sweep efficiency. Another property of the

iterative procedure is that the solutions to macroscopic model equations appear initially as the travelling waves. However, they are subsequently transformed into shock fronts or, alternatively, decay into rarefaction waves. Unfortunately, in many cases the well spacing is rather dense and, consequently, the travelling waves might not have sufficient space to develop. Consequently, the two mathematical models applied in the iterative procedure do not necessarily adequately represent the essential mechanisms responsible for increased oil recovery efficiency of the WAG injection.

7. Elliptic regions and three-phase Buckley-Leverett problem

In the idealized case with zero gravity and relative permeabilities of Corey type, the eigenvalues are always real (Trangenstein (1988)). With gravity included and with different relative permeability relationships this is not necessarily the case. Several authors have studied the problem of imaginary eigenvalues (Jackson and Blunt (2000), Fayers (1989), Trangenstein (1988)). Jackson and Blunt (2000) show that elliptic regions (i.e. regions in the saturation space where the eigenvalues are imaginary) occupying a significant part of the saturation space are present for a physically realizable model of a porous medium (a bundle-of-tubes model). They conclude that elliptic regions appear to be an inevitable consequence of a non-trivial three-phase flow model. But, is it physically possible for a real flow system to attain states located inside an elliptic region? Trangenstein (1988) does not think that this is the case and concludes that the practical meaning of the non-hyperbolic regions is that they represent regions of unattainable saturations. Nature cannot create reservoirs with these unstable mixtures, wells cannot inject them, and the resulting reservoir fluid can never reach them. Nevertheless, in real-life reservoir simulation relative permeability relationships are used that are not necessarily physical. This holds in particular when upscaling and pseudo functions are involved. Therefore we must consider elliptic regions a fact of life.

The system examined by Jackson and Blunt (2000) is physically realizable. Unfortunately, it is not representative for the conditions found in a typical Danish North Sea chalk reservoir. In the rest of this chapter we will try to answer the question whether elliptic regions are something to worry about in conjunction with the simulation of this type of reservoirs.

7.1 The Equation System

The three-phase Buckley-Leverett problem may be specified as follows:

$$\phi \frac{\partial S_w}{\partial t} + \frac{\partial v_w}{\partial x} = 0 \tag{7.1}$$

$$\phi \frac{\partial S_g}{\partial t} + \frac{\partial v_g}{\partial x} = 0 \tag{7.2}$$

$$S_o = 1 - S_w - S_g \tag{7.3}$$

where

$$v_w = f_w\{v_T + [\lambda_o(\rho_w - \rho_o) + \lambda_g(\rho_w - \rho_g)]g_x K\} \tag{7.4}$$

$$v_g = f_g\{v_T + [\lambda_o(\rho_g - \rho_o) + \lambda_w(\rho_g - \rho_w)]g_x K\} \tag{7.5}$$

$$v_o = f_o\{v_T + [\lambda_w(\rho_o - \rho_w) + \lambda_g(\rho_o - \rho_g)]g_x K\} \tag{7.6}$$

$$g_x = g\frac{dD}{dx} \tag{7.7}$$

$$f_w = \frac{\lambda_w}{\lambda_T} \tag{7.8}$$

$$f_g = \frac{\lambda_g}{\lambda_T} \tag{7.9}$$

$$f_o = \frac{\lambda_o}{\lambda_T} \tag{7.10}$$

$$\lambda_T = \lambda_w + \lambda_g + \lambda_o \tag{7.11}$$

$$v_T = \lambda_w + v_g + v_o \tag{7.12}$$

The assumptions are:

1. Constant porosity
2. All phases are incompressible
3. No capillary pressure

The three phase Buckley-Leverett problem exhibits elliptic regions if the eigenvalues of the matrix A are complex, where

$$A = \begin{Bmatrix} \frac{\partial v_w}{\partial S_w} & \frac{\partial v_w}{\partial S_g} \\ \frac{\partial v_g}{\partial S_w} & \frac{\partial v_g}{\partial S_g} \end{Bmatrix} \tag{7.13}$$

7.2 Jackson and Blunt Example Case

Jackson and Blunt (2000) have posed the question whether the elliptic regions are an inevitable consequence of three-phase flow or just a non-physical artifact of extrapolating relative permeability functions beyond regions studied experimentally. They answered the question by demonstrating that elliptic regions may occupy a significant portion of the saturation space for a physically realizable bundle-of-tubes model of a porous medium.

The following parameters and functions were used in their example case:

Viscosities:

$$\mu_w = 1 \text{ cp} \tag{7.14}$$
$$\mu_o = 0.75 \text{ cp} \tag{7.15}$$
$$\mu_g = 0.2 \text{ cp} \tag{7.16}$$

Relative permeabilities:

$$k_w = S_w^{1.41667} \tag{7.17}$$

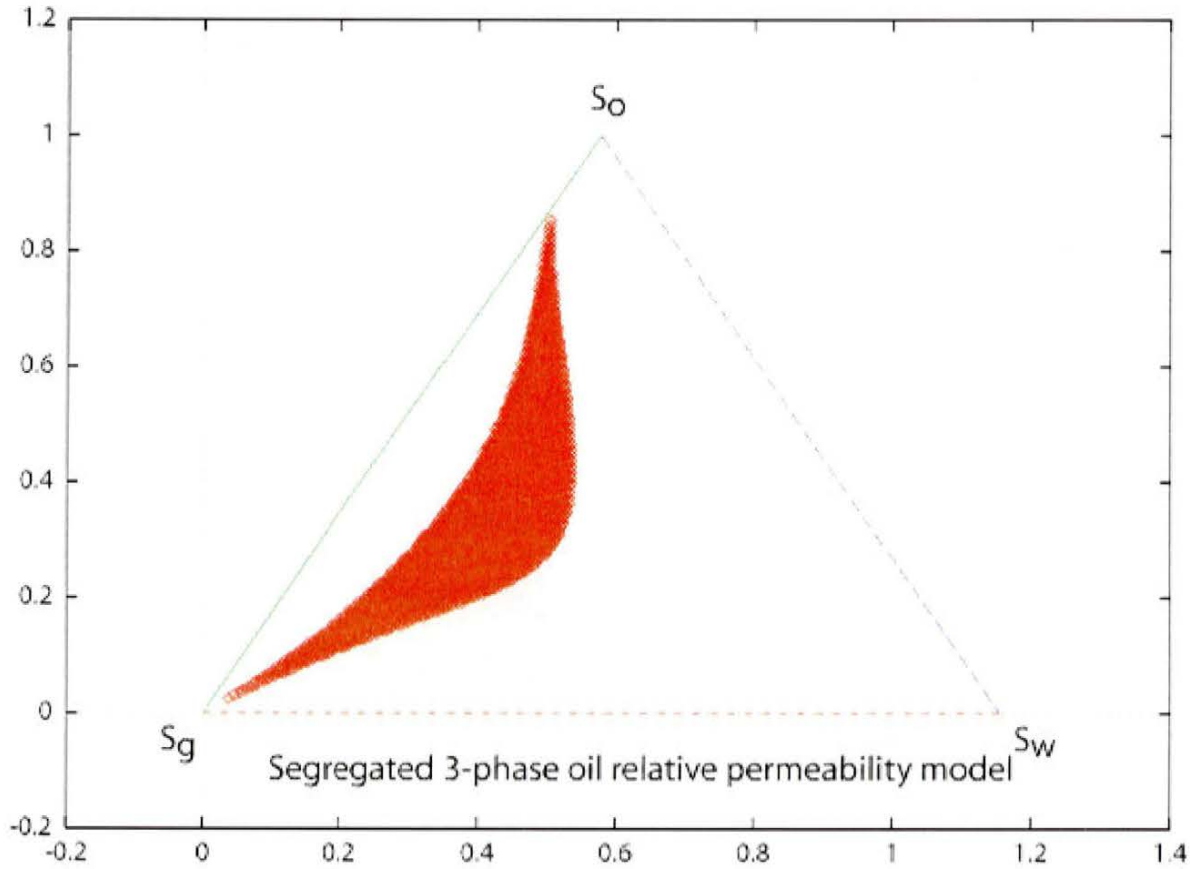

Figure 7.1 Elliptic region for Jackson & Blunt example case

$$k_g = 1. - (1. - S_g)^{1.41667} \tag{7.18}$$

$$k_o = 1. - k_w - k_g \tag{7.19}$$

Gravity to viscous forces:

$$\frac{K(\rho_w - \rho_o)g_x}{v_T \mu_o} = 1.5 \tag{7.20}$$

$$\frac{K(\rho_o - \rho_g)g_x}{v_T \mu_o} = 1.5 \tag{7.21}$$

$$\frac{K(\rho_w - \rho_g)g_x}{v_T \mu_o} = 3. \tag{7.22}$$

All critical and residual saturations are zero.

The elliptic region calculated for this problem is the black region shown in Figure 7.1. The region is different from the one given by Jackson and Blunt (2000). The reason for this is not apparent.

7.3 Viscosity Dependence

Now, while the above problem is physically realizable it is not typical of what you would find in a North Sea chalk reservoirs A more realistic set of viscosities would be:

$$\mu_w = 0.4 \text{ cp} \tag{7.23}$$
$$\mu_o = 0.3 \text{ cp} \tag{7.24}$$
$$\mu_g = 0.04 \text{ cp} \tag{7.25}$$

As seen in Figure 7.2 this change in viscosities has very little influence upon the elliptic region.

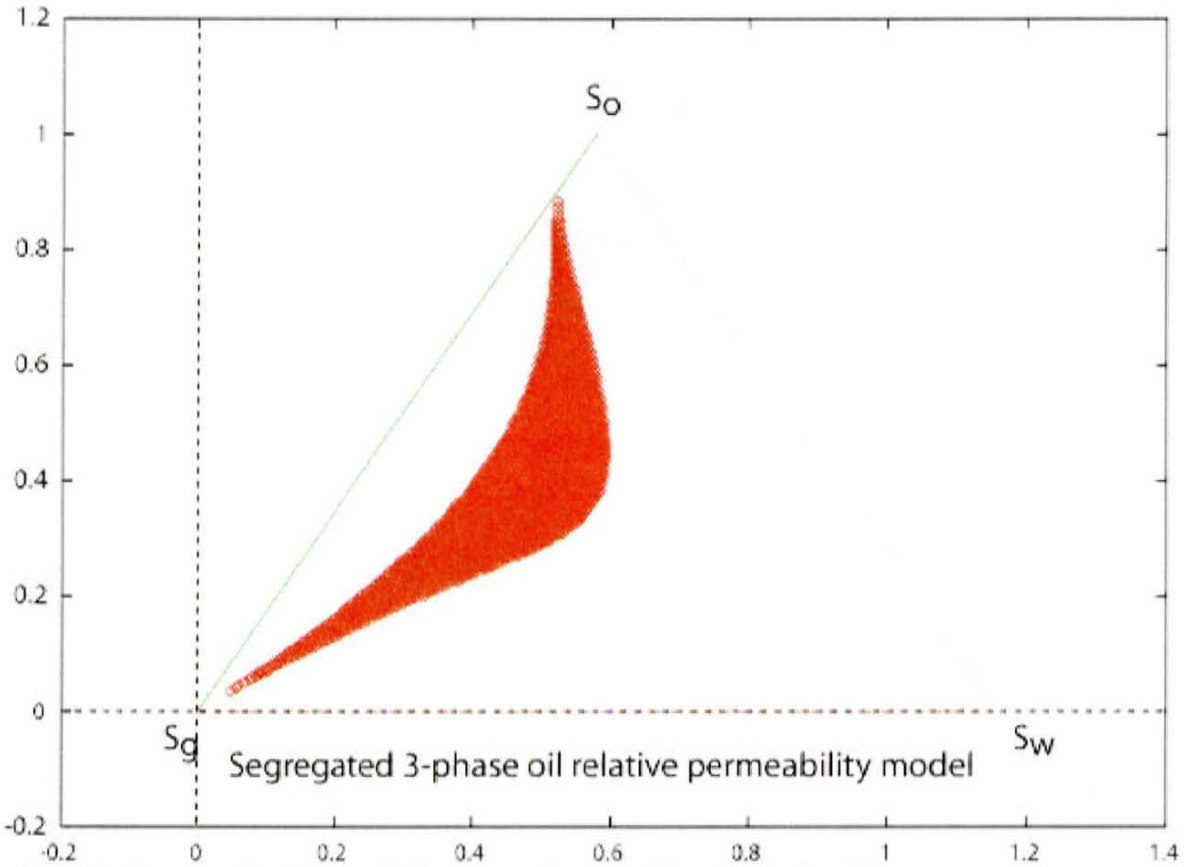

Figure 7.2 Elliptic region for Jackson & Blunt example case with realistic viscosities

7.4 Realistic Gas Relative Permeability Function

Next, we try to introduce a more realistic gas relative permeability functions:

$$k_g = S_g^{1.41667} \tag{7.26}$$

This change in the shape of the gas relative permeability function has a more profound influence of the size and shape of the elliptic region (Figure 7.3)

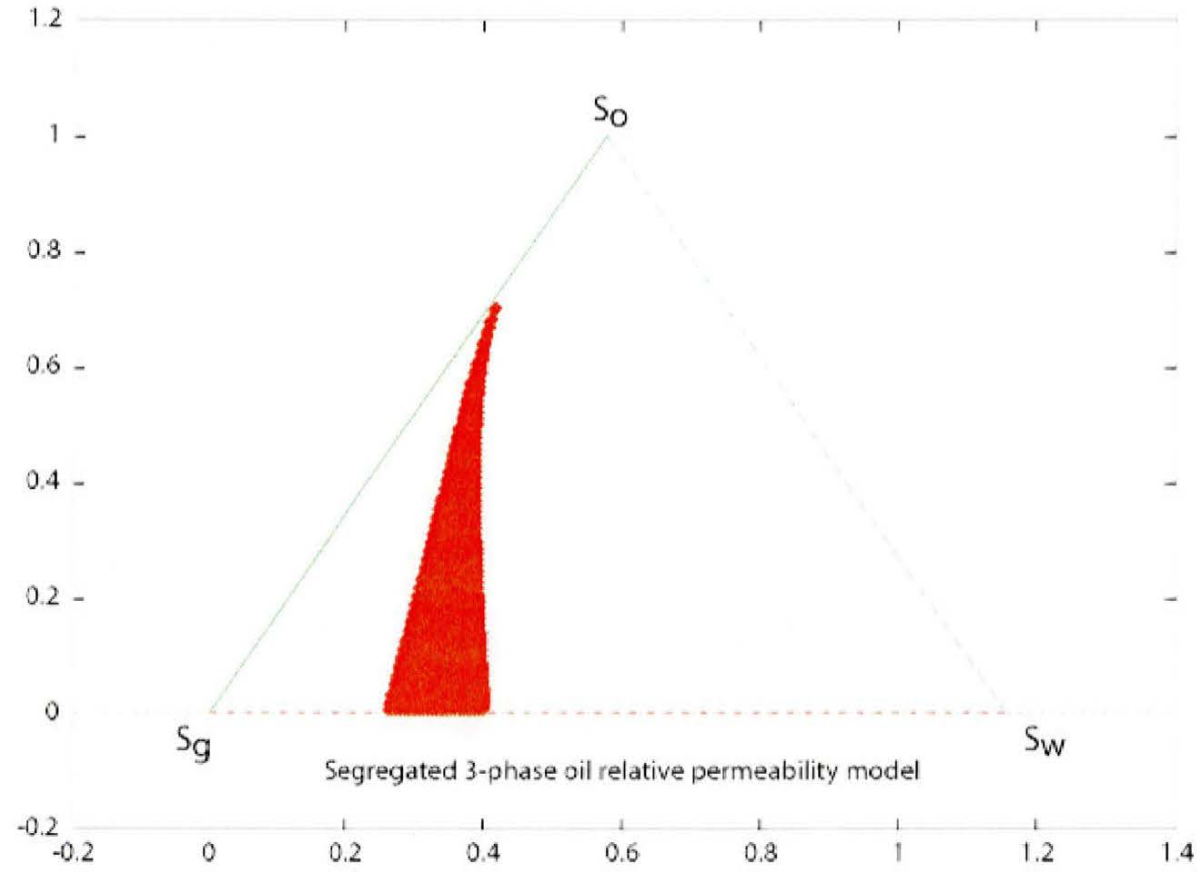

Figure 7.3 Elliptic region for Jackson & Blunt example with realistic viscosities and gas relative permeability

7.5 Realistic Water Relative Permeability Function

Now, for North Sea chalk the power in the expression for the water relative permeability is typically larger than 1.7. To see the effect of this parameter the elliptic region was evaluated for the relative permeability functions

$$k_w = S_w^{4.} \tag{7.27}$$

$$k_g = S_g^{1.4} \tag{7.28}$$

A comparison of the elliptic regions in Figures 7.3 and 7.4 shows that the elliptic region is sensitive to the form of the water relative permeability.

Fig. 7.4. J&B example with realistic viscosities, gas and water relative permeabilities

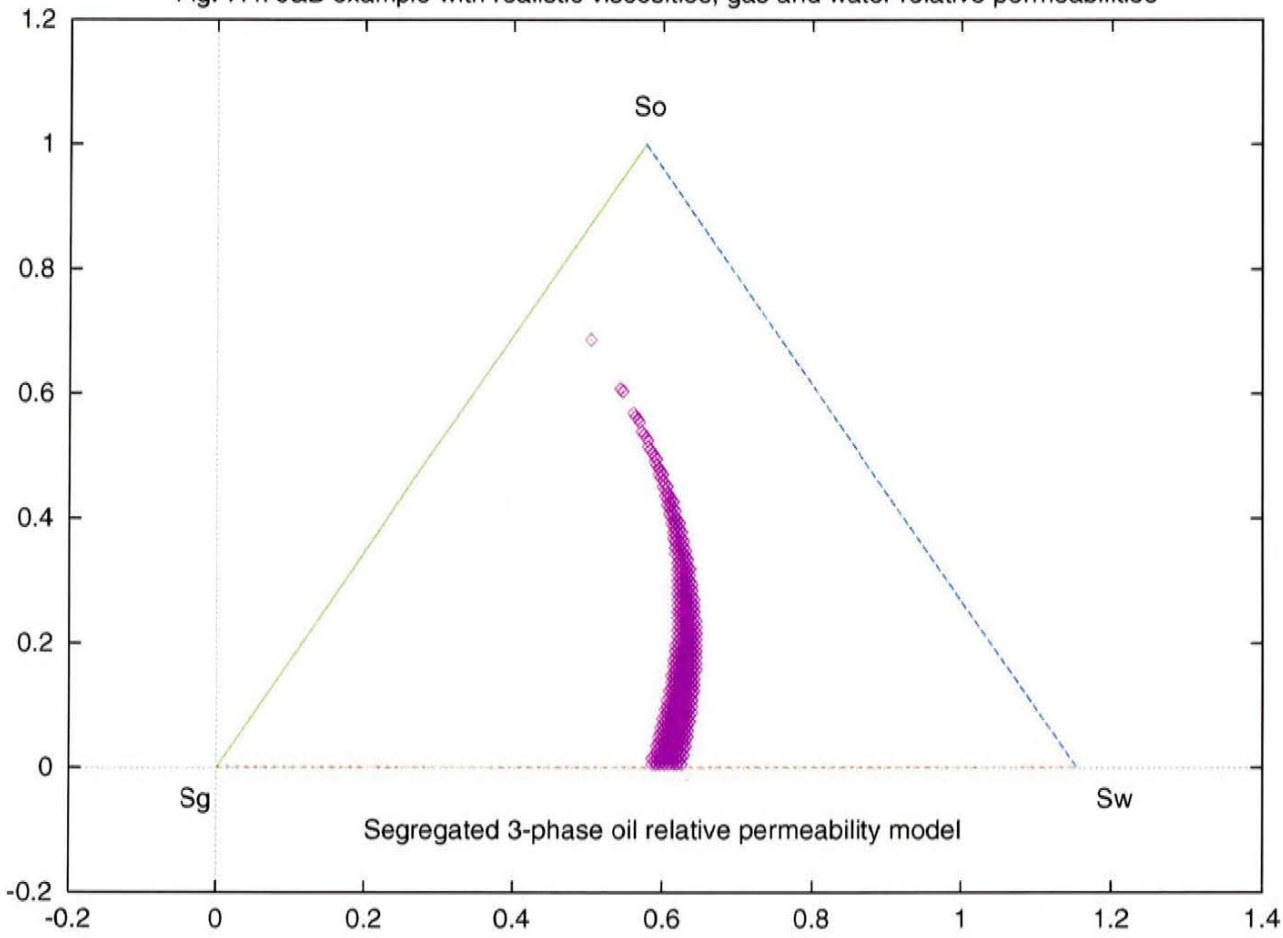

7.6 Introduction of Non-Zero Residual and Critical Saturations

The calculations made so far have been carried out with residual and critical saturations set equal to zero. We will now introduce values that are typical for North Sea chalk reservoirs:

$$S_{wc} = 0.05 \tag{7.29}$$
$$S_{gc} = 0.01 \tag{7.30}$$
$$S_{orw} = 0.25 \tag{7.31}$$
$$S_{org} = 0.20$$

The relative permeabilities are given by

$$k_w = (S_w^*)^{4.} \tag{7.32}$$
$$k_g = (S_g^*)^{1.4} \tag{7.33}$$
$$k_o = 1. - k_w - k_g \tag{7.34}$$

where

$$S_w^* = \frac{(S_w - S_{wc})}{(1. - S_{wc})} \tag{7.35}$$

$$S_g^* = \frac{(S_g - S_{gc})}{(1. - S_{org} - S_{wc} - S_{gc})} \tag{7.36}$$

The introduction of non-zero critical and residual saturations moves the elliptic region a little bit towards smaller gas saturations (Figure 7.5). The shape is not changed very much.

Fig. 7.5. J&B ex. with realistic visc., gas and water rel. perms. and residual/critical saturations

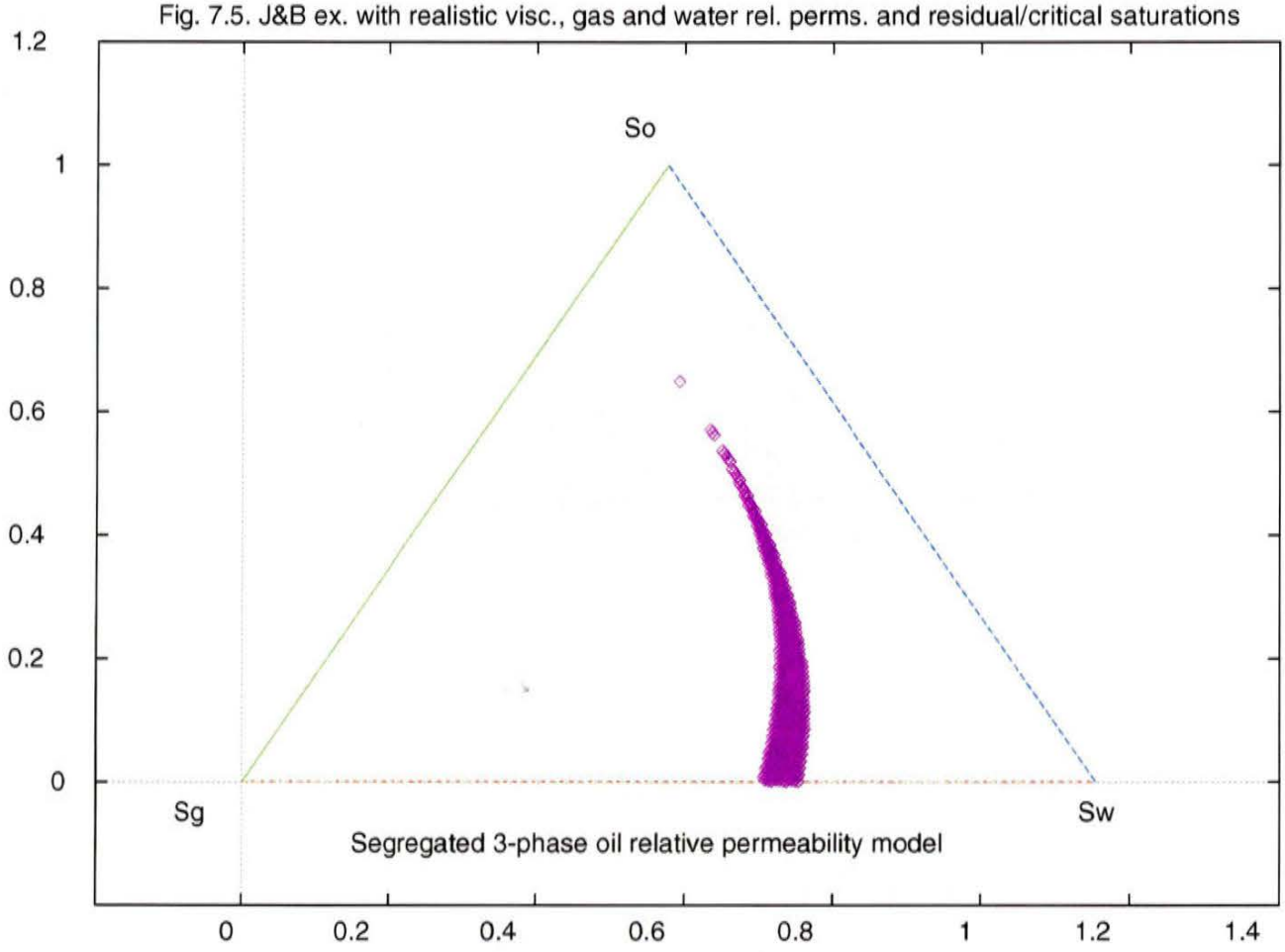

7.7 Realistic Oil Relative Permeability

The oil relative permeability function used so far (eq. (7.34)) is not normally used in reservoir simulations. For example, in the commercial reservoir simulator ECLIPSE the oil relative permeabilities in an oil-water and an oil-gas system are specified separately. The three-phase oil relative permeability is calculated from one of three models. The default model is obtained from the assumptions that in each grid cell 1) the oil is homogeneously distributed and 2) the gas and water phases are completely gravity segregated. This model is referred to as the segregated model. The two other models available are the Stone I and Stone II model, respectively.

The oil relative permeabilities in the oil-water and oil-gas systems are specified as follows:

$$k_{ow} = (S_{ow}^*)^{2.} \tag{7.37}$$

$$k_{og} = (S_{og}^*)^{2.} \tag{7.38}$$

where

$$S_{ow}^{*} = \frac{(S_o - S_{orw})}{(1. - S_{orw} - S_{wc})} \tag{7.39}$$

$$S_{og}^{*} = \frac{(S_o - S_{org})}{(1. - Sg - S_{wc})} \tag{7.40}$$

Next we will examine how the elliptic region depends upon the applied three-phase oil relative permeability model. The relative permeabilities for water and gas are given as above in eqs. (7.32) and (7.33).

Fig. 7.6. J&B ex. with realistic fluid parameters, Segregated 3-phase oil relative permeabiliy

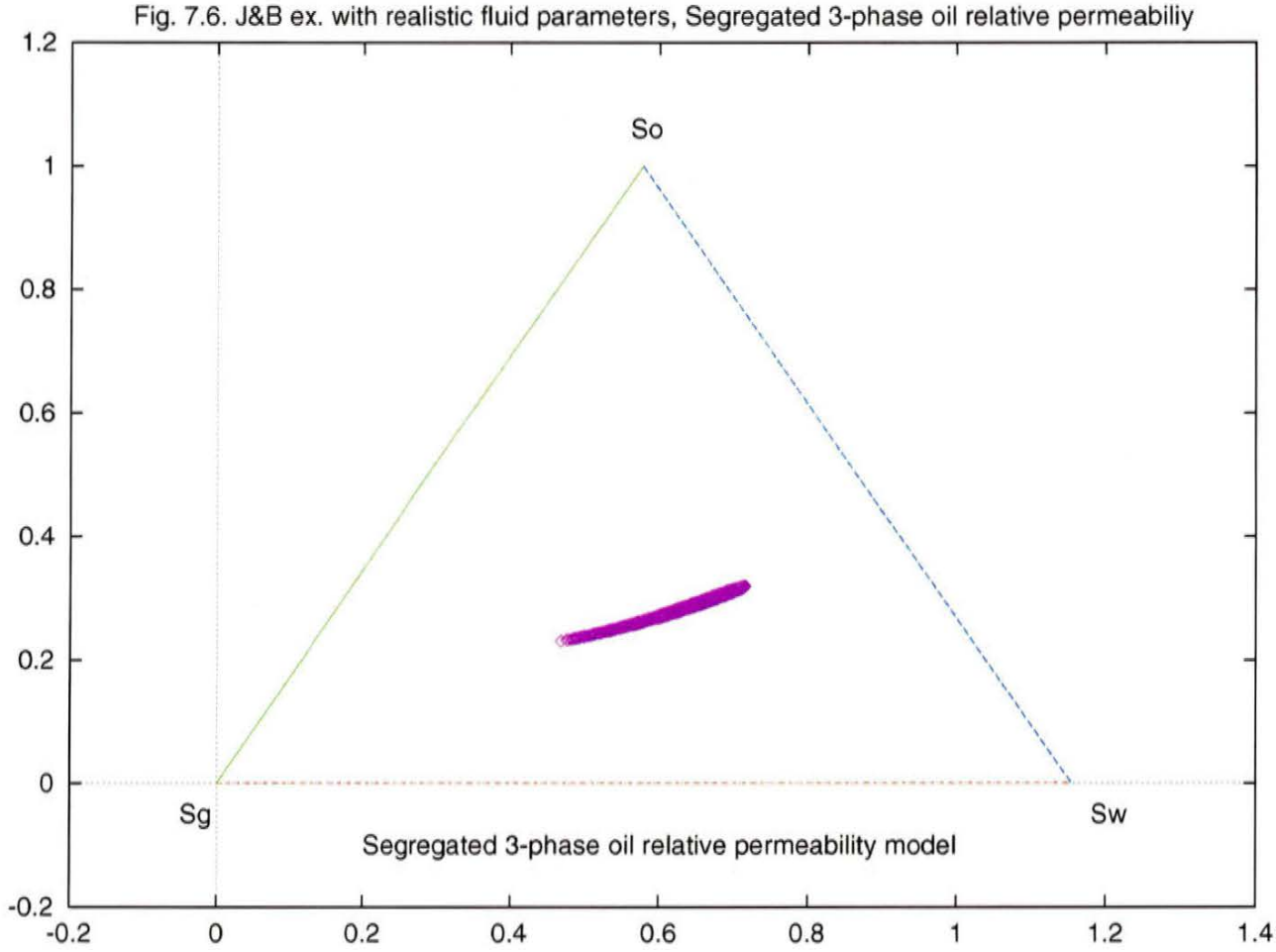

7.7.1 The Segregated Model

The expression for the three-phase oil relative permeability is

$$k_o = \frac{(S_w - S_{wc})k_{ow} + S_g k_{og})}{(S_w + S_g - S_{wc})} \tag{7.41}$$

The resulting elliptic region is shown in Figure 7.6. It is seen to be completely different and much smaller than the region obtained when the three-phase oil relative permeability is given by eq. (7.34).

7.7.2 The Stone I Model

The expression for the three-phase oil relative permeability is

$$k_o = k_{ocw} SS_o F_w F_g \tag{7.42}$$

where

$$k_{ocw} = k_{ow}(S_{wc}) \tag{7.43}$$

$$SS_o = \frac{(S_o - S_{om})}{(1. - S_{om} - S_{wc})} \quad \text{if So} > S_{om} \tag{7.44}$$

$$SS_o = 0. \qquad \text{if } S_o > S_{om} \tag{7.45}$$

$$S_{om} = \min\{S_{rwr}, S_{org}\} \tag{7.46}$$

$$F_w = \frac{k_{ow}}{k_{ocw}(1. - SS_w)} \tag{7.47}$$

$$F_g = \frac{k_{og}}{k_{ocw}(1. - SS_g)} \tag{7.48}$$

It turns out that there is no elliptic region in this case. The umbilic point (where the two real eigenvalues are equal) is given by (S_w, S_g, S_o) = (0.15, 0.60, 0.25). The eigenvalue is equal to 0.00188.

7.7.3 The Stone II Model

The expression for the three-phase oil relative permeability is

$$k_o = k_{ocw}\left(\frac{k_{ow}}{k_{ocw}} + k_w\right)\left(\frac{k_{og}}{k_{ocw}} + k_g\right) - k_w - k_g \tag{7.49}$$

The elliptic region in this case is different from what has been seen before regarding shape as well as location in the saturation space, cf. Figure 7.7.

It must be concluded that the presence, size, shape and location of an elliptic region is very much dependent upon the shape of the relative permeability curves.

Fig. 7.7. J&B ex. with realistic fluid parameters, Stone II 3-phase oil relative permeabiliy

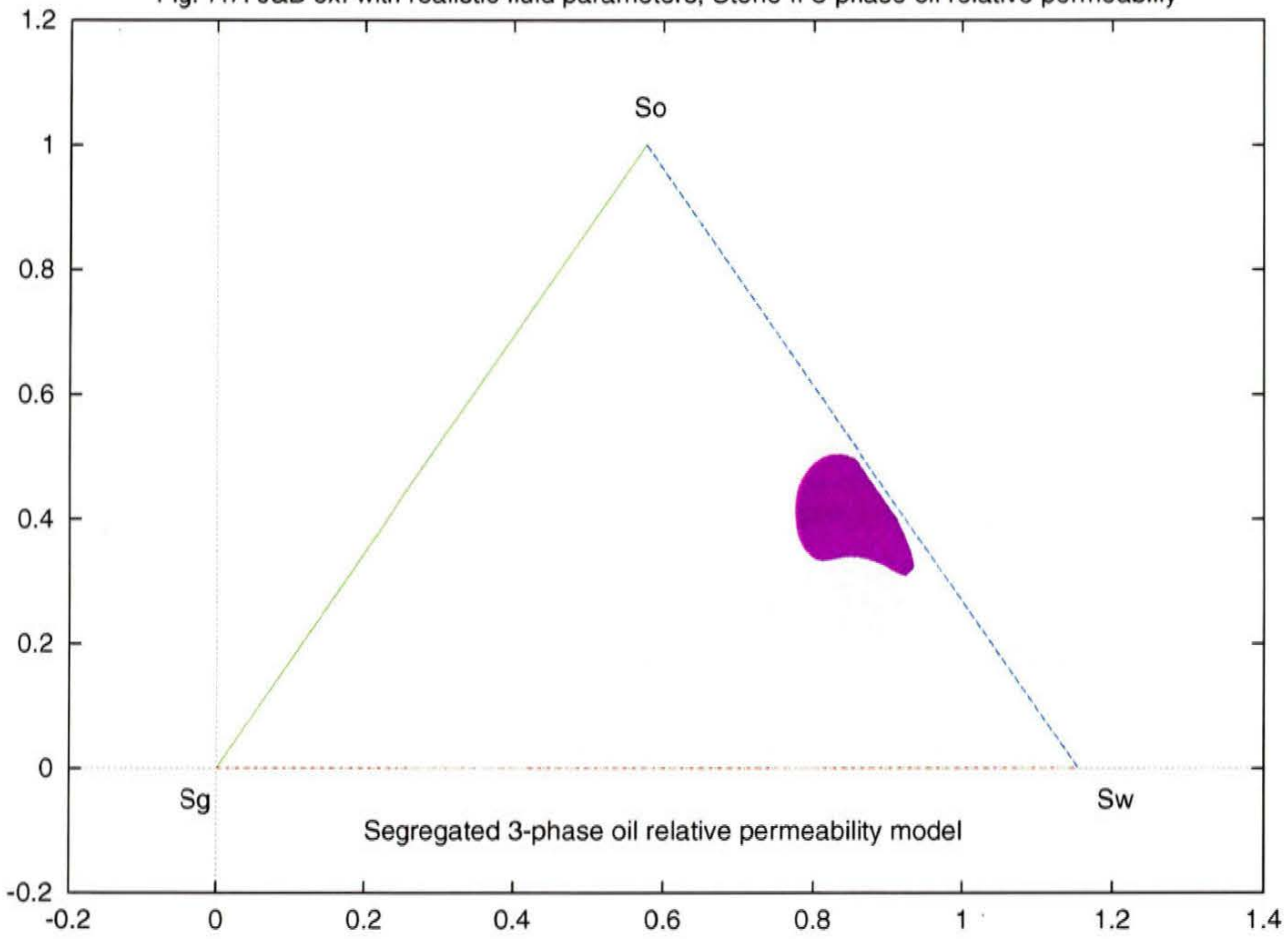

7.7.4 Effect of Gravity to Viscous Forces Ratios

The effect of the gravity to viscous force ratios is examined by using the segregated three-phase oil relative permeability model.

Reduction of the gravity to viscous forces ratios by a factor of 10 to

$$\frac{K(\rho_w - \rho_o)g_x}{v_T \mu_o} = 0.15 \tag{7.50}$$

$$\frac{K(\rho_o - \rho_g)g_x}{v_T \mu_o} = 0.15 \tag{7.51}$$

$$\frac{K(\rho_w - \rho_g)g_x}{v_T \mu_o} = 0.3 \tag{7.52}$$

results in a reduction of the elliptic region, cf. Figures 7.6 and 7.8. This is to be expected as the elliptic region disappears completely when the gravity to viscous forces ratios are zero.

Fig. 7.8. J&B ex. with realistic fluid parameters, reduced gravity to viscous forces ratio

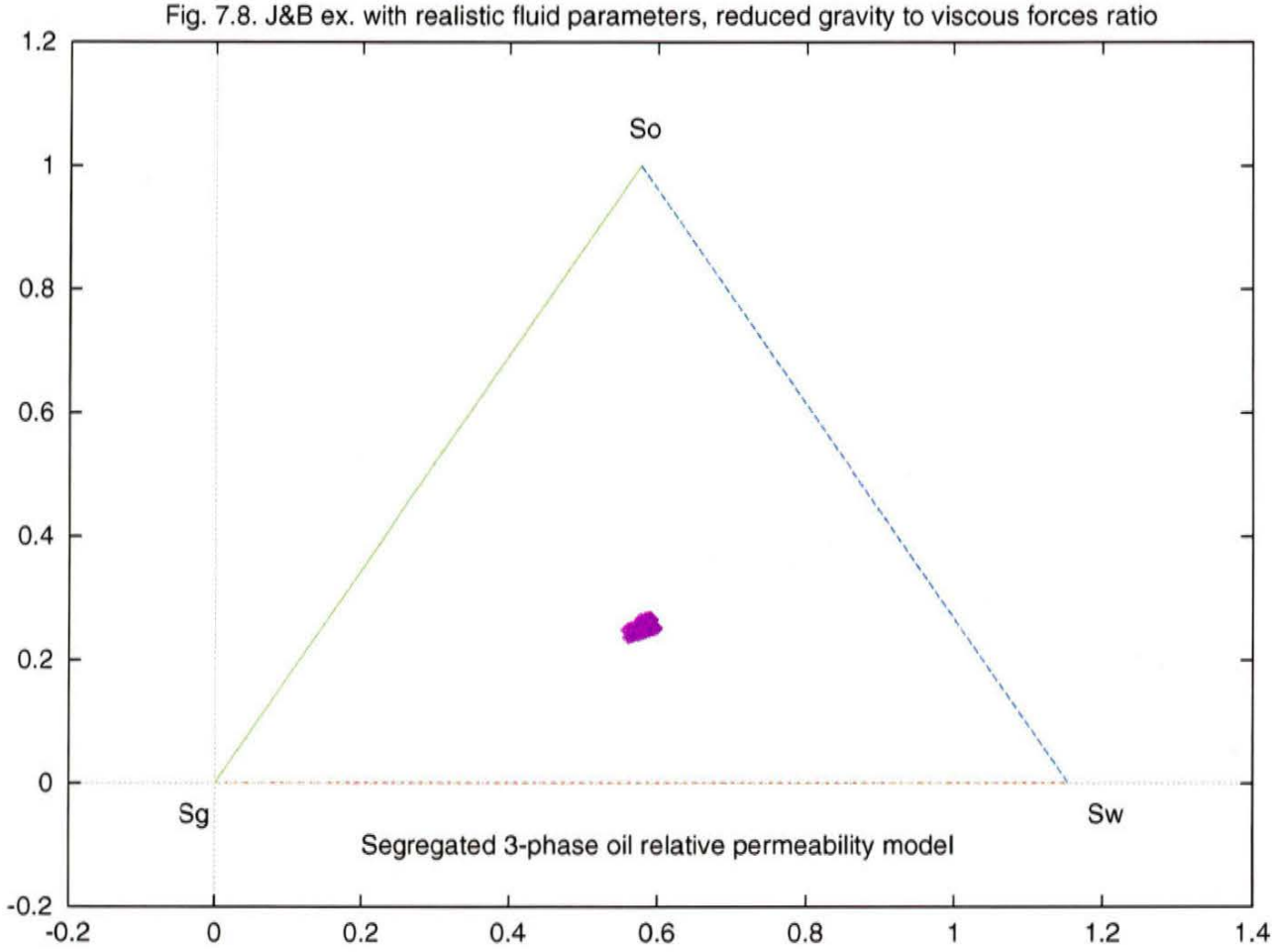

When the ratio of gravity to viscous forces is increased by a factor of 10 to

$$\frac{K(\rho_w - \rho_o)g_x}{v_T \mu_o} = 15. \tag{7.53}$$

$$\frac{K(\rho_o - \rho_g)g_x}{v_T \mu_o} = 15. \tag{7.54}$$

$$\frac{K(\rho_w - \rho_g)g_x}{v_T \mu_o} = 30. \tag{7.55}$$

The elliptic region is still present, but it is reduced, Figure 7.9.

Fig. 7.9. J&B ex. with realistic fluid parameters, increased gravity to viscous forces ratio

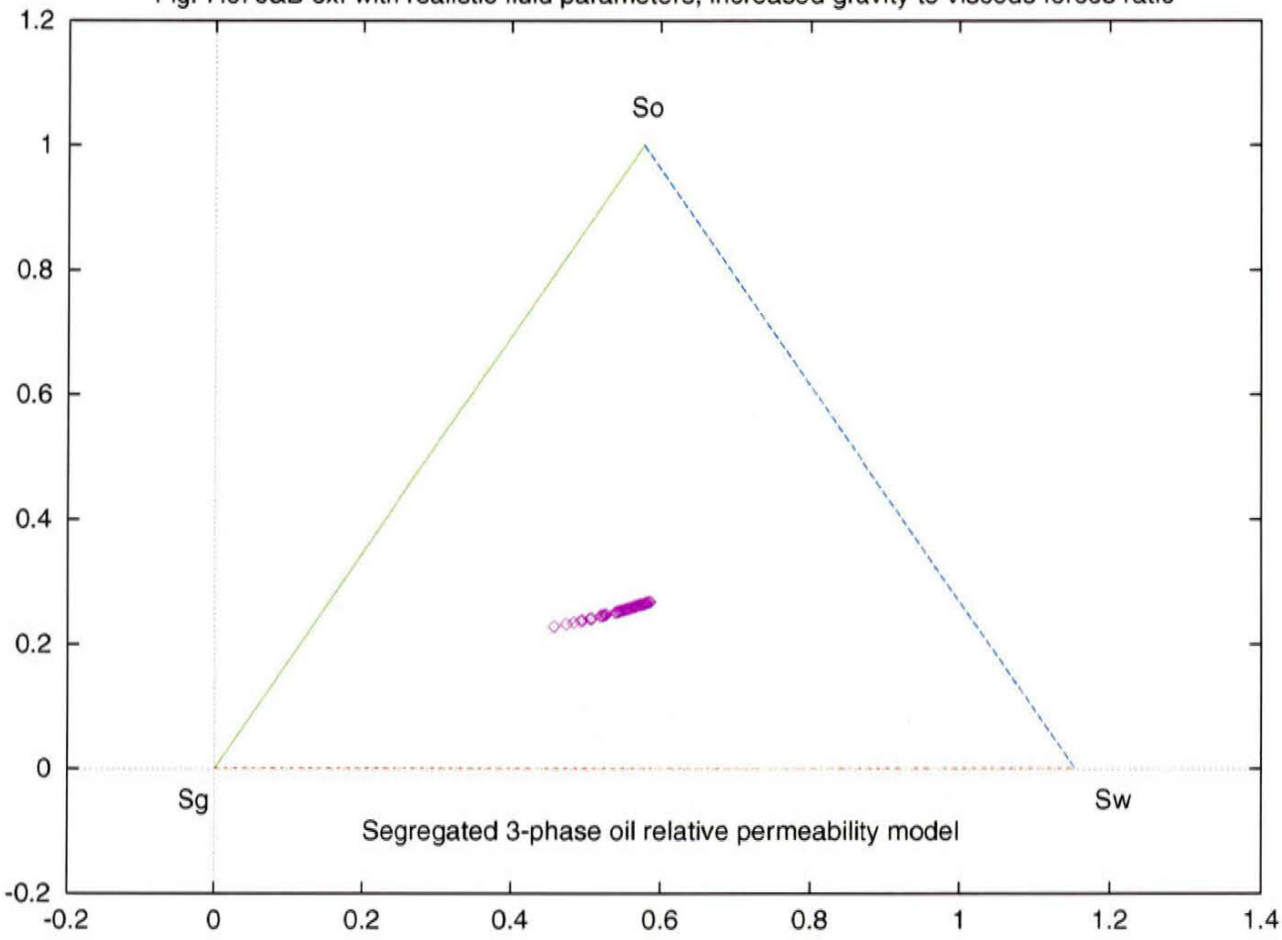

7.8 Discussion

The results obtained indicate that elliptic regions can indeed occur in realistic reservoir problems, but for conditions typical of North Sea chalk reservoirs they appear to be small.

Jackson and Blunt (2000) present some example solutions for three-phase flow with gravity and capillary pressure. They find that for cases where the saturation path goes through an elliptic region even small amounts of capillary pressure have a significant stabilizing effect on the solution. Now, in North Sea chalk reservoirs the capillary pressures are high. This in combination with only small elliptic regions lead to the conclusion that elliptic regions pose no problem in the simulation of this kind of reservoirs.

The assumption that the gas is incompressible appears to be rather severe. Trangenstein (1988) shows however, for a strictly hyperbolic black-oil model, that neither compressibility nor interphase mass transfer effects influence the characteristic speeds. It seems reasonable to expect that the same holds for elliptic regions.

8. Concluding remarks

The goal of micromodel experiments is to link pore-scale transport mechanisms to hydrocarbon recovery efficiency. Consequently, the artificial porous networks should reproduce as many pore-scale transport mechanisms as possible. The use of the RIE etching technique and the double etching depths has made it possible to create micromodels, which imitate chalks in a more efficient manner than the older micromodels. In particular, pore sizes of the developed micromodels are only a single order of magnitude larger than the typical pore sizes of North Sea chalk. Also, the film flow can be studied by creating micromodels with 'connected corners'. On the other hand, the absolute permeability of the new micromodels is at least three orders of magnitude higher than the permeability of real North Sea chalks. Thus, the micromodels manufactured during this project might be unable to reproduce some transport mechanisms that are active at the pore-scale in real-life chalk reservoirs. In addition, one of the drawbacks of micromodels with smaller dimensions of the pores is that measurement of injection pressure during experiments and phase saturations in the micromodels' pore space become much more complicated. In particular, the injection of fluids into a micromodel requires extremely accurate control of the injected volumes. This, in turn, imposes high precision demands on the equipment as well as on experimental conditions. Moreover, in GEUS 1, GEUS 2, and GEUS 3 micromodels observations were limited by shading effects and estimation of saturation could only be performed on small sections of the micromodels. This means that phase saturations can only be measured with limited precision by the numbers method.

One of the conclusions derived from this project is that quasistatic network simulators can act as a link between the pore-scale and the macroscopic scale in the iterative procedure for establishing selfconsistent relative permeability functions. However, it turns out that the quasistatic model of the three-phase transport cannot explain increased recovery efficiencies of WAG injection as compared to water or gas injection. More precisely, the instability of oil layers and the associated high residual oil saturation encountered in the network model seems contradictory to the observations of increased oil recovery on the field scale. It is possible, however, that improved recovery efficiencies could be attributed to other effects present on a different scale e.g., a scale where the gravitational effects or other effects such as solution of the gas phase in the oil phase are important.

Finally, it should be noted that a successful use of the iterative procedure presupposes that the concept of relative permeability is well defined both at the macroscopic and microscopic levels. For some recovery processes this might require an expansion of the relative permeability concept in order to capture all the essential parts of the displacement process. In particular, the network simulator should include both the steady state and the unsteady-state transport mechanisms. Consequently, for more complex recovery processes, such as WAG injection, a *dynamic* network simulator (cf. e.g., Mani and Mohanty (1998)) might be a suitable replacement of its quasistatic counterpart in the iterative procedure aimed at determination of selfconsistent relative permeability functions.

9. References and bibliography

Adamson, A. W.: Physical Chemistry of Surfaces, fifth Edition, John Wiley and Sons, New York City (1990).

Ahmed, U., Crary, S.F. and Coates, G.R.: "Permeability Estimation: The Various Sources and Their Interrelationship," SPE 19604. *JPT*, (May, 1991), p. 578.

Aker, E., Måløy, K. J., Hansen, A., and Bartrouni, G. G.: "A Two Dimensional Network Simulator for Two-Phase Flow in Porous Media," *Transport in Porous Media* (1998) **32**, pp. 163-186.

Akin, S., Schembre, J. S., Bhat, S. K., and Kovcsek, A. R.: "Spontaneous Imbibition Characteristics of Diatomite," *Journal of Petroleum Science and Engineering* (2000) **25** pp. 149-165.

Andersen, M. A..: "Petroleum Research in North Sea Chalk," Joint Chalk Research Phase V (1995), RF-Rogaland Research.

Anderson, William G.: "Wettability Literature Survey-Part 1: Rock/Oil/Brine Interactions and the Effects of Core Handling on Wettability," *Journal of Petroleum Technology* (October, 1986 a) pp. 1125-1144.

Anderson, William G.: "Wettability Literature Survey-Part 2: Wettability Measurement," *Journal of Petroleum Technology* (November 1986 b) pp. 1246-1262.

Anderson, William G.: "Wettability Literature Survey-Part 3: The Effects of Wettability on the electrical Properties of Porous Media," *Journal of Petroleum Technology* (December, 1986 c) pp. 1371-1378.

Anderson, William G.: "Wettability Literature Survey-Part 4: Effects of Wettability on Capillary Pressure," *Journal of Petroleum Technology* (October, 1987 a), pp. 1283-1300.

Anderson, William G.: "Wettability Literature Survey-Part 5: The Effects of Wettability on Relative Permeability," *Journal of Petroleum Technology* (November, 1987 b), pp. 1453-1468.

Anner, G. E.: "Planar Processing Primer," van Nostrand Reinhold, NewYork (1990).

Appel, C. C., Bilde-Sørensen, J., and Horsewell, A.: "Application of the Environmental Scanning Electron Microscope in Material Science," paper presented at the 13th Electron Microscopy Congress, Ankara, Turkey, September 1-4 (1997)

Archie, G. E.: "The Electrical Log as an Aid in Determining Some Reservoir Characteristics," *Trans. AIME* (1942) **146**, 54-62

Avraam, D. G., Kolonis, G. B., Roumeliotis, T. C., Constatinides, G.N. and Payatakes, A. C.: "Steady-State Two-Phase Flow Through Planar and Nonplanar Porous Media". *Transport in Porous Media* (1994) **16** No. 1, pp. 75-103.

Avraam, D. G. and Payatakes, A. C.: "Flow regimes and relative permeabilities during steady-state two-phase flow in porous media," *Journal of fluid Mechanics* (1995) **vol**. 293, pp. 207-236.

Azzam, M. I. S. and Dullien, F. A. L.: " Flow in Tubes with Periodic Step Changes in Diameter: A Numerical Solution," *Chemical Engineering Science* (1977) **32**, pp. 1445-1455.

Aziz, K. and Settari, A.: "Petroleum Reservoir Simulation", Elsevier (1986).

Babadagli, T.: "Efficiency of Capillary Imbibition Dominated Displacement of Nonwetting Phase by Wetting Phase in Fractured Porous Media," *Transport in porous Media* (2000) **40**, pp. 323-344.

Bakke, S. and Øren, P. E.: "3-D Pore-Scale Modeling of Heterogeneous Sandstone Reservoir Rocks and Quantitative Analysis of the Architecture, Geometry and Spatial Continuity of the Pore Network". Paper SPE 35479 presented at the European 3-D Reservoir Modeling Symposium, Stavanger, Norway, April 16-17, 1996.

Balan, B., Mohaghegh, S. and Ameri, S.: "State-of-the-Art in Permeability Determination From Well Log Data: Part 1 - A Comparative Study, Model Development," SPE 30978. Paper presented at Eastern Regional Conference & Exhibition, Morgantown, West Virginia, September 17-21 (1995).

Bech, N., Olsen, D. and Nielsen, C.M.: "Determination of Oil/Water Saturation Functions of Chalk Core Plugs From Two-Phase Flow Experiments," SPE 49325 and 60769. *SPE Reservoir Evaluation & Engineering* (February, 2000) pp. 50-59.

Bedrikovetsky, P.: "A new Mathematical Model for EOR Displacement Honoring Oil Ganglia," SPE 38892. Paper presented at the 1997 SPE Annual Technical Conference and Exhibition, San Antonio, Texas October 5-8 1997.

Bedrikovetsky, P., Marchesin, D., and Ballin, P.: "Mathematical Theory for Two Phase Displacement with Hysteresis (With Application to WAG Injection)," paper presented at the 5th European Symposium on the Mathematics of Oil Recovery, Leoben, Austria, September 3-6 (1996).

Bekri et al.: "Pore Geometry and Transport Properties on North Sea Chalk," *Journal of Petroleum Science and Engineering* (2000) **25**, pp. 107-134.

Bell, J. B., Trangenstein, J. A. and Shubin, G. R.: "Conservation Laws of Mixed Type Describing Three-Phase Flow in Porous Media," *Journal of Applied Mathematics*. **46**, No. 6 December 1986.

Bernadiner, M. G.: "A capillary Microstructure of the Wetting Front," *Transport in Porous Media*, **30**, pp. 251-265.

Birovljev, A. et al.: "Gravity Invasion Percolation in Two-Dimensions: Experiment and Simulation," *Physical Review Letters* (1991) **67**, No. 5 pp. 584-587.

Blunt, M.: "Pore Level Modeling of the Effects of Wettability," (1997) SPE Paper 38435. *SPE Journal* **2** (December, 1997) pp. 494-510.

Blunt, M.: "An Empirical Model for Three-phase relative permeability," SPE 56474. Paper presented at the 1999 Annual SPE Technical Conference and Exhibition held in Houston, Texas, 3-6 October 1999.

Blunt, M. and King, S.: "Scaling of Viscous Fingering," *Physical Review A* (1988) **37** No. 10. pp. 3935-3941.

Blunt, M. and King, S.: "Relative Permeabilities from two- and Three-Dimensional Pore-Scale Network Modeling," *Transport in Porous Media*, **6** (1991) pp. 407-433.

Blunt, M., King, S. and Scher, H.: "Simulation and theory of two-phase flow in porous media," *Physical Review A* **46**, (1992) No 12. pp. 7680-7699.

Blunt, M., Zhou, D. and Fenwick, D.: "Three-Phase Flow and Gravity Drainage in Porous Media," *Transport in Porous Media*, **20** (1995) pp. 77-103.

Blunt, M., Fenwick, D. and Zhou, D.: "What determines Residual Oil Saturation in Three-Phase Flow?," SPE 27816. Paper presented at the SPE/DOE Ninth Symposium on Improved Oil Recovery held in Tulsa, Oklahoma, U.S.A., 17-20 April 1994.

Blunt, M and Fenwick, D.: "Pore-level Modeling of Three-phase Flow in Porous Media," Proceedings of the 8th European Symposium on Oil Recovery, Vienna, Austria (May, 1995).

Bonnet, J. and Lenormand, R.: "Constructing Micromodels for the Study of Multiphase Flow in Porous Media," *Revue de L'Inst. Francais du Petrole* **42**, pp. 477-480, 1977.

Borbiaux, B. J. and Kalaydian, F. J.: "Experimental Study of Cocurrent and Countercurrent Flows in Natural Porous Media," SPE 18283. *SPE Reservoir Engineering* (August, 1990) pp. 361-368.

Borre, M. and Fabricius, I. L.:" Chemical and Mechanical Processes during Burial Diagenesis of Chalk: An Interpretation Based on Specific Surface Data of Deep-sea Chalk Sediments," *Sedimentology* (1998) **45**, pp. 755-769.

Braun, E.M. and Holland, R.F.: "Relative Permeability Hysteresis: Laboratory Measurements and a conceptual Model," *SPE Reservoir Engineering* (August, 1995) pp. 222-228.

Broadbent, S. R. and Hammersley, J. M.: *Proc. Camb. Phil. Soc*, (1957) **53**, 629

Brown, R. J. S. and Fatt, I.: "Measurement of Fractional Wettability of Oil Field Rocks by the Nuclear Relaxation Method," *Trans. AIME* (1956) **207** pp. 262-264.

Bryant, S. and Blunt, M.: "Prediction of relative permeability in simple porous media," *Physical Review A* (1992) **46,** No. 4. pp. 2004-2011.

Carlson, F. M.: "Simulation of Relative Permeability Hysteresis to the Non-Wetting Phase," SPE 10157. Paper presented at the 56th Annual Fall Technical Conference and exhibition of the Society of Petroleum Engineers of AIME, held in San Antonio, Texas, October 5-7, 1981.

Cazabat, A. M.: "Experimental Aspects of Wetting," *Elsevier Science Publishers B.V.*, (1990).

Chardaire-Riviere, C., Chavent, G., Jaffre, J. and Bourbiaux.: "Simultaneous Estimation of Relative Permeabilities and Capillary Pressure," Paper SPE 19680, *SPE Formation Evaluation*, (December, 1992) pp. 283-289.

Chatzis, I. and Dullien, F. A. L.: "Modeling Pore Structure of 2-D and 3-D Networks with Application to Sandstone," *J. Can Petroleum Technology* **16**, 97 (1977)

Chatzis, I., Kantzas, A. and Dullien, F.A.L.: "On the Investigation of Gravity assisted Inert Gas Injection Using Micromodels, Long Berea Sandstone Cores, and Computer-Assisted Tomography," SPE 18284. Paper presented at the 63rd Annual Technical Conference and Exhibition, Houston, Texas, October 2-5 (1988 a).

Chatzis, I., Kuntamukkula, M. S. and Morrow, N. R.: "Effect of Capillary Number on Microstructure of Residual Oil in Strongly Water-wet Sandstones," *SPE Reservoir Engineering* (August, 1988). pp. 902-912. (1988 b)

Chen, J-D. and Wilkinson, D.: "Pore-Scale Viscous Fingering in Porous Media," *Physical Review Letters*, **55** (1985) No. 18, pp. 1892-1895.

Christensen, J. R., Stenby, E. H. and Skauge, A.: "Review of WAG Field Experience," SPE 39883. Paper presented at the 1998 SPE International Petroleum Conference, Villahermose, Mexico March 3-5 1998.

Chtioui, A.: "Irreducible Water Saturation in Chalk," MS thesis No. 268, Institute of Geology and Geotechnical Engineering, Technical University of Denmark (1999).

Cieplak, M. and Robbins, M. O.: "Influence of Contact Angle on Quasistatic Fluid Invasion of Porous Media," *Physical Review B* (1990) **41**, No- 16 pp. 11508-11521

Civan, F. and Donaldson, E.C.: "Relative Permeability From Unsteady State Displacements with Capillary Pressure Included," *SPE Formation Evaluation*, (June, 1989) , pp. 189-193.

Civan, F. and Evans, R. D.: "Relative Permeability and Capillary Pressure Data from Non-Darcy Flow of Gas/Brine Systems in Laboratory Cores," SPE 26151. Paper prepared for presentation at the SPE Gas Technology Symposium held in Calgary, Alberta, Canada, 28-30 June 1993.

Coates, G.R. and Dumanoir, J.L.: "A new Approach to Improved Log-Derived Permeability," *The Log Analyst* (January-February, 1974) **15**, No.1 pp.17-29.

Coates, G.R and Denoo, S.: "The Producibility Answer Product," *The Technical Review Schlumberger*, Houston (June, 1981) **29**, No. 2 pp. 55-63.

Coelho, D., Thovert, J-F, and Adler, P. M.: "Geometrical and Transport Properties of Random Packings of Spheres and Aspherical Particles," *Physical Review E* (1997) **55,** No. 2 pp. 1-20.

Collins, S. H. and Melrose, J.C.: "Adsorption of Asphaltenes and Water on Reservoir Rock Minerals," SPE 11800. Paper presented at the International Symposium on Oilfield and Geothermal Chemistry, Denver, Colorado, June 1-3 (1983).

Coskunar, G.: "Microvisual Study of Multiphase Gas Condensate Flow in Porous Media," *Transport in Porous Media* (1997) **28**, pp. 1-18.

Dawe, A. and Grattoni, C. A.: "The Visualization of the Pore-Scale Physics of Hydrocarbon Recovery from Reservoirs," *First Break*, (November, 1998) pp. 341-385.

Dennis, H., Baillie, J., Holt, T. and Wessel-Berg, D.: "Hydrodynamic Activity and Tilted oil-water Contacts in the North Sea," presented at NPF Conference, Haugesund. September (1998).

Deryagin, B. V.: "Definitions of the Concept of, and Magnitude of the Disjoining Pressure and Its Role in the Statics and Kinetics of Thin Layers of Liquids," *Colloid Journal of USSR* **17** (1955).

Dias, M. M. and Payatakes, A. C.: "Immiscible Microdisplacement and Ganglion Dynamics in Porous Media," *Reviews in Chemical Engineering*, (1984) **2** No. 2

Dias, M. M. and Payatakes, A. C.: "Network models for two-phase flow in porous media. Part 1. Immiscible microdisplacement of non-wetting fluid," *Journal of Fluid Mechanics* (1986 a) **164** pp. 305-336.

Dias, M. M. and Payatakes, A. C.: "Network models for two-phase flow in porous media. Part 2. Motion of oil ganglia," *Journal of Fluid Mechanics* (1986 b) **164**. pp. 337-358.

Diaz, C. E, Chatzis, I, Dullien, F. A. L (1986). "Simulation of Capillary Pressure Curves Using Bond Correlated Site Percolation on a Simple Cubic Network'. *Transport in Porous Media*, **2** no. 3 June 1987, pp. 215-240.

Dijke, M. I. J. van, Sorbie, K. S. and McDougal, S. R.: " A Process-Based Approach for Three-Phase Capillary Pressure and Relative Permeability Relationships in Mixed-Wet Systems," SPE 59310. Paper presented at the 2000 SPE/DOE Improved Oil Recovery Symposium, Tulsa, Oklahoma, April 3-5 2000. (2000 a)

Dijke, M. I. J. van, McDougal, S. R. and Sorbie, K. S.: "Three-phase Capillary Pressure and Relative Permeability Relationships in Mixed-Wet Systems," Accepted for publication in *Transport in Porous Media*, (July, 2000). (2000 b)

Dijke, M. I. J. van, Sorbie, K. S. and McDougal, S. R.: " Saturation-dependencies of three-phase relative permeabilities in mixed-wet and fractionally-wet systems," Accepted for publication in *Advances in Water Resources* (June, 2000). (2000 c)

Dixit, A. B., McDougall, S. R., Buckley, J. S., and Sorbie, K. S.: "Empirical Measurement of Wettability in Porous Media and the Relationship Between Them Derived From Pore Scale Modeling," *Transport in Porous Media*, **40** (2000), pp. 27-54.

Dixit, A. B., McDougall, S. R. and Sorbie, K. S.: "Pore-Scale Modeling of Wettability Effects and Their Influence on Oil Recovery," SPE 35451. Paper presented at the SPE/DOE tenth Symposium on Improved Oil Recovery held in Tulsa, OK, 21-24 1996.

Dixit, A. B., McDougall, S. R. and Sorbie, K. S.: "A Pore-Level Investigation of Relative Permeability Hysteresis in Water-Wet Systems," SPE 37233. Paper presented at the 1997 SPE International Symposium on Oilfield Chemistry, Houston, Texas, 18-21 February 1997.

Dong, M. and Chatzis, I.: "The Imbibition and Flow of a Wetting Liquid along the Corners of a Square Capillary Tube," *Journal of Colloid and Interface Science* (1995) **172**, pp. 278-288.

Dong, M. and Dullien, F. A. L.: "A New Model for Immiscible Displacement in Porous Media," *Transport in Porous Media* (1997) **27**, pp. 185-204.

Dong, M. and Dullien, F. A. L.: "Effects of Capillary Forces on Immiscible Displacement in Porous Media," SPE 56676. Paper presented at the 1999 SPE Annual Technical Conference and Exhibition, Houston, Texas October 3-6 1999.

Dong, M., Dullien, F.A.L., and Chatzis, I.: "Imbibition of oil in Film Form over Water Present in Edges of Capillaries with an angular Cross-section," *Journal of Colloid & Interface Science*, **172**, pp. 278-288 (December, 1995)

Dullien, F. A. L.: " Porous Media – Fluid Transport and Pore Structure," Academic Press Inc., New York (1979)

Dullien, F. A. L.: "Characterization of Porous Media - Pore Level," *Transport in Porous Media*, (1991) **6** no. 5 & 6, pp. 567-581.

Eclipse 100, 95A Release, Intera Information Technologies Ltd, Highlands Farm, Henley-on-Thames, Oxfordshire, U.K., 1994.

Edinburgh Petroleum Service: Conventional Core Analysis (1996 a).

Edinburgh Petroleum Service: Application to Petrophysics and Reservoir Engineering (1996 b).

Egbogah, E. O. and Dawe, R. A..: "Microvisual Studies of Size Distribution of Droplets in Porous Media," *Bull. Of Can. Pet. Geol.* **28** No. 2 (1980) pp.200-210.

Ehrlich, R.: "Viscous Coupling in Two-Phase Flow in Porous Media and its Effect on Relative Permeabilities," *Transport in Porous Media*,(1993) **11** No. 3, pp. 201-218.

Engstrøm, F.: "A New Method to Normalize Capillary Pressure Curves," paper SCA 9535 presented at the 1995 International Symposium of the Society of Core Analysts, San Francisco, September 12-14.

Falls, A. H. and Schulte, W. M.: "Features of Tree-component, Three-Phase Displacement in Porous Media," *SPE Reservoir Engineering* (November, 1992)

Fatt, I.: " The Network Model of Porous Media," *Trans AIME* (1956) **207** pp. 144-181.

Fayers, F. J.: " Extension of Stone's Method 1 and Conditions for Real Characteristics in Three-Phase Flow," *SPE Reservoir Engineering* (November, 1989) pp. 437-445.

Fenwick, D. H. and Blunt, M.: "Pore level modelling of three phase flow in porous media," Proceedings of the 1995 8th European Symposium on Improved Oil Recovery, Vienna, Austria, 1995.

Fenwick, D. H. and Blunt, M.: "Calculating Three-Phase Relative Permeabilities Using Network Modeling," presented at the 5th European Conference on the Mathematics of Oil Recovery, Leoben, Austria, 1996. (1996 a)

Fenwick, D. H. and Blunt, M.: " Use of Network Modeling to Predict Saturation Paths, Relative Permeabilities and Oil Recovery for Three-phase Flow in Porous Media," SPE 38881. Paper presented at the 1997 SPE Annual Technical Conference and Exhibition, San Antonio Texas, U.S.A. 5-8 October 1997.

Fenwick, D. H. and Blunt, M.: "Network Modeling of Three-phase Flow in Porous Media," *SPEJ*, (1998) **3**, 86-97.

Fenwick, D. H. and Blunt, M.: "Three-dimensional Modeling of Thee Phase Imbibition and Drainage," *Advances in Water Resources* (1996) **21**, No. 2 pp. 121-143. (1996 b)

Fenwick, D. H. and Lenormand, R.: "MDU: A Model for Dynamic Upscaling," Paper presented at the 1998 19th IEA Collaborative Project on Enhanced Oil Recovery, Carmel California.

Forchheimer, P. H.: *Z. Ver. Deutsch. Ing.* (1901) 45, 1781.

Frette, O. A., Måløy, K. J., Schmittbuhl, J. and Hansen, A.: "Immiscible displacement of viscosity-matched fluids in two-dimensional media," *Physical Review E*, (1996) **55** No. 3 pp. 2969-2975.

Frette, V., Feder, J., Jøssang, T., and Meakin, P.: "Buoyancy-Driven Fluid Migration in Porous Media," *Physical Review*, **68** (1992) No. 21 pp. 3164-3167.

Furuberg, L., Måløy, K. J. and Feder, J.: "Intermittent Behaviour in Slow Drainage," *Physical Review E* (January, 1996) **53**, No. 1 pp. 966-977.

Gauglitz, P. A., Radke, C. J.: "The Dynamics of Liquid Film Breakup in Constricted Cylindrical Capillaries," *Journal of Colloid and Interfacial Science* (1990) **134** No. 1, pp. 14-40.

de Gennes, P. G., Hua, X. and Levinson, P.: "Dynamics of Wetting : Local contact angles," *Journal of Fluid Mechanics*, (1990) **212**, pp. 55-63.

Gladfelter, R. E. and Gupta, S. P.: "Effects of Fractional Flow Hysteresis On Oil Recovery of Tertiary Oil," SPE 7577. Paper presented at the 53rd Annul Technical Conference and Exhibition, Houston, Texas October 1-3, 1978.

Grader, A. S. and O'Meara, D. J.: "Dynamic Displacement Measurement of Three-Phase Relative Permeabilities Using Three Immiscible Liquids," SPE 18293. Paper presented at the 63rd Annual Technical Conference and Exhibition, Houston, Texas, October 2-5 (1988).

Guo, Y.: "Importance of capillary Hysteresis on Core flooded Experiments," paper presented at the 8th IOR Symposium, Vienna, Austria, May 16-17 (1995).

Guzman, R. E. and Fayers, J. F.: "Solutions to the Three-Phase Buckley-Leverett Problem," Paper presented at the 5th European Conference on the Mathematics of Oil Recovery, Loeben, Austria, September 3-6, 1996.

Haines, W. B.: *Journal of Agricultural Science* (1930), **20**, p. 97

Hall, A. C., Collins, S. H. and Melrose, J. C.: "Stability of Aqueous Water Films in Athabasca Tar Sands," SPE 10626. *Society of Petroleum Engineers Journal* (April, 1983), pp. 254-258.

Hassanizadeh, M. and Gray, W. G.: "General conservation equations for multi-phase systems: 1. Averaging procedure," *Advanced Water Resources*, (1979 a) **2** pp. 1-16.

Hassanizadeh, M. and Gray, W. G.: "General conservation equations for multi-phase systems: 2. Mass, momenta, energy and entropy equations," *Advanced Water Resources*, (1979 b) **2** pp. 17-29.

Hassanizadeh, M. and Gray, W. G.: "General conservation equations for multi-phase systems: 1. Constitutive theory for porous media flow," *Advanced Water Resources*, (1979 c) **2** pp. 30-45.

Hassanizadeh, M. and Gray, W. G..: "Mechanics and thermodynamics of multiphase flow in porous media including interphase boundaries, " *Advanced Water Resources*, (1990) **13**. No 4 pp. 169-185.

Hazlet, R. D., Coles, M E., Jones, K. W., Andrews, B, Dowd, B, Siddons, P. and Perskin, A..: "Development in Synchrotron X-Ray Microtomography for Application to Flow in Porous Media," Paper SCA 9630 presented at the 1996 International Symposium for Core Analysts, Montpellier, France, September 8-10 1996.

Heiba. A. A, Davis, H. T. and Scriven, L. E..: "Effects of Wettability on Two-Phase Relative Permeabilities and Capillary Pressures," SPE 12172. Paper presented at the 58th Annual Technical Conference and Exhibition held in San Francisco, CA, October 5-8, 1983.

Heiba. A. A, Sahimi, M., Davis, H. T. and Scriven, L. E.: "Percolation Theory of Two-Phase Relative Permeability," SPE 11015. *SPE Reservoir Engineering*, (February, 1992) pp. 123-132.

Hirasaki, G. J.: "Wettability: Fundamentals and Surface Forces," SPE 17367, *SPE Formation Evaluation*, (June, 1991) pp. 217-225.

Honarpour, M. and Mahmood, S. M.: "Relative Permeability Measurements: An Overview". *Journal of Petroleum Technology* (August, 1988), pp. 963-966.

Hoshen, J. and Kopelman, R. (1976).: "Percolation and Cluster distribution. I. Cluster multiple labeling technique and critical concentration algorithm," *Physical Review* **14** No. 8 pp. 3438-3445, (October, 1976).

Hui, M. and Blunt, J.: "Effects of Wettability on Three-Phase Flow in Porous Media," *Journal of Physical Chemistry B* (2000) **104**, pp. 3833-3845. (2000 b)

Ioannidis, M. A. and Chatzis, I.: "Network Modeling of Pore Structure and Transport Properties of Porous Media," *Chemical Engineering Science* (1993) **48** No. 5 pp. 951-972.

Israelachvili, J and Drummond, C.: "Fundamental studies of Oil-Surface-Water Interactions and its relationships to Wettability," presented at the 5th Symposium on the Evaluation of Reservoir Wettability and Its on Oil Recovery, June 22-24, 1998, Trondheim, Norway.

Jackson, M. and Blunt, M.: "Dynamic upscaling from the Pore to the Reservoir Scale," paper presented at the 21st IEA Annual Workshop and Symposium, Edinburgh, UK, September 20-22, 2000.

Jacobsen, N., Engstrøm, F., Uldall, A. and Petersen, N. W.: "Delineation of Hydrodynamic/Geodynamic Trapped Oil in Low Permeable Chalk," SPE 56514. Paper presented at the 1999 Annual Technical Conference and Exhibition, Houston October 3-6 (1999).

Jerauld, G. R.: "Prudhoe Bay Gas/Oil Relative Permeability," *SPE Reservoir Engineering* (February, 1997), pp. 66-73.

Jerauld, G. R. and Rathmell, J. J.: "Wettability and Relative Permeability of Prudhoe Bay: A Case Study in Mixed-Wet Reservoirs," *SPE Reservoir Engineering* (February, 1997), pp. 58-65.

Jerauld, G. R. and Salter, S. J.: "The Effects of Pore Structure on Hysteresis in Relative Permeability and Capillary Pressure: Pore-Level Modeling," *Transport in Porous Media*, (1990) **5** No. 2 pp. 103-152.

Johnson, E. F., Bossler, D. P., Nauman, V. O. (1959). "Calculation of Relative Permeability from Displacement Experiments," *Trans AIME (1959)* **216**, pp. 370-372.

Kalaydjian, F. J-M., Moulu, J-C., Vizika, Olga and Munkerud, P. K.: "Three-Phase Flow in Water-Wet Porous Media: Determination of Gas/Oil Relative Permeabilities Under Various Spreading Conditions" (1993) SPE 26671. Paper prepared for presentation at the 68th Annual Technical Conference and Exhibition of the Society of Petroleum Engineers held in Houston, Texas, 3-6 October 1993.

Kalaydjian, F.: "Origin and Quantification of Coupling Between Relative Permeabilities for Two-Phase Flows in Porous Media," *Transport in Porous Media*, (1990) **5** No. 3 pp. 215-230.

Kalaydjian, F.: "Dynamic Capillary Pressure Curve for Water/Oil Displacement in Porous Media: Theory vs. Experiment," SPE 24813. Paper presented at 67th Annual Technical Conference and Exhibition, Washington D.C., October 4-7 (1992 a).

Kalaydjian, F.: "Performance and Analysis of Three-Phase Capillary Pressure Curves for Drainage and Imbibition in Porous Media," SPE 24878. Paper presented at 67th Annual Technical Conference and Exhibition, Washington D.C., October 4-7 (1992 b).

Kantzas, A. and Chatzis, I.: "Network simulation of relative permeability curves using a bond correlated-site percolation model of pore structure," *Chemical Engineering Communications* (1988) **69** pp. 191-214.

Kantzas, A. and Chatzis, I., and Dullien, F. A. L.: "Enhanced Oil Recovery by Inert Gas Injection," SPE 17379. Paper presented at the SPE/DOE Enhanced Oil Recovery Symposium, Tulsa, Oklahoma, April 17-20 (1988 a).

Kantzas, A. and Chatzis, I., and Dullien, F. A. L.: "Mechanisms of Capillary Displacement of Residual Oil by Gravity-Assisted Inert gas Injection," SPE 17506. Paper presented at the Rocky Mountain Regional Meeting, Caspar, Wyoming, May 11-13 (1988 b).

Keller, A. A., Blunt, M. and Roberts, P. V.: "Micromodel Observations of the Role of Oil Layers in Three-Phase Flow," *Transport in Porous Media* (1997) **26**, pp. 277-297.

Killough, J. E.: "Reservoir Simulation With History-Dependent Saturation Functions," AIME Transactions (1976).

Kirkpatrick, S.: "Percolation and Conduction," *Reviews of Modern Physics*, **45** No. 4, pp. 574-588, (October, 1973).

Klinkenberg, L. J.: *API Drill. Prod. Pract.* **200** (1941)

Koplik, J.: "Creeping flow in two dimensional networks," *Journal of Fluid Mechanics*, (1982) **119** pp. 219-247.

Koplik, J. and Lasseter, T. J.: " Two-Phase Flow in Random Network Models of Porous Media," SPE 11018. *SPEJ* (1985) **25**, pp. 89-100.

Kovscek, A. R., Wong, H. and Radke, C. J.: "A pore-Level Scenario for the Development of Mixed wettability in Oil Reservoirs," *AIChE Journal* **39**, No. 6, pp. 1072-1085.

Kozeny, J.: "Über Kapillare Leitung des Wassers im Boden," *Sitzungsberichte der Wiener Akademie der Wissenschaften* (1927) **136**, 271-306.

Land, C. S. : "Calculation of Imbibition Relative Permeability for Two- and Three-phase Flow From Rock Properties," *Trans. SPE of AIME* (1968) **243**, pp. 149-156 (SPEJ)

Laroche, C, Vizika, O. and Kalaydjian, F.: "Network Modeling as a tool to predict Three-phase Gas Injection in Heterogeneous Wettability Porous Media," Paper presented at the 5th International Symposium on Evaluation of Reservoir Wettability and Its Effect on Oil Recovery, June 22-24 Trondheim, Norway (1998).

Larsen, J. A. and Skauge, A.: "Simulation of the Immiscible WAG process Using Cycle Dependent Three-Phase Relative Permeabilities," SPE 56475. Paper presented at the 1999 Annual Technical Conference and Exhibition, Houston, Texas, October 3-6 (1999).

Legait, B.: "Laminar Flow of Two Phases through a Capillary Tube with Variable Cross-section. *J. Coll. Int. Sci.*, **96**, pp. 28-38.

Lenormand, R., Eisenzimmer, A. and Delaplace, Ph.: "Improvements of the Semidynamic Method for Capillary Pressure Measurements," SCA Paper 9531 presented at the 1995 International Symposium of Core Analysts, San Francisco September 12-14, 1995.

Lenormand, R., Eisenzimmer, A. and Zarcone, C.: "A novel method for Determination of water/oil Capillary Pressures of Mixed Wettability Samples," Paper SCA 9322 presented at the 1993 International Symposium of the Society of Core Analysts, Houston , Texas, August 9-11 1993.

Lenormand, R., Toubol, E. and Zarcone, C.: "Numerical models and experiments on immiscible displacements in porous media," *Journal of Fluid Mechanics* **189**, (1988) pp. 165-187.

Lenormand, R., Zarcone, C., and Sarr, A.: "Mechanisms of the displacement of one fluid by another in a network of capillary ducts," *Journal of Fluid Mechanics* (1983) **135**, pp. 337-353.

Lenormand, R and Zarcone, C.: "Physics of Blob Displacement in a two-dimensional Porous Medium," *SPE Formation Evaluation*, (March, 1988), pp. 271-275.

Lenormand, R and Zarcone, C.: "Role of Roughness and Edges during Imbibition on Square Capillaries," SPE 13264. Paper presented at the 59th Annual Technical Conference and Exhibition held in Houston, Texas, September 16-19, 1984.

Lerdahl, T. R. Øren. P., and Bakke, S.: "A predictive Network Model for Three-Phase Flow in Porous Media," SPE 59311. Paper presented at the 2000 SPE/DOE Improved Oil Recovery Symposium, Tulsa, Oklahoma, April 3-5 (2000)

Leverett, M. C.: "Capillary Behaviour of Porous Solids," *Petroleum Technology* (August, 1940) pp. 152-169.

Leverett, M. C. and Lewis, W. B.: "Steady Flow of Gas-Oil-Water Mixtures through Unconsolidated Sands," *Trans. AIME* (1941) **142**, 107-116.

Li, Y and Wardlaw, N. C.: "Mechanisms of Nonwetting Phase Trapping during Imbibition at Slow Rates," *Journal of Colloid and Interface Science* (February, 1986) **109**, No. 2 pp. 473-486.

Li, Y., Laidlaw, W. G. and Wardlaw, N.C.: "Sensitivity of Drainage and Imbibition to Pore Structures as Revealed By Computer Simulation of Displacement Process," *Advances in Colloid Interface Science* (1986), **26**, pp. 1-68.

Longeron, D. G., Argaud, M. J., and Feraud, J. P.: " Effect of Overburden Pressure and the Nature and Microscopic Distribution of Fluids on Electrical Properties of Rock Samples," *SPE Formation and Evaluation* (June, 1989) pp. 194-202.

Lord, C. J., Johlman, C. L. and Rhett, D. W.: "Is Capillary Suction a Viable Cohesive Mechanism in Chalk?," SPE 47310. Paper presented at the SPE/ISRM Eurock '98 held in Trondheim, Norway, July 8-10, 1998.

Mahers, E. G.: "Mass Transfer and Interfacial Phenomena in Oil Recovery," Ph.D thesis, Imperial College (August, 1983)

Mani, V. and Mohanty, K. K.: "Effect of the Spreading Coefficient on Three-Phase Flow in Porous Media," *Journal of Colloid and Interfacial Science* (1997) **187** pp. 45-56.

Mani, V. and Mohanty K. K.: "Pore-level Network Modeling of Three-phase Capillary Pressure and Relative Permeability Curves," *SPEJ* (September, 1998) pp. 238-248.

Marchesin, D. and Plohr, B. J.: "Wave Structure in WAG Recovery," SPE 56480. Paper presented at the 1999 SPE Annual Technical Conference and Exhibition, Houston, Texas October 3-6, 1999.

Marck, J. C. van der, Matsuura, T., and Glas, J.: " Viscous and Capillary Pressures During Drainage: Network Simulations and Experiments," *Physical Review E* (November, 1997) **56**, No. 5 pp. 5675-5687.

Martys, N., Cieplak, M, and Robbins, W. O.: "Critical Phenomena in Fluid Invasion of Porous Media," *Physical Review Letters* (1991) **66**, No. 8 pp. 1058-1061

Marsouk, I., Takezaki, H. and Miwa, M.: " Geologic controls on Wettability of Carbonate Reservoirs, Abu Dhabi, U.A.E," SPE 29883. Paper presented at the SPE Middle East Oil Show held in Bahrain, 11-14 March 1995.

Maslov, S.: "Time Directed Avalanches in Invasion Models," *Physical Review Letters* (1995) **74**, No. 4 pp. 562-565.

Mason, G. and Morrow, N. R.: "Capillary Behavior of a Perfectly Wetting Liquid in irregular Triangular Tubes," *Journal of Colloid and Interface Science* (1991) **141**, No. 1, pp. 262-274.

Mason, G. and Morrow, N. R.: "Effect of Contact Angle on Capillary Displacement Curvatures in Pore Throats Formed by Spheres," *Journal of Colloid and Interface Science* (1994) **168**, pp. 130-141.

Mattax, C. C. and Kyte, J. R.: " Ever Seen a Waterflood?," *Oil and Gas Journal* **59** no. 42 (1961) pp.(115-128).

McDougal, S. R. and Sorbie, K. S. (1997). "The application of network modeling techniques to multiphase flow in porous media," *Petroleum GeoScience*, **3** pp. 161-169.

McDougal, S.R., Dixit, A. B. and Sorbie, K. S.: "The Use of Capillarity Surfaces to Predict Phase Distributions in Mixed-Wet Porous Media," paper presented at the 5th European Conference on the Mathematics of Oil Recovery, Loeben, Austria (1996).

McDougal, S. R. and Sorbie, K. S.: "Estimation of Critical Gas Saturation During Depletion in Virgin and Water Flooded Reservoirs," *Petroleum Geoscience* **5** (1999), pp.299-233.

McKellar, M. and Wardlaw, N. C.: "A method of making Two-dimensional Glass Micromodels of Pore Systems," *Journal of Can. Pet. Tech.* **21** no. 4 (1982) pp. 39-41.

Meakin, P., Feder, J., Frette, V., and Jøssang, T.: "Invasion Percolation in a Destabilizing Gradient," *Physical review E* (September, 1992) **46**, No. 6 pp. 3357-3368.

Megson, J. B.: "The North Sea Chalk Play: examples from the Danish Central Graben," *Geological Society Special Publication* (1992) No. 67, pp. 247-282.

Melrose, J. C.: "Interpretation of Mixed Wettability in Reservoir Rocks," SPE 10971. Paper presented at the 1982 SPE Annual Fall Technical Conference and Exhibition, New Orleans September 26-29 (1982).

Melrose, J. C.: "Use of Water-Vapor Desorption Data in the Determination of Capillary Pressures at Low Water Saturations," *SPE Reservoir Engineering* (August, 1988) pp. 913-918.

Melrose, J. C.: "Valid Capillary Pressure Data at Low Wetting Phase Saturations," SPE 18331. *SPE Reservoir Engineering* (February, 1990) pp. 95-99.

Melrose, J. C.: "Scaling Procedures for Capillary Pressure Data at Low Wetting-Phase Saturations," *SPE Formation Evaluation* (June, 1991) pp. 227-232. (1991 a)

Melrose, J. C.: "Comparison of Different Techniques for Obtaining Capillary Pressure Data in the Low-Saturation Region," SPE 22690. Paper presented at the 66th Annual Technical Conference and Exhibition, Dallas, Texas, October 6-9 (1991). (1991 b)

Miller, C. A. and Neogi, P. "Interfacial Phenomena - Equilibrium and Dynamic Effects". Marcel Dekker, INC. New York and Basel.

Mogensen, K.: "Multiphase flow in Low-Permeable Chalk – X-ray CT Scanning and Pore-level Modeling," Ph.D. thesis (1998), Department of Chemical Engineering, Technical University of Denmark.

Mogensen, K and Stenby, E.: "A Dynamic Two-Phase Pore-Scale Model of Imbibition," *Transport in Porous Media* **32**, (1998) pp. 299-327.

Mogensen, K., Stenby, E., Shrleckha, B., and Barker, V. A.: "Comparison of Iterative Methods for Computing the Pressure Field in a Dynamic Network Model," *Transport in Porous Media* (1999) **37**, pp. 277-301.

Mohanty, K. K., Davis, H. T, Scriven, L. E.: "Physics of Oil Entrapment in water-wet rock," SPE 9406, *SPE Reservoir Engineering*, (February, 1987), pp. 113-128.

Mohanty, K. K., Davis, H. T. and Scriven, L.E.: "Thin Films and Fluid Distribution in Porous Media," *Surface Phenomena in Enhanced Oil Recovery*, D.O Shah (Ed.), Plenum Press (1981).

Mohanty K. K. and Salter, S. J.: "Multiphase Flow in Porous Media: II. Pore-Level Modeling," SPE 11018. Presented at the 57th Annual Fall Technical Conference and Exhibition held in New Orleans, Los Angeles, USA, September 26-29 1982.

Morrow, N. R. and Harris, C. C.: "Capillary Equilibrium in Porous Materials," *SPE Journal*. (March, 1965) **5** pp. 15-24.

Mortensen, J., Engstrøm, F. and Lind, I.: "The Relation Between Porosity, Permeability, and Specific Surface of Chalk from the Gorm Field, Danish North sea," SPE 31062. *SPE Reservoir Evaluation and Engineering* (June, 1998) pp. 245-251.

Naar, J. and Wygal, R. J.: Three-phase Imbibition Relative Permeability. *SPEJ.*, **1**, 254-258.

Ng, K. M., Davis, H. T. and Scriven, L. E.: " Visualization of Blob Mechanics in Flow Through Porous Media," *Chem. Eng. Sci.* **33** (1978) 1009-1017.

Nielsen C.M. et al.: "Determination of Saturation Functions of Tight Core Samples Based on Measured Saturation Profiles," paper SCA 9721, Proceedings of the 1997 International Symposium of the Society of Core Analysis, Calgary, September 7-10 (1997).

Nilsen, L. S., Øren, P. E., and Bakke, S.: "Prediction of Relative Permeability and Capillary Pressure from a Pore Model," SPE 35531. Paper presented at the European 3-D Reservoir Modeling Conference, Stavanger, Norway, April 16-17 (1996).

Nordtvedt et al.: "Estimation of Three-Phase Relative Permeability and Capillary Pressure Functions, " paper presented at the 5th European Conference on the Mathematics of Oil Recovery, Leoben, Austria, September 3-6 (1996). *SPE Formation Evaluation* (December, 1997), pp. 221-226.

Nørgaard, J. V., Olsen, D., Springer, N. and Reffstrup, J.: "Capillary Pressure Curves for Low Permeability Chalk Obtained by NMR Imaging of Core Saturation Profiles," SPE 30605 and 55985. *SPE Reservoir Engineering* (April, 1999) **2**, pp. 141-148.

Olsen, D. Bech, N. and Nielsen, C. M.: "Determination of Saturation Functions and Wettability for Chalk based on Measured Fluid Saturations," *EFP-96 Report*, Geological Survey of Denmark and Greenland, J. nr. 1313/96-0005 (1998).

Olsen, D., Topp, S., Stensgaard, A., Nørgaard, J. V. and Reffstrup, J.: "Quantitative 1D Saturation Profiles on Chalk by NMR," *Magnetic Resonance Imaging*, (1996) **14** Nos. 7 & 8 pp. 847-851.

O'Meara, C. J., Hirasaki, G. J. and Rohan, J. A.: "Centrifuge Measurements of Capillary Pressure: Part 1-Outflow Boundary Condition," *SPE Reservoir Engineering*, (February, 1992) pp. 132-142.

Or, D. and Tuller, M.: "Liquid Retention and Interfacial Area in Variable Saturated Porous Media: Upscaling from Single-Pore to Sample-Scale Model," *Water Resources Research* (1999) **35**, No. 12 pp. 3591-3605.

Øren, P. E., Bakke, S. and Arntzen, O. J.: "Extending Predictive Capabilities to Network Models," Paper 38880 and 52052. *SPEJ* (December, 1997) pp. 324-335.

Øren, P. E. and Pinczewski, W. V.: "Effect of Wettability and Spreading on Recovery of Waterflood Residual Oil by Immiscible Gasflooding," *SPE Formation Evaluation* (June, 1994), *pp. 149-156.*

Øren, P. E., Billiotte, J. and Pinczewki, W. V.: "Mobilization of Waterflood Residual oil by Gas Injection for Water-Wet Conditions," *SPE Formation Evaluation* (March, 1992), pp.70-78.

Øren, P. E., Billiotte, J. and Pinczewski, W. V.: 'Pore-Scale Modeling of Waterflood Residual Oil Recovery by Immiscible Gas Flooding," SPE 27814. Paper was prepared for presentation at the SPE/DOE Ninth Symposium on Improved Oil Recovery held in Tulsa, Oklahoma, U.S.A., 17-20 April 1994.

Owete, O. S. and Brigham, W. E. (1987).: "Flow Behavior of Foam: A Porous Micromodel Study," *SPE Reservoir Engineering* (August, 1987) pp.315-323.

Paterson, L., Painter, S., Zhang, X., and Pinczewski, W. V.: "Simulating Residual Saturations and Relative Permeability in Heterogeneous Formations," *SPEJ* (September, 1998) pp. 211-218.

Paterson, L., Lee, J. and Pinczewski, W. V.: "Three-Phase Relative Permeability in Heterogeneous Formations," paper SPE 38882 presented at the 1997 Annual Technical Conference and Exhibition, San Antonio, October 5-8 1997.

Payatakes, A. C.: "Dynamics of Oil Ganglia during Immiscible Displacement in water-wet Porous media," *Ann. Rev. Fluid Mechanics* (1982).

Payatakes, A. C. and Dias, M. M.: "Immiscible Microdisplacement and Ganglion Dynamics in Porous Media," *Reviews in Chemical Engineering*, (1984) **2** No. 2, pp. 86-174.

Payatakes, A. C. and Valavanides, M. S.: True to mechanism macroscopic theory of steady state two phase flow in porous media. Presented at the XII International Conference on Computational Methods in Water Resources, Plenary Session, Crete, Greece, June 15-19 1998, Computational Mechanics Publications, ISBN 1853124877, pp. 3-10.

Pereira, C. G., Pinczewski, W. V. Chan, D. Y. C., Patterson, L. and Øren, P-E.: "Network Model for Drainage Dominated Three-phase Flow in Porous Media," *Transport in Porous Media* (1996), **24** p.167.

Pilotti, M.: "Generation of Realistic Porous Media by Grains Sedimentation," *Transport in Porous Media* (1998) **33**, pp. 257-278.

Press, W. H., Flannery, B. P., Teukolski, S. A. and Vetterling, W. T.: "Numerical Recipes," Cambridge University Press (1992).

Ramakrishnan, T. S. and Cappiello, A.: "A New Technique To Measure Static and Dynamic Properties of a Partially Saturated Porous Medium," *Chemical Engineering Science* (1991) **46**, No.4 pp. 1157-1163.

Ransohoff, T. C. and Radke, C. J.: "Laminar Flow of a Wetting Liquid along the Corners of a Predominantly Gas Occupied Noncircular Pore," *Journal of Colloid and Interfacial Science*, (February 1988), **121** no. 2, pp. 392-401.

Richardson, J. G., Kerver, J. K., Hafford, J. A. and Osoba, J. S.: "Laboratory Determination of Relative Permeability," *Petroleum Transactions, AIME*, **195**, pp. 187-196, (1952).

Roof, J. G. (1970).: "Snap-Off of Oil Droplets in Water-Wet Pores". *Trans AIME*, **249** (1970).

Rose, W.: "Measuring Transport Coefficients Necessary for the Description of Coupled Two Phase Flow of Immiscible Fluids in Porous Media," *Transport in Porous Media*, (1988). **3** no. 2, pp.163-172.

Rose, W.: "Data Interpretation Problems to be Expected in the Study of Coupled Fluid Flow in Porous Media," *Transport in Porous Media*, (1989). **4**, pp.185-198.

Røgen, B., Gommesen, L. and Fabricius, I.: "Grain size distribution of Chalk Image Analysis of Electron Micrographs," In Press, *Computers and Geoscience*.

Sahimi, M.: "Flow Phenomena in Rocks," *Review of Modern Physics* (1993) **65**, No. 4, pp. 1395-1534.

Sahimi, M.: "Nonlinear Transport Processes in Disordered Media," *AIChe Journal* (March, 1993) **39**, No. 3 pp. 369-386.

Sahni, A., Guzman, R. and Blunt, M.: "Theoretical Analysis of Three-Phase Flow Experiments in Porous Media," SPE 36664. Paper presented at the Annual Technical Conference and Exhibition, Denver, Colorado, October 6-9 1996.

Salathiel, R. A.: "Oil Recovery by Surface Film Drainage in Mixed-wettability Rocks," *JPT*, (1973) **25**, 1216-1224.

Saraf, D. N., Batycky, J. P., Jackson, C. H., and Fisher, D. B.: "An Experimental Investigation of Three-Phase Flow of Water-Oil-Gas Mixtures Through Water-Wet Sandstones," SPE 10761. Paper presented at the 1982 California Regional Meeting, San Francisco, March 24-25 (1982).

Schatzinger, R. A.: "Chalk Pore Systems: Qualitative and Quantitative Aspects of Pore Geometry," Paper presented at the 1985 second North Sea Chalk Symposium, Stavanger Norway.

Scheidegger, A. E.: "The Physics of Flow Through Porous Media,"3rd Ed., Univ. of Toronto Press, Toronto (1974).

Scholle, P. A.: " Chalk diagenesis and its relation to petroleum exploration: Oil from chalks a modern miracle?," *The American Association of Petroleum Geologists Bulletin* (1977) **62** No. 7 982-1009.

Scholle, P.A., Albrechtsen, T., Tirsgaard, H.: "Formation and Diagenesis of Bedding Cycles in 'uppermost Cretaceous Chalk of the Dan Field, Danish North Sea," *Sedimentology*. **45**, pp. 223-243.

Sissavat, S., Jing, X. D. and Zimmermann, R. W.: "Effect of Stress on the Hydraulic Conductivity of Rock Pores," *Phys. Chem. Earth* (A) (2000), **25,** No. 2, pp. 163-168.

Skauge, A, et al.: "Effects of Organic Acids and Bases and Oil Composition on Wettability," SPE 56673. Paper presented at 1999 Annual Technical Conference and Exhibition, Houston, Texas, October 3-6. 1999.

Soll, W. E., Celia, M. A., and Wilson, J. L.: "Micromodel Studies of Three-Fluid Porous Media Systems: Pore-Scale Processes Relating Capillary Pressure-Saturation Relationship," *Water Resources* September (1993), **29** No. 9 pp. 2963-2974.

Spinler, E. A. and Baldwin, B. A.: "Capillary Pressure Scanning Curves by Direct Measurement of Saturation," paper SCA 9705 Proceedings of the 1997 International Symposium of the Society of Core Analysis, Calgary, September 7-10 (1997).

Stauffer, D and Aharony, A.: "Introduction to Percolation Theory," Taylor and Francis (1994).

Suchomel, B. J., Chen, B. M. and Allen, M. B.: "Network Model of Flow, Transport and Biofilm Effects in Porous Media," *Transport in Porous Media* (1998) **30**, pp. 1-23.

Swanson, B. F.: "Microporosity in Reservoir Rocks – Its Measurement and Influence on Electrical Resistivity," paper presented at the twenty-sixth SPWLA Annual Logging Symposium, June 17-20, 1985

Szabo, M. T.: "New Methods for Measuring Imbibition Capillary Pressure and Electrical Resistivity Curves by Centrifuge," *SPE Journal* (1974) **14** pp. 243-252.

Tehrani, D. H., Danesh, A., Sohrabi, M., and Henderson, G.: "Enhanced Oil Recovery by Water Alternating Gas (WAG) Injection," paper presented at the 21st IEA Conference and Symposium, Edinburgh, UK, September 20-22, 2000.

Thomassen, J. B. and Jacobsen, N. L. (1994). "Dipping Fluid Contacts in the Kraka Field, Danish North Sea," SPE 28435. Paper presented at the 69th Annual Technical Conference and Exhibition, New Orleans September 25-28 (1994).

Thompson, L. F., Wilson, C. G. and Bowden, M. J.: Introduction to Microlithography, 2nd edition, American Chemical Society, Washington DC, 1994.

Timur, A.: "An investigation of Permeability, Porosity and Residual Water Saturation Relationship for Sandstone Reservoirs," *The Log Analyst* (July-August, 1968) **9**, No. 4 pp. 8.

Tixier, M.P.: "Evaluation of Permeability From Electric-Log Resistivity Gradients," *Oil and Gas Journal* (June, 1949) pp. 113-121.

Trangenstein, J. A.: "Multiphase flow in porous media – Lecture notes in engineering," Springer Verlag New York Inc. (1988).

Tsakiroglou, C. D. and Fleury, M.: "Pore Network Analysis of Resistivity Index from Water-Wet Porous Media," *Transport in Porous Media* (1999) 35 pp.89-128.

Tsakiroglou, C. D. and Fleury, M.: "Resistivity of fractional wettability porous media," *Petroleum Science and Engineering* (1999) 22 pp.253-278.

Tsakiroglou, C. D. and Payatakes, A. C.: "Mercury Intrusion and Retraction in Model Porous media". *Advances in Colloid and Interface Science* (2000) 23 pp. 773-789.

Tsakiroglou, C. D. and Payatakes, A. C.: "Characterization of the pore structure of reservoir rocks with the aid of serial sectioning, mercury porosimetry and network simulation," *Advances in Water Resources* (1998) 75 pp. 215-253.

Turian, R. M. and Kessler, F. D.: "Capillary Flow in a Noncircular Tube," *AIChe Journal* (April, 2000) **46**, No. 4 pp. 695-706.

Tzimas, G. C., Matsuura, T., Avraam, D. G., Van der Brugghen, W., Constantinides, G. N. and Payatakes, A. C.: "The Combined Effect of the Viscosity Ratio and the Wettability during Forced Imbibition through Nonplanar porous media," *Journal of Colloid and Interface Science* (1997) vol. **189**, pp. 27-36.

Valavanides, M. S., Constadinides, G. N., and Payatakes, A. C.: "Simulation of the Motion of Oil Ganglia in Consolidated Porous Media. Crowding Effects," paper presented at the 5th European Conference on the Mathematics of Oil Recovery, Leoben, Austria, September 1996.

Vejbæk, O. V. and Kristensen, L.: "Downflank hydrocarbon potential identified using seismic inversion and geostatistics: Upper Maastrichtian reservoir unit, Dan Field, Danish Central Graben," *Petroleum Geoscience* (2000) **6,** pp. 1-13.

Velev, O., Constantinides, G. N., Avraam, D. G., Payatakes, A. C. and Borwankar, R. P.: "Investigation of Thin Liquid Films of Small Diameters and High Capillary Pressures by a Miniaturized Cell," *Journal of Colloid and Interfacial Science* (1995) **175** pp. 68-76.

Vizika, O. and Lombard, J-M.: "Wettability and Spreading: Two Key Parameters in Oil Recovery With Three-Phase Gravity Drainage," *SPE Reservoir Engineering*, (February, 1996) pp. 54-60.

Wan, J., Tokunaga, T. K., Tsang, C-F and Bodvardson, G. S.: "Improved glass micromodel methods for studies of flow and transport in fractured reservoir," *Water Resources Research*, (1996) **32** No. 7 pp. 1955-1964.

Wardlaw, N. C.: "The Effects of Geometry, Wettability, viscosity and Interfacial Tension on Trapping in Single Pore-Throat Pairs," *J. of Can. Pet. Tech.* (1982), **21**, 21-27.

Wardlaw, N. and Coskuner, C.: "Petrographic Image Analysis for Prediction of Petrophysical Properties and Waterflood Displacement Efficiency: Some Missing Link," SCA paper 9720, Proceedings of the 1997 International Symposium of Core Analysis, Calgary, September 7-10 (1997).

Whitaker, S.: "Flow in Porous Media I: A Theoretical Derivation of Darcy's Law," *Transport in Porous Media* (1986). **1**, pp. 3-25.

Wilkinson, D: and Willemson, J. F.: "Invasion percolation: a new form of percolation theory," *Journal of Physics A*, (1983) **16** pp. 3365-3376.

Winter, A: "Antonows Rule 85 Years Later," *Heterogeneous Chemistry Reviews*, (1995) **2** pp. 269-308.

Winter, A., Larsen, J. K. and Krogsbøl, A.: "Evaluation of EOR Processes Using Network Models," Technical Report for EFP-94 Project J. no. 1313/94 – 0003. Geological Survey of Denmark and Greenland.

Witten, T. A. and Cates, M. E..: "Tenuous Structures from Disorderly Growth Processes," *Science* (June, 1986), **232** pp. 1607-1612.

Wong, H., Morris, S. and Radke, C. J.: "Three-Dimensional Menisci in Polygonal Capillaries," *Journal of Colloid and Interface Science* (1992) **148** No. 2, pp. 317-336.

Worthington, P. F., Pallatt, N., and Toussaint-Jackson, J. E.: " Influence of Microporosity on the Evaluation of Hydrocarbon Saturation," *SPE Formation Evaluation*(June, 1989) pp. 203-209.

Wyllie, M. R. J.: "The Fundamentals of Well Log Interpretation," Academic Press, New York (1963).

Wyllie, M. R. J. and Cardner, G. H. F.: "The Generalized Kozeny-Carman Equation'. Its Application to Problems in Multiphase Flow in Porous Media," *World Oil* (March, 1958), pp. 121-128.

Wyllie, M. R. J. and Rose, W. D.: "Some Theoretical Considerations related to the Quantitative Evaluation of the Physical Characteristics of Reservoir Rock from Electrical Log Data," *Journal of Petroleum Technology* (1950) **189**, pp. 105-118.

Yanuka, M.: "The Mixed Bond-Site Percolation Problem and Its Application to Capillary Phenomena in Porous Media," *Journal of Colloid and Interface Science* (1990) **134**, No. 1, pp. 198-205.

Yearbook of the Geological Survey of Denmark and Greenland (1999): Edited by Knud Binzer and Arne Dinesen, Geological Survey of Denmark and Greenland.

Yeomans, J. M.: "Statistical Mechanics of Phase Transition," *Clarendon Press, Oxford, (1992).*

Yortsos, Y. C. and Fukas, A. S.: "An analytical Solution for Linear Waterflood Including the Effects of Capillary Pressure," *SPE Journal*, (February, 1983), pp. 115-124.

Zhou, D.: "Interaction of Fluids and Pore Structure in Porous Media," Lecture notes on Multiphase Flow in Porous Media, Course PE 211. Department of Petroleum Engineering, Stanford University, California (1996).

Zhou, D., Fayers, F. J. and Orr, F. M.: "Scaling Multiphase Flow in Simple Heterogeneous Porous Media," SPE 27833. Paper was first presented at the ASME Winter Meeting, New Orleans, Nov. 28 - Dec. 3, 1993.

Zhou, D., Blunt, M. and Orr, F. M.: "Hydrocarbon Drainage along Corners of Noncircular Capillaries," *Journal of Colloid and interface Science* (1997) **187**, pp. 11-21.

Zhou, D. and Blunt, M.: "Effect of spreading coefficient on the distribution of light non-aqueous phase liquid in the subsurface," *Journal of Contaminant hydrology*, (1997) **25**, pp. 1-19.

Zhou, D., Arbabi, S. and Stenby, E.: "Effect of Wettability on the Electrical Properties of Reservoir Rocks," paper SCA 9624 presented at the 1996 International Symposium for Core Analysts, Montpellier, France, September 8-10, 1996.

Appendix A: Structural Properties of Network Models

A1. Network Model

This appendix describes a class of mathematical models underlying the network simulator implemented in course of this project. It is an extension of the overview given in Section 4.2.1.

The implemented network model consists of a regular cubic lattice containing lx nodes in the flow direction and ly and lz nodes in the two directions transversal to the flow direction (cf. Figure A1). The total number of nodes is $N = lx \cdot ly \cdot lz$. A node is connected to a neighboring node through a link, which represents a pore throat and two adjoining pore chambers. The distance between two adjacent nodes l_{node} and the coordination number Z are the same for all nodes. For two-dimensional lattices the coordination number Z is either 4 or 8. For three-dimensional lattices each node can have either $Z = 6, 8, 12, 14, 18, 20,$ or 26 neighbors.

The nodes located in the first or the last row of the lattice are connected to the forward or backward pointing node representing the inlet and outlet chamber, respectively. Periodic boundary conditions are imposed on the lattice faces transversal to the y- and z-direction reducing finite size effects during the simulations. A random number varying between 0 and 1 generated by the uniform distribution function gives the size of a chamber. Similarly, the size of the pore throat, r_t , is assumed to be described by a random number varying between 0 and 1.

A connection between two nodes consists of a node representing the first chamber, the link representing the pore throat, and another node representing the second chamber. The length of the pore chamber, l_c , is given by its pore size, r_c , while the length of the pore throat, l_t , is given by the distance between two neighboring nodes reduced by the size of two adjacent pore chambers belonging to the same connection. Thus, pore chambers must be smaller than half the node distance in order for the pore chambers not to overlap.

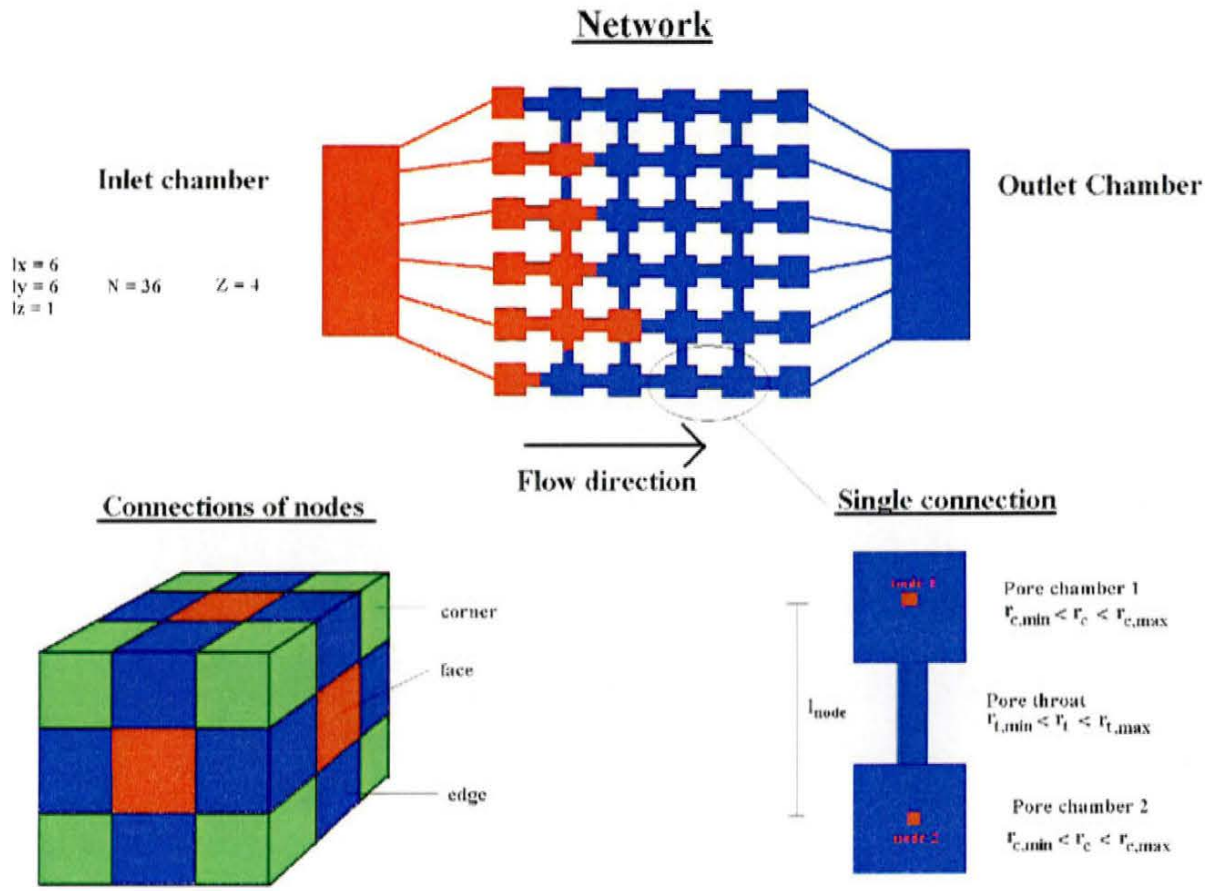

Figure A1. Structural properties of the network model. Each pore chamber is connected to other pore chambers by pore throats. Connections can be of three principal types: corner, edge or face of the cube. Thus, coordination numbers between 4 and 26 can be implemented in the network. The pore sizes are randomly chosen between a minimum and a maximum pore size, which are input parameters.

Both pore chambers and pore throats are assumed to have square cross-sections. The volume of a pore chamber V_c is given by

$$V_c = 8 \cdot r_c^3 , \tag{A-1}$$

while the volume of the pore throat V_t is given by

$$V_t = 4 \cdot l_t \cdot r_t^2 . \tag{A-2}$$

The porosity of the network is given by

$$\phi = \frac{\sum_{i=1}^{N} V_c + \sum_{j=1}^{N*Z/2} V_t}{lx * ly * lz * l_{node}^3} , \tag{A-3}$$

and the total cross-sectional area of the network sample is calculated by

$$A_{net} = lx \cdot ly \cdot l_{node}^2 . \tag{A-4}$$

A2. Conductance of Single Phase

Single-phase flow between two nodes is assumed to be laminar with negligible inertial forces. The conductance g of a single phase through a pore with a constant square cross-section and length, l_{pore}, is given by

$$g = \frac{\pi \cdot r_{effective}^4}{8 \cdot \mu \cdot l_{pore}}, \tag{A-5}$$

where μ is the viscosity of the flowing phase and the effective radius, $r_{effective}$, is given by

$$r_{effective} = \sqrt{\frac{A_{pore}}{\pi}}, \tag{A-6}$$

where A_{pore} is the cross-sectional area of the pore.

The total resistance to flow between two nodes i and j is given by the sum of the resistances associated with the pore throat, $1/g_{t,ij}$, and by the resistances of the two adjacent pore chambers, $1/g_{c,i}$ and $1/g_{c,j}$. The total conductance $g_{t,ij}$ between two nodes is therefore given by the following expression

$$\frac{1}{g_{total,ij}} = \frac{1}{g_{c,i}} + \frac{1}{g_{t,ij}} + \frac{1}{g_{c,j}}. \tag{A-7}$$

Thus, for pore chambers larger than the pore throats, the resistance to flow is primarily controlled by pore throats while pore chambers control the saturation. Consequently, the volumetric flow rate of a single phase q_{ij} between two nodes i and j is given by

$$q_{ij} = g_{total,ij}\left(P_i - P_j\right), \tag{A-8}$$

where P_i and P_j are the pressures of the flowing phase at the nodes i and j, respectively.

The flowing phase is assumed to be incompressible and the mass balance of a single node is given by

$$\sum_{j=1}^{Z} q_j = 0. \tag{A-9}$$

The total conductance of the pore network can be calculated by solving the system of equations describing the conservation of volume for all nodes. More precisely, this system of equations is obtained by substituting eq. (A-8) into eq. (A-9). More precisely, the volume balance for each node leads to N equations with N unknown pressures, which can be formulated in a matrix form as follows

$$\mathbf{G} \cdot \mathbf{P} = \mathbf{0} \tag{A-10}$$

where **G** is an $N \times N$ matrix containing the conductances between the adjacent nodes and **P** is a vector of length N that contains the pressure at the nodes.

Depending on the choice of boundary conditions, either the total flow rate through the network Q_{net} or the pressure drop across the network, ΔP_{net}, can be calculated. The absolute permeability, k_{net}, of the network is subsequently determined from Darcy's law

$$k_{net} = \frac{Q_{net} \cdot \mu \cdot lx \cdot l_{node}}{\Delta P_{net} \cdot A_{net}} . \qquad \text{(A-11)}$$

A3. Conductance of Two Immiscible Phases

Micromodel experiments conducted during this project involving GEUS 3 micromodel have shown that close to the outlet chamber oil was produced as droplets. This phenomenon is probably caused by the flow through the four triangular-like corner regions of capillary tubings. The break-up of the oil phase was also observed in experimental studies conducted by other research groups. In particular, Aker et al. (1998) observed the break-up of the oil phase during drainage in their micromodel studies. However, due to negligence of the corner flow, they were unable to give a plausible explanation of this phenomenon.

Movement of ganglia in two-phase flow requires high capillary numbers, which are rarely encountered in natural core experiments flooding schemes. Consequently, discontinuous oil transport has been excluded as an admissible mechanism in the network simulator developed in the course of this project. This leaves the following four basic phase configurations for the drainage displacement (cf. Figure A2):

- **Configuration 1:** The connection is entirely filled with water and there is only flow of water and no flow of oil between the two pore chambers.

- **Configuration 2:** Water is located in the corners and oil in the center of the pores with a square cross-section. The water and the oil phases are considered as flowing in compartments separated by the oil-water interface. There is no interaction between the phases.

- **Configurations 3a and 3b:** The oil phase displaces the water phase or, alternatively, the water phase displaces the oil phase depending on the direction of motion of the meniscus. Moreover, the water phase can escape around the meniscus along the corners similarly to configuration 2. Thus, the water can enter the water filled pore either because it is displaced by the head meniscus or because it flows from the opposite pore chamber along the corner and into the water filled pore throat and chamber.

- **Configuration 4:** The presence of two menisci in the connection is treated as a superposition of the configurations 3a and 3b. The motion of the menisci is therefore independent of each other which is in accordance with the observations of the from the micromodel experiments where two menisci were also seen to enter the same connection and subsequently coalesce.

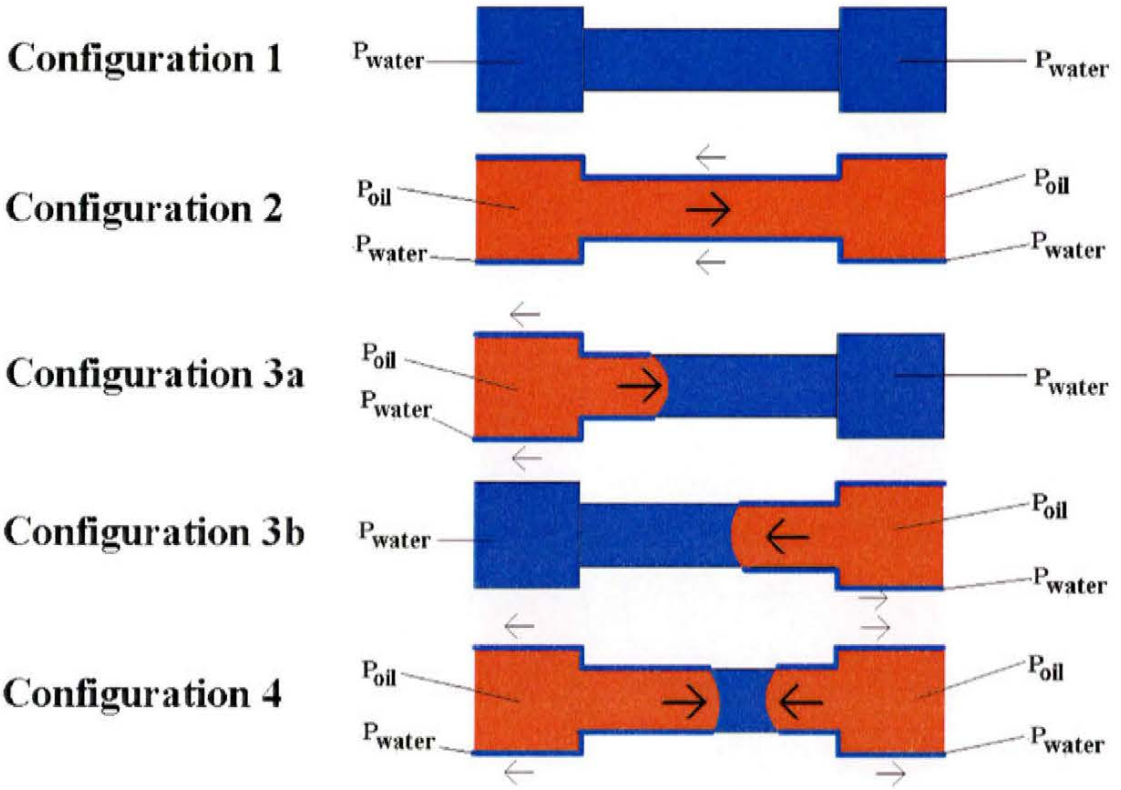

Figure A2. Four principal fluid configurations between two nodes. Water is always connected and the water pressure is defined for all nodes. The water and the oil phases flow in two separate compartments in the configuration 2. Configurations 3a and 3b are symmetric and essentially can be considered as representing the same transport mechanism. In (3a) oil displaces water, in (3b) the roles of oil and water are reversed. In configuration 4 oil displaces water by two opposite menisci. Thick arrows indicate flow of oil while thin arrows indicate flow of water along the corners of the capillary tube.

A.3.1 Conductance of Water Phase

In the case of configuration 1 the conductance of the aqueous phase, g_{ww} , is calculated in the same manner as in the single-phase case (eq. (A-5)).

In the case of configuration 2,water may be present in the corners of the pore. Ransohoff and Radke (1988) performed finite element calculations of the resistance to flow for the wetting phase in the corner of an angular tube. They calculated the so-called resistance factor β for different sets of half angle of the corner α, contact angles θ_{ow}, roundness of corner r_d, and boundary conditions described by the factors f_1 and $f_{2\,\text{defined}}$ below. Thus, the conductance of the water phase present in the corners is given by

$$g_{ww} = \frac{A_w \cdot r_{ow}^2}{\beta \cdot \mu_w \cdot l_{pore}}, \qquad \text{(A-12)}$$

where A_w is the flow area of the water phase and μ_w is viscosity of the water phase.

Zhou (1996) approximated the dimensionless resistance factor by an analytical expression given by

$$\beta = \frac{12 \cdot \sin(\alpha) \cdot (1-\psi_4)^2 \cdot (\psi_1 - \psi_4 \cdot \psi_2) \cdot (\psi_3 + f_2 \cdot \psi_4 \cdot \psi_2 - r_d \cdot (1 - f_1 \cdot \psi_4))^2}{(1-\sin(\alpha))^2 \cdot \psi_4^2 \cdot (\psi_1 - \psi_4 \cdot \psi_2 - (1-\psi_4) \cdot r_d^2)^3}, \quad \text{(A-13)}$$

where

$$\psi_1 = \cos^2(\alpha + \theta_{ow}) + \cos(\alpha + \theta_{ow}) \cdot \sin(\alpha + \theta_{ow}) \cdot \tan(\alpha), \quad \text{(A-14)}$$

$$\psi_2 = 1 - \frac{\theta_{ow}}{\frac{\pi}{2} - \alpha}, \quad \text{(A-15)}$$

$$\psi_3 = \frac{\cos(\alpha + \theta_{ow})}{\cos(\alpha)}, \quad \text{(A-16)}$$

$$\psi_4 = \left(\frac{\pi}{2} - \alpha\right) \cdot \tan(\alpha). \quad \text{(A-17)}$$

The degree of roundness of the corner is described by r_d as a number between 0 (sharp corner) and 1 (round corner). In this work the cross-sections are assumed to be perfectly square and the roundness r_d = 0. The factor f_1 describes the boundary condition of the flow at the wetting phase and the porewall and f_2 describes the boundary condition at the oil-water interface. A no slip condition corresponds to an f-value = 1 while a no stress value corresponds to an f-value = 0. For the water porewall boundary conditions a no slip condition seems reasonable considering that roughness of the porewall might restrict the movement of the water molecules close to the porewall. On the oil-water interface a no slip condition is more appropriate because the molecules are less restricted in their motion.
In the case of configurations 3 and 4, the resistance to flow of the water phase is calculated as a linear combination of inverse expressions of eq. (A-5) and eq. (A-12). The weight of the two contributions is determined by the fraction of pores occupied by oil, $x_{meniscus}/l_{pore}$, where $x_{meniscus}$ is the distance between the beginning of the chamber or throat and the position of the head meniscus.

The principal radius of curvature of the oil water interface, r_{ow}, used to calculate the conductance of the water phase in eq. (A-12), is determined by the local phase pressures. The curvature of the arc meniscus is determined by the local phase pressure.

A.3.2 Conductance of Oil Phase

The conductance of the oil phase between two oil nodes, g_{oo}, in configuration 2 is calculated by eq. (A-5) using the viscosity of oil μ_o instead of the viscosity of the water phase and an effective radius calculated by

$$r_{effective} = 0.5 \cdot \left(\sqrt{\frac{A_o}{\pi}} + r_t\right), \quad \text{(A-18)}$$

where A_o is the cross-sectional area of the oil phase.

A.3.3 Oil Displacing Water

The configurations 3 and 4 are fundamentally different from the configurations 1 and 2. This is due to one or two head menisci present between two nodes. In the configurations 1 and 2, the driving force of oil or water is the pressure difference between either the oil phase or the water phase pressure in the two nodes. In other words, the flow of oil and water is not influenced by the presence of the head meniscus.

In the case of configurations 3 and 4 the presence of the head meniscus makes the problem more difficult to resolve. The motion of the meniscus is determined by the oil phase pressure at the node from which the meniscus has advanced into the pore and by the water phase pressure of the opposite node. Consequently, a conductance must be assigned to the connection between the oil phase pressure and the water phase pressure of the two connected nodes. The resistance to flow between oil filled and water filled node (configuration 3) is calculated as the resistance to flow of the oil phase given by eq. (A-5) and eq. (A-18). This resistance is weighted by the fraction of the pore filled with oil plus the resistance to flow of the water phase given by eq. (A-5) weighted by the fraction of the pore filled with water. The conductance of a connection with the configuration 3 is thus given by

$$\frac{1}{g_{ow}} = \frac{x_{meniscus}}{l_{pore}} \cdot \frac{8 \cdot \mu_o \cdot l_{pore}}{\pi \cdot r_{effective}^4} + \left(1 - \frac{x_{meniscus}}{l_{pore}}\right) \cdot \frac{8 \cdot \mu_w \cdot l_{pore}}{\pi \cdot r_{effective}^4} \qquad \text{(A-19)}$$

The calculation of the effective radii of the water and the oil phases are based on the areas of the water and oil phases respectively. For symmetric reasons the conductance of configuration 3b is the same as for the configuration 3a,

$$g_{wo} = g_{ow}. \qquad \text{(A-20)}$$

Configuration /Conductance	g_{ww}	g_{oo}	g_{ow}	g_{wo}
1	A-11	-	-	-
2	A-12	A-11, A-19	-	-
3a	A-11, A-12	-	A-11, A-19, A-5	-
3b	A-11, A-12	-	-	A-11, A-19, A-5
4	A-11, A-12	-	A-11, A-19, A-5, A-12	A-11, A-19, A-5, A-12

Table A1. Summary of conductance calculation. The conductances are calculated by the equations shown based on the four cases.

It should be noted that conductance of the aqueous phase is calculated twice. Both as the water displaces water and as the oil displaces water. Thus, the network simulator most likely overestimates the conductance of the water phase. However, once the meniscus is inside the connection, the water-water conductance, g_{ww} , is considerably smaller than the conductance where the oil phase displaces the water g_{ow}. The advantage of using this description of the motion of menisci is that for configuration 4 the oil phase can displace the water phase from two opposite nodes having a connection filled with oil phase from either side. Thus, the menisci can advance into a connection independently of each other being controlled by the phase pressures. The conductances of the configuration 4 are calculated as in the case of the configuration 3 by taking into account

different positions of the two menisci. In contrast to the case 3, the two conductances are generally not the same. An overview of the conductance calculation is shown in Table A1.

The calculation of the conductances can be regarded as separate tubes connecting the water phase pressure of two nodes and the oil phase pressures of the two nodes (cf. Figure A3).

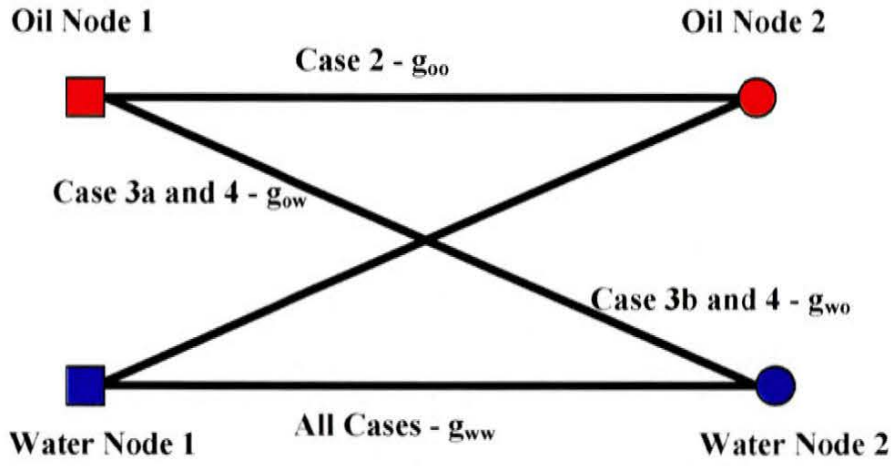

Figure A3. Schematic drawing of the connection of the two phases between two nodes.

In principle, the water and oil nodes could also be connected within the same node. This corresponds to motion of the oil-water interface associated with storage of fluid in a pore. However, the movement of the interfaces within a pore is difficult to quantify but is probably controlled by the ability of the water to escape along the corners of the pore. The movement of interfaces within a node is due to the change of water and oil phase pressure in this model is neglected and only the conductances of the phases are changed with change in phase pressures.

A.3.4 Conservation of Mass for Two Phases

In the case of two-phase flow there are two mass balances, one for the water phase and one for the oil phase. Similarly to the single-phase flow, the two phases are assumed incompressible and the mass balance of each phase is equivalent to the volume balance. If a node point is occupied by oil the flow of oil into the node must equal the flow of oil out of the node and the volume balance is equivalent to the volume balance for a single phase (cf. eq. (A-10)). If a node point has not been invaded by oil there is no flow of oil into or out of the node and the mass balance is automatically fulfilled.

Water is present in all nodes because it acts as the wetting phase. The flow of water is due to water entering a node from a neighboring node because the water pressure is higher in the neighboring node. Alternatively, water can enter the node because a meniscus is entering the connection from neighboring oil filled node. The volume balance of the water assumes the following form

$$\sum_{j=1}^{Z} q_{ij,ww} + q_{ij,ow} = 0\,, \qquad \text{(A-21)}$$

where $q_{ij,ww}$ is the flowing rate of water entering the node from another water node and $q_{ij,ow}$ is its counterpart pertaining water entering the node by meniscus displacement.

Similarly, the oil phase can enter a node from a neighboring node either because of a gradient in the oil phase, or because a meniscus is retracting. Consequently, the volume balance for the oil phase is given by

$$\sum_{j=1}^{Z} q_{ij,oo} + q_{ij,wo} = 0 , \qquad \text{(A-22)}$$

where $q_{ij,oo}$ is flowing rate of the oil entering the node from another oil node and $q_{ij,wo}$ pertains to oil entering the node by meniscus displacement.

In a matrix formulation the conservation of mass can be written as

$$\mathbf{G} \cdot \mathbf{P} = \mathbf{0} , \qquad \text{(A-23)}$$

where **G** is $2N \times 2N$ matrix containing all the conductance elements of the network. **P** is a $1 \times 2N$ matrix containing the phase pressures of the nodes. The phase pressures at the nodes are represented by the pairs of oil and water phase pressures. Using both phase pressures leads to a matrix containing 4 times as many elements as compared to the formulation of Aker et al. (1998). Consequently, considerable more computational effort is needed to determine the pressure field for a network of the same size.

A.3.5 Capillary Pressure and Curvature of Fluid Interfaces

The description of the flow has so far been based solely on the conductance of the two phases between nodes. However, the presence of a head meniscus between two nodes as in configuration 3 or 4 is associated with a pressure jump across the interface. The pressure jump depends on the size of the pore in which the meniscus is located. The entry pressures of pore chambers and throats are calculated prior to invasion of the network.

One of the major differences between the existing network models is the treatment of the variation of the capillary pressure with the position of a meniscus while it enters a connection. Lenormand et al. (1988), van der Marck (1997), Blunt and King (1991), Pereira et al. (1996) and Koplik and Lasseter (1985) do not allow non-zero conductances of the phases in a connection where the pressure field in the preceding time step was less than the entry pressure of the connection.

Mogensen et al. (1999) recognized that the pressure solution depends on whether the connection is open to flow. He argued that closing a connection could result in a pressure field where that connection would be open. Mogensen et al. (1999) argued that since a finite number of possible combinations of open and blocked connections exist and the system is realizable, there exists a combination of open and blocked connections where the new solution of the pressure does not change the combination of open and blocked connections.

Aker et al. (1998) studied a drainage case where the pressure jump across a meniscus was allowed to change with the position of the meniscus. They assumed that the cross-sectional area of

connecting tubes was hourglass shaped. Consequently, the capillary pressure jump across a meniscus also varies smoothly with the position of the meniscus although the cross-sectional area is assumed constant. The capillary change zone is placed in the connection where the capillary entry pressure varies linearly between the pore chamber value and the pore throat value (cf. Figure A4). More precisely, it is situated symmetrically around the two chamber-throat boundaries of a connection. The length of the capillary change zone l_{zone} is given as a fraction of the distance between the nodes and can be changed as an input parameter. For positions of the meniscus inside the chamber, but outside the capillary change zone, the capillary pressure jump across a meniscus is equal to the entry pressure of the pore chamber. For positions of the meniscus inside the pore throat, but outside the capillary change zone, the entry pressure of the pore throat is used.

The rationale behind the gradual change of the capillary pressure is that in reality the capillary pressure is well defined for any position of the meniscus inside the connection between two nodes. The curvature of the fluid interfaces will adjust according to the local phase pressures even though the meniscus does not enter the throat. Micromodel experiments show that the curvature of the interface changes as a meniscus is about to enter a pore throat. Also, the change in position of the meniscus is accompanied by water flow in the connecting pore. Thus, instead of letting the local phase pressure change by blocking the connection, the meniscus is allowed to adjust its position inside the pore according to the pressure field.

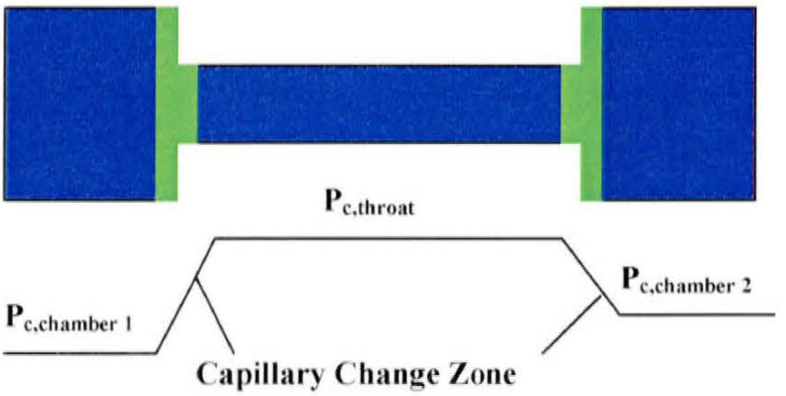

Figure A4. Change of capillary pressure with the position of the meniscus. The capillary pressure varies linearly between the value of the pore throat and the pore chamber.

The effect of including the capillary pressure jump across a meniscus term is that flow between two node points (cf. eq. (A-9)) must be rewritten to include the pressure jump across the fluid interfaces if a head meniscus is present in a connection.

$$q_{ij} = g_{total,ij,ow} \cdot \left(P_{i,o} - P_{j,w} - P_{c,ij}\right). \qquad \text{(A-24)}$$

In order to preserve the matrix representation of the problem the capillary pressure jump times the conductance term is moved to the right hand side (**RHS**) of the matrix equation which transforms eq. (A-24) to the following form

$$\mathbf{G} \cdot \mathbf{P} = \mathbf{RHS}, \qquad \text{(A-25)}$$

where **RHS** is a $2N$ vector containing all the capillary terms of the connections where menisci are present.

A.3.6 Boundary Conditions

A set of boundary conditions concerning the faces of the network is specified. In particular, periodic boundary conditions are imposed on the network faces transversal to the y- and z-direction. For the remaining two network faces it is necessary to specify one boundary condition for each face. For the inlet face, either a constant injection rate or a constant injection pressure of the oil phase can be specified. For the outlet face, a constant outlet pressure is always specified for the water phase. The constant pressure boundary condition is introduced by adding a conductance to the diagonal element of the conductance matrix and adding the same value multiplied by the desired pressure to the right hand side. This is done for both the inlet and the outlet side.

The constant injection rate is usually adopted in core experiments because it is easier to control a constant injection rate and measure the pressure drop across the core than control a constant injection pressure and measure the injection rate. A constant injection rate boundary condition can be invoked in the model by introduction of a pseudo inlet chamber that works as a source of the oil phase.

Appendix B: Pilot Study of Three-Phase Saturation Determination

B1. NMR Pilot Study of Three-phase System

This appendix describes a pilot study undertaken to investigate the feasibility of quantitative saturation determination by Nuclear Magnetic Resonance (NMR) techniques in a three-phase system that could serve as a model for investigating WAG processes. The intention of the study is to decide whether it technically is practicable to make spatially resolved quantitative determinations of the fluid saturations of a three-phase system within a chalk sample mounted in a core holder. It is not the intention of the study to make WAG experiments or to discuss the relevance of the fluid system in question.

Grader & O'Meara (1988) presented experimental work using the fluid system water – decane – benzyl alcohol. This fluid system consists of three immiscible phases, with a mutual solubility of approximately 5 p.u. between the water component and the benzyl alcohol component. The mutual solubility of decane with both the water component and the benzyl alcohol component is very low. Grader & O'Meara (1988), working with three-phase relative permeability, used the system as a model of the system water – oil – gas, with the benzyl alcohol phase being a model of the oil phase and the decane phase being a model of the gas phase. They used glass bead samples and bulk fluid saturations determined by separator data for their work.

The present pilot study uses the water–decane–benzyl alcohol fluid system of Grader & O'Meara (1988) in connection with chalk samples and spatially resolved fluid saturation determinations by NMR, with the aim of providing a relevant model for future experimental WAG studies on chalk samples. A method for providing spatially resolved fluid saturation data is necessitated by the strong capillary forces in chalk, as opposed to the glass bead samples of Grader & O'Meara (1988). The primary aim of the study is to evaluate the potential of the Chemical Shift Imaging (CSI) principle of NMR to provide such fluid saturation data. This principle has been used for some time at GEUS to obtain fluid saturation data in connection with core flooding experiments (Olsen et al, 1994, Bech et al., 2000), but only for two-phase system. The challenge of the pilot study is to extend the existing techniques to a three-phase fluid system.

B2. Experimental Technique

B.2.1 Core Flooding Technique

A cylindrical plug sample of Maastrichtian chalk from the oil zone of the Tyra gas field was selected for the study. Table B1 reports some petrophysical parameters of the sample, which is named T3A. It is fairly homogeneous, but contains some hairlines. The sample is considered typical for the reservoir.

Table B2 reports some parameters of the fluid system water – n-decane – benzyl alcohol. Distilled water was used for the water phase.

Only one experimental cycle of sample preparation and following NMR measurement was conducted. The sample preparation procedure aimed at creating a sample containing significant

Table B1. Petrophysical parameters of sample T3A.	
Length	= 68.3 mm
Diameter	= 37.5 mm
Bulk volume	= 75.9 ml
Pore volume	= 34.9 ml
Porosity	= 0.460
k	= 5.0 mD

Table B2. Fluid properties @ 20 °C.		
Fluid	Viscosity (cp)	Density (g/ml)
Water	1.04	0.998
n-decane	0.92	0.730
Benzyl alcohol	4.98	1.045

concentrations of all three phases at one end, and the phases water and n-decane only at the other end. In this way a well-known experimental condition would exist at one end of the sample, which could be compared to the new three-phase condition at the other end. The desired condition was created by the following procedure:

1. Sample T3A was cleaned by Soxhlet cleaning with methanol followed by Soxhlet cleaning with toluene.
2. The sample was saturated to S_w = 100 p.u. (percent units) by imbibition in vacuum, followed by flooding with water at 5 ml/h with a back pressure of 4 bar.
3. A flooding with n-decane at 16 ml/h was conducted resulting in a bulk S_w = 29.7 p.u. and a bulk S_o = 70.3 p.u. At this time the fluid distribution within the sample probably was dominated by a strong end effect (Bech et al., 2000).
4. To reduce the end effect a flooding with water at 16 ml/h was conducted resulting in a bulk S_w = 80.7 p.u. and a bulk S_o = 19.3 p.u. An NMR measurement confirmed that the fluid distribution within the sample now was fairly homogeneous.
5. A three-phase fluid distribution was created by injecting benzyl alcohol at 16 ml/h into the sample. The injection was stopped before breakthrough, leaving two-phase water – n-decane region in the outlet end of the sample.

Degassed fluids were used for all preparations. Between preparation step 5 and the NMR final measurements, a 21-hour time lapse allowed the fluid distribution within the sample to equilibrate. From preparation step 2 to the end of the NMR measurements, the sample resided in a non-magnetic Hassler-type core holder, with a confining pressure of 18 bar. Due to the fragile nature of the sample, the displacement pressure was kept low during the whole experiment. The maximum differential pressure across the sample was 5.5 bar.

B.2.2 NMR Experimental Technique

A 4.7 T SISCO experimental NMR scanner was used for the NMR work. It was equipped with a 154 mm diameter insert gradient set, capable of producing magnetic gradient up to 140 mT/m along any of three orthogonal directions, with a rise rate of $5.4*10^5$ mT/m*s. The gradient set provides active shielding and eddy current compensation. A Radio Frequency (RF) coil of slotted tube resonator design with good signal homogeneity until a maximum length of 9 cm was used.

The fluid distribution in the sample was determined by a chemical shift (CSI) technique that allows resolution of NMR signals at specific chemical shift values in two spatial dimensions (2D). The pulse sequence is a spin-echo type sequence, which uses a gauss-shaped RF pulse to selectively excite the desired signal. This method requires that the water and oil resonances are well-separated (Horsfield et al., 1990), which was the case for the present work. The water and n-decane resonances were 700 Hz apart, and the benzyl alcohol and water resonances were 400 Hz apart.

Linewidth was 119, 74 and 167 Hz (FWHM), respectively for the benzyl alcohol, water and n-decane resonances. A selective gauss-shaped pulse of 8.19 ms with a nominal selectivity of 490 Hz allowed separate excitation of the three main signals. However, benzyl alcohol in addition to the main resonance has minor resonances close to the water resonance. An interference correction procedure calibrated on a water – n-decane – benzyl alcohol phantom corrected the main part of the interference. A gauss-shaped pulse was used for slice selection resulting in a slice thickness of 4 mm.

B.2.3 NMR Calculations.

The experimental NMR data were processed according to the following procedure to produce quantitative saturation data.

B.2.3.1 Interference Correction.

The interference between benzyl alcohol and water was quantified by NMR measurements on a phantom containing benzyl alcohol, water and n-decane. The measurements were conducted with the same pulse sequence as the measurements on sample T3A. As a result of the measurements the water signal of every voxel of sample T3A were corrected by 40 % of the benzyl alcohol signal of the same voxel. The validity of the correction is indicated by the condition that a strong signal in the inlet end fitting of the raw water sensitive image is nearly removed, in accordance with the condition that the occurrence of large amount of water in the inlet fitting is unlikely. The interference correction is estimated to remove most of the interference from benzyl alcohol on water, but inevitably increases the noise in the water sensitive image. The measurements on the benzyl alcohol - water - n-decane phantom confirmed that no other interferences exist between the three fluid phases.

B.2.3.2 Relaxation Correction.

Single-exponential modelling is known to provide good relaxation correction in chalk samples (Bech et al., 2000), and the present work therefore corrects measured magnetisation's according to the model

$$M(t) = M(t=0)\exp(-t/T_2) + E \quad \text{(B-1)}$$

where E is the signal level (noise) at $t=\infty$. The CSI pulse sequence used in the present work has a large $t_{e,min}$, 10.45 ms, which results in long extrapolations from $M(t=t_{e,min})$ to $M(t=0)$. The apparent spin-spin time constant T_2^* for the three fluid phases varies from 3.5 to 12.6 ms, with the lowest values relating to water and the highest values relating to n-decane. The ratio $M(t=t_{e,min})/M(t=0)$ varies between 0.05 and 0.44. These long extrapolations for the models with low $M(t=t_{e,min})/M(t=0)$ ratio are the main cause of the poor signal/noise ratios in some parts of the saturation models (Figures B1, B2 and B3). The signal/noise ratio is particularly bad in the water-dominated images close to the inlet end of the sample, where the water content is low.

B.2.3.3 Proton Density Correction

The calculated voxel $M(t=0)$ magnetisation's were transformed to voxel relative fluid volumes by applying a proton density correction. The proton densities were calculated from the chemical formula of the fluids.

B.2.3.4 Fluid Saturation Calculation

Voxel fluid saturations were calculated form the voxel relative fluid volumes assuming that

$$S_{water} + S_{n-decane} + S_{benzyl\ alcohol} = 1 \quad \text{(B-2)}$$

This assumption is justified by the consistent use of degassed fluids, and the initial water flooding with a backpressure of 4 bar.

B3. Results

Maps of S_{water}, $S_{n-decane}$ and $S_{benzyl\ alcohol}$ are presented in Figures B1, B2 and B3, respectively. Each map shows the distribution of a particular fluid phase in an axial slice of thickness 4 mm throughout the sample. The grey scale and sample position in the three maps are identical, allowing direct comparison.

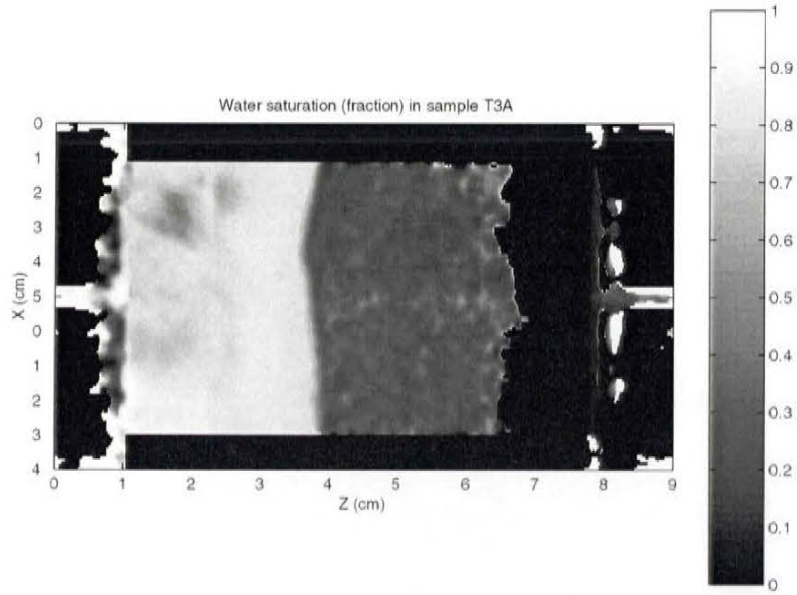

Figure B1. Distribution of the water phase in sample T3A. The inlet end is towards right.

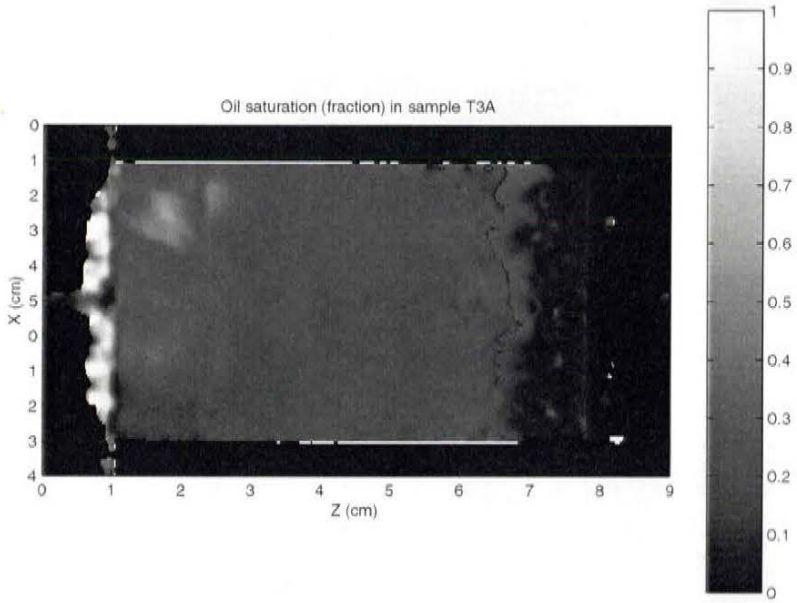

Figure B2. Distribution of the n-decane phase in sample T3A. Same sample position as in Fig. B1.

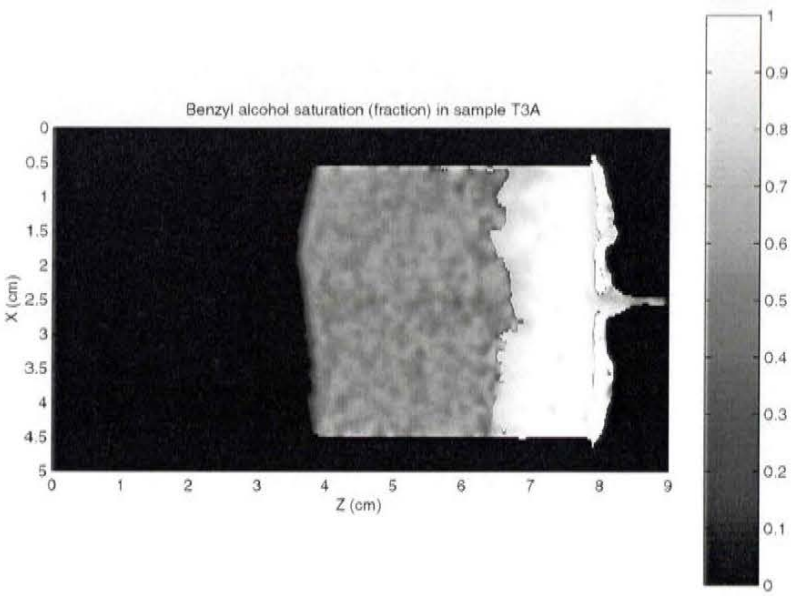

Figure B3. Distribution of the benzyl alcohol phase in sample T3A. Same sample position as in Fig. B1.

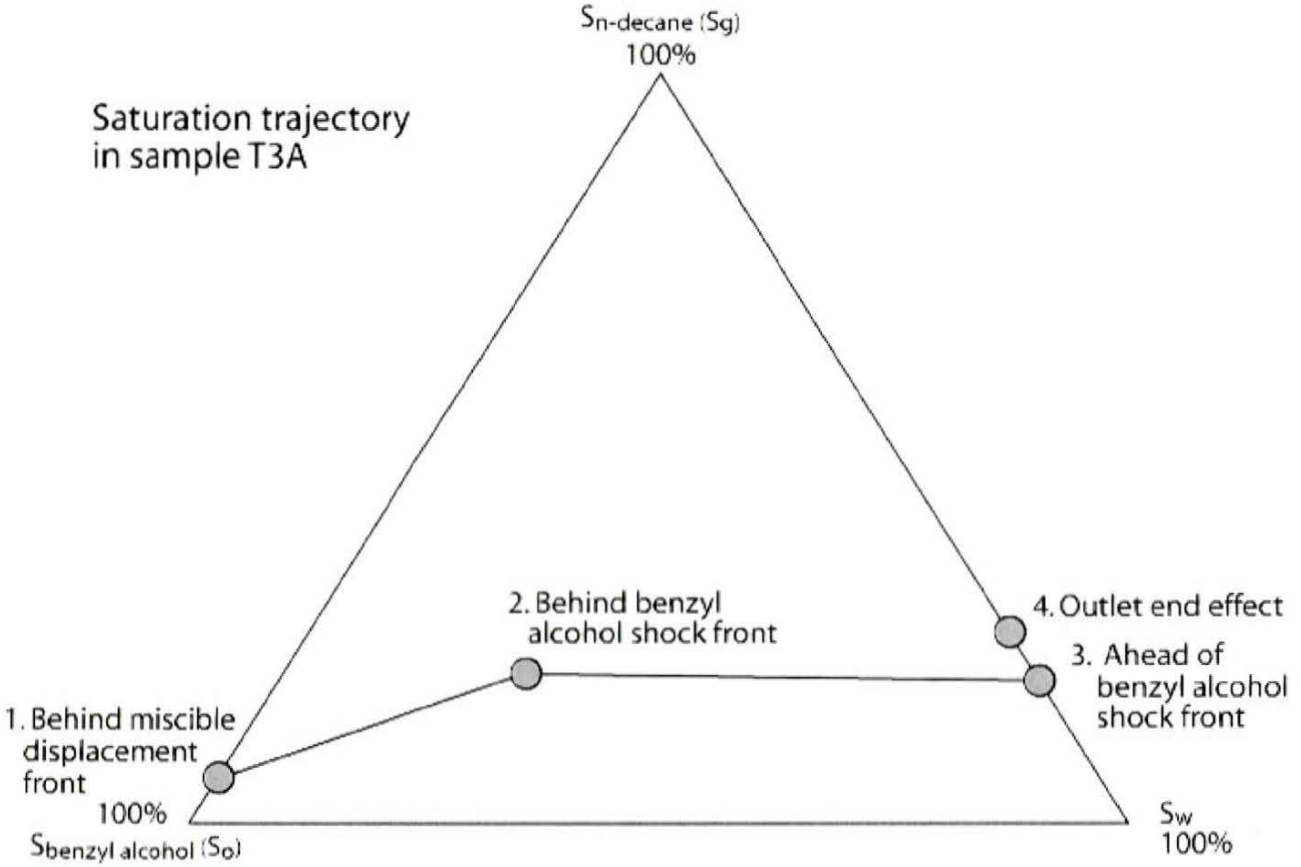

Figure B4. Position of characteristic regions within sample T3A in the ternary fluid diagram water – n-decane – benzyl alcohol.

The inlet end fitting is seen at the right end of the sample, and the outlet end fitting at the left end. The distribution of fluids is characterized by four regions. Region no. 1 occupies approximately 1 cm along the length of the sample adjacent to the inlet end fitting. It is characterized by a high saturation of benzyl alcohol, 94.0 ± 3.8 p.u., a low saturation of n-decane, 6.0 ± 3.8 p.u., and a saturation of water below the detection limit which is approximately 5 p.u. for water. The variation in fluid saturation within the regions is quantified by the standard deviation of the mean of the pixel fluid saturations. Going through the sample towards the outlet end, Region no. 2 occupies a length segment that measures approximately 2.5 cm measured along the length of the sample. It is separated from Region no. 1 by a sharp, irregular boundary with a significant change in the saturation of all three fluids. The saturation of benzyl alcohol drops to 55.0 ± 3.8 p.u., the saturation of n-decane increases to 19.7 ± 1.4 p.u., and the saturation of water increases above the detection limit to 25.3 ± 4.7 p.u.. Further along the sample axis, Region no. 3 occupies a length segment of approximately 1.0 cm. It is separated from Region no. 2 by a very sharp, gently curved boundary with a pronounced change in the saturation of water and benzyl alcohol, while the saturation of n-decane remains nearly unchanged. The saturation of benzyl alcohol drops below the detection limit, which is estimated to be at approximately 3 p.u., the saturation of n-decane decreases to 18.7 ± 1.3 p.u., and the saturation of water increases to 81.2 ± 1.8 p.u. Further along the sample axis, adjacent to the outlet end fitting, Region no. 4 occupies a length segment of approximately 1.5 cm. It is grades from Region no. 3 without any sharp boundary by an increase in the saturation of n-decane and a matching decrease in the saturation of water, and an increased variation in the saturation of both phases. The saturation of benzyl alcohol remains below the detection limit (undoubtedly it is zero), the saturation of n-decane increases to 22.3 ± 6.9 p.u., and the saturation of

Table B3. Bulk fluid determinations of sample T3A.		
	Separator data (p.u.)	NMR data (p.u.)
S_{water}	44.2	41.4
$S_{n\text{-}decane}$	19.1	18.7
$S_{benzyl\ alcohol}$	36.7	39.9

water decreases to 77.3 ± 6.9 p.u. Small regions within Region no. 4 have saturations of n-decane above 50 p.u. Figure B4 gives the positions on the four main regions in the ternary diagram water – n-decane – benzyl alcohol. The symbols S_g and S_o in parentheses denote the phases for which respectively $S_{n\text{-}decane}$ and $S_{benzyl\ alcohol}$ act as models in the work of Grader et al. (1988).

Region no. 1 is interpreted to represent a sample volume where flow of benzyl alcohol has depleted the content of water by dissolution. Pure benzyl alcohol may dissolve approximately 5 p.u. of water, and the flow of pure benzyl alcohol close to the inlet have carried most or all of the water that remained behind the benzyl alcohol shock front further downstream. A peculiar condition is that the saturation of n-decane is also depleted in Region no. 4. Benzyl alcohol and n-decane are reported to have very little mutual solubility and, therefore, benzyl alcohol should not be able to deplete the n-decane by dissolution. A possible explanation is that the depletion of the water phase enabled the residual n-decane droplets that remained after the passage of the benzyl alcohol shock front to pass downstream through the pore throats. Region no. 1 thus is interpreted to be the result of the benzyl alcohol phase not being in equilibrium with the other two fluid phases. In future experiments with this fluid system the benzyl alcohol phase should be equilibrated with the other two phases before entering the sample.

Region no. 2 is interpreted to represent the normal condition behind the benzyl alcohol shock front, with the three fluid phases being in equilibrium. It is noteworthy that saturation gradients are virtually absent within this region. The benzyl alcohol shock front between Region no. 2 and Region no. 3 is remarkably sharp with no sign of fingering. Indeed the shock front is even sharper than apparent from Figure B1 and B3, because these are based on filtered data sets. From the raw data, it is seen that the whole saturation change takes place in less than 0.5 mm.

Region no. 3 is interpreted to represent the normal condition ahead of the benzyl alcohol shock front. In this region too, saturation gradients are virtually absent. Compared to Region no. 3., Region no. 4 is characterized by a larger mean saturation of n-decane, and a much more heterogeneous fluid distribution. The raw NMR data clearly shows that the heterogeneous fluid distribution is connected with sample heterogeneities. It is suggested that the increased content of n-decane represents the capillary end effect.

The reproducibility of pixel fluid saturations may be estimated from the standard error of the mean in regions assumed to be homogeneous. In this way the reproducibility of the pixel fluid saturation at the 1σ level is estimated to be 2-5 p.u. for water depending on the amount of interference from benzyl alcohol. The appearance of regions of low water saturations is the main problem because the relaxation modelling becomes very imprecise. The reproducibility of pixel fluid saturations is estimated to be 1.5 p.u for n-decane, and approximately 3 p.u for benzyl alcohol.

The accuracy of pixel fluid saturations cannot be directly determined. However, the mean NMR fluid saturations of the whole sample region agree well with the bulk saturations of the sample determined from separator data, cf. Table B3. The deviation between the two methods varies between 0.4 p.u. and 3.2 p.u. This deviation includes any error caused by comparing the fluid saturation of a 4 mm slice with the fluid saturation of the whole sample. An estimate of the pixel

accuracy may be given as the bulk accuracy plus the pixel reproducibility, i.e. accuracy between 2 p.u. and 7 p.u. at the 1 σ level.

B4. Test of 1D CSI method

A preliminary test of the 1D CSI method of Olsen et al. (1994) was made. The acquired data have not been processed, but a raw data set is presented in Figure B5. The water, n-decane and benzyl alcohol signals are well resolved, and the sample and fluid system is considered well suited for 1D flooding experiments similar to the work of Bech et al. (2000).

Relative to the 2D CSI method the 1D CSI method has the following advantages and disadvantages:

1. The 1D method acquires signal from the whole sample volume.
2. Much shorter echo times may be used resulting in significantly better accuracy and precision.
3. Acquisition time for the 1D method is approximately one third for comparable measurements, while the data processing time is approximately one half.
4. Information for one spatial dimension is lost for the 1D method.

In case of flooding experiments, the 1D method will often be advantageous, because such experiments are essentially 1D experiments. The existence of transverse fluid movements and longitudinal fingering may be checked by a 2D method.

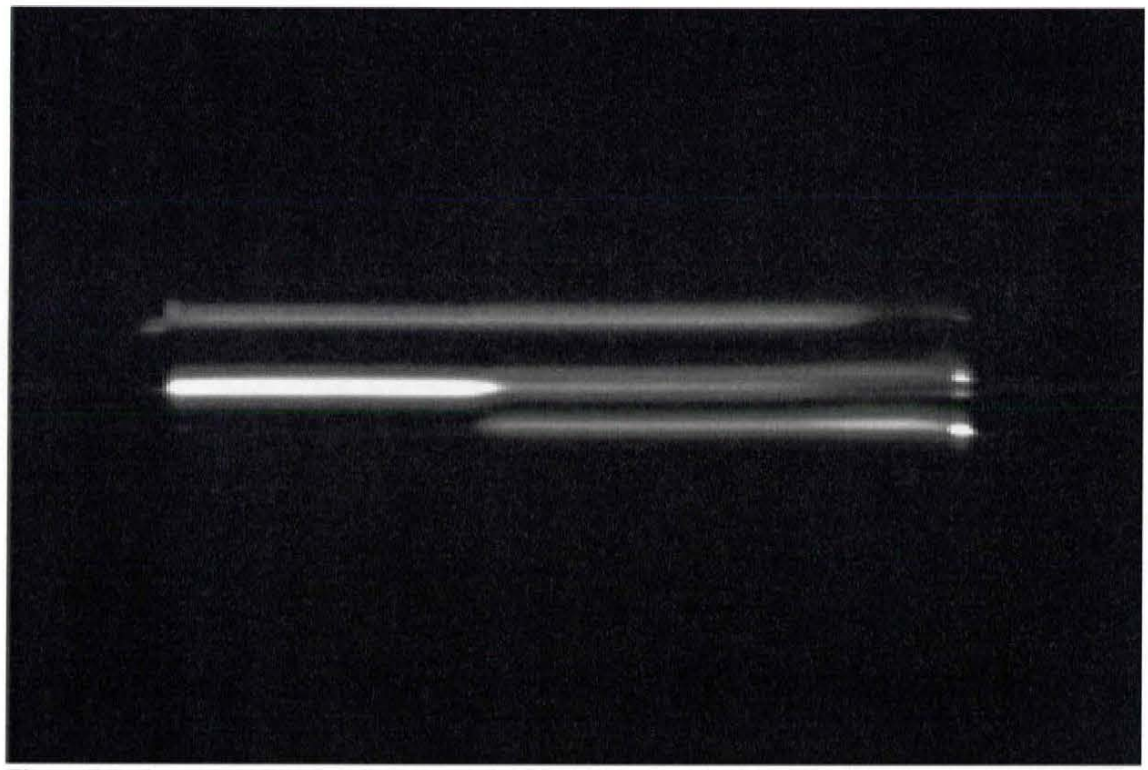

Figure B5. Raw NMR data set acquired with a 1D CSI pulse sequence. The frequency axis is vertical with a range of 8000 hz. The spatial dimension is horizontal with a range of 9 cm. The spatial dimension has the same orientation as in Figs. B1, B2 and B3, i.e. the sample inlet is towards the right. The top trace is the oil signal, the middle trace is the water signal with interfering benzyl alcohol, and the bottom trace is the main benzyl alcohol signal.

B5. Conclusions

* 2D quantitative saturation maps using the fluid system water - n-decane - benzyl alcohol may be produced for chalk samples with a 2D CSI technique. The reproducibility of the pixel fluid saturation is between 1.5 and 4 p.u. at the 1 σ level. The accuracy of the mean fluid saturation for the whole sample is 3 p.u. or better.
* For flooding experiments that are essentially 1D experiments a 1D CSI technique appears to be an attractive alternative to the 2D method.

B6. Acknowledgments

The Danish Research Center of Magnetic Resonance is acknowledged for providing access to the 4.7 T SISCO NMR scanner.

Appendix C: Papers

C1. Three-Phase Immiscible WAG Injection: Micromodel Experiments and Network Models

C2. Thin Films, Oil Layers, and Three-Phase Flow in Porous Media

C3. Multiscale Modeling of Relative Permeabilities

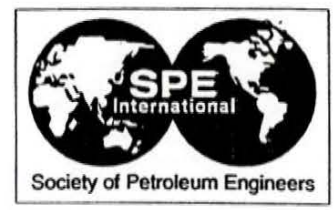

SPE 59324

Three-Phase Immiscible WAG Injection: Micromodel Experiments and Network Models

J.K. Larsen, SPE, Technical University of Denmark, N. Bech, SPE, and A. Winter, SPE, Geological Survey of Denmark and Greenland

This paper was prepared for presentation at the 2000 SPE/DOE Improved Oil Recovery Symposium held in Tulsa, Oklahoma, 3–5 April 2000.

Abstract

This paper is concerned with planning and optimization of three-phase immiscible Water-Alternating-Gas (WAG) injection processes. This goal is achieved by applying an iterative procedure linking the pore-level displacement mechanisms with a macroscopically defined WAG process.

Introduction

The adopted investigation strategy starts with an experimental micromodel study of a WAG injection process. Micromodels are physical analogs of a discrete mathematical model of porous media. In micromodels used in this study pore networks were etched in silicon and covered by transparent glass plates with similar surface properties.

The goal of the micromodel experiments is to identify the pore-scale displacement mechanisms ensuring small residual oil saturations and increased oil relative permeabilities in three-phase sweep displacement patterns. The pore-scale mechanisms identified during micromodel experiments are then incorporated into a three-dimensional mathematical network model based on percolation theory. The role of the network model is to determine the relative permeability functions for a prespecified saturation path traversing the domain of three-phase coexistence. The relative permeability functions is then used as input to a 1-D reservoir simulator which computes its own saturation trajectory.

The saturation path used by the network and its counterpart produced by the reservoir simulator may not be the same. Consequently, an iterative procedure, similar to that suggested by Fenwick and Blunt[3], is started. The goal of the iterative procedure is to compute a set of relative permeabilities for the three coexisting phases that yield identical saturation paths for the network model and the macroscopic 1-D simulator.

Injection and Initial Conditions for the WAG Process

The petrophysical parameters used in the computations described in this paper are the same as in Marchesin and Plohr[2].

Three sets of macroscopic WAG injections coresponding to different proportion of injected fluid volumes are considered. The injection cycles of the three sets are as follows:

- 65% water and 35% gas,
- 60% water and 40% gas,
- 55% water and 45% gas.

During each cycle one percent of the total pore volume is injected. The total number of cycles is 43. The initial state of the reservoir is the same in the three cases, namely 76% oil, 16% water and 8% gas.

In all cases the initial point of the saturation path traversing the triangular domain of the three-phase coexistence is situated near the oil vertex (see Figure 1). The final point appears at the opposite edge corresponding to a depleted oil reservoir.

The saturation profiles versus position for the three sets of initial conditions for the oil, water, and gas phases, obtained using a 1-D reservoir simulator (*Eclipse 100*) with 1000 grid points are shown in Figures 2,3, and 4, respectively.

In the case where capillarity is ignored, the oil saturation profiles are practically identical to those obtained by solving the Riemann problem underlying WAG injection processes[2]. The Riemann problem is defined as a conservation law together with initial data consisting of two constant states separated by a discontinuity (see LeVeque[8]). A state is defined as a point in the saturation triangle, i.e., a value of a vector $s = (S_o, S_w, S_g)$. More specifically, for three-phase flow, the Riemann problem is defined as the solution of the following system of partial differential equations:

$$s_t + A s_x = 0, \qquad (1)$$

inside the domain Ω defined as follows

$$\Omega = \{(S_w, S_g); 0 < S_w, S_g; S_o = 1 - S_w - S_g < 1\},$$

for $-\infty < x < \infty$ and $t \geq 0$, with the initial condition

$$s(x,\ t=0) = \begin{cases} s_l & x < 0, \\ s_r & x > 0, \end{cases} \qquad (2)$$

where s_l and s_r are constant states usually referred to as the left state and the right state, respectively.

The solution of the Riemann problem underlying a three-phase WAG injection process contains in addition to classical Buckley-Leverett shock waves and auxiliary slow waves two new types of waves: a shock wave of intermediate speed and a fast, decaying, oscillatory injection wave[2].

The three wave groups can also be seen by inspecting the oil saturation profile computed by the 1-D reservoir simulator corresponding to the initial condition where 60% of injected fluid volume consists of water and 40% is gas (cf. Figure 2).

The first group is a slow wave group extending from S^L to S^A, S^A being a constant state. The second constant state, S^B, is connected to the right state S^R by a weak Buckley-Leverett shock wave representing the fast wave group. The shock wave connecting the slow and fast wave groups, extending from to S^A to S^B, represents a new type of shock wave. It is referred to as a *transitional* shock wave. The amplitude of this new type of wave can be considerably larger as compared with the classical Buckley-Leverett shock wave. Figure 2 shows three oil saturation profiles corresponding to initial conditions 65% water and 35% gas, 60% water and 40% gas, and 55% water and 45% gas, respectively. Marchesin and Plohr[2] pointed out that presence of transitional waves is associated with substantial improvement of recovery efficiency of WAG injection processes.

Network Model for Three-Phase Flow

Three-phase flow displacement mechanisms observed in micromodel experiments consist of the classical two-phase mechanisms[10] and a new class of mechanisms referred to as the double mechanisms where one two-phase mechanism is associated with another two-phase mechanism. Keller et al[5] and Øren et al.[12] have presented a number of double mechanisms appearing in three-phase flow based on micromodel experiments.

All three-phase double mechanisms are associated with a critical pressure thresholds which must be reached to ensure their activation. Consequently, the injection of one of the three phases for a given fluid configuration in the network will lead to a well defined sequence of pore events associated with a given capillary pressure sequence.

The network model is made up of a regular cubic lattice with 30 x 15 x 15 pores. The nodes of the lattice correspond to pore bodies while bonds correspond to throats. In order to reduce finite size effects periodic boundary conditions are imposed on the faces of the lattice perpendicular to the flow direction.

The pores are assumed to have square cross sections . The pores and throats are assigned sizes corresponding to the inscribed radius of their square cross section. The pore size distribution is uniform in the intervals [10 μm , 20 μm] and [5 μm -10 μm] for the pores and throats, respectively.

Moreover, the distance between the pore bodies is set equal to 52 microns. The length of the pores is set to twice the pore radius. Finally, the length of the pore throats varies and is calculated as the distance between the pore bodies minus their radii.

Phase Saturations in a Single Pore

In a single pore there are four possible fluid configurations with different numbers of participating phases. The four cases are as follows:

- water
- water and oil
- water and gas
- oil, water, and gas.

All three phases are assumed to be incompressible. Consequently, the saturations of the three phases are given by the capillary pressures of the three possible interface configurations, the geometry of the pore and the contact angles of the phases.

The volume of the pore bodies is given by the following expression

$$V_b = 8r_b^3, \qquad (3)$$

where r_b is the inscribed radius of the pore body. The volume of the throat is given by

$$V_t = 4r_t^2 \cdot l_t, \qquad (4)$$

where r_t is the inscribed radius of the throat and l_t is the length of the throat.

In the case of oil and water present in a pore throat or pore body, the volume of the water in the pore is given by

$$V_w = A_w \cdot l_t, \qquad (5)$$

where

$$A_w = 4r_{ow}^2 \begin{pmatrix} cot(\alpha) \cdot cos^2(\alpha+\theta) + \\ -\left(\frac{\pi}{2} - (\alpha+\theta)\right) + \\ +\left(cos(\alpha+\theta) \cdot sin(\alpha+\theta)\right) \end{pmatrix}, \qquad (6)$$

where r_{ow} is the curvature radius of the water-oil interface, α is the half angle of corner, and θ is the contact angle between oil and water.

The volume of the oil phase is given by

$$V_o = A_o \cdot l_t, \tag{7}$$

The area of the oil phase is given by

$$A_o = 4r_t^2 - A_w. \tag{8}$$

For pore bodies the expressions are the same except that the lengths and radii are for the pore bodies.

In the case of a gas-water system the expressions for the volume and area of the gas phase are similar to eq. (7) and eq. (8) as gas essentially plays the same role as oil. However, different values for the contact angle and the interfacial curvature are used.

In the case of three phases coexisting in the pore, oil appears as a layer separating gas and water [3,4]. The area of the oil in this case is given as the difference of the wetting area in the case where oil and water are pressent and the case in which gas and water are present. If this area is negative due to the actual capillary pressures, the oil layer is absent[3,4].

Conductance of the phases in a single pore

In the simplest case when a pore or throat is completely filled by one phase the conductance can be determined using Poiseuille's law (Fenwick and Blunt [3,4])

$$g = \frac{\pi r_{eff}^4}{8\mu_\alpha l}, \tag{9}$$

where $r_{eff} = \sqrt{\frac{A_t}{\pi}}$, μ_α is the viscosity of the α phase, and A_t is the area of the cross-section of the pore or throat. Finally, r and l are the inscribed radius and the length of the pore or throat.

$$g_i^w = \frac{A_i^w r_{nw}^2}{R_{fw}\mu_w l}, \tag{10}$$

where A_i^w stands for the cross-sectional area of the aqueous phase in pore i, r_{nw} is the interfacial curvature of the interface separating the aqueous phase and the nonwetting fluid, and R_{fw} is a dimensionless resistance factor.

In the case where three phases coexist in a pore or throat, one can still use eq.(9) and eq.(10), but this time with $r_{eff} = \frac{1}{2}(\sqrt{\frac{A_g}{\pi}} + r)$. The conductance of an oil phase is given by the expression

$$g_o = \frac{A_c r_{go}^2}{\mu l_p R_{fo}} - g_w, \tag{11}$$

where A_c is the area in the corner covered by oil and gas and R_{fo} is the dimensionless resistance factor corresponding to the flow conditions of the oil phase.

The analytical expression for the dimensionless resistance factor developed by Zhou et al.[11] have been used in the calculations of phase conductances.

Computation of Three-Phase Relative Permeability

The incompressibility of the three phases leads to the mass balance equation in the following form

$$\sum_j^Z q_{\alpha,ij} = 0, \tag{12}$$

where $Z=6$ is the coordination number and $q_{\alpha,ij}$ stands for the flow rate of phase α between the pores i and j.

The flow rate is given by the following expression

$$q_{\alpha,ij} = g_{\alpha,ij}(P_{\alpha,i} - P_{\alpha,j}), \tag{13}$$

where $g_{\alpha,ij}$ stands for the conductance of phase α between the neighbouring pores i and j. It is defined as the harmonic mean of the conductance between the centers of pores i and j. More specifically,

$$\frac{1}{g_{\alpha,ij}} = \frac{1}{g_{\alpha,t}} + \frac{1}{2}(\frac{1}{g_{\alpha,i}} + \frac{1}{g_{\alpha,j}}) \tag{14}$$

where $g_{\alpha,i}$ represents the conductance of phase α in pore i, $g_{\alpha,j}$ is the conductance in pore j, and $g_{\alpha,t}$ is the conductance of the throat connecting pores i and j.

One of the important tasks performed by the network model is to determine the relative permeability functions as it traverses a saturation path in the three-phase region. The main steps of the calculation procedure are as follows (Fenwick and Blunt[4]):

- A representative section of the network model is chosen for the calculation of relative permeabilities to avoid inlet and outlet boundary effects.
- The saturation of the desired phase is determined using the method outlined in the preceding section.
- The non-wetting phase and intermediate phase are examined to find out whether either of the phases is continuous from one end of the selected section to the other. If a phase is not continuous its relative permeability is assumed to be zero.
- The conductance of a phase between the pores i and j in the selected section of the network is determined using the harmonic mean.

- Constant boundary conditions are imposed on each side of the selected section of the network.
- The mass balance condition (eq. (12)) is combined with eq. (13) for the flow rate between each pore.
- The computed pressures of the pores are used to determine the flow rates the phase in and out of the selected section of the network using eq. (13).
- The multiphase version of Darcy's law is used to determine the relative permeabilities of each phase at the desired saturation.

The Iterative Procedure

Flow at the pore level is described by the network model. At the field-scale it is computed by means of a reservoir simulator. The link between the two levels is provided by relative permeabilities and saturation paths obtained from the network model and reservoir simulator, respectively.

The field scale model is one-dimensional (1-D) with given fluid properties, initial and operating conditions. For a given set of relative permeabilities the reservoir is produced for a time, t_{max}, sufficiently large to ensure that any shocks and rarefaction waves are resolved. The resulting saturation path is given by the saturations $\{S_{wi}, S_{oi}, S_{gi}, i = 1,\ldots, n_x\}$ corresponding to the time $t = t_{max}$. Using this field-scale saturation path a three-phase displacement is now carried out with the network model. This displacement produces a new set of relative permeabilities. If the relative permeabilities from the network model are equal to those used in the reservoir model the relative permeabilities are called self-consistent. This means that the network model computes relative permeabilities for a sequence of saturation changes that is the same as the sequence that results from a 1-D field-scale simulation using the same relative permeabilities (Fenwick and Blunt (1998))[3].

In general, however, the two sets of relative permeabilities will be different. The relationship between them can be written as follows

$$k_{r\alpha,nm} = g(k_{r\alpha,sim}),\ \alpha = w, o, g \qquad (15)$$

where subscripts *nm* and *sim* refer to the network model and reservoir simulator, respectively. The function g represents the sequence of field- and micro-scale calculations outlined above. In order to compute the set of self-consistent relative permeabilities we must solve the non-linear equation system

$$k_{r\alpha,nm} - g(k_{r\alpha,sim}) = 0, \quad \alpha = w, o, g \qquad (16)$$

In both the simulator and the network model the relative permeability for each phase is specified as function of the phase saturation by means of tables. If each tabel has ntab entries the total number of unknowns in Eq. (16) is

$$n = 3 * (n_{tab} - 1), \qquad (17)$$

assuming that only the entries $k_{r\alpha}(0) = 0$ are given. In order to reduce the number of unknowns the relative permeabilities are approximated by means of analytical functions, viz.:

$$k_{rw}(S_w) = f_{rw}(a_{w,1}, a_{w,2},\ldots, a_{w,nw}, S_w) \qquad (18)$$

$$k_{ro}(S_o) = f_{ro}(a_{o,1}, a_{o,2},\ldots, a_{o,no}, S_o) \qquad (19)$$

$$k_{rg}(S_g) = f_{rg}(a_{g,1}, a_{g,2},\ldots, a_{g,ng}, S_g) \qquad (20)$$

The non-linear function defining the self-consistent set of relative permeabilities can be written as follows

$$\bar{F}(\bar{a}) = 0 \qquad (21)$$

where

$$\bar{F}(\bar{a}) \equiv \bar{a} - \bar{f}(\bar{a}) \qquad (22)$$

and

$$\bar{a}^T = \{a_{w,1},\ldots a_{w,nw}, a_{o,1},\ldots a_{o,no}, a_{g,1},\ldots a_{g,ng}\} \qquad (23)$$

The function F is defined by the following sequence of calculations:

For a given (guessed or computed) set of parameters, $\bar{a}$

- Compute the relative permeabilities from Eqs. (18– 20).
- Calculate the corresponding field-scale saturation path.
- Using this field-scale saturation path a three-phase displacement is now carried out with the network model producing a new set of relative permeabilities.
- New values of the parameters $\bar{a}$ are then determined by least-square-fitting the analytical expressions Eqs. (18-20) to the relative permeabilities from the network model.
- If the new and old parameter values agree within a specified tolerance then stop else return to step 1 and repeat the iteration cycle.

The field-scale reservoir simulations are carried out by ECLIPSE 100. The non-linear equation system (eq. (20)) is solved by the MINPACK algorithm HYBRD (Garbow et al. (1980)).

Acknowledgements

The authors are grateful to M.J. Blunt, D.H. Fenwick, D. Marchesin, and B.J. Plohr for stimulating discussions concerning microscopic and macroscopic models of three-phase flow in porous media.

The micromodels used in this study were manufactured in cooperation with Microelectronic Centre (MIC) affiliated to Technical University of Denmark (DTU).

Nomenclature

A	=	2x2 matrix
A_α	=	area of phase α
a	=	parameter in analytical expression
$\bar{a}$	=	vector of parameters
α	=	fluid phase ($\alpha = \{o, w, g\}$)
f	=	nonlinear function
f_r	=	relative permeability specified analytically
F	=	nonlinear function
g	=	nonlinear function
g	=	gas
g	=	conductance of a fluid phase
$g_{\alpha,j}$	=	conductance of phase α in pore i.
$g_{\alpha ij}$	=	conductance of α phase between i and j
k_r	=	relative permeability, fraction
k_{rw}	=	relative permeability to water, fraction
k	=	Number of unknowns
n_{tab}	=	Number.of table entries
n_x	=	Number of axial grid cells in the simulator
o	=	oil
$R_{f\alpha}$	=	dimensionless resistance factor for α phase
r_{ow}	=	curvature radius of the water-oil interface
r_b	=	inscribed radius of pore body
r_t	=	incribed radius of pore throat
s	=	vector of three phase saturations (S_o,S_w,S_g)
s_t, s_x	=	partial derivatives of s w.r.t t, x
S_α	=	saturation of α phase, fraction
t	=	time, days
q	=	flow rate
V_b	=	volume of pore body
V_t	=	volume of pore throat
w	=	water
Z	=	coordination number of a lattice

Subscripts

g	=	gas
j	=	phase index
max	=	maximum
ng	=	number of parameters in analytical expression for the gas relative permeability
no	=	number of parameters in analytical expression for the oil relative permeability
nw	=	number of parameters in analytical expression for the water relative permeability
nm	=	network model
o	=	oil
s	=	vector of three phase saturations
sim	=	simulator or simulation
w	=	water

Superscripts

T	=	transposed

References

1. *ECLIPSE 100*, 95A Release, Intera Information Technologies Ltd., Highlands Farm, Henley-on-Thames, Oxfordshire, U.K., 1994.
2. Marchesin, D. and Plohr B.J., "Wave Structure in WAG Recovery", SPE Paper No. 56480, 1999.
3. Fenwick, D.H. and Blunt M.J, "Network Modeling of Three Phase Flow in Porous Media", SPE Journal Vol. 3, 86-97, (March 1998).
4. Fenwick, D.H. and Blunt M.J., "Three-dimensional Modelling of Three-Phase Imbibition and Drainage", Advances in Water Resources, vol. 21, No. 2, 121-143, 1998.
5. Keller A., Blunt M.J and Roberts V., " Micromodel Observation of the Role of Oil Layers in Three-Phase Flow", Transport in Porous Media, vol. 26, 277-297, 1997.
6. Ransohoff, T.C. and Radke C.J., "Laminar Flow of a Wetting Liquid along the Corners of a Predominantly Gas-Occupied Noncircular Pore", J. Colloid and Interface Science, vol. 121, 392-401, 1988.
7. Garbow, B.S., Hillstrom, K.E. and More, J.J.: MINPACK Project, Argonne National Laboratory, March 1980.
8. LeVeque, R.J., Numerical Methods for Conservation Laws", Birkhauser, Basel, 1994.
9. Saraf, D.N., Batycky P.J., and Fisher D.B., "An Experimental Investigation of Three-Phase Flow of Water-Oil-Gas Mixture Through Water-Wet Sandstones". SPE Paper No. 10761, 1982.
10. Lenormand, R. Zarcone, C., and Sarr A., "Mechanisms of theDisplacement of One Fluid by Another in a Network of Capillary Ducts", J. Fluid Mechanics, vol. 135, 337-353, 1983.
11. Zhou, D., Blunt M., and Orr, F.M., "Hydrocarbon Drainage along Corners of Noncircular Capillaries", J. Fluid Mechanics, vol. 187, 11-27, 1997.

12. Øren, P.E., Billiotte, J., Pinczewski, W.V., Pore-Scale Network Modelling of Waterflood Residual Oil Recovery by Immiscible Gas Flooding". SPE Paper No. 27814, 1994.

Fig. 1. Saturation Paths for Three Different WAG Injections

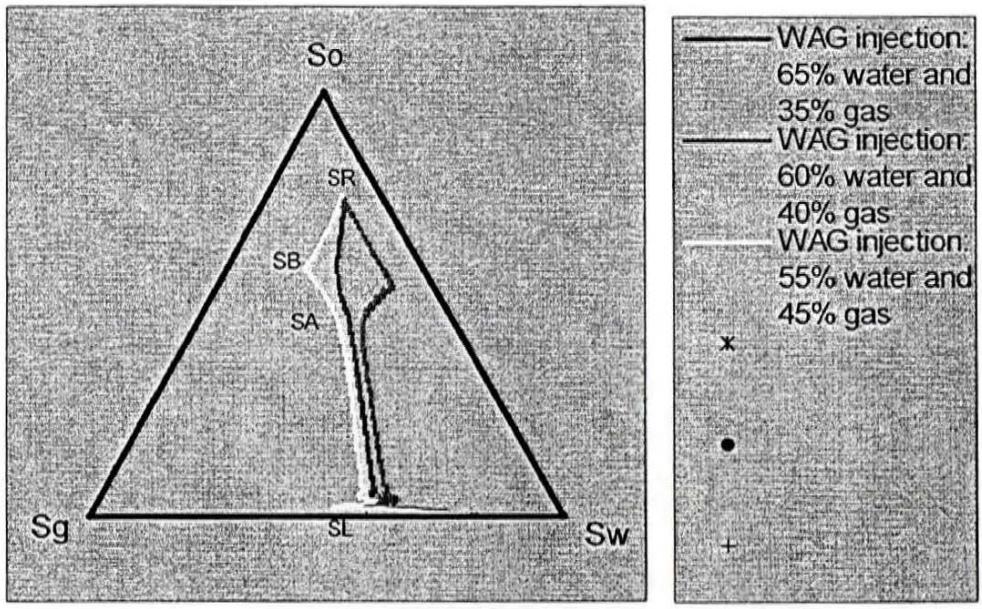

Fig. 2. Oil Saturation vs. Axial Length

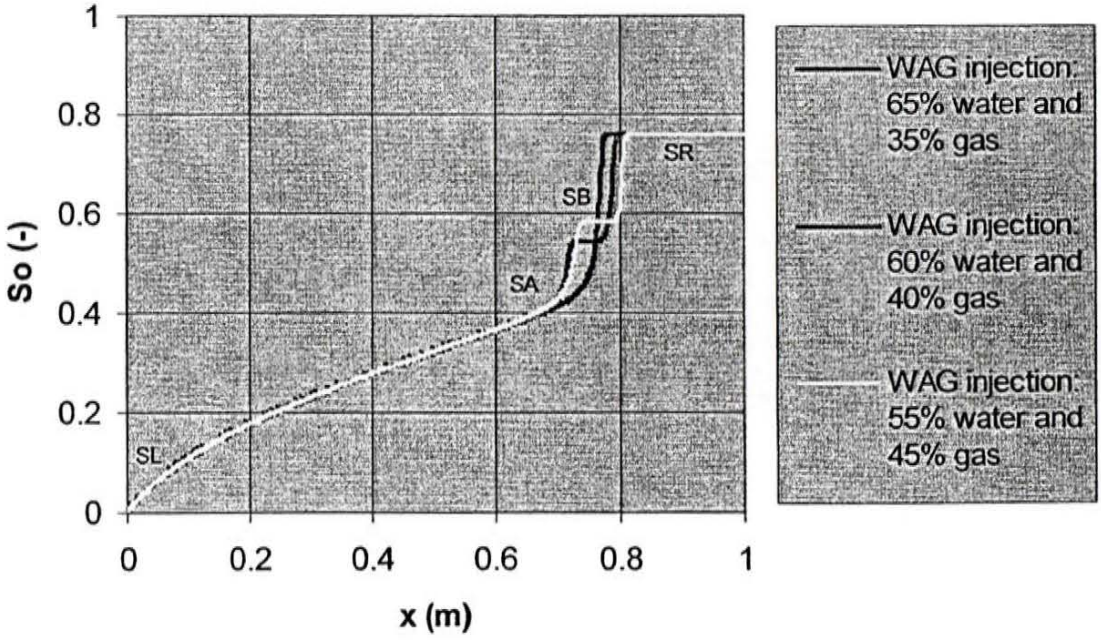

Fig. 3. Water Saturation vs. Axial Length

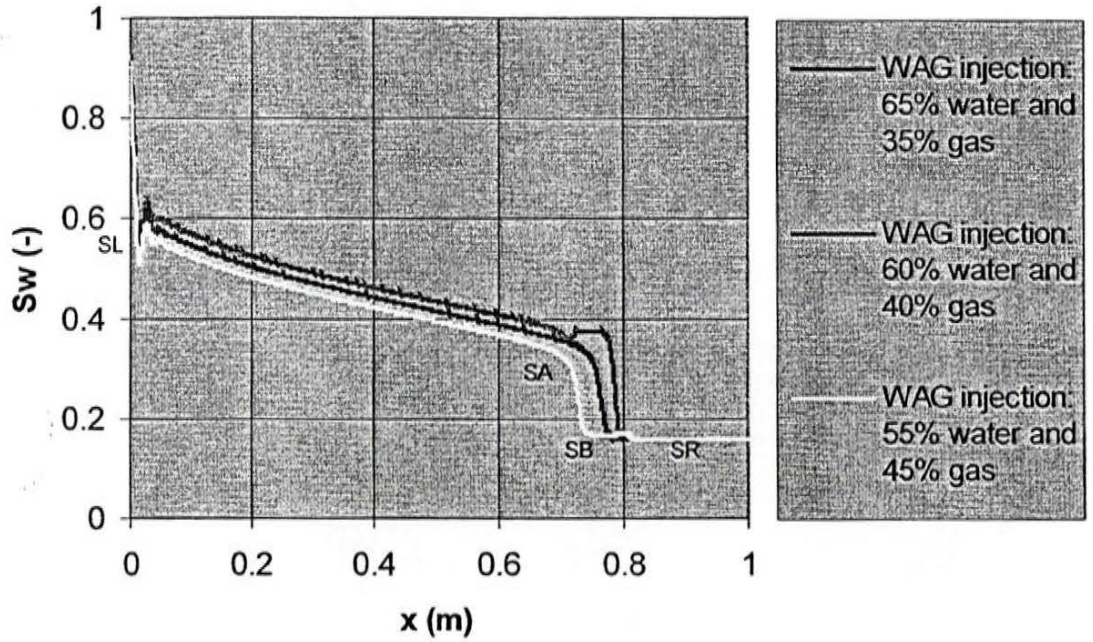

Fig. 4. Gas Saturation vs. Axial Length

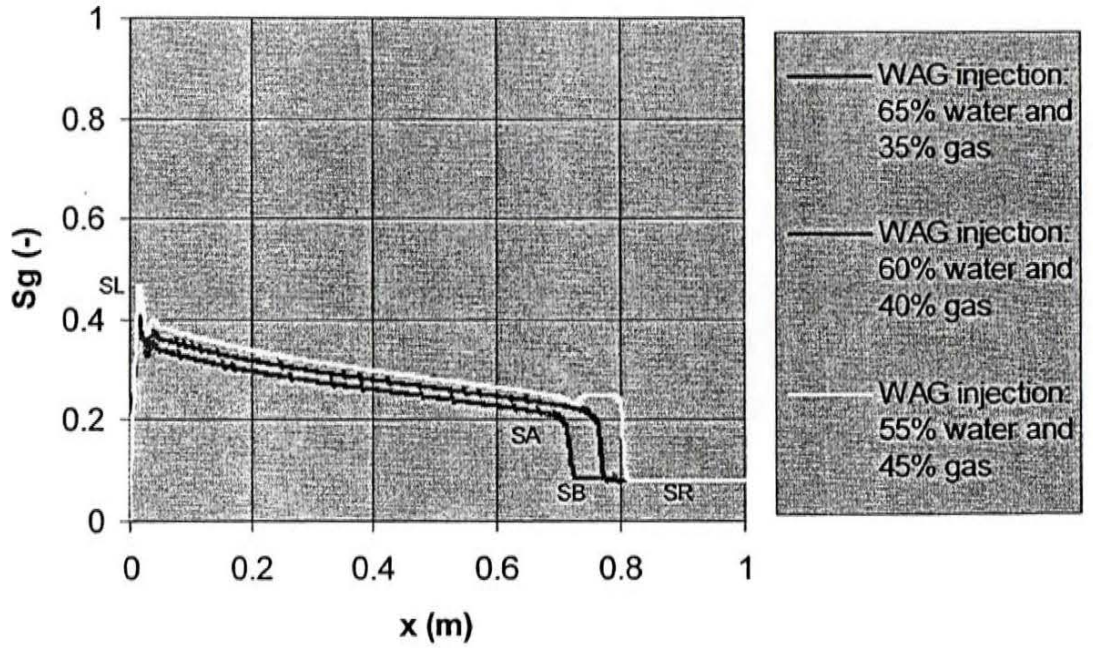

Submitted to International Journal of Thermophysics

Thin Films, Oil Layers, and Three-Phase Flow in Porous Media[1]

Anatol Winter[2,3]

[1]Paper presented at the Fourteenth Symposium on Thermophysical Properties, June 25-30, 2000, Boulder, Colorado, U.S.A.

[2]Geological Survey of Denmark and Greenland, Thoravej 8, DK-2400 Copenhagen NV, Denmark.

[3] To whom correspondence should be adressed.

ABSTRACT

This paper is concerned with two transport mechanisms governing three-phase displacement in porous networks. The first mechanism appears in three-phase mixtures near a tricritical point. In this case the system is in the complete wetting regime. The oil phase creates *thin* films situated between aqueous and gas phases through which it can be drained. The thermodynamical model involved in planning of oil recovery processes near a tricritical point is described. It consists of the model of van der Waals of a diffuse interface and that of Griffiths' of near-tricritical mixtures. The second transport mechanism involves *thick* oil layers sandwiched between water and gas in wedges of angular capillaries. Calculations using an idealized model of a capillary tubing with angular cross section show that for adequate combinations of pore geometry and fluid properties such layers are thermodynamically favorable even for three-phase systems in the partial wetting regime.

KEY WORDS: complete wetting; oil film; oil layer; oil reservoir; partial wetting; pore network; spreading coefficient.

1. INTRODUCTION

The oil phase in hydrocarbon reservoirs appears in two different connectivity regimes:

- the continuous regime in which oil spans large portions of the porous network extending over many pore diameters.
- the "blob regime" in which oil mainly exists as disconnected ganglia.

The continuous regime can be found in virgin reservoirs, i.e. before the start of oil production. On the other hand, as more and more of oil is produced and the reservoir pressure gradually decreases, the continuity of the oil phase breaks down.

The transition between the two regimes takes place after some amount of oil has been produced. Thus, the oil phase remaining in the reservoir consists of myriads of disconnected ganglia.

Consider now an isolated oil ganglion blocking a capillary of a nonuniform cross-section.

The ganglion is assumed to be under the influence of an external pressure gradient and the opposing force due to the capillary pressure. The balance of forces acting on the ganglion can be stated as follows:

$$P_2 = P_1 + \frac{2\sigma_{ow}}{R_2}, \tag{1}$$

$$P_3 = P_4 + \frac{2\sigma_{ow}}{R_1}, \tag{2}$$

where σ_{ow} is the oil-water interfacial tension. R_1 and R_2 are the downstream and upstream mean radii of curvature, respectively. P_1, P_2, P_3, and P_4 are the pressures associated with the ganglion's rear and front oil-water interfaces (see Figure 1).

Combining eq.(1) and eq. (2) gives,

$$P_4 - P_1 = 2\sigma_{ow}(\frac{1}{R_2} - \frac{1}{R_1}). \tag{3}$$

The pressure drop in the aqueous phase is given by

$$P_1 - P_4 = \Delta\Psi_w \tag{4}$$

where $\Delta\Psi_w$ is the drop of pressure potential. Substituting for $P_1 - P_4$ in eq.(3) gives,

$$2\sigma_{ow}(\frac{1}{R_1} - \frac{1}{R_2}) = \Delta\Psi_w. \tag{5}$$

The transport velocity of the aqueous phase can be estimated from the Hagen-Pouseille equation:

$$\vartheta_w = -\frac{a^2}{8\mu}(\frac{\Delta\Psi_w}{l}) \tag{6}$$

where l is the approximate length of the pathway, a is its average radius, and μ is the viscosity of the aqueous phase.

Combining eqs. (4) and (6) gives the following expression:

$$2\sigma_{ow}(\frac{1}{R_1} - \frac{1}{R_2}) = \frac{8\mu_w\vartheta_w l}{a^2}. \tag{7}$$

Thus the length, l, of the ganglion is given by the following expression,

$$l = 2\sigma_{ow}(\frac{1}{R_1} - \frac{1}{R_2})/(\frac{8\mu_w\vartheta_w}{a^2}). \tag{8}$$

The approximate volume of the ganglion (neglecting its extreme ends) is as follows:

$$\Xi = \pi R_{av}^2 l = (0.25\pi R_2^2 a^2(\frac{1}{R_1} - \frac{1}{R_2}))/(\frac{\mu_w\vartheta_w}{\sigma_{ow}}). \tag{9}$$

The above expression can be stated in a more compact way by introducing a dimensionless group of parameters, N_c, defined as follows,

$$N_c = \frac{\mu\vartheta_w}{\sigma_{ow}}. \tag{10}$$

N_c is often referred to as the capillary number.

Equation (9) can be reformulated as follows.

$$\Xi = \frac{0.25R_{av}^2 a^2}{N_c}(\frac{1}{R_1} - \frac{1}{R_2}). \tag{11}$$

The total amount of oil left in the interconnected network of capillaries can be obtained by replacing the quantities appearing in eq.(11) by their statistical averages. Consequently, eq.(11) can be rewritten as follows,

$$S_{or} = \frac{const.}{N_c}, \tag{12}$$

where S_{or} is the residual oil saturation representing the total volume of the oil phase left in the network after the loss of continuity.

Typical values of N_c at the end of a water injection are approximately $10^{-7} - 10^{-6}$. It is usually assumed that N_c must be increased to $10^{-4} - 10^{-2}$ in order to mobilize a significant amount of the residual oil. Such an increase of the capillary number can be achieved, for example, by injecting water a into the formation. However, a significant increase of water velocity, ϑ_w, is only possible to the extent one can increase the pressure gradient created by the injection pumps by the same order of magnitude. Similarly, one can increase the viscosity of water by injecting water-soluble polymers. However, such action will be hampered by its limited effect on the oil flow rate. This is the reason why the only way to achieve a significant increase in capillary number, N_c, in eq.(12) is to decrease the interfacial tension σ (cf. eq.(10)). The oil-water interfacial tension can be reduced, for example, by injecting a surfactant into the formation. This leads to creation of a three-phase fluid mixture in the subsurface characterized by the ultralow oil-water interfacial tension and modified wetting properties Wetting properties of near-critical three-phase fluid mixtures relevant to enhanced oil recovery processes are described in the next section.

2. WETTING REGIMES IN OIL RESERVOIRS

Hydrocarbon reservoirs contain three coexisting phases: water, oil, and gas. Depending on the value of the initial spreading coefficient, S^i,oil can either spread as a thin wetting film or create a lense situated between the water and gas phases. The initial spreading coefficient S^i is defined by the following expression,

$$S^i = \sigma_{gw} - (\sigma_{ow} + \sigma_{go}), \tag{13}$$

where σ stands for the interfacial tension, the subscript g stands for gas, w represents water, and o indicates oil.

Figure 2 shows the forces acting at the three-phase contact line along which water, oil, and gas phases meet. The oil phase at the gas-water interface originates either from adsorption from the vapor phase or can be attributed to spreading. The

equilibration of the three coexisting phases leads to a notion of the equilibrium spreading coefficient,

$$S^{eq} = \sigma^{e}_{gw} - (\sigma^{e}_{ow} + \sigma^{e}_{go}), \tag{14}$$

The equilibrium spreading coefficient, S^{eq}, is either negative or equal to zero. More specifically, when $S^{eq} = 0$, the oil phase completely wets the gas-water interface. On the other hand, for $S^{eq} < 0, it$ only partially wets the gas-water interface. It should be noted that the equilibrium spreading coefficient S^{eq} can never be positive. If, momentarily, it were gas-water interface would immediately coat itself with a layer of the aqueous phase, replacing the supposedly higher free energy per unit area of the direct gas water contact, σ_{gw},by the supposedly lower sum of the free energies per unit area of gas-oil and oil-water contacts, $\sigma_{go} + \sigma_{ow}$, thereby lowering the free energy of the system [1].

The message contained in the above statement is that the spreading coefficient may change as the thermodynamic state of the system varies. Over a certain range of a chemical potential (or another thermodynamical field) the spreading coefficient may be negative. Otherwise, it is equal to zero (see Figure 3a). The transition between the two regimes occuring at $\mu = \mu*$ is the wetting transition predicted theoretically by Cahn [1]. In particular, presence of a wetting transition can be deduced theoretically in three-phase mixtures close to a tricritical point. The deduction procedure is based on van der Waals-Cahn-Hilliard theory of near-critical interfaces briefly described in the next section.

3. VAN DER WAALS THEORY OF INTERFACES

This section describes van der Waals theory of an interface separating two coexisting phases in its modern version applicable to a large family of multicomponent systems whose behavior can be described in terms of a suitable order parameter. Before we state a formal definition of the order parameter, we make a distinction between two types of intensive thermodynamic variables: fields and densities [2]. By fields we understand those variables, that have the same values in the coexisting phases (e.g., pressure, temperature, chemical potential, etc.). On the other hand, the variables which have different values in each coexisting phase (e.g., mole fraction, composition, etc.) are referred to as densities.

The order parameter can be thought of as some linear combination of density variables characterizing the system under consideration. It is usually interpreted as a numerical measure of the "amount of order" that exists in the neighborhood of the thermodynamical state characterizing the system under consideration.

Consider first a multicomponent mixture consisting of two coexisting phases (e.g., two liquid phases or a liquid phase in equilibrium with its vapor). The order parameter is denoted by X. X_α and X_β stand for the values of X in the bulk α and β phases, respectively. When the coexisting α and β phases correspond to a one-component liquid and its vapor, X can be interpreted as equal to $\rho - \rho_c$ where ρ is the specific density of the liquid and ρ_c is its value at the critical point. In the region of two-phase coexistence, the order parameter takes the value X_α in the α phase and X_β in the β phase.

Let's denote the interfacial free energy density of a two-phase system by $f(X)$. It is well known that $f(X)$ is a continuous function in X with a characteristic "hump" corresponding to the two-phase region $\rho_\alpha - \rho_c = X_\alpha \prec X_\beta = \rho_\beta - \rho_c$ [3]. The fundamental assumption of van der Waals theory is that the interfacial free energy is a sum of two components. The first component is the function $-V(X)$ defined as the difference between $f(X)$ and the straight line. The second component is an expression proportional to the square of the composition gradient i.e.,

$$\Psi(z) = -V(X(z)) + \frac{1}{2}m(\frac{dX}{dz})^2, \tag{15}$$

where z is a distance in a direction perpendicular to the plane of the interface and m is a positive constant.

The total free interfacial energy per unit area is defined as follows.

$$\sigma = \int_{-\infty}^{\infty} \{-V(X(z) + \frac{1}{2}m(\frac{dX}{dz})^2\}. \tag{16}$$

It should be noted that

$$\lim_{z \to -\infty} X = X_\alpha \tag{17}$$

and

$$\lim_{z \to \infty} X = X_\beta. \tag{18}$$

The equilibrium density profile is the function $X(z)$ that minimizes σ in eq.(16).

The equilibrium density profile can also be obtained in a different way utilizing an analogy between the above mentioned minimization problem and the particle moving in a one-dimensional space subject to potential $V(X)$ [1]. In the particle analogy, the $X(z)$ that minimizes σ is the position coordinate of the particle

moving between X_α and X_β (Hamilton's principle). Thus the equilibrium density profile can be obtained from the Euler-Lagrange equation (L is the Lagrangian of the system).

$$\frac{\partial L}{\partial X} = \frac{d}{dt}(\frac{\partial L}{\partial X}), \tag{19}$$

or, equivalently

$$m(\frac{d^2X}{dz^2}) = -\frac{\partial V}{\partial X}. \tag{20}$$

Thus eq.(16) can be restated as follows,

$$\sigma = \int_{-\infty}^{\infty}(-V + K)dz = \int_{X_\alpha}^{X_\beta}\sqrt{-2mV(X)}dX \tag{21}$$

where $K = \frac{1}{2}m(\frac{dX}{dz})^2$ is the kinetic energy of the particle and σ corresponds to the action defined as the integral of momentum over coordinate.

The above equation will be used in the calculations of the equilibrium spreading coefficient in a multicomponent mixture exhibiting tricritical behavior. The necessary framework for such calculations is the Van der Waals-Landau-Griffiths model of three-phase equilibria near a tricritical point. This model is briefly described in the next section.

4. GRIFFITHS MODEL

The main assumptions of the Griffiths model of a tricritical behavior are as follows [2]:

1. The free energy density is an analytic function of the fields and densities.

2. In a sufficiently small neighborhood of a tricritical point, the free energy density can be expanded in a power series of the one-dimensional order parameter Ψ,

$$F(\Psi) = a_1\Psi + a_2\Psi^2 + a_3\Psi^3 + a_4\Psi^4 + \Psi^6. \tag{22}$$

The a_i are model fields that are related to the physical fields f_k (such as e.g., temperature and pressure) by the linear relations,

$$a_i = \sum_{k=1}^{4}\alpha_{ik}(f_k - f_{kt}). \tag{23}$$

The coefficients α_{ik} are initially unknown and appear as a matrix of constant coefficients. f_{kt} are the values of f_k at the tricritical point.

The absence of the term a_5 is due to the fact that it can always be eliminated by replacing Ψ by $\Psi + \Psi_0$ in choosing Ψ_0 appropriately. Furthermore, the coefficient a_6 must be positive (for thermodynamic stability) and can be set equal to unity.

In his model Griffiths uses a free energy defined by the following relation

$$\Omega = \Omega_r + \Omega_s, \tag{24}$$

where the regular part, Ω_r, is an analytic function of the fields and the singular part, Ω_s, is given by the following equation,

$$\Omega_s = \min_{\Psi} F(a_1, a_2, a_3, a_4; \Psi). \tag{25}$$

The order parameter Ψ takes different values in the coexisting phases. More precisely, these values appear at the absolute minima (with respect to Ψ) of F (cf. eq.(22)) for a fixed value of $a = (a_1^*, a_2^*, a_3^*, a_4^*; \Psi)$. If these minima occur for several values of Ψ then each of these values can be ascribed to a distinct phase and $\{a_j^*\}$ belong to an appropriate coexistence manifold in the field space diagram.

Griffiths [2] has shown that for the class of mixtures exhibiting tricritical behavior one can associate the temperature with the field a_4, i.e. $a_4 \sim (T - T_t)/T_t$ where T_t is temperature corresponding to the tricritical point. Consequently, by keeping a_4 fixed one obtains an isothermal section of the phase diagram. An example of such a section is shown in Figure 4. Three-phase region is spanned by an infinite series of triangles. The points in the interior of each triangle represent the overall compositions of the three-phase mixtures. The compositions of the three phases lie at the triangles' vertices. As the tricritical point is approached, a_4 traverses a range of negative values toward $a_4 = 0$. This approach is not arbitrary: it is controlled by three different exponents describing the geometry of the three-phase region near the tricritical point. More specifically, thickness of the stack of triangles shrinks as $|a_4|^{3/2}$; the altidude of each triangle vanishes as $|a_4|$; and the length of the three-phase region (measured as the length of the longest side of the triangle) varies as $|a_4|^{1/2}$. As shown in Figure 5, near the tricritical point the three points representing the coexisting phases become asmptotically collinear. Consequently, there is always a phase, which in all its properties, is intermediate between the two other phases.

Prediction of multiphase behavior of a concrete mixture requires knowledge of the relation between the model variables and their experimental counterparts [4]. However such knowledge is not necessary if one is only interested in qualitative

properties of the phase behavior. In this case one can disregard the regular part of the free energy, Ω_r, because it does not affect the nature of the phase diagram. By a "phase diagram" we mean here the set of points at which two, or more phases, coexist. Thus a phase diagram is essentially a "map" of the singular part of the free energy, Ω_s

The minimization of the total thermodynamical potential, Ω, with respect to Ψ results in a cubic equation [1,2],

$$\Psi^3 + \frac{1}{2}a_4\Psi + \frac{1}{2}a_3 = 0, \tag{26}$$

with three real roots Ψ_α, Ψ_β, and Ψ_γ provided that $a_4 \prec 0$ and $\mid a_3 \mid \preceq 4(-a_4/6^{\frac{3}{2}})$.

The solution of eq.(26) can be written in a unified way as follows,

$$\Psi_\delta = A\cos\varphi_\delta, \tag{27}$$

where

$$\phi_\delta = \begin{cases} 120+\theta & \text{if} \quad \delta = \alpha \\ 120-\theta & \text{if} \quad \delta = \beta \\ \theta & \text{if} \quad \delta = \gamma \end{cases} \tag{28}$$

It should be noted that θ lies in the interval $0 < \theta \prec 60^\circ$, $A = (-\frac{2a_4}{a_3})^{\frac{1}{2}}$, and $a_4 < 0$.

The fields a_i can reformulated as follows [4],

$$a_1 = \frac{3}{8}A^5\cos\theta, \tag{29}$$

$$a_2 = \frac{9}{16}A^4, \tag{30}$$

$$a_3 = -\frac{1}{2}A^3\cos 3\theta. \tag{31}$$

According to the van der Waals theory of interfaces, the interfacial tension between phases α and β is given by the expression,

$$\sigma = m_1\int_{\psi_\alpha}^{\psi_\beta}\sqrt{-V(\Psi)}d\Psi, \tag{32}$$

where $m_1 is$ a smoothly varying function of fields.

Following Griffiths [2,5,6] the excess free energy density is given by,

$$\sigma_{\alpha\beta} = \sigma_0(\Psi_\beta - \Psi_\alpha)^3(3\Psi_\gamma) \qquad (\sigma_0 = const.), \tag{33}$$

$$\sigma_{\beta\gamma} = \sigma_0(\Psi\gamma - \Psi_\beta)^3(3\Psi_\alpha). \tag{34}$$

Summarizing, the calculation of interfacial tensions in the three-phase region are performed according to the following algorithm:

1. Specify the overall composition $\rho = (\rho_\alpha, \rho_\beta, \rho_\gamma)$ and fix $a_4 \prec 0$.
2. Select $a_3(\rho)$ such that $\mid a_3 \mid \preceq 4(-\frac{a_4}{6})^{\frac{3}{2}}$ and find θ (cf. eq. (31).
3. Calculate Ψ_α, Ψ_β, and Ψ_β from eq. (27).
4. Find $\sigma_{\alpha\beta}, \sigma_{\beta\gamma}$ from eq. (33) and eq. (34).

The equilibrium spreading coefficient S^{eq}(cf. eq.(14) and, consequently, the type of wetting regime, can be now readily determined. The interfacial tension plots corresponding to the path 2 in the composition space which enters the three-phase region through a tieline where two phases are in equilibrium (cf. Figure 4) and leaves it through a similar tieline is shown in Figure 6.

5. OIL LAYERS IN THE PORE SPACE

This section is concerned with a simple model describing behavior of three phases in a wedge appearing in pore space [7,8]. The oil-water contact angle is assumed to be smaller than the gas-oil contact angle i.e, $\theta_{ow} < \theta_{go}$ (see Figure 7a). In addition, only the radii of the curvature, r_{ow} and r_{go},of the oil-water, and gas-oil interfaces in the plane of the edge are assumed to be finite. Consequently, the oil-water- and gas-oil capillary pressures are given by $P_{cow} = \sigma_{ow}/r_{ow}$ and $P_{cgo} = \sigma_{go}/r_{go}$, respectively. The oil layer ceases to be stable as soon as the oil-water-solid contact line coincides with the gas-oil-solid contact line (see Figure 7b). In this case, the distance AB shown in Figure 7b for an interface of radius r and contact angle θ is given by the following expression,

$$AB = r\frac{\cos(\theta + \beta)}{\sin\beta}, \tag{35}$$

where β is half angle of the wedge and $\theta + \beta < \pi/2$.

A ratio of interfacial curvatures associated with oil-water and gas-oil interfaces is defined as follows,

$$R = \frac{r_{ow}}{r_{go}} = \frac{P_{cgo}}{P_{cow}} \frac{\sigma_{ow}}{\sigma_{go}}. \tag{36}$$

If $r_{go} >> r_{ow}$,then the oil layer becomes very thick. As $R- > 0$, only oil remains in the wedge. The coincidence of the oil-water-solid and gas-oil-solid contact lines occurs at the critical ratio R_c of interfacial curvatures R_c,

$$R_c = \frac{\cos(\theta_{go} + \beta)}{\cos(\theta_{ow} + \beta)}. \tag{37}$$

Thus, a stable oil layer separating gas and water is possible only when $R < R_c$. For $R > R_c$, the oil layer is absent and there is a gas-water interface in the wedge.

Assuming that a molecular film of water covers the porewalls and that the system is water-wet (i.e., $\theta_{ow} = \theta_{gw} = 0$), the balance of forces at the gas-oil-solid contact line gives the following relationship,

$$\sigma_{gw} = \sigma_{go} \cos\theta_{go} + \sigma_{ow}. \tag{38}$$

Eq.(38) can be restated as follows,

$$\cos\theta_{go} = 1 + \frac{S^{eq}}{\sigma_{go}}. \tag{39}$$

Using the above relationship, the critical ratio R_c defined by eq.(37) is given by the following expression,

$$R_c = 1 + \frac{S^{eq}}{\sigma_{go}} - (-\frac{S^{eq}}{\sigma_{go}})^{\frac{1}{2}}(2 + \frac{S^{eq}}{\sigma_{go}})^{\frac{1}{2}} \tan\beta. \tag{40}$$

Figure 3b explains behavior of oil layers present in a wedge as the spreading. coefficient decreases from zero to a negative value. It turns out that the critical ratio R_c decreases as the spreading coefficient S^{eq} decreases. This explains why in strongly water-wet systems oil layers may be present for $S^{eq} < 0$, and absent for $S^{eq} = 0$.

6. FINAL REMARKS

The simultaneous equilibrium of three phases has been described in two cases: (a) the complete wetting regime near a tricritical point and (b) in a capillary tubing of polygonal cross-section. In the former case the macroscopic condition that must be imposed on the three coexisting phases is absence of a line of three-phase contact or, equivalently, that the equilibrium spreading coefficient $S^{eq} = 0$. In the case where three-phases are situated in the edge of a polygonal tubing, it is possible to link the capillary pressures associated with the water-gas, oil-gas, and oil-water interfaces with their interfacial curvatures using Laplace equation of capillarity. Consequently, unlike the former case, the oil layers in wedges of capillary tubings can be found even when $S^{eq} < 0$. However, as the spreading coefficient decreases, the the critical ratio R^c also decreases and oil layers become less likely to exist.

REFERENCES

1. J.S. Rowlinson and B. Widom, *Molecular Theory of Capillarity* (Oxford University Press, 1982).

2. Griffiths R.B., Thermodynamical model for ternary and quarternary fluid mixtures. *J. Chem. Phys.* **60**:195 (1974).

3. Tisza L., *Generalized Thermodynamics* (The MIT Press, 1966).

4. M. Kaufman and R.B. Griffiths, Thermodynamic model for tricritical mixtures with application to ammonium sulfate + ethanol + benzene. *J. Chem. Phys.* **76**:1508 (1982).

5. B.Widom , Noncritical interface near a critical endpoint, *J. Chem. Physics*, **67**:872 (1977).

6. D.J. Klinger, M.J. Fisher, and B. Widom, Surface tension variation in multiphase fluid systems, *J. Phys. Chem.*, **87**:2841 (1983).

7. D.H. Fenwick and M. Blunt, Three-dimensional modeling of three phase imbibition and drainage, *Advances in Water Resources,* **21**:121 (1998).

8. M. Dong, F.L. Dullien, and I. Chatzis, Imbibition of oil in film form over water present in edges of capillaries with an angular cross section, *J. Colloid and Interface Science*, **172**:21 (1995).

CAPTIONS

Figure 1: Entrapped oil ganglion blocking a capillary.

Figure 2: (a) Oil phase spread on water in the presence of their common vapor prior to equilibration. The initial spreading spreading coefficient $S^i < 0$. (b) The configuration of three equilibrated phases in the complete wetting regime ($S^{eq} = 0$). (c) The configuration of three equilibrated phases when $S^{eq} < 0$.

Figure 3: (a) Variation of the equilibrium spreading coefficient S^{eq}as a thermodynamic field μ changes. At $\mu = \mu^*$ there is a transition between the complete and partial wetting regimes [1]. (b) Variation of the equilibrium spreading coefficient S^{eq} in a square-sectional tubing as the critical ratio of capillary pressures R_c decreases.

Figure 4: Three-phase region in an isothermal composition space. It is a three-dimensional volume spanned by an infinite series of triangles (three of which are shown in the Figure. The points in the interior of each triangle represent the overall compositions of mixtures whose phase compositions lie at the triangles' vertices. The lines $K_{1,2}$ and $K_{2,3}$ are critical phases in equilibrium with a noncritical phase (C and A). Also shown are paths 1 and 2 along which the interfacial tension is often experimentally investigated.

Figure 5: Schematical representation of the three-phase region as a tricritical point is approached (after [1]).

Figure 6: Interfacial tension determined using the Landau-Griffiths model. vs. distance in the isothermal density space corresponding to path 2 shown in Figure 4.

Figure 7: (a) Configuration of oil, water, and gas in an angular corner with half angle β: the oil layer is stable (b) Configuration of the three-phases where the gas-oil and oil-water interfaces touch at point B: the oil layer is unstable (modified after [7]).

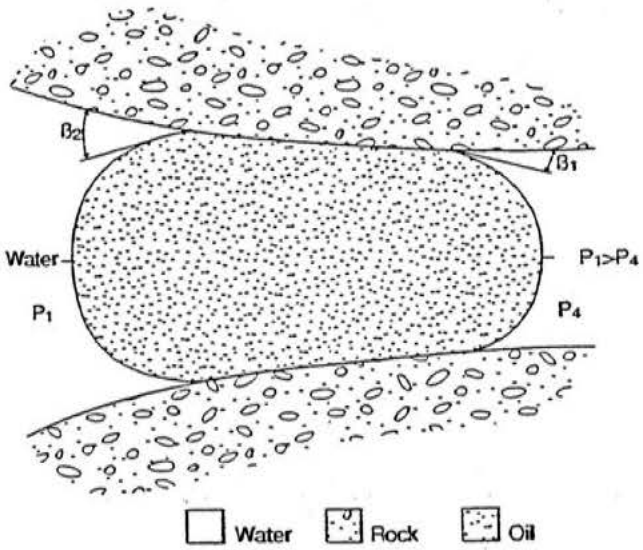

A. Winter, Figure 1

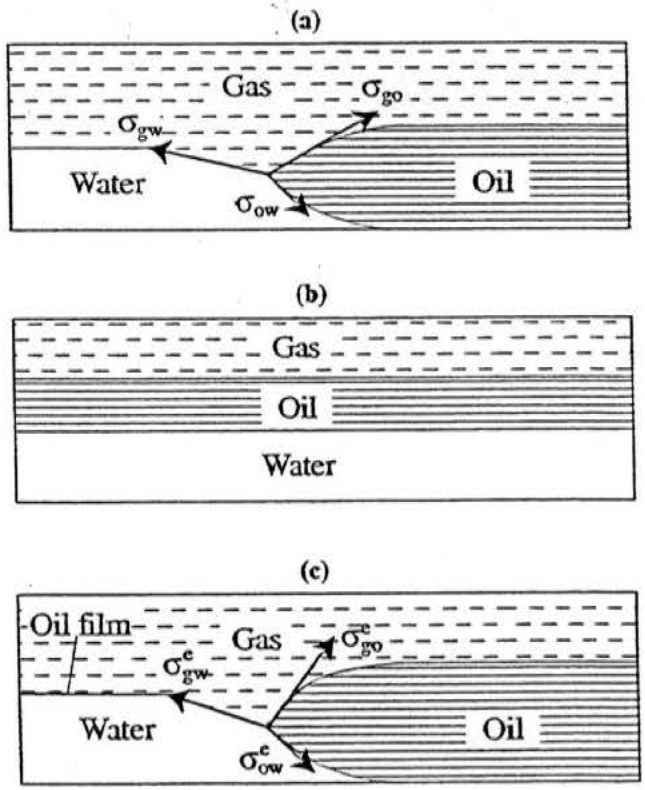

A. Winter, Figure 2

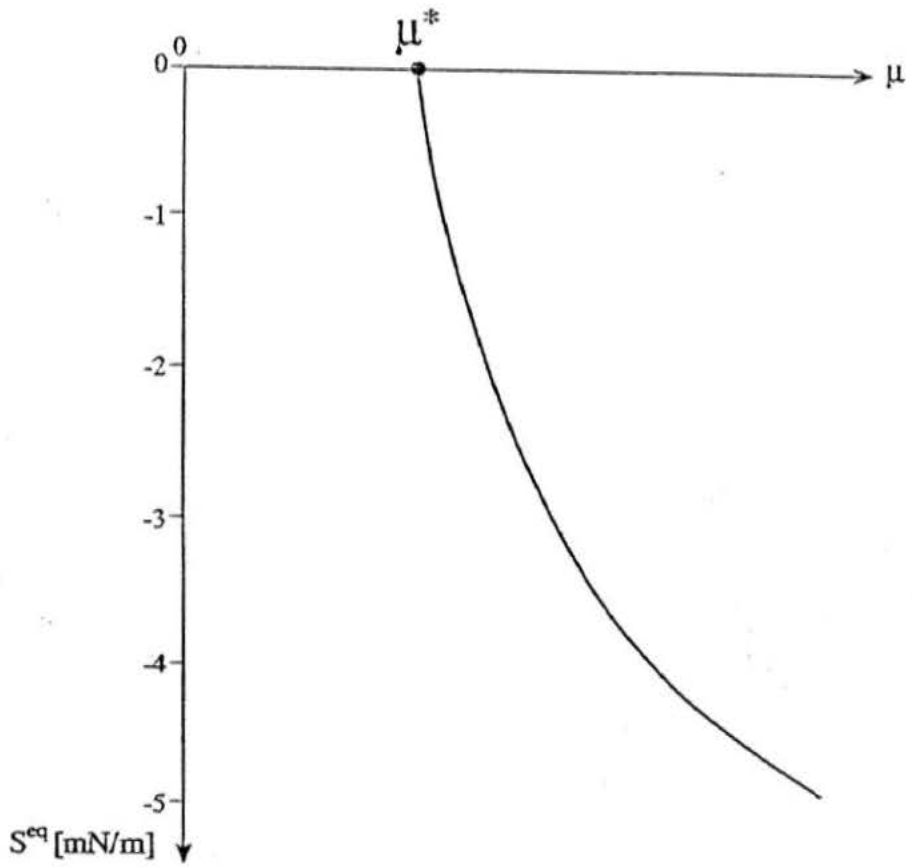

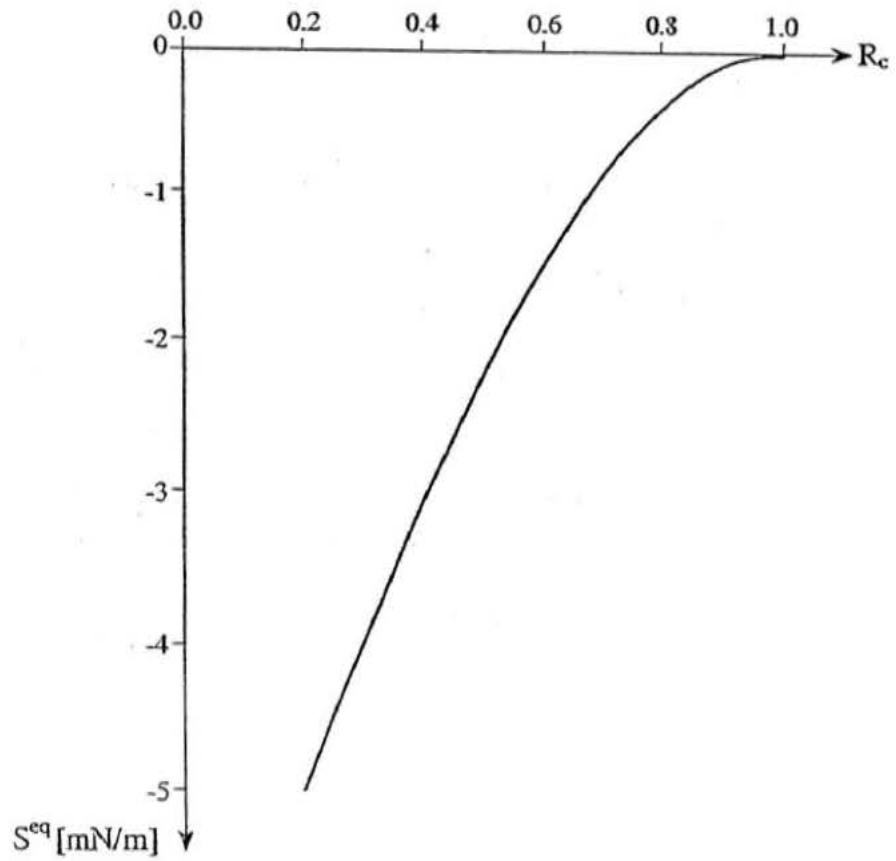

A. Winter
Figure 3

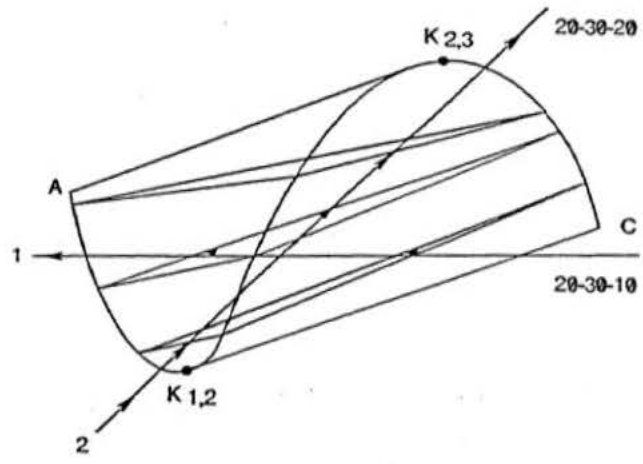

A.Winter

Figure 4
VHN02.00.010 AW EOR/20

A. Winter

Figure 5

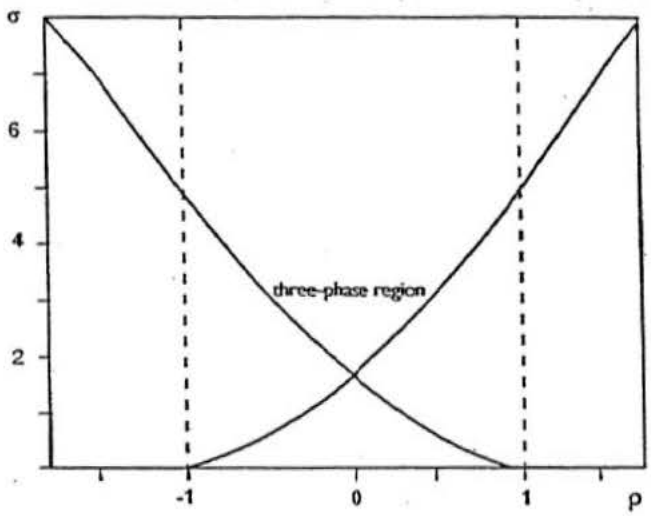

Figure 6
A. Winter

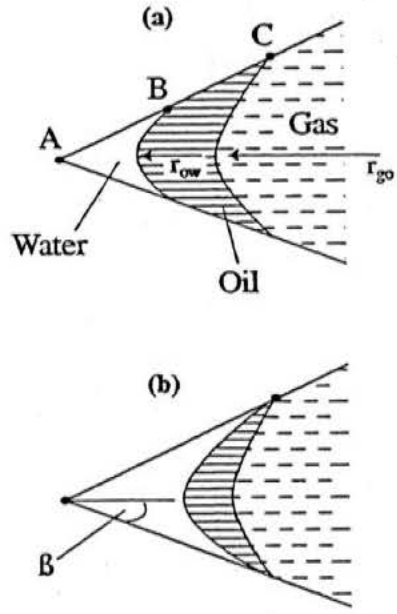

A. Winter, Figure 7

MULTISCALE MODELING OF RELATIVE PERMEABILITIES[4]

A. Winter[1], J.K. Larsen[2,3], and N. Bech[1]

Geological Survey of Denmark and Greenland, Thoravej 8, DK-2400 Copenhagen NV, Denmark[1], Enviroment and Resources, Technical University of Denmark, DK-2800 Lyngby, Denmark[2]

Abstract:

Hydrocarbon reservoir simulators describe transport processes at the scale of a grid block (~1000 m^3). However, relative permeabilities are measured in laboratory experiments using small plugs cut from reservoir core (~ 100 cm^3). Consequently, a major task in performing realistic field simulations is that of relating laboratory core measurements to the grid-block scale. This is the upscaling problem.

This paper describes a two-scale strategy aimed at determination of three-phase relative permeabilities for gas injection and Water-Alternating-Gas (WAG) injection processes, respectively. A large separation and weakly coupling is assumed between the individual scales.
More specifically, two models describing three-phase transport at the pore- and macroscopic scales, respectively, are introduced. In particular, a network simulator and 1-D grid-based reservoir simulator of three-phase displacement are implemented and sequentially resolved in separate calculations. The relative permeabilities determined from a computation at the pore-scale are iteratively fed into a computation at the macroscopic scale. At the fixed point of the iteration procedure the self-consistent saturation trajectories and the associated relative permeability functions for three coexisting phases (oil, water, and gas) are determined. Finally, the conditions under which the iterative procedure leads to self-consistent three-phase relative permeabilities are discussed.

---

[3] Present address: Maersk Oil and Gas AS, Esplanaden 50, 1263 Copenhagen K, Denmark.
[4] Accepted for presentation at the 22-nd IEA Workshop and Symposium, September 9-12, 2001, Vienna, Austria.

1. Checkerboards and Balloons: Two Classes of Complex Model Systems

Checkerboards

The checkerboard-type systems can be viewed as model systems in which the spanning vectors of length ξ are invariant under spatial translations. The magnitude of ξ represents the range of statistical correlations. More precisely, a checkerboard-type system consists of identical squares of length ξ. It appears as a homogeneous one when observed using an optical instrument with a minimal resolution scale $a > \xi$. On the other hand, when the range ξ of the statistical correlations between the squares is too short to generate collective macroscopic effects, the scales decorrelate. Consequently, fluctuations taking place inside an elementary square do not affect the system as a whole. Thus, an investigation of the system can be reduced to a study involving only a single square. Another useful interpretation of ξ is to view it as a value separating the microscopic properties pertaining to a single square from the macroscopic scale pertaining to the entire system. In local microscopic analyses, the quantities associated with scales larger than ξ are constant and can be considered as parameters. Thus, the impact of microscopic fluctuations on the macroscale is accessible only by averaging which effectively eliminates randomness.

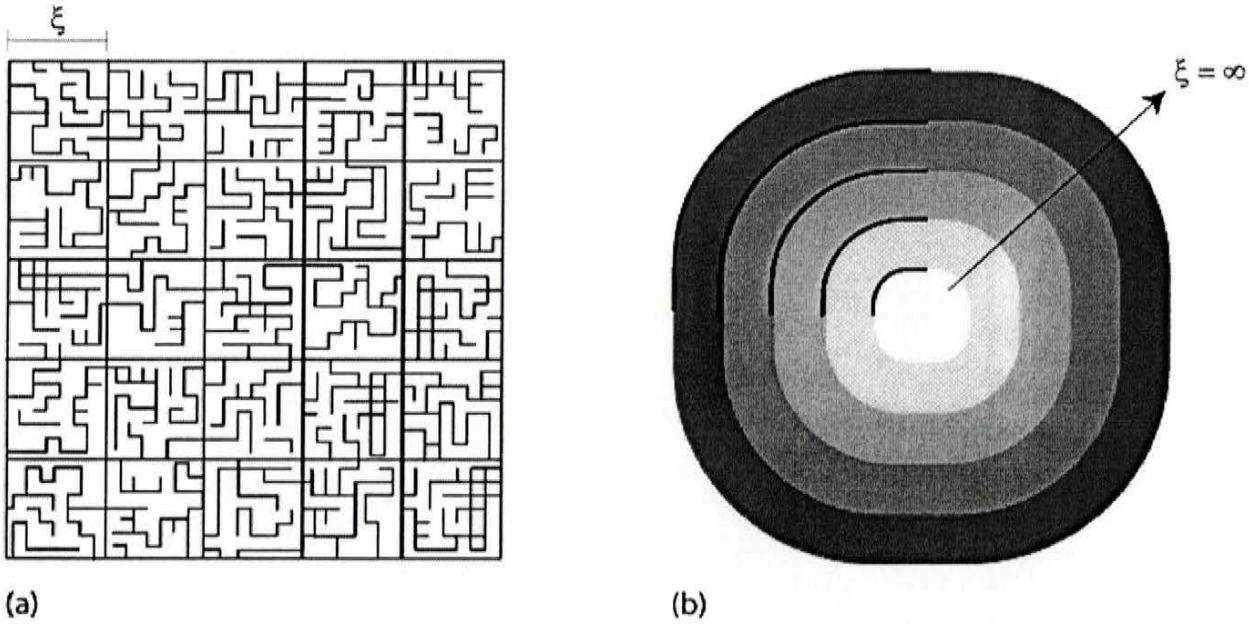

Figure 1. Two types of complex systems: (a) checkerboard-type system: after several "inverse decimations" of a continuous porous medium, the microscopic scale is reached. (the initial checkerboard-type system and the result of the last inverse decimation are shown). The microscale properties, such as pore geometry and topological properties of the porous network and those of the checkerboard-type system are described by *two different models*. (b) Balloon-type systems with infinite characteristic lengths. The bold line preserves its structural and topological properties as the balloon surface is dilated (modified after Lesne, 1998).

Balloons

Entirely different model porous media are balloon systems that have a self-similar structure throughout a large range of scales. Balloon systems do not have any characteristic length with exception of their size and a minimal scale below which the model is no longer valid. More precisely, in self-similar systems a characteristic scale $\xi > 0$ must coincide with its dilations $k\xi$. Consequently, it must be infinite. This is why in balloon-type systems, in contrast to checkerboard systems, the microscopic fluctuations can be observed at the macroscale. Blowing the balloon leads to dilations and deformations of the balloon surface. However, its topological and structural properties remain the same. It should be noted that in the case of balloon-type systems it is not possible to introduce decomposition into a set of statistically independent subsystems. Any fluctuation on the microscale is reflected on every other scale.

2. Scales and Characteristic Sizes

The notion of characteristic size occupies a central position in the study of mathematical models of multiphase fluid flow in porous media. Broadly speaking, it links properties of pore spaces to the scale on which they are investigated. Also, it provides means to impose stratification on external parameters controlling mechanisms of multiphase transport.

There is no unique definition of characteristic size. This reflects the fact, that *only its magnitude* has a real physical meaning. Three examples of alternative ways to define the characteristic size of a hypothetical petrophysical property $K(x)$, which depends on a position coordinate x, are given below (cf. Lesne, 1998):

- The dominating behavior of $K(x)$ is oscillating. The characteristic scale can be determined by performing Fourier analysis of $K(x)$. In the case where there is only one peak in the spectrum, ξ_K is uniquely defined as the wavelength of the maximal spectral component.
- Presence of multiple peaks in the spectrum indicates that $K(x)$ has several characteristic scales. An average over a large number of oscillations $\langle\ \rangle$ is given by an approximate analytic formula:

$$\xi_K \sim 2\frac{\langle \sup K \rangle - \langle \inf K \rangle}{\left\langle \left| \frac{dK}{dx} \right| \right\rangle} \tag{1}$$

- In the case where K is of the form $K_\alpha(x) = k(x/\alpha)$, the characteristic sizes of K and k are linked by $\xi_K = \alpha\xi_k$ where α is a dimensionless quantity.

One of the key issues in multiscale modeling is how the different scales are linked to each other. The degree of coupling between the scales depends on the physics governing the system under consideration. Consequently, in some computational approaches to modeling of multiscale systems the scales are treated sequentially in separate calculations. In other, they are treated concurrently. It

should be noted that sometimes the scales are so strongly coupled that multiscale modeling cannot be used.
It turns out that in systems with weakly coupled scales, the phenomena associated with each scale are most efficiently treated sequentially: parameters determined from the computation at small scale and subsequently fed into a computation at a larger scale. The iterative procedure for the determination of self-consistent relative permeabilities described in Section 6 is an example of a sequential coupling between two scales.

3. Quasi-static Network Simulator

The network simulator is set up on a cubic lattice in three spatial dimensions. The number of nodes in each direction is *lx, ly,* and *lz.* The total number of nodes is $N = lx \cdot ly \cdot lz$. The distance between the nodes, l_{node} , is a lattice constant. Each typical node is connected to six neighboring nodes. The inlet face is defined as the first row of nodes in the *x*-direction and the outlet face as the last row of nodes. Flow takes place from the inlet face to the outlet face. Periodic boundary conditions have been assumed on the faces perpendicular to the flow directions to minimize the finite size effects.

The lattice nodes represent pore chambers. The links between the nodes stand for pore throats. Pore sizes are defined by the uniform distribution function with the limiting values given by $r_{t,\max}$, $r_{t,\min}$, for the pore throats and $r_{c,\max}$, $r_{c,\min}$, for the pore chambers, respectively. The pore throats and pore chambers are assumed to have square-sections.

A number varying between 0 and 1 described by the random probability distribution function gives the size of a chamber. Similarly, a random number varying between 0 and 1 describes the size of the pore throat, rt.

The network simulator developed in the course of this project was based on a quasi-static network model. In quasi-static network models the capillary pressure is imposed on the network. The final, static positions of all fluid-fluid interfaces are subsequently determined. Dynamic aspects of pressure propagation within the model and interface dynamics are not considered. For more details about quasi-static network models the reader is referred e.g. to Fenwick and Blunt (1996; 1997, 1998).

4. Macroscopic Model of Three-Phase Flow

Macroscopic model of three-phase immiscible and incompressible flow in one dimension consists of the following relationships stated for each of coexisting phases (cf. eq. (2)):

- Darcy's law generalized to three-phase flow,
- the mass conservation equation,
- the condition for the capillary equilibrium relating the phase and capillary pressures.

The equations defining the model are as follows.

$$
\begin{aligned}
&u_i = -k\lambda_i \frac{\partial p_i}{\partial x}, \\
&\lambda_i = \frac{k_{ri}(s_1, s_2)}{\mu_i}, (i = 1,2,3), \\
&\phi \frac{\partial s_i}{\partial t} + \frac{\partial u_i}{\partial x} = 0, (i = 1,2,3), \\
&s_1 + s_2 + s_3 = 1, \\
&p_3 - p_1 = P_1(s_1, s_2), \\
&p_2 - p_3 = P_2(s_1, s_2),
\end{aligned}
\tag{2}
$$

where $i=\{1,2,3\}$ ($i=1$, represents the phase with the strongest wetting preference with respect to the porewalls, $i=2$ is its counterpart with the weakest wetting preference, and $i=3$ is the phase with the intermediate wetting preference. Thus, in the case of a water-wet hydrocarbon reservoir the indices 1,2,3 stand for water, oil, and gas, respectively. On the other hand, for an oil-wet reservoir these indices represent oil, gas, and water. Moreover, u_i is the flow velocity, μ_i - viscosity, p_i - pressure, ϕ_i porosity, P_1 and P_2 are the capillary pressures, k- the absolute permeability, k_{ri} - the relative permeability to *i-th* phase, and x the coordinate.

By eliminating the phase pressures p_i the model is reduced to following system of coupled equations

$$
\begin{aligned}
&\phi \frac{\partial s_1}{\partial t} + U \frac{\partial F_1}{\partial x} = -k \frac{\partial}{\partial x}\left\{\lambda_1\left[(1 - F_1)\frac{\partial P_1}{\partial x} + F_2 \frac{\partial P_2}{\partial x}\right]\right\}, \\
&\phi \frac{\partial s_2}{\partial t} + U \frac{\partial F_2}{\partial x} = k \frac{\partial}{\partial x}\left\{\lambda_2\left[F_1 \frac{\partial P_1}{\partial x} + (1 - F_2)\frac{\partial P_2}{\partial x}\right]\right\}, \\
&U = \sum_{i=1}^{3} u_i, \\
&\frac{\partial U}{\partial x} = 0, \\
&F_i(s_1, s_2) = \lambda_i \left(\sum_{J01}^{3} (\lambda_j)\right)^{-1}
\end{aligned}
\tag{3}
$$

The flux functions, $F_i(s_1, s_2)$ (cf. eqs. (3)), are defined in the saturation triangle described by the inequalities $\Delta_s = \{s_1 \geq 0, s_2 \geq 0, s_1 + s_2 \leq 1\}$ and $F_1 \geq 0, F_2 \geq 0, F_1 + F_2 \leq 1$. Moreover, $F_i = 0$ for $s_i = 0$ and $F_i = 1$ for $s_i = 1$. Consequently, the map $s \to F(s)$ transforms the saturation triangle into

another triangle, Δ_F. The vertices and sides of Δ_s are mapped into their counterparts belonging to Δ_F. More precisely, the triangle Δ_F can be decomposed into three domains corresponding to one-phase flow, two-phase flow. and three-phase flow, respectively. As the saturation of any of the three phases decreases, its continuity breaks down. The capillary forces are usually much stronger than the available pressure gradient keeping the emerging ganglia immobile. Thus, both the relative permeability k_{ri} and the flux function F_i become equal to zero.

5. Evolvability of Macroscopic Models of Three-Phase Transport

One of the key properties of the macroscopic model of three-phase transport with negligible capillary forces is its evolvability (cf. eq. (5) with $P_1 \approx 0, P_2 \approx 0$). It has a simple geometric interpretation. Consider two saturations, s_1 and s_2 in the saturation triangle and the flux functions $F_1(s_1, s_2)$ and $F_2(s_1, s_2)$.

Small increments of saturations, ds_1 and ds_2, result in modifications of the two flux functions: $F_i(s_1 + ds_1, s_2 + ds_2) = F_i + dF_i$ (i=1,2). Eq. (5) with negligible capillary forces at the point (s_1, s_2) is referred to as being *evolvable* if there exist two directions resulting in proportional increments of the flux functions (cf. Varchenko et al., 1992).

$$\begin{aligned} dF^{(1)} &= \left(dF_1^{(1)}, dF_2^{(1)}\right) \\ dF^{(2)} &= \left(dF_1^{(2)}, dF_2^{(2)}\right) \end{aligned} \tag{4}$$

On the hand, the increment (ds_1, ds_2) results in a change of direction and magnitude of the vector (dF_1, dF_2), the system is referred to as being *non-evolvable* (cf. Figure 2). An important issue is whether the loss of evolvability at the macroscale can be related to pore-scale transport mechanisms, such as e.g., the snap-off mechanism.

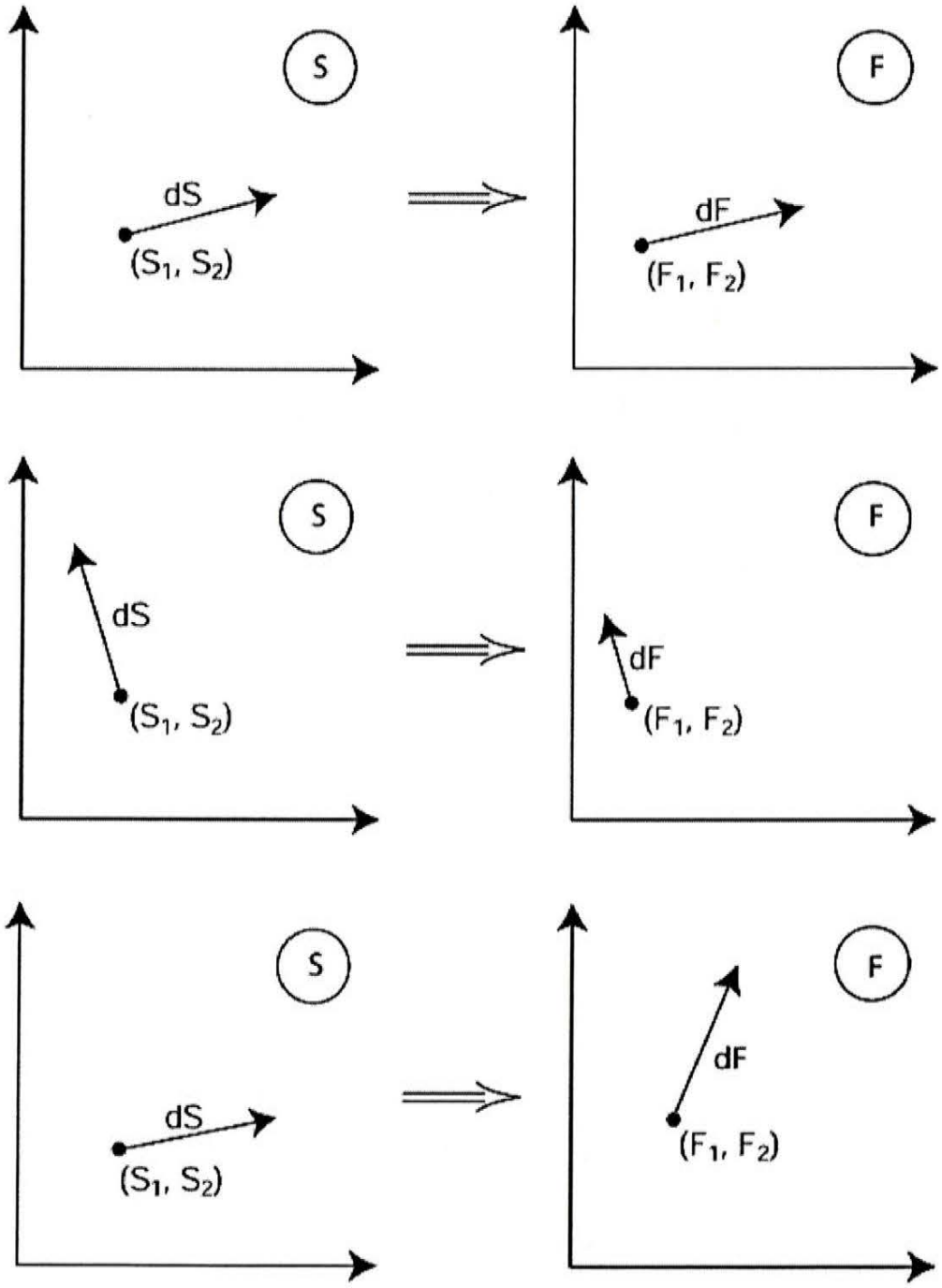

Figure 2. Evolvability of macroscopic models of three-phase transport in porous media. The two upper rows represent evolvable system; the bottom row shows a non-evolvable system (after Varchenko et al., 1992).

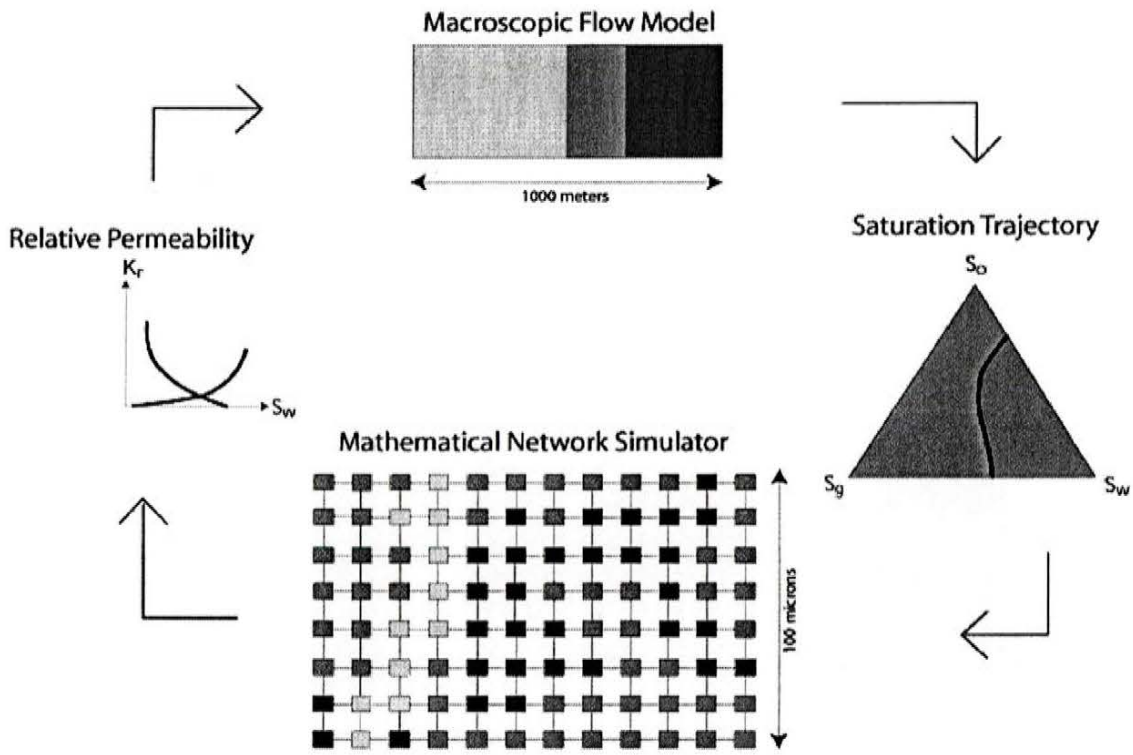

Figure 3. Schematic drawing of the self-consistent procedure. An initial guess of relative permeability functions is fed to the macroscopic flow model that generates a saturation trajectory. The network simulator follows that trajectory producing a set of three relative permeability functions. The iterative procedure continues until there is no more change in the saturation path.

6. Iterative Procedure

Fenwick and Blunt (1997) described the iterative procedure for determination of self-consistent permeabilities. More specifically, in their paper gas is injected into a waterflooded reservoir. By linking the relative permeability functions determined by the network simulator to the macroscopic reservoir simulator and iteratively computing a saturation path, until the relative permeability functions became scale-invariant, the self-consistent saturation paths and the associated relative permeability functions were obtained. Thus, the relative permeability functions create a link between the pore-level scale and the macroscopic scale.

The iterative procedure applied for obtaining self-consistent three-phase relative permeability functions for three-phase flow in porous medium is as follows (cf. Figure 3):

- Given initial conditions, injection conditions, viscosities of the phases, the network simulator performs a displacement into three-phase region of the saturation triangle.
- The displacement results in a set of three-phase relative permeabilities tabulated as functions of their own saturations for the selected path.
- The tabulated values are input into a one-dimensional reservoir simulator based on Buckley-Leverett model for three-phase flow. The reservoir simulator performs displacement for the same initial and injection conditions as those adopted at the microscale. The resulting saturation path is obtained by plotting the saturations of all grid plots on a ternary diagram.

- The saturation paths produced by the network simulator and those determined by the reservoir simulator are compared. If the two paths are different, the network simulator follows the path obtained from the reservoir simulator. If the paths coincide, the iteration stops.

7. Self-consistent Relative Permeability Functions for Gas Injection

The iterative procedure was initially applied to a gas injection process. The saturation trajectory was generated by the macroscopic model using Corey-type relative permeability functions: $k_{rw} = S_w^2$, $k_{ro} = S_o^2$ and $k_{rg} = S_g^2$. The phase viscosities were $\mu_w = 1.0$, $\mu_o = 0.3$, and $\mu_g = 0.2$. The initial phase saturations were $S_w = 0.4$ and $S_o = 0.6$. The injection of gas corresponds to the left state given by $S_l = (1.0, 0)$. The network simulator was tested on a 30 × 15 × 15 three-dimensional network. The initial guess of relative permeability functions resulted in a saturation trajectory shown in Figure 4.

The initial condition of the network was obtained by the invasion percolation process mimicking the filling of the reservoir with oil. The injection pressure was set to a fraction of the entry pressure of the smallest throat. The saturation of the aqueous phase was $S_w = 0.3$ after injection of oil. The network was then allowed to imbibe water to reach the initial saturation point at $S_w = 0.4$. It should be noted that the first part of the saturation trajectory is a two-phase displacement process where no gas is present. Thus, the gas saturation did not increase until $S_w = 0.34$. The tracking algorithm successfully followed the saturation trajectory of the macroscopic flow model. The distance between the nodes was typically 0.5 saturation units. The network model needed between 20-40 pore-level displacement mechanisms to reach the each desired saturation point on the macroscopic saturation trajectory. It should be noted that some pore-level displacement mechanisms did not lead to a change in saturation because the pore was located outside the zone where saturation was calculated. In the case where no critical pressure lines were crossed by changing capillary pressure, no pore-level displacement mechanisms occurred. However, the saturation still changed, because changes of interfaces' curvature on the pore-level led to a small change in saturation.

The network simulator successfully followed the macroscopic saturation trajectory during the first iteration within a deviation of the specified 0.5 saturation units (cf. Figure 4). The corresponding movement in the capillary pressure space is shown in Figure 5. In most cases, the injection of gas resulted in both increased oil-gas and oil-water capillary pressures. It should be noted that the oil layers remained stable along the entire saturation trajectory. Consequently, the oil phase remained well connected. The stability of oil layers was a consequence of the direction of the saturation trajectory which generally 'demanded' less water causing increased oil-water capillary pressure and more gas causing increased oil-gas capillary pressure.

The displacement mechanisms were dominated by single oil-water Haines' jumps followed by Haines' jumps of gas into the continuous oil phase. The oil-gas Haines' jumps have significantly lower critical pressure than double drainage mechanisms because secondary events are absent when gas invades the continuous oil phase. Consequently, no double drainage mechanisms were activated along the macroscopic saturation trajectory.

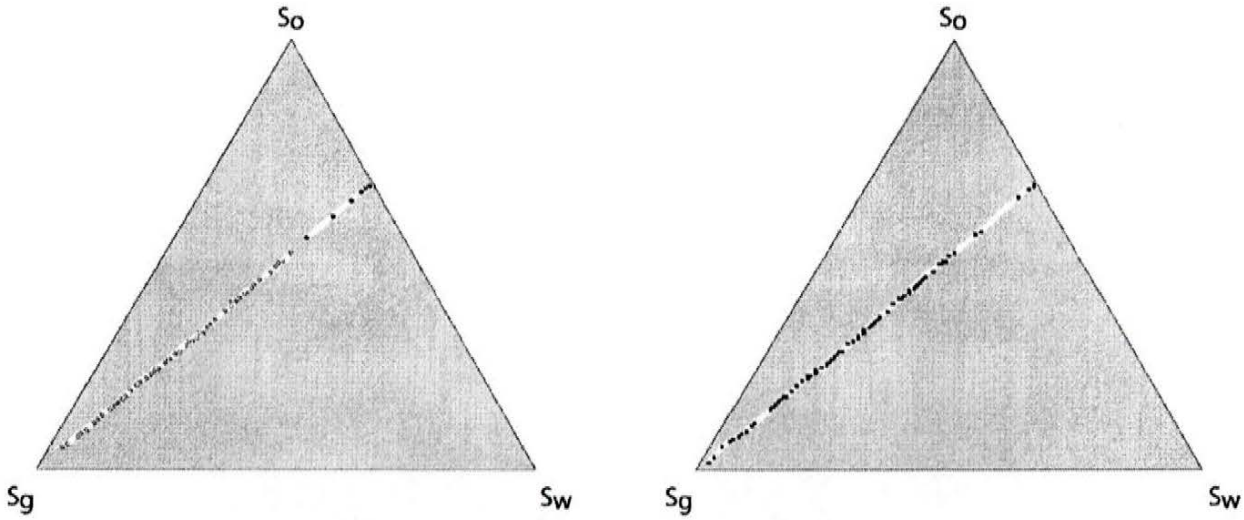

Figure 4. Tracking of the saturation trajectory by the network simulator. The saturation triangle to the left shows the saturation trajectory to be followed in white and the actual saturation trajectory followed by the network simulator in black. To the right is shown the actual followed saturation trajectory at the final state of the simulation. An accuracy of 0.5 saturation units was used.

Figure 5 shows the calculated relative permeability functions of the three phases. Also shown are the initial Corey-type relative permeability functions. The relative permeability functions span four orders of magnitude. The relative permeability function of the gas phase was zero for saturations below $S_g = 0.32$. At $S_g = 0.32$ the gas cluster first spanned the network and connected the inlet to the outlet. The relative permeability at this point was 10^{-2}. For gas saturations in the interval $0.32 < S_g < 0.43$, the relative permeability of the gas only increased slightly because the conductance of the gas phase was controlled by the 'red' bonds in the backbone of the gas cluster. Consequently, the increased relative permeability was solely due to larger effective flow area of the gas phase inside the pores making up the backbone of the gas cluster. At a gas saturations above $S_g = 0.43$ the gas phase began to form a well-connected cluster.

The aqueous phase was continuous throughout the entire saturation trajectory. At the initial two-phase conditions $S_w = 0.4$ the relative permeability was approximately10^{-2}. The relative permeability function decreased gradually to a value as low as 10^{-4}. A crossover behavior in the relative permeability function was observed around $S_w = 0.35$. This reflected the relative permeability of the water phase changing from being controlled by the configuration 1 with pores entirely filled with water to configuration 2, configuration 3 and configuration 4 with pores where the conductance of the water phase is controlled by the corner flow (cf. Figure 6). The relative permeability of water below the crossover point approximately scaled with saturation to the second power in agreement with the observations of Fenwick and Blunt (1998).

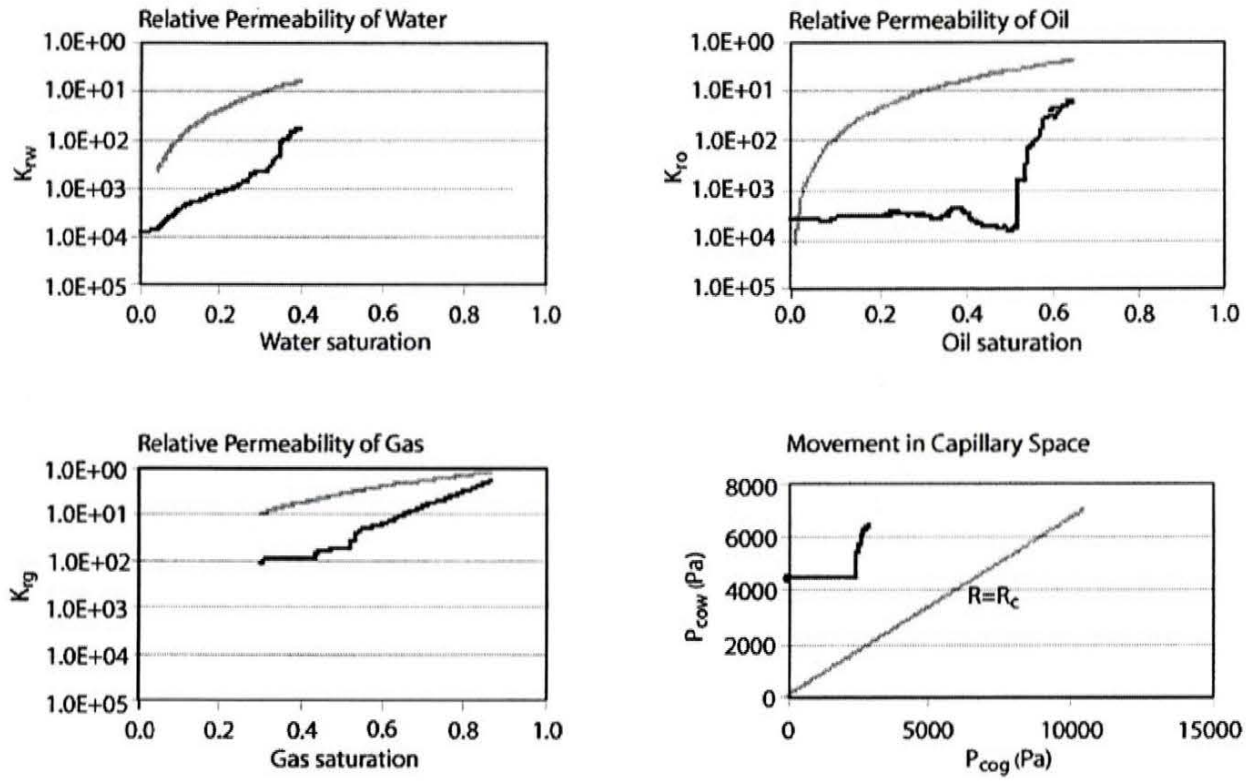

Figure 5. Relative permeability functions for oil, water and gas calculated by the network simulator is shown in black. The initial Corey-type relative permeability functions are shown in gray. The movement in capillary space is shown in the lower right hand corner where the straight line $R = R_c$ indicates the stability limit for oil layers.

The relative permeability of the oil phase was initially controlled by the configuration 2 appearing in pores with oil flowing through the pore centers. The relative permeability of the oil phase quickly decreased as gas displaced oil from the center of the pores. The conductivity of the oil phase was reduced nearly two orders of magnitude with a change of oil saturation from $S_o = 0.6$ to $S_o = 0.5$. Further reduction of the oil saturation led to an interesting phenomenon. The increased oil-water capillary pressure forced the oil to invade new pores. Consequently, the oil phase formed a well-connected cluster on the network level. Although the effective flow area of the oil phase within the individual pores was reduced, the overall conductance of the oil phase on the network level increased. More precisely, below the oil saturation $S_o = 0.5$, the oil relative permeability fluctuated between 10^{-4} and 10^{-3}. Thus, the relative permeability of the oil phase below $S_o = 0.5$ was primarily controlled by how well that phase was connected in the porous network.

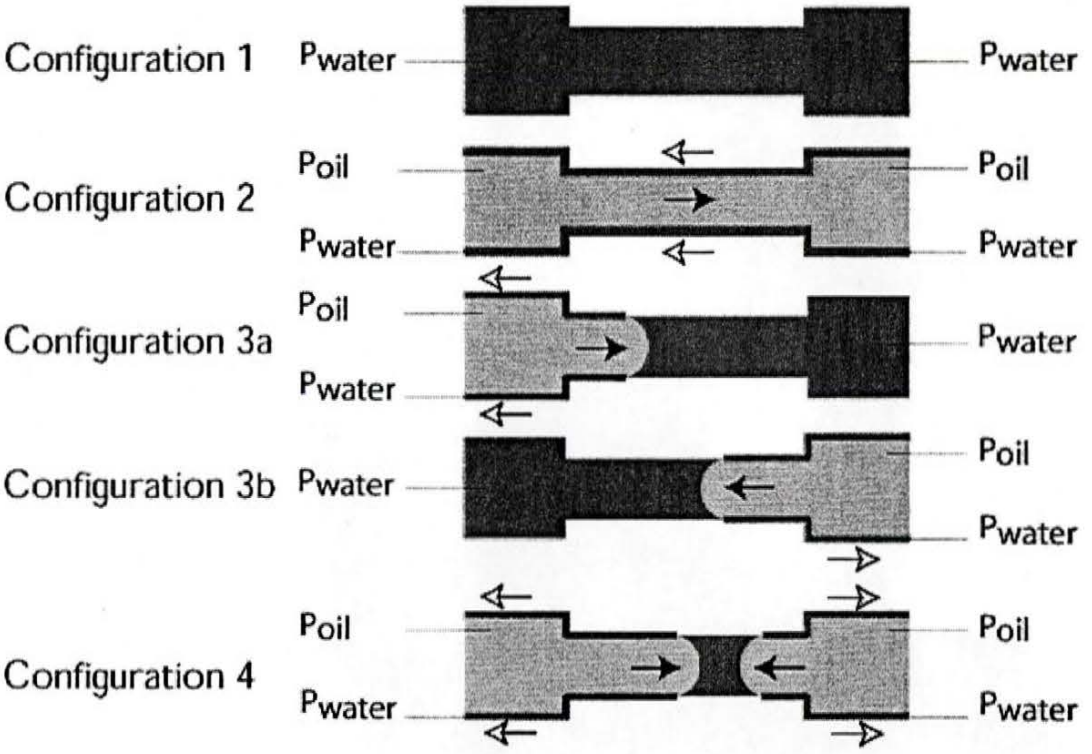

Figure 6. Four principal fluid configurations between two nodes. Water is always connected and the water pressure is defined for all nodes. The water and the oil phases flow in two separate compartments in configuration 2. Configurations 3a and 3b are symmetric and essentially can be considered as representing the same transport mechanism. In (3a) oil displaces water, in (3b) the roles of oil and water are reversed. In configuration 4 oil displaces water by two opposite menisci. Thick arrows indicate flow of oil while thin arrows indicate flow of water along the corners of the capillary tube.

8. Convergence of Iterative Procedure for Gas Injection

The search for self-consistent relative permeability functions was pursued by the iterative procedure. The self-consistent relative permeability functions of the seventh iteration are shown in Figure 7. Also shown are the relative permeability functions determined in the sixth iteration and the corresponding movements performed by the network simulator in the capillary pressure space.

The relative permeability functions of gas and water did not change much during the remaining iterations. Consequently, the water and gas relative permeability functions appeared to be functions of their own saturations during the search for self-consistent relative permeability functions. However, it should be noted that the movement in capillary pressure space was very different for each of the seven iterations.

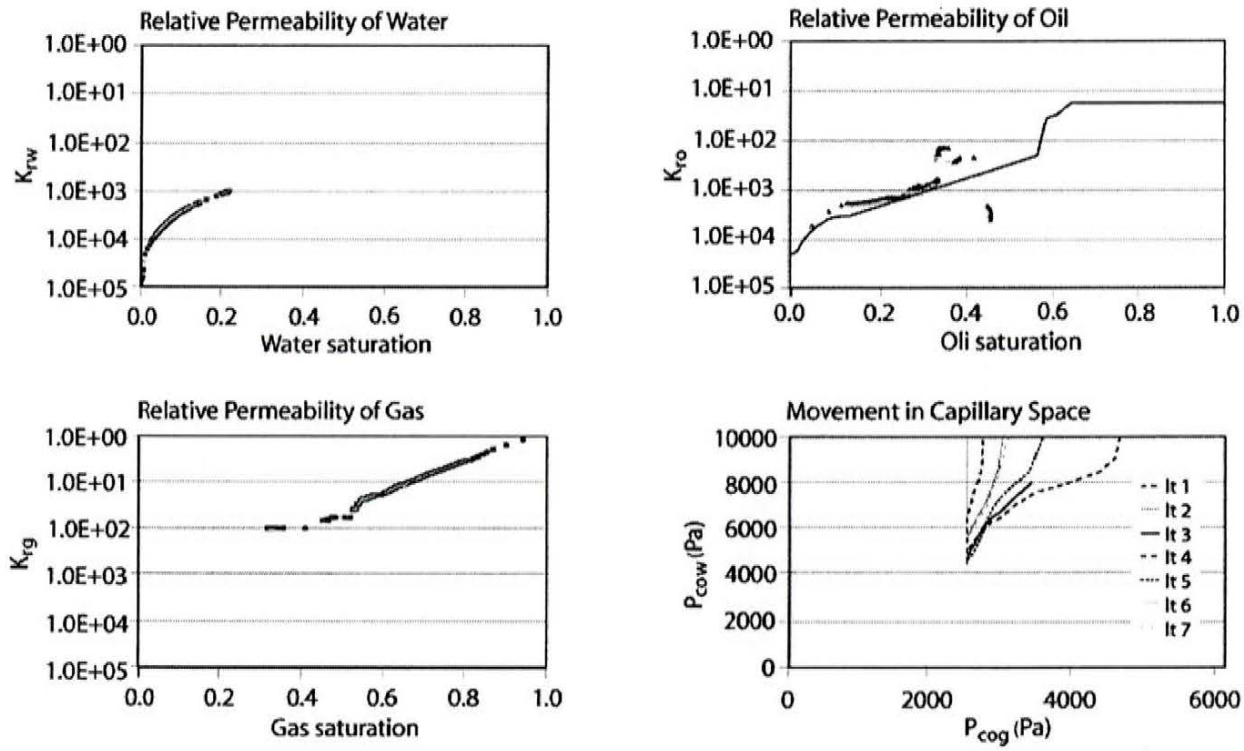

Figure 7. The self-consistent relative permeability functions for gas injection with initial conditions S = (0.0, 0.4) using Corey-type relative permeability functions as initial guess for the saturation trajectory. The movement in the capillary pressure space is shown for all seven iterations.

The relative permeability function of oil posed some difficulties because the ECLIPSE 100 simulator requires that the relative permeability functions for the oil phase is monotonically increasing with increasing phase saturation. This requirement was not always fulfilled by the relative permeability functions delivered by the network simulator. In particular, for the higher oil saturations the network model yielded increasing relative permeability for decreasing oil saturation. The higher conductivity was caused by the fact that oil displaced water that caused formation of highly conductive configuration 2 (cf. Figure 6). On the other hand, gas displaced oil from pores that did not belong to the backbone of the oil cluster. Consequently, smaller oil saturation could cause an increase in oil conductance and non-increasing relative permeability functions of the oil phase. This is the reason why in the range $0.176 < S_o < 0.57$ it was necessary to approximate the relative permeability functions of the oil phase by a straight line and search for the self-consistent relative permeability function by changing the slope of that line. Thus, using the relative permeability functions from the network model in the macroscopic model was associated with a subjective adjustment of the relative permeability function. Nevertheless, the iterative procedure converged in spite of the fact that as much as seven iterations were needed. The slow convergence was caused by oscillations of the relative permeability function of the oil phase around the self-consistent relative permeability function. More precisely, during the iteration procedure significant parts of the saturation trajectories were located on the gas-oil base line corresponding to very low water saturations (cf. Figure 8).

The movement in capillary space can be better understood by considering the saturation trajectories associated with the movements in capillary pressure space. The saturation trajectories oscillated

around the self-consistent saturation trajectory. The oscillation reflects the movements in capillary pressure space that are located either above or below the self-consistent trajectory in the capillary pressure space. The saturation trajectories with a significant parts located on the oil-water base line corresponded to movements in capillary space where the oil-water capillary pressure was too large as compared to the final self-consistent trajectory in capillary pressure space.

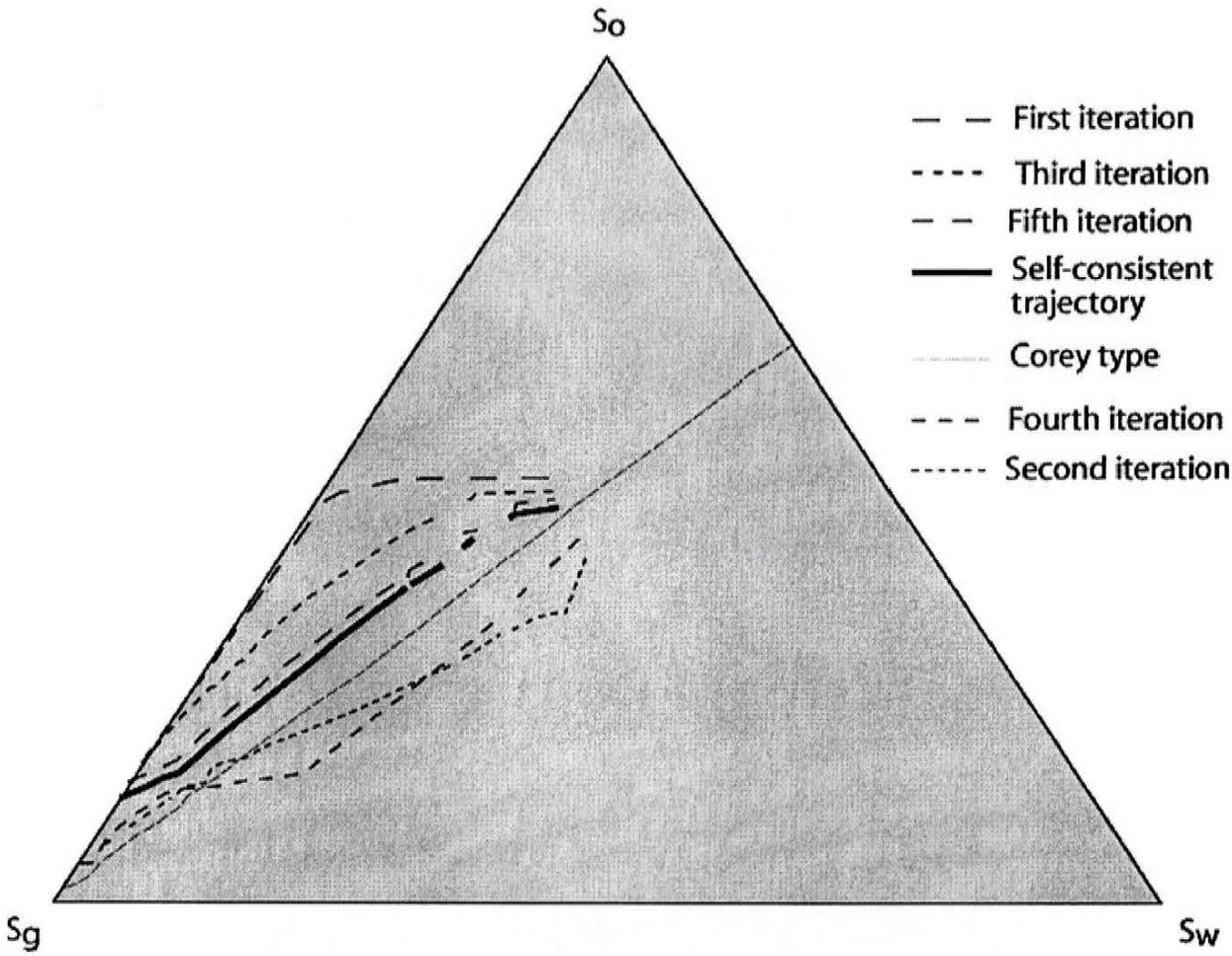

Figure 8. Saturation trajectories of the seven iterations followed by the network simulator. The initial saturation of all the trajectories is S_r = (0.0, 0.4), but is only shown for the saturation trajectory of the initial Corey-type relative permeability functions. The convergence of the iterative procedure is slow because the iterations oscillate around the self-consistent saturation trajectory. It should be noted that some of the trajectories are located on the gas-oil base line corresponding to no water. Low water content corresponds to a high oil-water capillary pressure.

Comparisons of the different movements in capillary pressure space and the corresponding movements in the saturation triangle have shown that the capillary pressure response is structurally stable: its changes appear to be moderate for moderate changes in saturation trajectory. In other words, two saturation trajectories close to each other are associated with movements in capillary pressure space, which are also close to each other. However, that is not to say that the relative permeabilities do not change drastically as functions of phase saturation. Moreover, the

macroscopic simulator does not exhibit the property of structural stability in the case where a small change in relative permeability functions results in a drastic change of a saturation trajectory.

9. Selfconsistent WAG Injection Sequences

The iterative procedure was applied to a WAG injection sequence. Three cases corresponding to different injection ratios between water and gas were tested. The initial state was chosen as $S_r = (S_g, S_w) = (0.08, 0.16)$. The injection ratios corresponding to the left state $S_l = (S_g, S_w) = (0.35, 0.65)$, $S_l = (S_g, S_w) = (0.40,0.60)$ and $S_l = (S_g, S_w) = (0.45, 0.55)$ were investigated using the Corey-type relative permeability functions $k_{rw} = S_w^2$, $k_{ro} = S_o^2$ and $k_{rg} = S_g^2$. The adopted values of fluid viscosities were as follows: $\mu_w = 0.5$ $\mu_o = 1.0$ and $\mu_g = 0.3$. The initial saturation trajectories determined from the macroscopic model are shown in Figure 9.

The movement in capillary space for the WAG injection sequence with $S_l = (S_g, S_w) = (0.45, 0.55)$ is shown in Figure 9. The combination of increased water and gas saturations along the saturation trajectories led to use of the snap-off, I_1-, and I_2- imbibition displacement mechanisms of water displacing oil. The imbibition displacement mechanisms were a consequence of decreasing oil-water capillary pressure. In addition, the increased gas saturation caused increasing oil-gas capillary pressure. Consequently, the movement in the capillary space occurred towards the region in the capillary pressure space where oil layers were unstable.

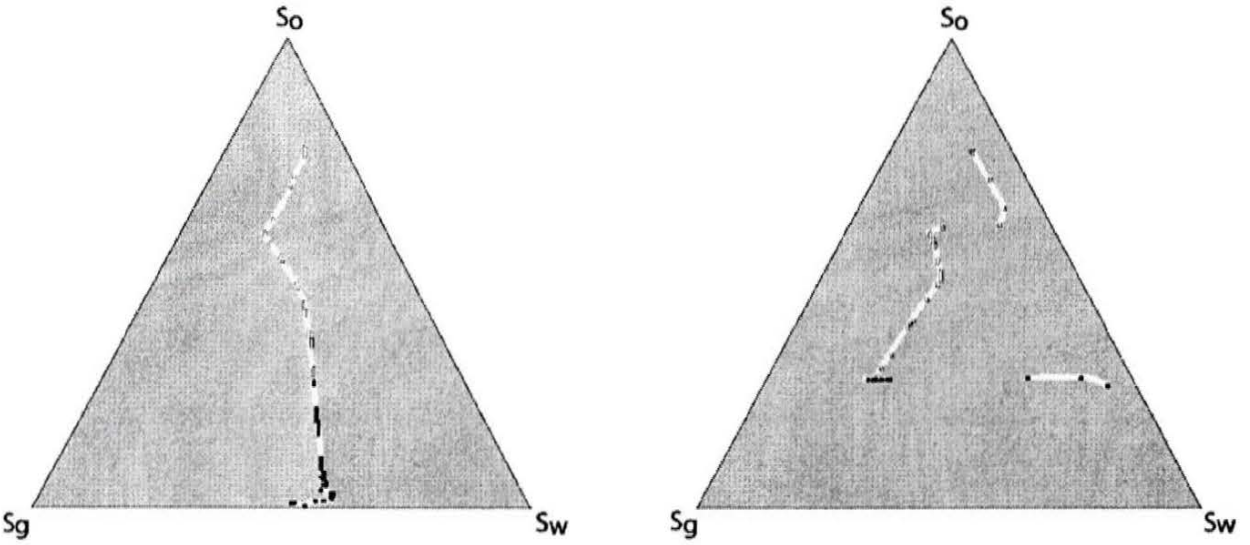

Figure 9. Saturation trajectories for the first two iterations. The initial trajectory of the macroscopic simulator is shown to the left while the second iteration trajectory based on the relative permeability functions of the first trajectory is shown to the right.

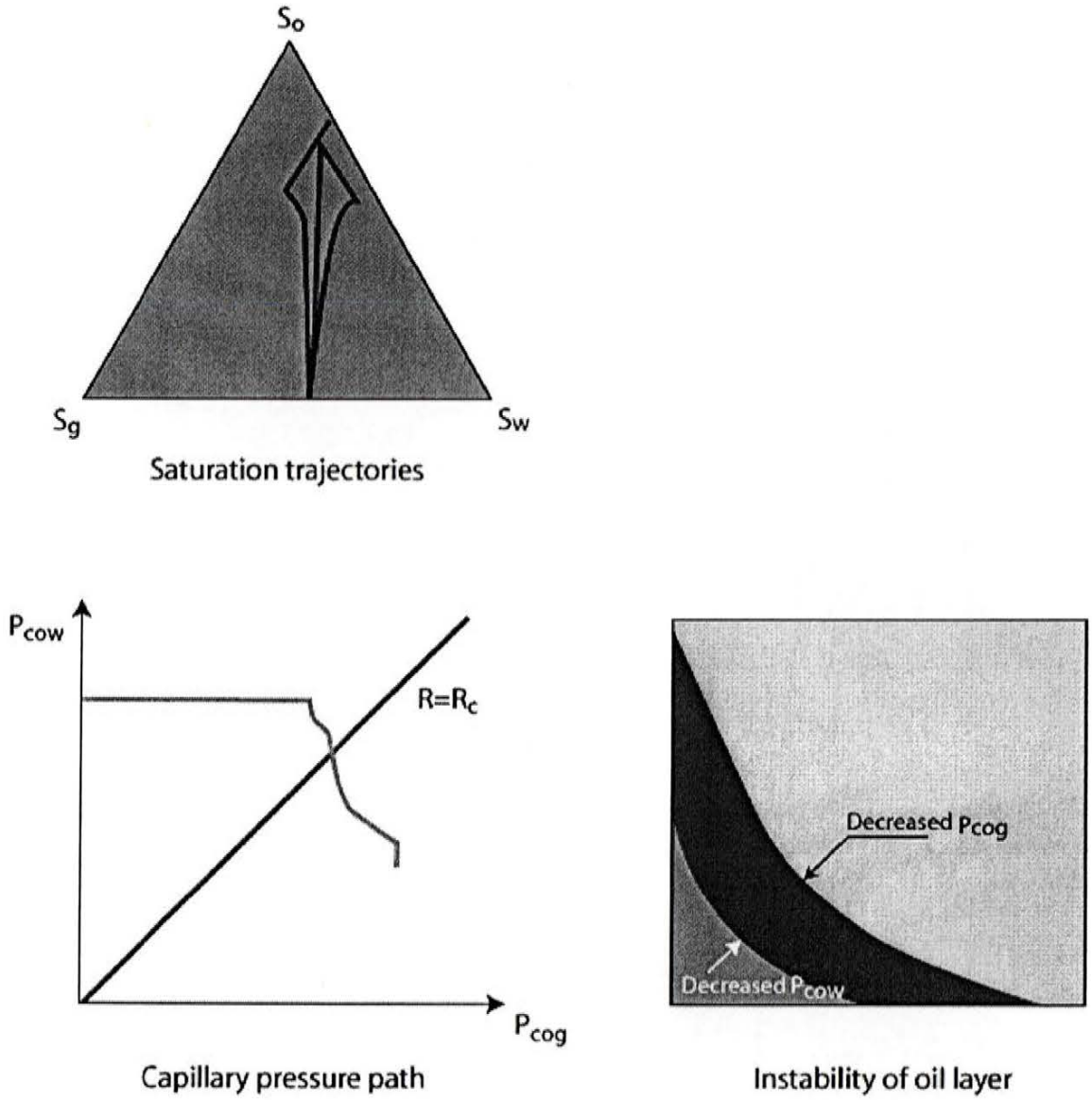

Figure 10. Trajectories in the saturation and capillary pressure spaces during WAG injection. The movement is generally towards the unstable oil layer. The saturation trajectories impose higher water saturation and higher gas saturation causing the oil-water and the oil-gas interfaces to move towards each other causing the collapse of the oil layer.

The movement in the capillary pressure space in the network simulator corresponds to movement of the oil-water interface towards the center of the pore. The oil-gas interfaces are pushed towards the corner of the pores (cf. Figure 10). This reduces both the effective flow area available to the oil phase on the pore-level and the connectivity of the oil phase on the network level.

The movement in capillary pressure space causes the network model to encounter the domain of the residual oil saturation much earlier than the saturation corresponding to the injection conditions given by the left state S_l. Once the oil layers became unstable the injection of gas caused break-up

of the oil phase into discontinuous oil ganglia which could be mobilized by double drainage mechanisms. This was in particular the case with $S_l = (S_g, S_w) = (0.35, 0.65)$ and $S_l = (S_g, S_w) = (0.4, 0.6)$. The lowest residual oil was encountered for the left state $S_l = (S_g, S_w) = (0.45, 0.55)$. This case was then investigated more thoroughly.

In the first iteration of the network model residual oil was encountered at $S_o = 0.3$. Consequently, the macroscopic saturation model cannot yield a saturation trajectory below the residual oil saturation because the oil phase becomes immobile at this saturation.

The iterative procedure collapsed after the second iteration when the network model generated relative permeability functions which caused the macroscopic model to return a saturation trajectory which was located in the upper third of the saturation triangle. The oil phase had become discontinuous at an oil saturation $S_{oc} = 0.59$ (cf. Figure 11). Recall that the oil phase relative permeability of discontinuous oil by definition is zero. However, during computational experiments oil remained connected to the inlet and the outlet face and was thus displaceable in the network simulations.

There are two causes of the high S_{oc} saturation. The first cause was that the gas phase invaded the oil phase by Haines' jumps while the oil layers were still stable and good connectivity of the oil phase existed. This invasion of oil by gas took place in larger pores. Subsequently, when the oil layers became unstable the connectivity of the oil phase was effectively reduced in the most conductive pores. The second cause that led to high discontinuous oil saturation was that the gas phase invaded the oil phase. The oil phase could not establish stable layers and, consequently, broke up into ganglia unable to conduct oil. However, it should be noted that the gas phase was capable of pushing the discontinuous oil phase thereby reducing the saturation of that phase.

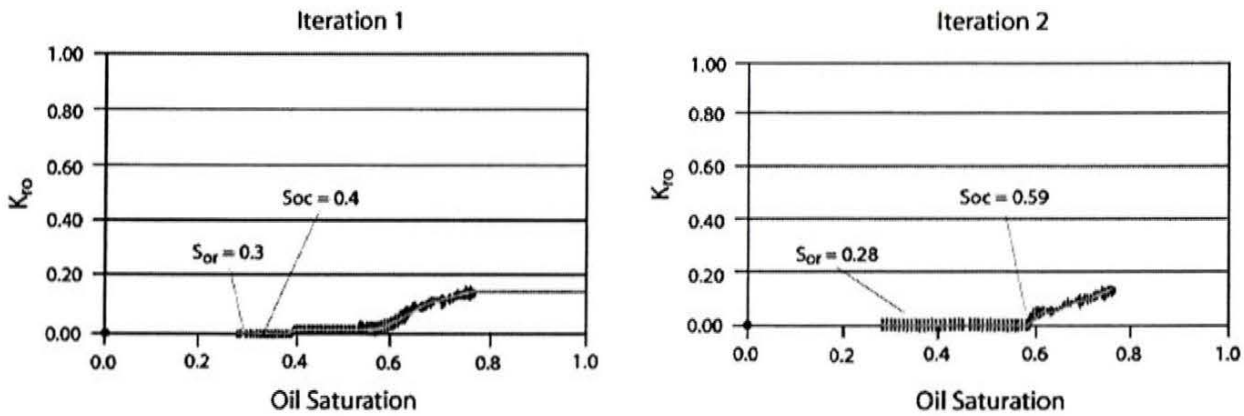

Figure 11. Relative permeability functions obtained for the two first iterations of the S_l = (0.55, 0.45). The markers indicate the relative permeability functions obtained by the network model while the gray lines indicate the relative permeability function forwarded to the macroscopic flow model. S_{or} indicates the residual oil while S_{oc} marks discontinuous oil saturation where the conductance of the oil phase becomes zero.

10. Concluding Remarks

The collapse of the iterative procedure during WAG injection process raises two critical issues concerning the iterative procedure.

The first issue concerns calculations of conductance of the oil phase for saturations below the discontinuous oil saturation. The second issue deals with the high residual oil saturations which seems to be in disagreement with the field observations where WAG recovery has been reported to yield increased recovery efficiency.

Problems concerning determination of relative permeabilities by the network model and its definition in Darcy's law have been addressed by Mani and Mohanty (1998). In their model, the saturation of the pore space can change inside the network even in the case where the relative permeability to a phase is zero. However, the macroscopic flow model can describe changes in phase saturation only in the case of a nonzero mobility of that phase. Consequently, the area of the saturation triangle where a phase is mobile is different for the two models. This creates an obstacle for the convergence process, because by changing saturation of a phase in the network model one cannot follow the saturation trajectory produced by the macroscopic model into the region of the residual oil saturation.

.

Mani and Mohanty (1998) have suggested a network model where the conductance of a phase consists of two contributions: steady-state conductance and unsteady-state conductance. They proposed the following formulation of Darcy's law for multiphase flow

$$v_i = -\frac{k \cdot k_{ri}}{\mu_i} \nabla P_i + v_{unsteady-state} \tag{5}$$

The mechanisms governing steady-state transport are similar to those underlying relative permeabilities in quasi-static network models: given the total flow into or out of the section of the network, the phase viscosity, the imposed pressure drop, and the absolute permeability, transport coefficients are calculated from the multiphase Darcy's law. The flow can take place through films, layers, or in pores where the conductance of the phase can be derived by assuming the laminar flow. The key assumption in the definition of the steady-state conductance is that the flowing phase is continuous and the pressure drop is given by the generalized Darcy's law.

The unsteady-state conductance is represented by the response of the system to a change in capillary pressure. This response leads to a time dependency of the saturation change in the network model controlling the time for a pore-scale event to take place. More precisely, in order to adequately capture the relative permeability concept, a dynamic network simulator must replace the quasi-static network simulator

It should be noted that changes in capillary pressure due to changes in one phase pressure could affect the saturation of another phase. Consequently, the inclusion of the unsteady-state conductance can be regarded as a coupling between the conductances of one phase and the pressure gradient associated with a different phase.

The high residual oil saturation of the WAG injection processes predicted by the network simulator is in disagreement with high recovery efficiencies reported in field studies (cf. Christensen, Stenby, and Skauge, 1998). The recovery factor is usually controlled by three basic recovery mechanisms: the vertical sweep, horizontal sweep and microscopic displacement efficiency. The negligence of these effects by the network- and macroscopic model may significantly influence efficiency of oil recovery.

In general, increased oil-water capillary pressure in the network model leads to thicker oil layers. Compared to gas injection, WAG injection is characterized by a movement in the capillary pressure space towards the region where oil layers are unstable. Thus, it appears that the increased oil recovery efficiency may not be explained by the presence of oil layers on the pore-level i.e. the microscopic displacement efficiency. Moreover, the effects of gravitation might actually also play a role on the network level. In addition, the network simulations have shown that computational results were sensitive to the initial placement of the gas phase in the network. More precisely, oil conductivity was lost faster when gas was assigned to the entire end-face of the network as compared to the assignment to a single pore or to a limited number of pores.

In conclusion, the two models used in the iterative procedure do not necessarily adequately represent some of the essential processes responsible for increased oil recovery efficiency of WAG injection processes.

References

Christensen, J.R., Stenby, E.H., and Skauge, A.H., "Review of WAG Field Experience", SPE Paper No. 39883, 1998.

Fenwick, D. H. and Blunt, M.: "Calculating Three-Phase Relative Permeabilities Using Network Modeling", presented at the 5th European Conference on the Mathematics of Oil Recovery, Leoben, Austria, 1996.

Fenwick, D. H. and Blunt, M.: " Use of Network Modeling to Predict Saturation Paths, Relative Permeabilities and Oil Recovery for Three-phase Flow in Porous Media", SPE 38881. Paper presented at the 1997 SPE Annual Technical Conference and Exhibition, San Antonio Texas, U.S.A. 5-8 October 1997.

Fenwick, D. H. and Blunt, M.: "Network Modeling of Three-phase Flow in Porous Media", *SPEJ*, **3**, 86-97, 1998.

Lesne, A.: "Renormalization Methods. Critical Phenomena, Chaos, Fractal Structures", J. Wiley & Sons, 1998.

Mani, V. and Mohanty, K. K.: "Pore-level Network Modeling of Three-phase Capillary Pressure and Relative Permeability Curves," *SPEJ*, pp. 238-248, September 1998.

Varchenko, A.N. and Zazovski, A.F.: "Three-Phase Flow of Immiscible Fluids" (in Russian), Itogi Nauki (Ser. Mekhanika), **4**, pp. 98-153, 1992.

Appendix D

D1. Convergence of Iterative Procedure

This appendix contains additional information about the convergence of the iterative procedure aimed at determination of the selfconsistent relative permeability functions for the gas injection process. The initial saturations of oil and gas phases are $S_o = 0.6$ and $S_w = 0.4$, respectively. The result for each iteration is shown as a path in the capillary pressure space along with all the previous paths. The relative permeability functions are shown in blue for the current iteration, the previous iteration in red, and the iteration that was forwarded from the network simulator to the macroscopic simulator in the previous iteration as a green line. The continuous line is used to indicate that the relative permeability functions of the macroscopic simulator are continuous functions of phase saturations, whereas the network simulator yields the relative permeability functions at discrete values of phase saturations.

Relative Permeability of water

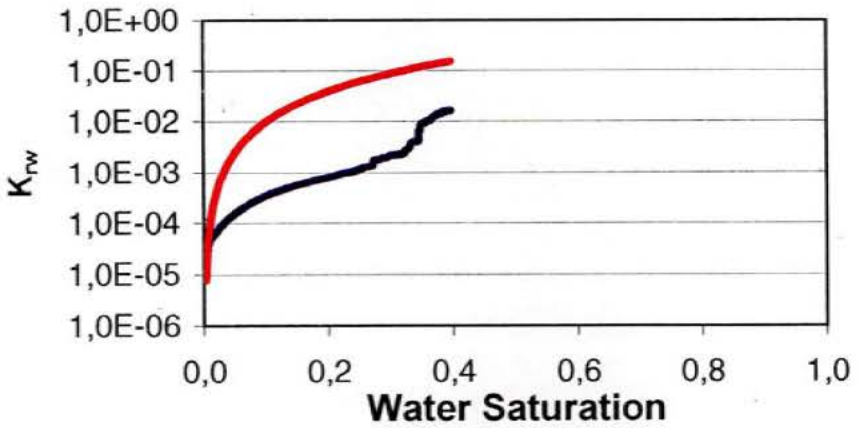

Oil Relative Permeability

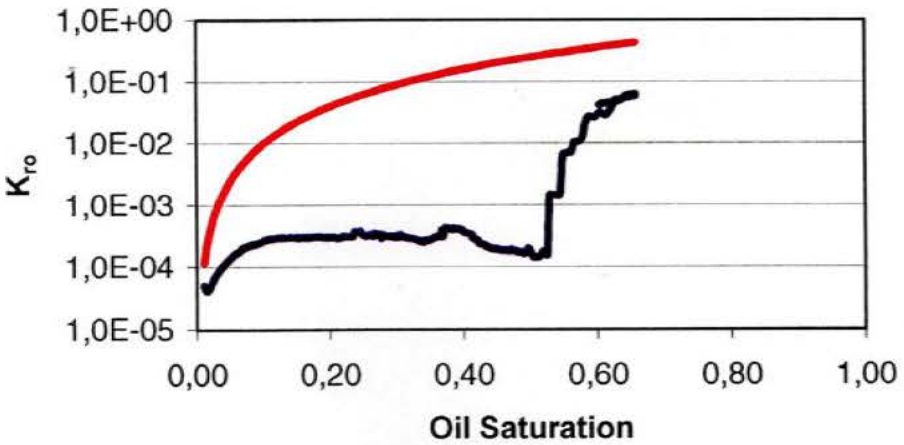

Gas Relative Permeability

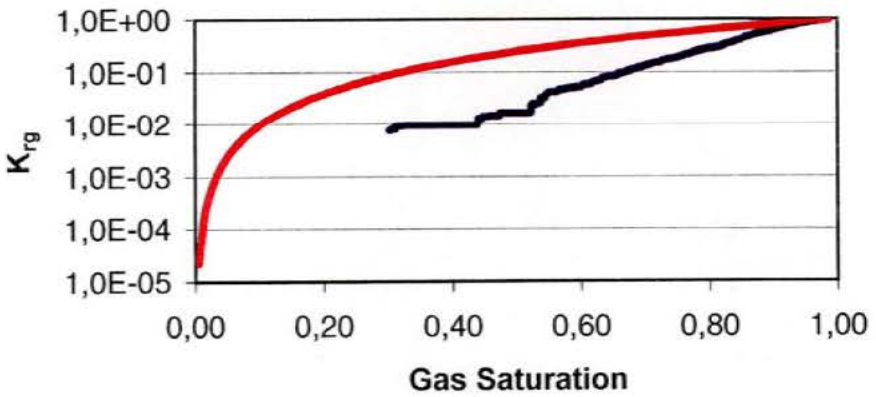

Capillary pressure space

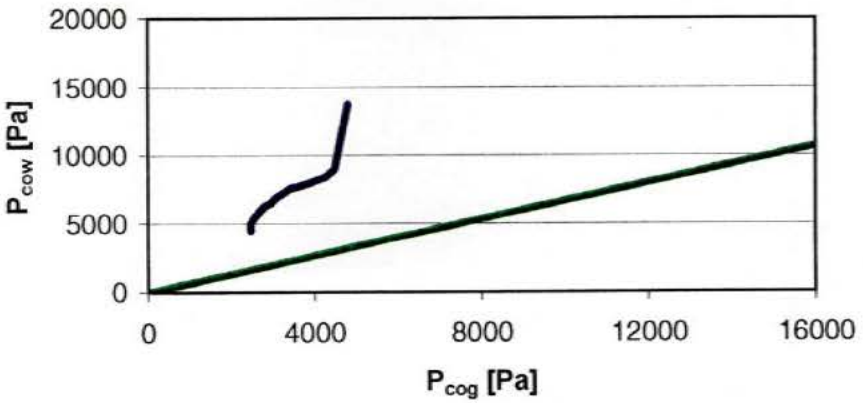

Relative Permeability of Water

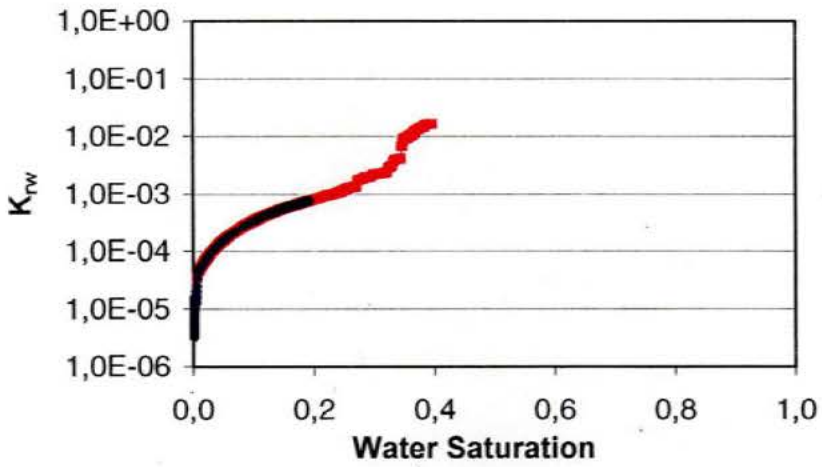

Relative Permeability of Oil

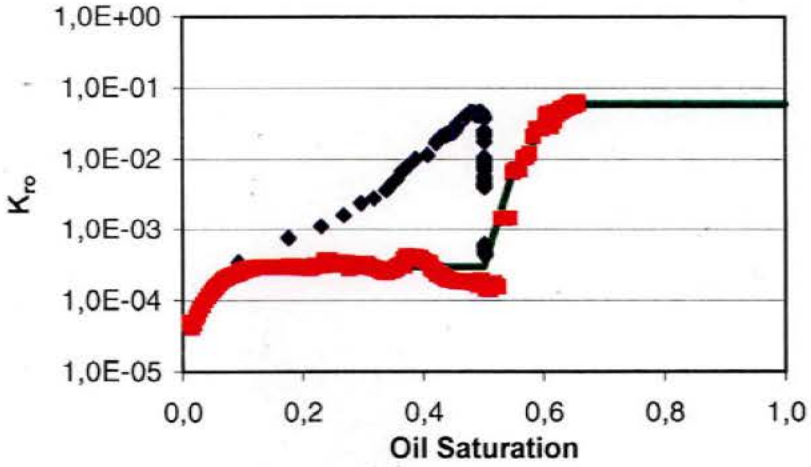

Relative Permeability og Gas

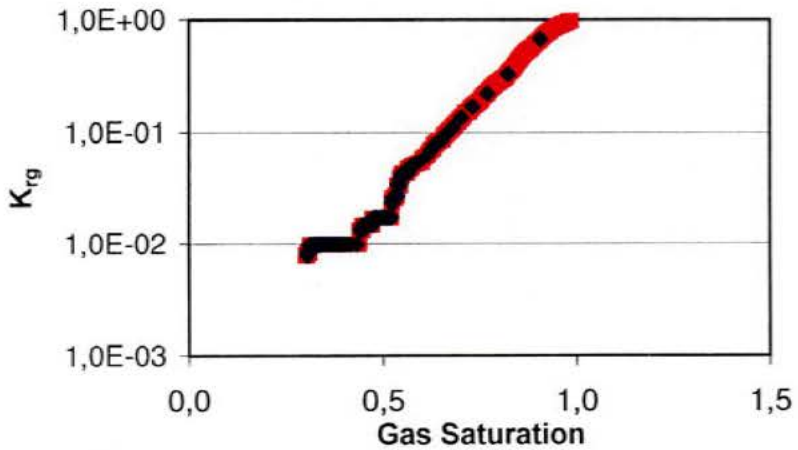

Capillary Pressure Space

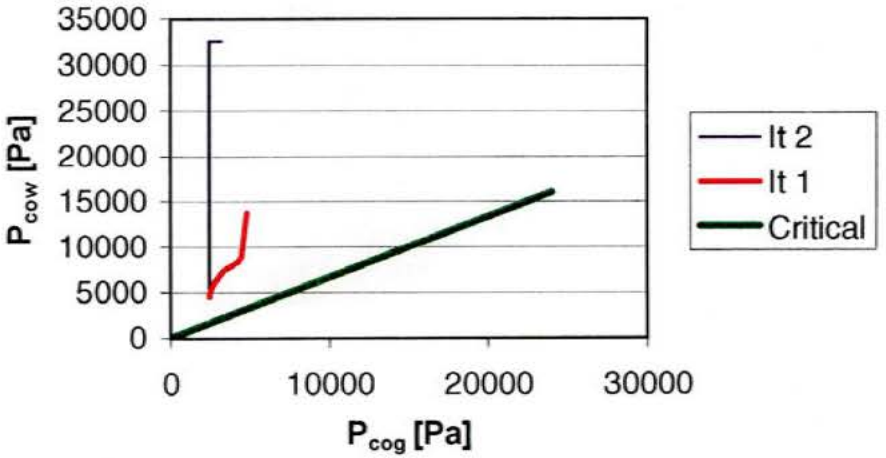

Relative Permeability of Water

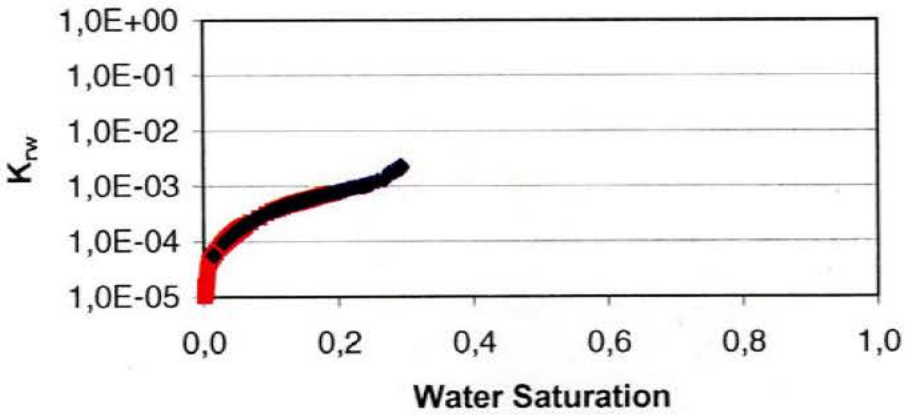

Relative permeability of Oil

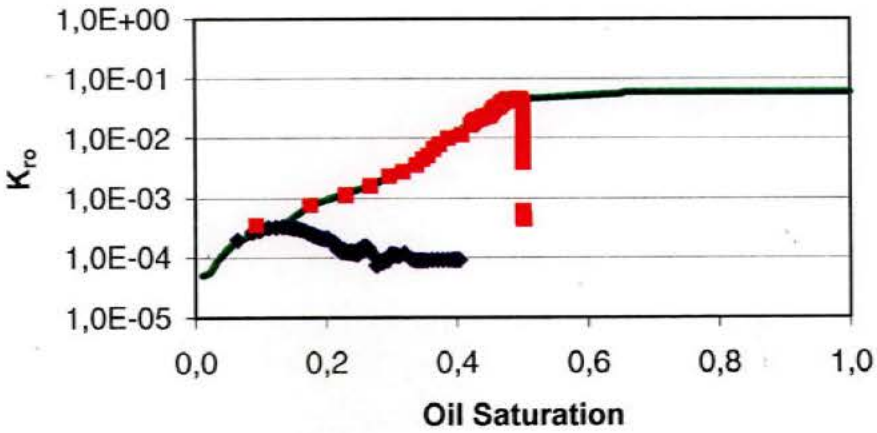

Relative Permeability of Gas

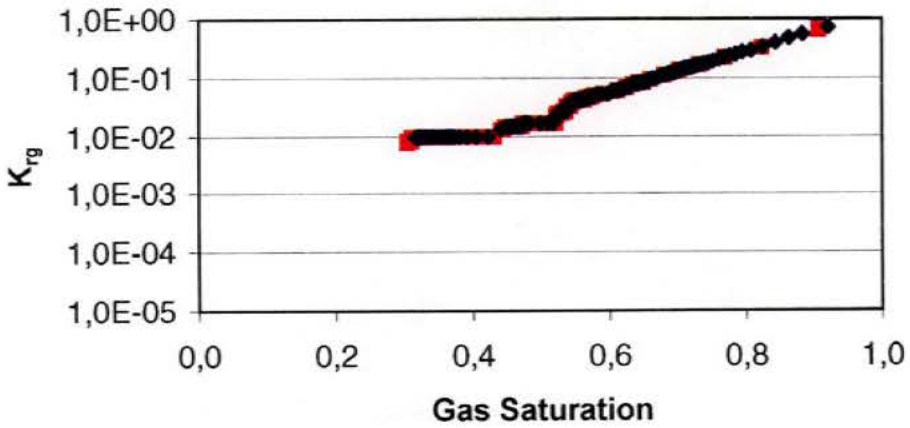

Capillary pressure space

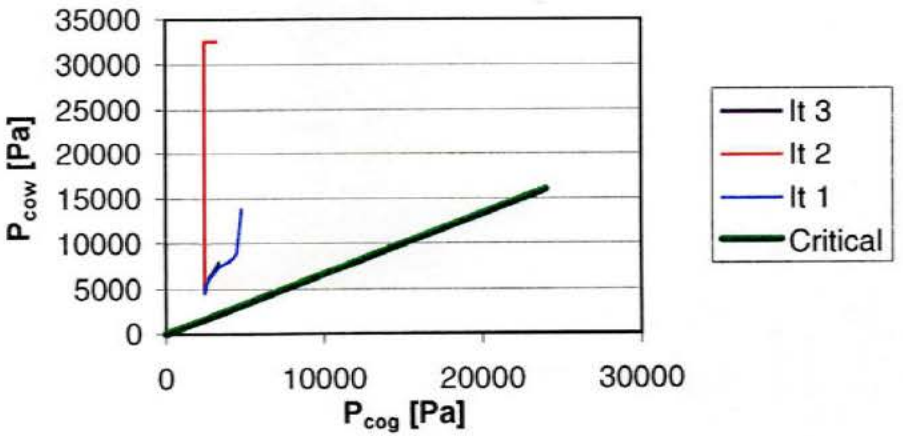

Relative Permeability of water

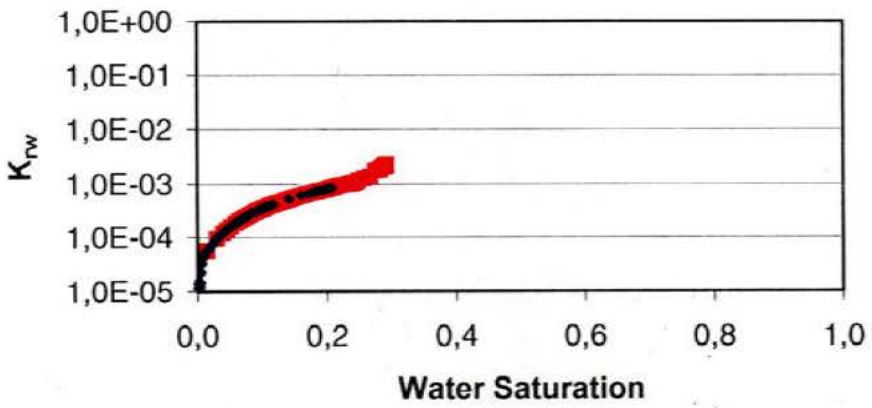

Relative Permeability of Oil

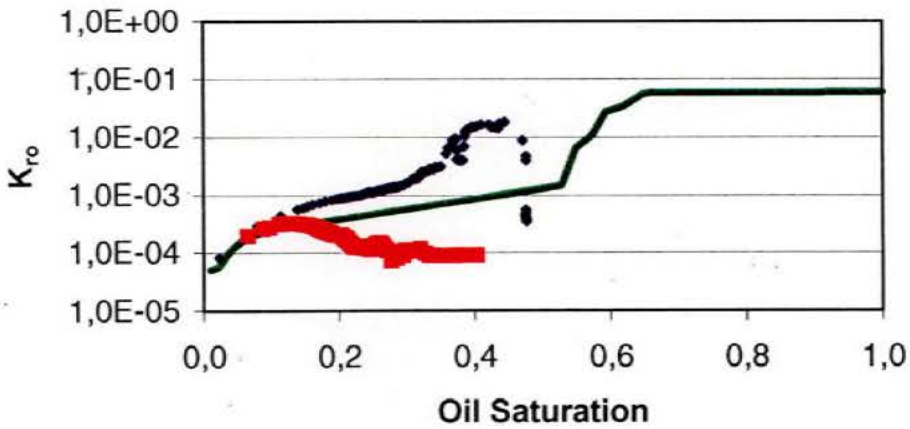

Relative Permeability of Gas

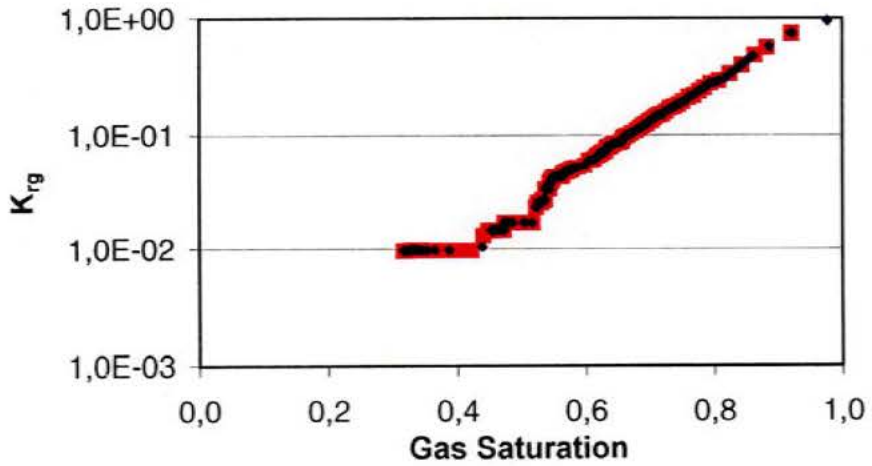

Capillary Pressure Space

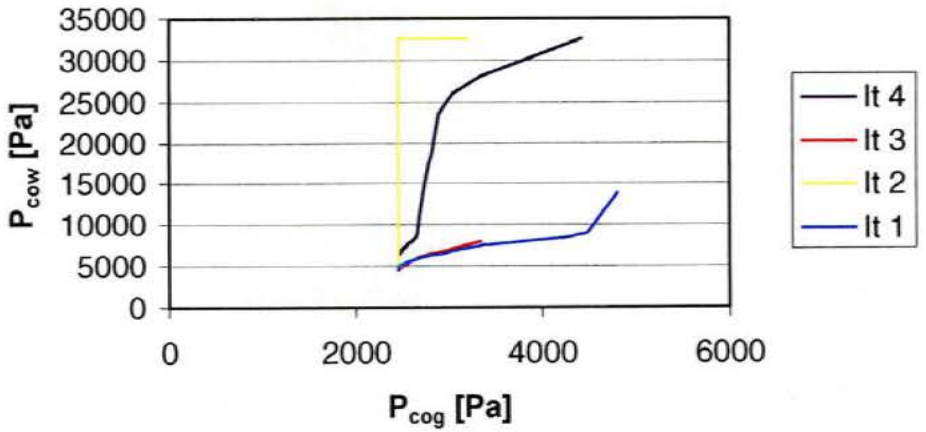

Relative Permeability of Water

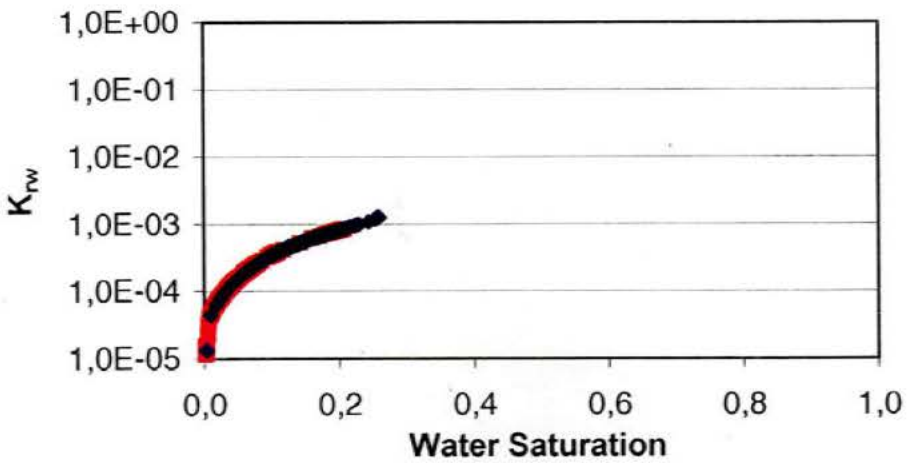

Relative Permeability of Oil

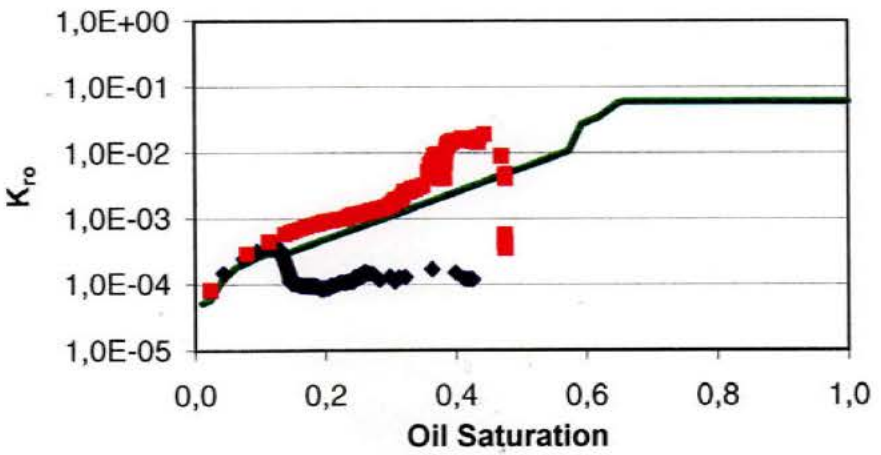

Relative Permeability of Gas

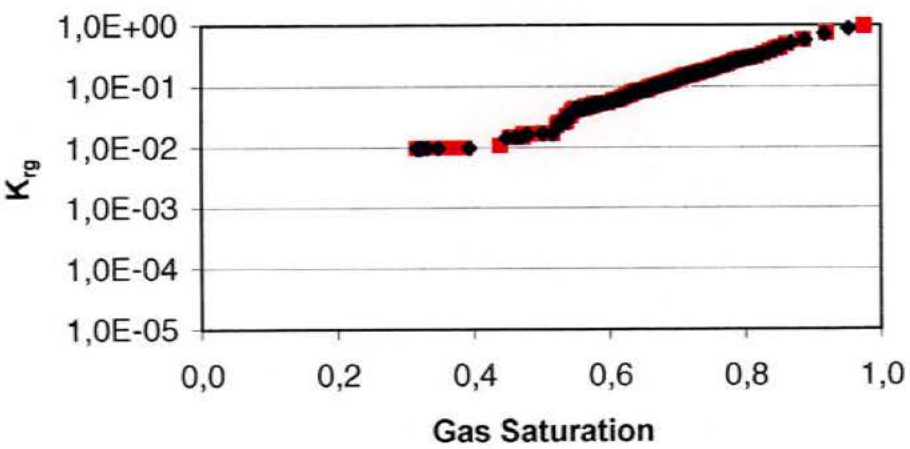

Capillary pressure space

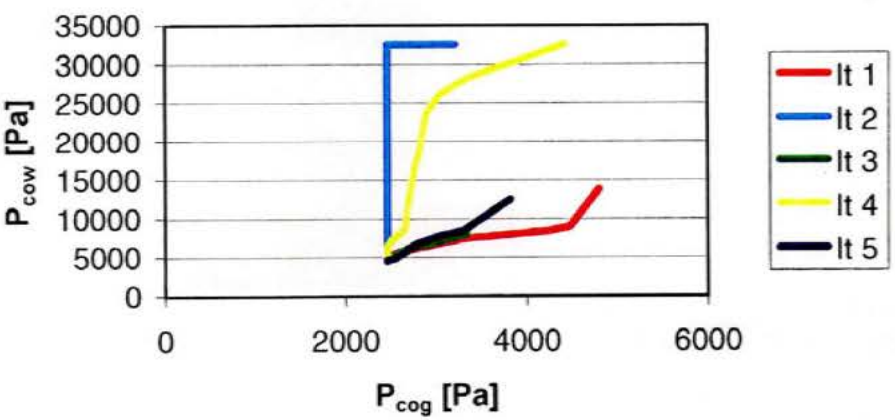

Relative Permeability of Water

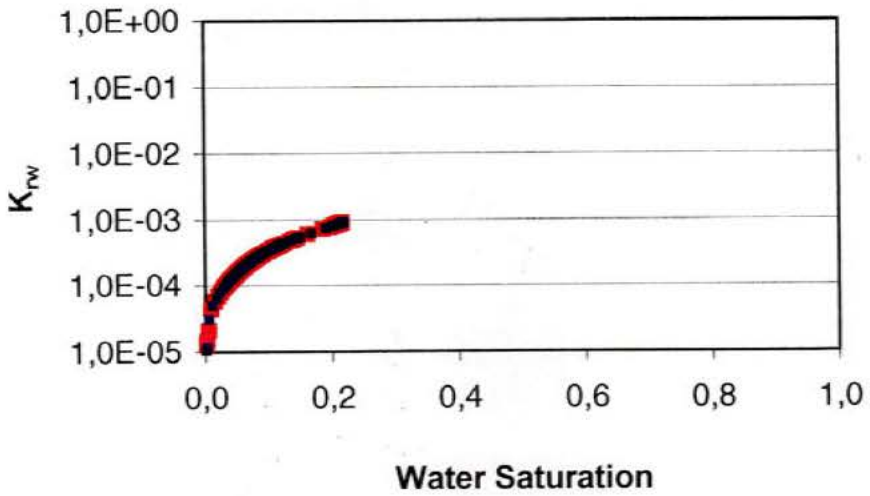

Relative Permeability of Oil

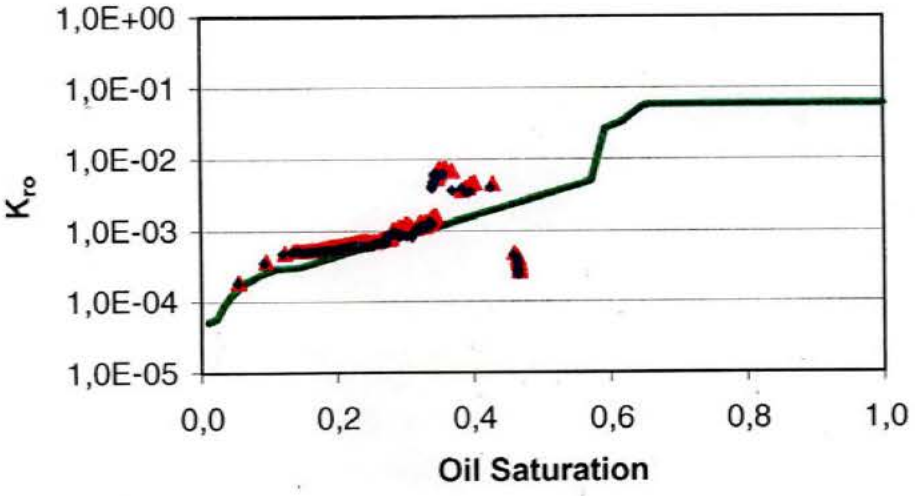

Relative Permeability of Gas

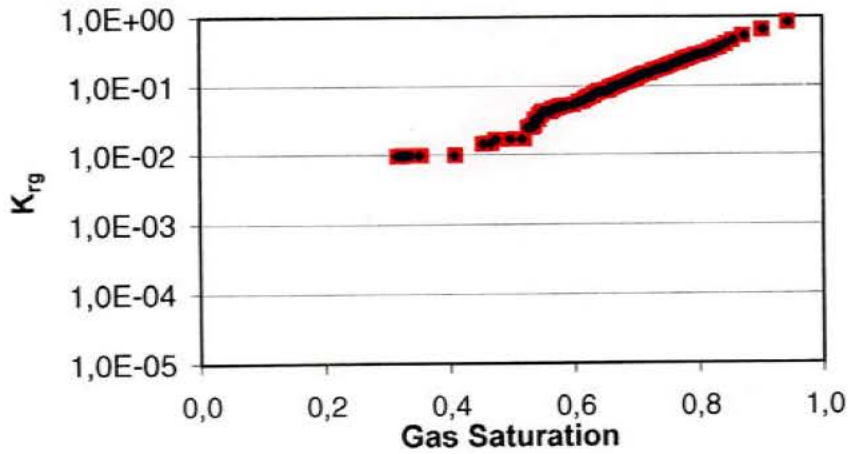

Capillary Pressure Space

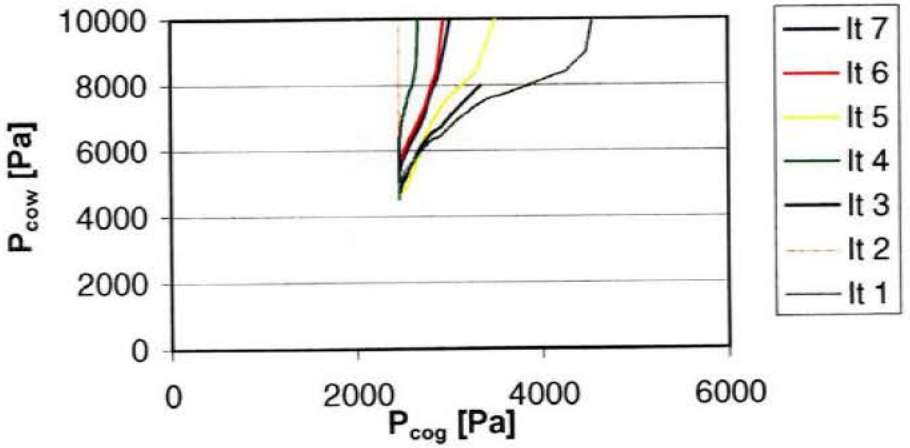

Relative Permeability of Water

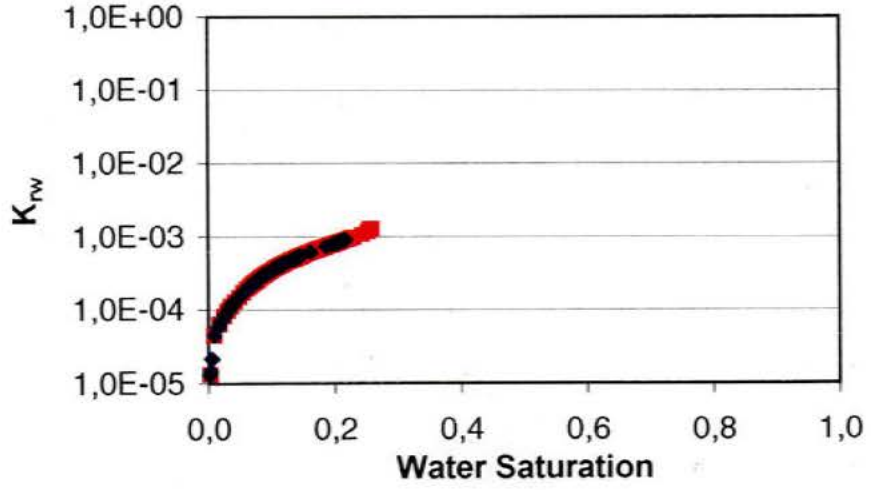

Relative Permeability of Oil

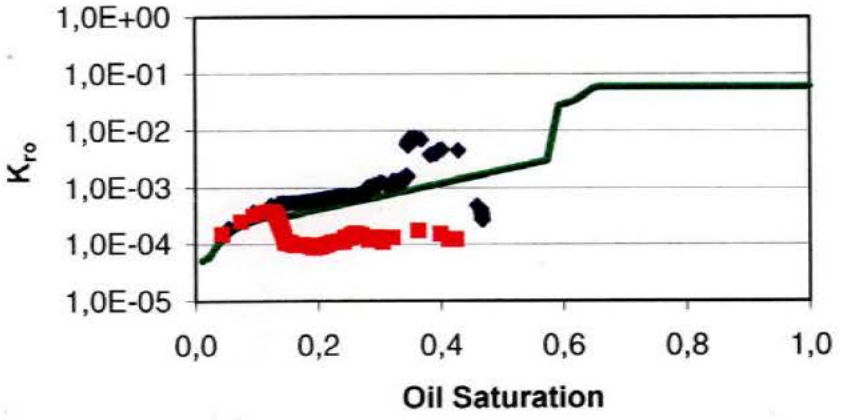

Relative Permeability of Gas

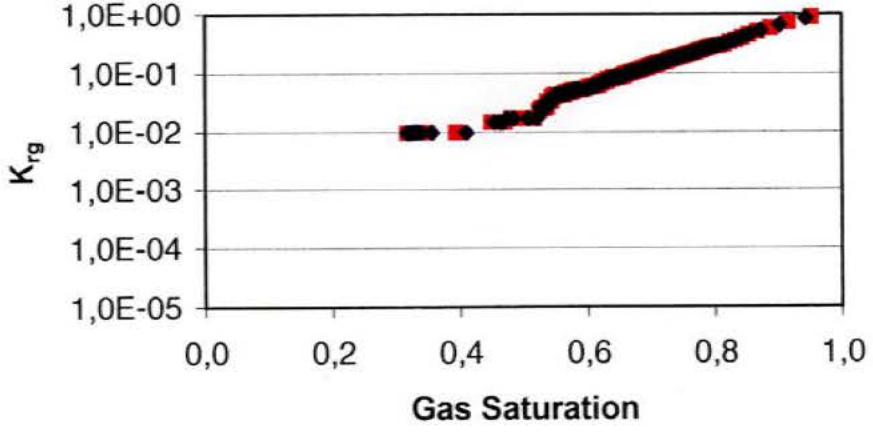

Capillary pressure Space